



Kent Academic Repository

Caujolle, Sophie (2019) *Fourier Domain Optical Coherence Tomography, a structural and a functional imaging modality.* Doctor of Philosophy (PhD) thesis, University of Kent,.

Downloaded from

<https://kar.kent.ac.uk/82202/> The University of Kent's Academic Repository KAR

The version of record is available from

This document version

UNSPECIFIED

DOI for this version

Licence for this version

UNSPECIFIED

Additional information

Versions of research works

Versions of Record

If this version is the version of record, it is the same as the published version available on the publisher's web site. Cite as the published version.

Author Accepted Manuscripts

If this document is identified as the Author Accepted Manuscript it is the version after peer review but before type setting, copy editing or publisher branding. Cite as Surname, Initial. (Year) 'Title of article'. To be published in *Title of Journal*, Volume and issue numbers [peer-reviewed accepted version]. Available at: DOI or URL (Accessed: date).

Enquiries

If you have questions about this document contact ResearchSupport@kent.ac.uk. Please include the URL of the record in KAR. If you believe that your, or a third party's rights have been compromised through this document please see our [Take Down policy](https://www.kent.ac.uk/guides/kar-the-kent-academic-repository#policies) (available from <https://www.kent.ac.uk/guides/kar-the-kent-academic-repository#policies>).

University of Kent
Doctoral Thesis

Fourier Domain Optical Coherence
Tomography, a structural and a
functional imaging modality

Author:

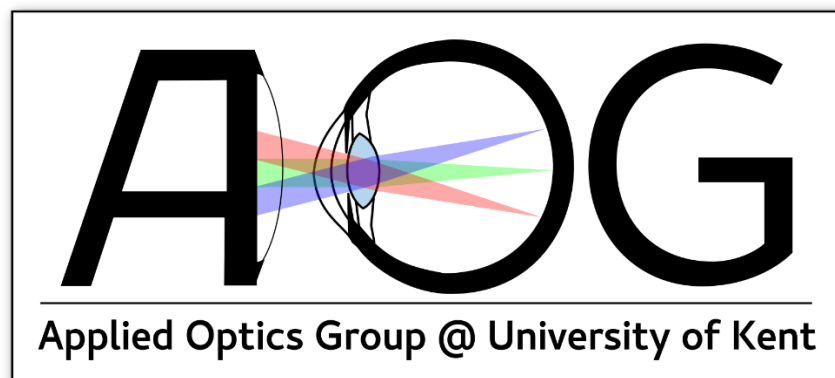
Sophie Caujolle

Supervisor:

Prof Adrian Gh. Podoleanu

*A thesis submitted in fulfilment of the requirements
the degree of Doctor of Philosophy
in the*

Applied Optics Group
School of Physical Sciences



June, 2019

A thesis submitted in collaboration with



and funded by



« Sans la curiosité de l'esprit, que serions-nous ? Telle est la beauté et la noblesse de la science : désir sans fin de repousser les frontières du savoir, de traquer les secrets de la matière et de la vie sans idée préconçue des conséquences éventuelles »

- Marie Skłodowska Curie -

Declaration of Authorship

I, Sophie CAUJOLLE, declare that this thesis titled, “Frequency Domain Optical Coherence Tomography, a structural and a functional imaging modality” and the work presented in it are my own. I confirm that:

- This work was done wholly or mainly while in candidature for a research degree at this University.
- Where any part of this thesis has previously been submitted for a degree or any other qualification at this University or any other institution, this has been clearly stated.
- Where I have consulted the published work of others, this is always clearly attributed.
- Where I have quoted from the work of others, the source is always given. With the exception of such quotations, this thesis is entirely my own work.
- I have acknowledged all main sources of help.
- Where the thesis is based on work done by myself jointly with others, I have made clear exactly what was done by others and what I have contributed myself.

Signed:

Date :

Abstract

Optical Coherence Tomography (OCT) is a non-invasive depth imaging technique based on the optical signal reflected from a sample. Over the last two decades it has become one of the primary biomedical imaging technologies, giving access to structural information in the sample with micrometre precision over a few millimetres in depth. Originally, OCT was exclusively used as a structural imaging modality, where functional features have also been retrieved using the phase of the light signal. From this, later extensions such as Optical Coherence Tomography Angiography (OCTA) have been implemented by retrieving structural data over time.

The first aim of this thesis was to enhance the structural OCT imaging resolution using a broadband (supercontinuum) light source from NKT Photonics A/S. Historically, this source was considered too noisy for biomedical imaging but, in this work, it has been shown that the visualisation of the different layers from a human cornea can be achieved, and that the results compare favourably to those obtained from a more traditional broadband source.

The second aim was to determine whether OCTA can be considered as a qualitative or quantitative method. To achieve this, OCTA software was implemented and tested using a tube filled with a 5% intralipid solution. The velocity of the solution was tuned using a pump. It was found that at higher velocities, higher OCTA values were obtained. From our results, we can conclude that OCTA methods are quantitative.

The final aim was to combine both OCT and OCTA in order to assess the viability of bovine embryos 7 days after fertilisation, which is the first time that this has been achieved. The evolution over the 7-day period was characterised using OCT and OCTA depth-resolved images. The resulting motion maps, combined with the OCT images, highlighted the parts of the samples which were moving and thus allowed the identification of the viable embryos and ensure a higher chance of fertilisation success.

Acknowledgements

I would like to acknowledge the European Commission and to have support my research through the UBAPHODESA project, grant number 607627. This has allowed me to travel and present my work in different conferences and learn from my pairs.

This thesis would have never been possible without the presence of amazing people surrounding me during these past few years.

First, I would like to acknowledge my supervisor Prof. Adrian Podoleanu for his help and trust in the last few years and to have allowed me to be part of the AOG group. Despite having more ideas than time to explain them, you have created this amazing international group and succeeded to make anyone entering feel at home.

But also, to my supervisor from NKT Photonics, Dr. Lasse Leick and Dr. Thomas Feutcher who help me to fight against my doubts, to believe in me and to have taught me to find a balance between work and personal life. This is a truly valuable skills to have while entering in industry.

Because “le fardeau supporté en groupe est une plume”, I would like to thank my team members from UBAPHODESA who went through along the same doubts and up-down and became with the years dear friends. And more specifically, Auf Félix, vom Laborpartner zum Freund. Danke, dass du immer die richtigen Worte gefunden hast, um mich zu ermutigen und mir in den schwierigen Momenten zu helfen (und es gab ein paar). Bitte hör auf, mich zu erschrecken. Ohne dich wäre dies nie eine abgeschlossene Arbeit gewesen! We are waiting you in Heidelberg. A Magalie qui malgré nos différences, a toujours su les mettre de côté pour me soutenir et m'épauler dans les moments difficiles.

To Sally and Manuel, thank you for the chin-up conversation, help and support through this long process. Thank you for the software helped, advised from an experimented scientist, daddy jokes and Kate Busch song during lunch lighting the last bits of the thesis. Special thanks to Sally who has taken the time to proof read and correct my bat-shit-insane English. I still own you a cake!!! I am waiting your visit in Heidelberg.

To Dr. Cernat and Dr. Bradu, more known as Ramona and Adrian for their wise advice and calm through writing my publication or to find the “phantom frequency” in my lab.

To the new generation, Adrian F. and Andy to have accepted me in their office full of Pepsis and crazy stuffs in the last few months and to have always been here to have a laugh. Good Luck, now it is your turn!!

In a more personal level,

Je voudrais aussi remercier mes parents qui sont mon plus grand exemple et m'ont toujours encouragée dans mon travail et à persévérer malgré que cela ait signifié de partir loin d'eux.

A mon frère qui m'a appris à être forte, indépendante et fière pour donner le meilleur de moi-même et à ma chère belle-sœur qui trouve toujours les mots pour adoucir ceux de mon frère. A mes deux petites nièces qui partent pour être des scientifiques et que j'essayerai d'amadouer pour le devenir. On a bien trop de médecins!!

I would like to thank Mike, my best friend and mon amoureux who has been here to correct and support me aligning my system during long and intense week-end and to proof read my thesis. The one, since then, that has encouraged me in any of my projects, even if it has the consequence of moving to Germany and allowed me to be who I am, a strong independent woman.

Merci à ma Manou qui nous a appris à être une véritable femme forte et indépendante, à ma tante Sylvie qui est un exemple pratique et, mes cousines Léa et Laure de m'avoir montrée la direction pour devenir une « femme Barbara Gould ». Avec mention spéciale pour Laure, pour m'avoir encouragée à candidater pour cette prestigieuse bourse.

A mon petit papi et ma petite mamie, partis bien trop tôt pour voir l'adulte que je suis devenue mais qui m'ont transmis la valeur du travail. Vous me manquez.

To Rosa, who was an amazing roommate in Copenhagen and now become one of my best friends. Thank you for your support, crazy talks and taking care of me when I was not able to. Slava, Slava la patata.

Contents

1. Introduction	13
1.1 Biomedical Imaging	13
1.2 Light Matter Interaction	15
1.3 Optical Coherence Tomography	17
1.4 OCT volume skeleton	20
1.5 Organisation of the Thesis	20
2. A structural modality: Ultrahigh resolution Optical Coherence Tomography (UHR-OCT)	29
2.1 Principle of Optical Coherence Tomography	29
2.1.A. Basics of OCT	29
2.1.A.1. Michelson interferometer	29
2.1.A.2. Mathematical description	31
2.1.B. Fourier Domain Optical Coherence Tomography	35
2.1.B.1. Time Domain OCT (TD-OCT) vs Fourier Domain OCT (FD-OCT)	35
2.1.B.2. Spectrometer based Optical Coherence Tomography (Sp-OCT)	39
2.1.C. Resolution in OCT	43
2.1.C.1. Transverse resolution	44
2.1.C.2. Axial Resolution	46
2.2 OCT and supercontinuum source	48
2.2.A. Preamble	48
2.2.B. Supercontinuum laser in biomedical imaging	50
2.2.C. SuperK from NKT Photonics	51
2.2.D. Dispersion characterisation	53
2.2.D.1. Simple dispersion compensation	54
2.2.D.2. Split spectrum method applied to dispersion compensation	56
2.2.E. Broadband source in OCT: Comparison between a Ti:Sa and a supercontinuum source - A case study	63
2.2.E.1 Introduction and Methods	63
2.2.E.2 Results and Discussion	65
2.2.E.3 Conclusion	66
2.3 OCT and complex Master Slave Interferometry (cMSI) method	71
2.3.A. Fourier Transform vs Complex Master Slave interferometry	71
2.3.A.1 Fourier Transform	71

2.3.A.2 Complex Master Slave interferometry (cMSI) method	73
2.3.B. cMSI: phase information conservative method	76
2.3.B.1 Introduction	76
2.3.B.2 Method	77
2.3.B.3 Results	79
2.4 Conclusion	81
3. A functional modality: motion detection with FD-OCT	89
3.1 Introduction	89
3.1.A. Definition	89
3.1.B. Motivation	89
3.1.C. Parameters for the moving backscattering centres	91
3.2 Optical Coherence Tomography Angiography (OCTA)	93
3.2.A. Preamble	93
3.2.A.1. Principle	93
3.2.A.2. Decorrelation vs Doppler effect	94
3.2.A.3 OCT system and phantom parameters	95
3.2.A.4. Structural image vs functional image dimension	96
3.2.B. Amplitude based methods	97
3.2.B.1. Speckle Variance (SV)	98
3.2.B.2. Amplitude Decorrelation (AD)	100
3.2.B.3. Amplitude Difference (D)	102
3.2.C. Phase based methods	103
3.2.C.1. Phase Difference (PD)	104
3.2.C.2. Phase Difference Variance (PDV)	106
3.2.D Applications	107
3.3 Qualitative or quantitative method	111
3.3.A. Flow rate vs Flow speed	112
3.3.B. Angio-amplitudes vs speed	115
3.3.C. Angio-amplitudes vs angle	120
3.3.D. Dependence of angio-amplitudes on the focus position	124
3.3.E. Conclusion	128
3.4 Improvement of the angiography image	130
3.4.A. Temporal averaging	131
3.4.B. Spectral averaging	135
3.4.C. Impact of the windowing function applied on the structural images: Gaussian vs Hamming	144
3.4.D. Conclusion	150
3.5 Angiographic Volume - Scanning procedure	151
3.5.A. Transverse optical resolution (Δx) vs Digital resolution (DR)	151
3.5.B. Ramp signal control	154

3.5.C. Stair signal control	157
3.5.D. Conclusion	160
3.6 Final Conclusion	161
4 OCTA for depth resolved assessment of the viability of bovine embryos - A case study	172
5 Conclusion	185

List of Abbreviation

AD	Amplitude Decorrelation
cMSI	Complex Master Slave Interferometry
D	Difference
FA	Fluorescence Angiography
FD-OCT	Fourier Domain Optical Coherence Tomography
FT	Fourier Transform
ICA	Indocyanine Green Angiography
MSI	Master Slave Interferometer
OCT	Optical Coherence Tomography
OCTA	Optical Coherence Tomography Angiography
OPD	Optical Path Difference
PAM	Photoacoustic Microscopy
PD	Phase Difference
PDV	Phase Difference Variance
RBC	Red Blood Cells
SC	Supercontinuum Source
SNR	Signal-to-Noise Ratio
Sp-OCT	Spectrometer-based Optical Coherence Tomography
SS-AD	Split Spectrum Amplitude Decorrelation
SSM	Split Spectrum Method
SS-OCT	Swept Source Optical Coherence Tomography
SS-PDV	Split Spectrum Phase Difference Variance
SS-SV	Split Spectrum Speckle Variance
SV	Speckle Variance
TD-OCT	Time Domain Optical Coherence Tomography
Ti:Sa	Titanium Sapphire

List of Publication

Peer reviewed papers

- **S. Caujolle**, R. Cernat, G. Silvestri, M. J. Marques, A. Bradu, T. Feuchter, G. Robinson, D. K. Griffin, and A. Podoleanu, "Speckle variance OCT for depth resolved assessment of the viability of bovine embryos," *Biomed. Opt. Express* 8, 5139-5150 (2017)
- E. R. Taylor, S. Cavuoto, D. M. Beal, S. Caujolle, A. Podoleanu, and C. Serpell, "Can Gold Nanoparticles Aid Electrophoretic Detection of Sulphur in Biomolecules? Development of Gold-PAGE", *ChemRxiv* (2018).

List of peer review conferences:

- Danish Optical Society annual meeting 2014 (no proceeding), Organiser: Danish Optical Society, Venue: DTU Risø, 13 – 14. November 2014, Website: <http://dops.dk/>
Type: Poster
Title: **Building up a thermal light source for spectral domain optical coherence tomography (OCT)**
- Danish Opening Ceremony of the International Year of Light (no proceeding), Organiser: Danish Physics Society, Venue: DTU Lyngby, 22 – 23 January 2015
Type: Poster
Title: **Building up a thermal light source for spectral domain optical coherence tomography (OCT)**
- Danish Optical Society annual meeting 2015 (no proceeding), Organiser: Danish Optical society, Venue: Odense University, 19 – 20. November 2015, Website: <http://dops.dk/> Poster
Title: **Split-Spectrum Amplitude Decorrelation Angiography using an ultra-broadband source**
Type: Poster

Authors: **Sophie Caujolle**, Felix Fleischhauer, Thomas Feuchter, Lasse Leick and Adrian Gh. Podoleanu

- Photonics West 2017

Type: Poster, Posters I: Technology and Image Processing, Paper 10053-86, Sunday 29 January 2017, 5:30 PM – 7:30 PM

Title: **Phase-sensitive, complex-domain master-slave interferometry**

Authors: Manuel J. Marques, **Sophie Caujolle**, Sylvain Rivet, Adrian Bradu and Adrian Gh. Podoleanu.

- European Conferences on Biomedical Optics, 2017, Munich, Germany

Type: Oral presentation

Title: **Comparison between a supercontinuum source and a titanium sapphire laser in achieving ultrahigh resolution spectral domain optical coherence tomography (SD-OCT)**

Authors: **Sophie Caujolle**, Unterhuber, Thomas Feuchter, Adrian Gh. Podoleanu and René Werkmeister

Proceedings reference: S. Caujolle, A. Unterhuber, T. Feuchter, A. Podoleanu, and R. M. Werkmeister, "Comparison between a Supercontinuum Source and a Titanium Sapphire laser in achieving ultra-high resolution Spectral Domain Optical Coherence Tomography (SD-OCT)," in *Optical Coherence Imaging Techniques and Imaging in Scattering Media II*, M. Wojtkowski, ed., Vol. 10416 of SPIE Proceedings (Optical Society of America, 2017), paper 1041608.

- 2nd Canterbury Conference on OCT, SPIE 10591, 2nd Canterbury Conference on OCT with Emphasis on Broadband Optical Sources, 1059108 (5 March 2018), 6-8 Sept 2017; doi: 10.1117/12.2282912;

Type: Oral presentation

Prize: Third place on Best presentation award

Chapter 1

Introduction

1.1 Biomedical Imaging

The expression “biomedical imaging” pertains to the different image modalities allowing visualisation of biological tissue. It is mainly used in the human body to establish clinical diagnosis. To distinguish between the different biomedical imaging systems and assign the right modality to a specific application, two parameters can be used, the resolution and the penetration depth (Fig.1.1). Resolution can be defined as the smallest resolved distance between two points. Penetration depth is the range within which the sample is imaged along the axial direction (incident beam direction). Depending on the modality, the values for penetration depth and resolution can range from micrometres to centimetres. Figure 1.1 shows different imaging techniques as a function of their target range [1].

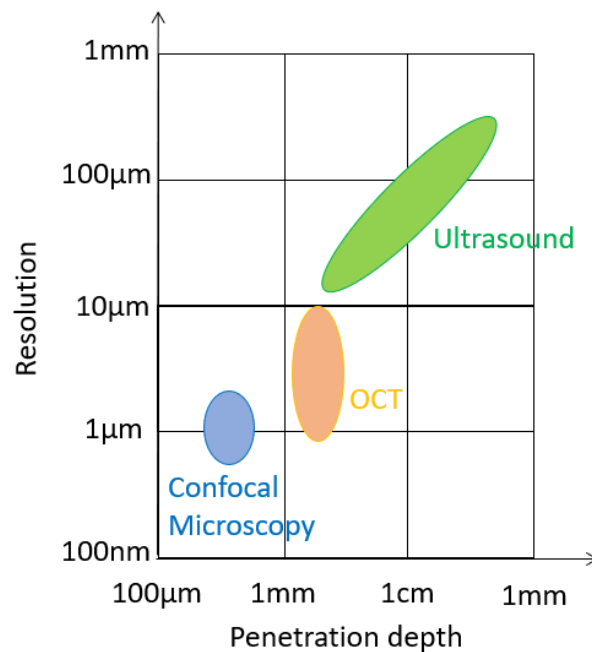


Fig.1.1 Penetration depth vs resolution for different imaging modalities adapted from [1].

The correct imaging technique depends upon the target and the detail that needs to be resolved. If the target is located deep within the tissue and the size of the features are large, there is no need for high resolution and alternative methods such as ultrasound may be more suitable. However, if the target is more superficial and high resolution is required, techniques such as confocal microscopy can be used. Currently, to create ultrahigh resolution images, for example for histology, the gold standard analysis is made with photon or electron microscopy [1]. Histology studies tissues and more exactly, cells which have a typical size of $1\mu\text{m}$ to several hundreds of microns. Its main goal is to distinguish between healthy tissue and malignant cells within a sample. This technique permits early diagnosis of cancers which increases survival rate exponentially and allows for lighter treatments. A first drawback is that it is invasive because it requires a biopsy to be taken from the patient. This requires to be prepared and sent to examination by a pathologist or a histologist. If the sample is on the skin, it is superficial and therefore not so difficult but in the case of a lung or a retina, direct access is not possible and heavier surgery is necessary. Another limitation is that the representation is in 2D and so, the visualization along the depth is partial. To overcome this, several slices can be cut to repeat the sample examination at different depths. This solution is restricted by the precision and the size of the dissection. Furthermore, because the observation is completely *ex-vivo*, it is not possible to study the tissue evolution. There is therefore a need to develop a 3D non-invasive ultrahigh resolution imaging method. Such a method in the biomedical imaging field is Optical Coherence Tomography (OCT).

OCT bridges the gap between ultrasound and confocal microscopy technologies by combining depth imaging with finer resolution (Fig.1.1). OCT is a non-invasive method [1] as it does not require contact like ultrasound and recently a push from clinicians have been made to improve its resolution to replace microscopy, the gold standard technology used in histology [2].

The possibility to reach ultrahigh resolution structural OCT images has been made achievable with the emergence of broadband light sources (Chapter 2). If in addition to the visualisation of small features, OCT could deliver functional information, this would increase the relevant application range of this technology (chapter 3) and allow for a full characterization of the sample.

1.2. Light Matter Interaction

When a light beam meets a solid, liquid or gaseous medium, a physical phenomenon occurs called “light matter interaction”. As seen in Fig. 1.2, such an interaction can be split into 5 processes: reflection, scattering, emission, transmission and absorption. To rebuild the information from the sample, different physical phenomena are used alone or combined depending on the considered biomedical imaging modalities. For example, photoacoustic microscopy (PAM) uses the absorption signal [3,4] to determine the composition of the sample whereas fluorescence lifetime imaging ophthalmoscopy is based on the emission signal [5]. For OCT, the scattering signal is most important, although the absorbed signal can also play a role in some OCT derivative technologies such as spectroscopic OCT [6-10].

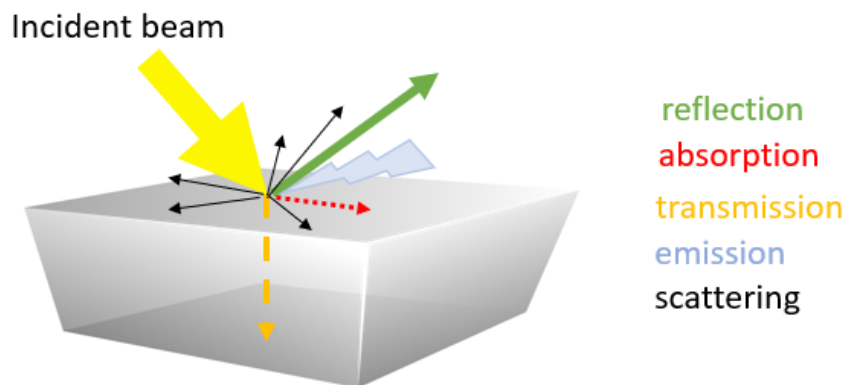


Fig. 1.2 Light matter interaction diagram

While the reflected signal propagates into a specific direction, the scattered light beam propagates in all directions. Three scattering models can be distinguished depending on the relative size of the particles, p in comparison with the incident beam wavelength λ [11]. In the case $p \gg \lambda$, it is a geometric scattering and it can be described with the optic laws in the paraxial approximation. If $p \ll \lambda$, the scattering signal is named as Rayleigh scattering and its amplitude evolves inversely proportional to the fourth power of the wavelength $\left(\frac{1}{\lambda^4}\right)$. In the last case, $p \sim \lambda$, it is the Mie scattering that is predominant. This is the main scattering model present in biological tissue and used in the different optical biomedical imaging modality. The reason is the similar size of the imaged particles and the propagated optical waves ($\sim \mu\text{m}$). In this model, the majority

of waves propagate whereas a small amount is backscattered. It is this backscattered signal, that contains the tissue information which is detected by the OCT system.

The parameters of the incident beam are directly linked with the type of light sources used. OCT technology can be applied to any wavelength as long as a light source is available (Chapter 2, section 2.1). OCT light sources have been typically developed for the near infrared region, defined as the therapeutic region, where absorption of main constituents in the living matter is small. It is important to choose wisely the central wavelength of the light source to enhance the penetration depth by minimizing the absorption. The main absorbers present in human tissue are melanin, collagen, water, lipids, and deoxygenated and oxygenated haemoglobin. Their absorption coefficients as a function of the wavelength absorption coefficients are represented in Fig. 1.3 [12-16] and play a key role in the choice of the central wavelength of the source.

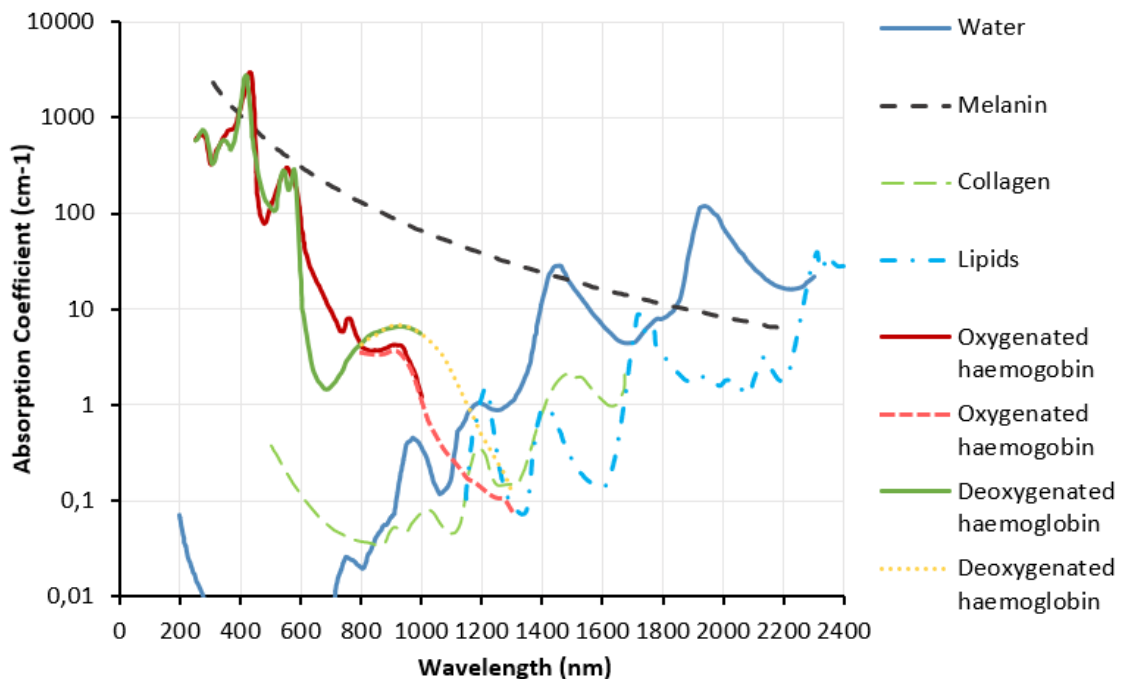


Fig. 1.3 Absorption coefficients as a function of the wavelength for main tissue components: melanin, collagen, lipids, oxygenated and deoxygenated haemoglobin [12-16].

For example, in the case of retinal imaging, the absorption curve considered most are from water because the vitreous humour, being the largest section of the eye to be crossed by the incident beam, has the same absorption properties as water. From figure 1.3, the optimum wavelength range to achieve the best performance is located toward shorter wavelength (< 900nm) or around 1060nm. If we consider skin imaging, a light source with a longer wavelength is more suitable due to the absorption curve of the melanin, the main absorbers in this tissue. Usually, it is an OCT light source centred around 1300nm that is used to keep a reasonable axial resolution (2.1.D.2).

For optical biomedical imaging, the region from 800 nm to 1500 nm is considered as the “optical window” [17] and the majority of OCT systems are designed to work in this range. However, with the improvement and the larger availability of light sources present on the market, OCT systems working within shorter wavelengths (visible range) [2, 18-19] or longer wavelengths [20,21] have been recently reported. The visible range has the potential to extract the oxygenation information based on the absorption curves from oxygenated and deoxygenated haemoglobin (high absorption, Fig. 1.3) and also to achieve ultrahigh resolution OCT [2, 18-19].

On the other hand, OCT at longer wavelengths (>1500nm) have recently been reported, applied to non-biomedical application such as non-destructive testing [22-27].

Further details about OCT technology will be given in Chapter 2 but in the next section, a short introduction of this technology is presented.

1.3. Optical Coherence Tomography

OCT in numbers

OCT technology has emerged over 27 years ago and can be seen as an extension of a method called low-coherence interferometry [1]. This imaging method has spread widely in ophthalmology over the past decades because of its ability to visualise ocular structures with high resolutions in lateral and axial directions [28]. OCT systems have

been extended to other tissues such as skin but also to non-medical applications for example non-destructive testing or art conservation and archaeology [22-27].

The figure 1.4 shows the evolution of the number of OCT publications by year for different fields of the four main applications: ophthalmology, cardiology, technology and dermatology [29-33]. In the last two decades, this number has continually increased due to expansion of its range of applications. OCT had a huge impact in ophthalmic research (Fig.1.4), Several companies are already active in this field such as Heidelberg, Carl Zeiss, Biooptigen, Optovue, Optopol, Canon, Topcon, etc. OCT's impact to eye imaging can be explained based on the previous non-accessibility to the retina. Fundus cameras have no depth resolution while scanning laser ophthalmoscopes perform imaging with a limited axial resolution. For the first time, by using OCT, clinicians were able to perform high resolution depth profiles of the retina. This opens access to the structural information and therefore OCT is considered as a revolution in the practice and diagnosis of eye diseases.

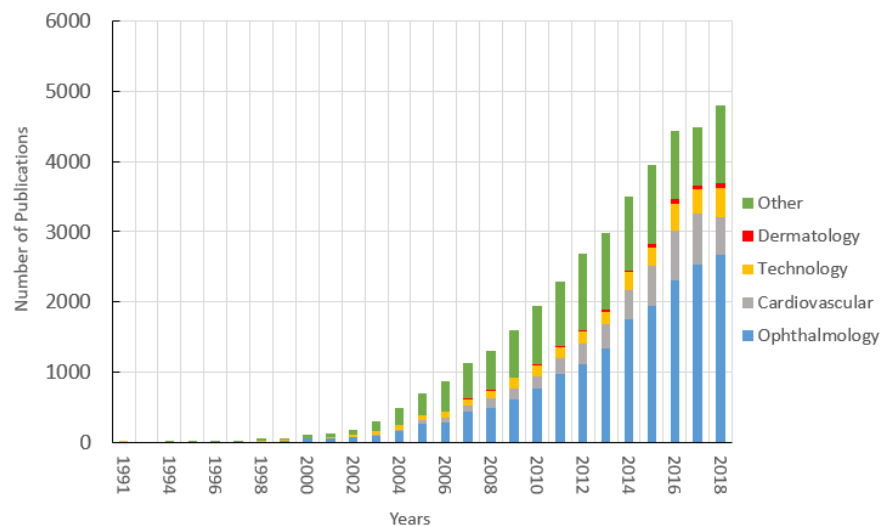


Fig. 1.4 OCT Publication by year extracted from PubMed for different applications [29-33].

OCT, a revolution in ophthalmology

Before the arrival of OCT in ophthalmology, only the slit lamp examination permitted the observation of anterior segment of the eye. For retinal examination, it was done by fundus examination. OCT allows to perform a very precise examination of the anterior part of the eye; tear film, cornea, conjunctiva, anterior chamber, iris, and of the posterior parts; retina, macula and optic disc, making acute diagnosis possible.

The OCT systems for eye imaging can be divided into two categories depending on the part being imaged.

OCT for anterior segment of the eye:

OCT is a non-invasive diagnostic and screening tool to detect angle closure glaucoma condition, to assess corneal thickness and opacity, to evaluate presurgical and postsurgical anterior chamber anatomy, to calculate intraocular lens power, guide laser-assisted cataract surgery, to assess complications following surgical procedures, and to image intracorneal ring segments [34-37]. It is also useful for the analysis of pathological processes such as dry eye syndrome, tumours, uveitis, and infections [38-41].

OCT for retina and optic nerve:

The main use of OCT in retinal imaging is to diagnose and understand the different pathologies affecting this part of the eye, notably, the three main causes of blindness in rich countries: age-related macular degeneration, glaucoma and diabetic retinopathy [28,42-44].

Even if the OCT images offer an exceptional visualization of the eye, the full potential of this technology is yet to be realised. The optical signal retrieved by OCT is a complex signal with an amplitude and a phase. The structural images, present in nearly every practice, are based on the amplitude of the optical signal. The phase information starts to be taken into account in some functional extension of the OCT such as Optical Coherence Tomography Angiography (OCTA). However, the question of whether the function information retrieved from the optical signal can be clinically relevant remains unanswered for now. Furthermore, considering that the eye is an extension of the brain through the optic nerve, the OCT enables different points of view in

interpreting retinal images for neurological diagnostic. If this is confirmed, a whole new range of applications could be considered from a single OCT scan volume.

1.4 OCT Volume skeleton

Before going further into the theory of OCT, some specific terminology needs to be introduced.

An OCT volume is represented by a simple parallelepiped in Fig. 1.5. The volume is generated based on different OCT principles, Time Domain or Frequency Domain OCT. This will be explained in further detail later on. An OCT volume can be seen as a juxtaposition of several B-scan images (red rectangle in Fig.2.15) in the transversal direction or a juxtaposition of C-scan images (green rectangle in Fig.2.15) in the axial direction. Each entities, B-scan or C-scan can be split into a combination of lines named A-scan and T-scan respectively. This is possible by the use of galvanometer scanner mirrors placed in the sample arm which scan the sample at different transverse position along x or y axis in Fig. 1.5.

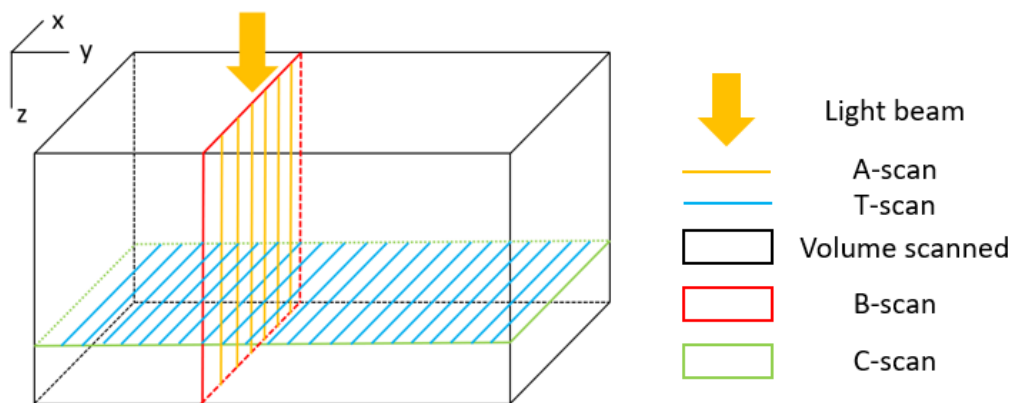


Fig.1.5 OCT Volume skeleton

1.5. Organisation of the thesis

This research activity presented in the thesis was supported by a project funded by the Marie Curie Actions with the Initial Training Networks of the European Research Council named "UBAPHODESA" for Ultrawide BAndwidth PHotonics DEvices,

Sources and Applications (grant number 607627). It was a collaboration between an industrial partner, NKT Photonics based in Denmark and the University of Kent in the United Kingdom. The work presented was half carried out at NKT Photonics and the second half at the University of Kent, including also collection of data from a study at the Medical University of Vienna.

Biomedical imaging handles two different types of images: structural and functional. The first one gives an inside view from the different layers and features of the sample with a certain precision given by the resolution of the system and penetration depth.

Using different optical or acoustic properties, it is possible to retrieve the functional information from the sample. Functional imaging, sometimes called physiological imaging, highlights the composition of the sample or the modification/evolution of structural features over time.

Usually, a biomedical imaging system is designed to deliver one or the other. Multimodal systems start to emerge that combine the different imaging modalities, for example using PAM/OCT technologies [3] that give access to structural and functional images simultaneously.

With the improvement and the diversification of the light source and detectors for OCT, finer structural images are possible. However, clinicians push to extract more information from the OCT images. By recovering the amplitude and the phase signals from the OCT reflected beam, it is possible to detect both structural and functional features of a sample.

A diagram to represent the different parts of the work is shown in Fig. 1.6. This thesis is approaching OCT technology as a structural modality (Chapter 2) and as a functional modality (Chapter 3). In the later, the functional information recovered is the moving parts of the sample. These two chapters have been completely separated but theoretical and experimental work for both modalities have been included in the same chapter. This allows both chapters to be read independently. At the end, a case study extracted from a peer review paper shows how both modalities can be combined to completely characterise a sample, in this case, a bovine embryo evolution.

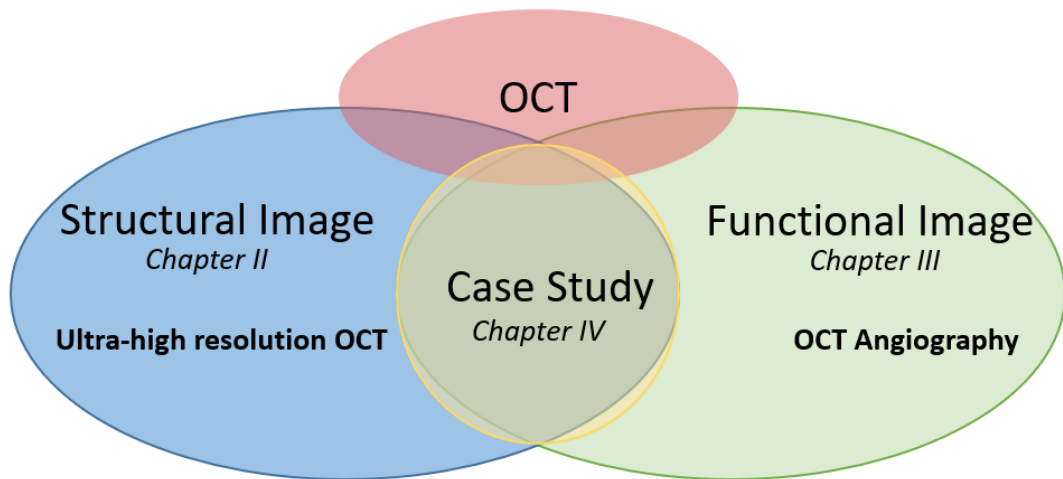


Fig.1.6 Schematic diagram of the organisation of the thesis

Chapter 2: A structural modality, ultrahigh resolution Optical Coherence Tomography

- *Theory Section:* The first part of this chapter is dedicated to explaining the principles of OCT and how the optical signal travels through the system and afterwards, recorded by the detector. The different parameters such as the axial or transversal resolution are defined.
- *Experimental Section:* The goal of this chapter is to present the work done to achieve ultrahigh resolution OCT. This employs a broadband source, a supercontinuum source from NKT Photonics A/S. After a short introduction on the supercontinuum generation, a study was developed on dealing with the dispersion that is introduced by the large bandwidth. Supercontinuum sources have been, for a long time, considered as unsuitable sources for biomedical imaging because of their noise level. Two broadband sources, a Titanium Sapphire laser and the supercontinuum source are compared and we conclude that despite larger noise than the Titanium Sapphire laser, the supercontinuum is still capable of delivering an ultrahigh resolution cornea image.
- *Experimental Section:* In the last section of this chapter, an alternative post-processing method is employed to replace the usual Fourier Transform. This

method, introduced by the Applied Optics Group at the University of Kent is tolerant to dispersion in the interferometer and nonlinearities in encoding the OPD on spectrum modulation. With further improvement as presented here, the method is used to retrieve the phase signal in addition to the amplitude, making this post processing method suitable for both structural and functional imaging.

Chapter 3: A functional modality, motion detection with Fourier Domain Optical Coherence Tomography

- *Theory Section:* The chapter starts with a short introduction on the need for motion detection and the moving backscattered parameters present in tissue (haemodynamic), before going onto the explanation of the principle of OCT Angiography (OCTA) and discussing the different methods based on the amplitude or on the phase of the optical signal.
- *Experimental Section:* The last sections of the chapter are devoted to studying if OCTA can be considered as a quantitative or qualitative measurement and how the OCTA images can be improved using spectral or temporal averaging.

Chapter 4: A case study, OCTA for depth resolved assessment of the viability of bovine embryos

- This chapter combines the structural and functional OCT modalities presented or developed in the two previous chapters. The structural and functional information for a bovine embryo were used to characterize its viability. The depth resolved profiles of day 7 post-IVF bovine embryo are used to extract the morphologic features while Speckle Variance (SV) detects motion on a micron scale. Both structural and functional features were monitored to study the embryo evolution over time.

References

- [1] J.G. Fujimoto and W. Drexler, "Optical Coherence Tomography: Technology and Applications," Springer-Verlag, Berlin, Heidelberg (2008).
- [2] P. Marchand, A. Bouwens, D. Szlag, D. Nguyen, A. Descloux, M. Sison, S. Coquoz, J. Extermann and T. Lasser, "Visible spectrum extended-focus optical coherence microscopy for label-free sub-cellular tomography," *Biomedical Optics Express*, 8:3343-3359. 10.1364/BOE.8.003343 (2017).
- [3] M. Bondu, M.J. Marques, P.M. Moselund, G. Lall, A. Bradu and A. Podoleanu, "Multispectral photoacoustic microscopy and optical coherence tomography using a single supercontinuum source," *Elsevier Photoacoustic*, 9:21-30 (2017).
- [4] M. Xu and L. V. Wang. "Photoacoustic imaging in biomedicine," *Review of Scientific Instruments*, 77:041101 (2006).
- [5] L.Sauer, K.M. Andersen, C. Dysli, M.S. Zinkernagel, P.S. Bernstein, and M. Hammer, "Review of clinical approaches in fluorescence lifetime imaging ophthalmoscopy," *Journal of Biomedical Optics*, 23(9), 091415 (2018).
- [6] F. Fleischhauer, S. Caujolle, T. Feuchter, R. Rajendram, L. Leick, and A. Podoleanu, "Spectroscopic low coherence interferometry using a supercontinuum source and an ultra broadband spectrometer," *Proc.SPIE*, 9697 (2016).
- [7] U. Morgner, W. Drexler, F.X. Krärtner, X.D Li, C. Pitris, E.P. Ippen and J.G. Fujimoto, "Spectroscopic optical coherence tomography," *Opt.Lett.*, 25(2):111-113 (2000).
- [8] C.C. Xu, D.L. Marks, M.N. Do, and S.A. Boppart, "Separation of absorption and scattering profiles in spectroscopic optical coherence tomography using a least-squares algorithm," *Opt. Express*, 12(20): 4790-4802(2004).
- [9] B.E. Bouma, S.H. Yun, B.J. Vakoc, M.J. Suter, and G.J. Tearney, "Fourier-domain optical coherence tomography: recent advances toward clinical utility," *Curr Opin. Biotechnol*, 20(1):111-118 (2009).
- [10] R. Leitgeb, M. Wojtkowski, A. Kowalczyk, C.K. Hitzenberger, M. Sticker, and A.F. Fercher, "Spectral measurement of absorption by spectroscopic

- frequency-domain optical coherence tomography,” *Opt. Lett.*, 25(11):820-822 (2000).
- [11] E. J. McCartney and F. F. Hall, “Optics of the atmosphere: Scattering by molecules and particles,” *Physics Today*, 30(5):76, (1977).
- [12] S. L. Jacques. “Optical properties of biological tissues: a review,” *Physics in Medicine & Biology*, 58(11):R37, (2013).
- [13] W. B. Gratzer and N. Kollias. Personal communication from Gratzer, Med. Res. Council Labs, Holly Hill, London, and N Kollias, Wellman Laboratories, Harvard Medical School, Boston, (1999).
- [14] H. Suzaki, “Noninvasive measurement of total hemoglobin and hemoglobin derivatives using multiwavelength pulse spectroscopy-In vitro study with a mock circulatory system,” *Proc. of the 28th IEEEEMBS Annual Int. Conf.*, New York City (2006).
- [15] R.R Anderson, W. Farinelli, H. Laubach, D. Manstein, A. N. Yaroslavsky, J. Gubeli III, K. Jordan, G. R. Neil, M. Shinn, W. Chandler, G. P. Williams, S. V. Benson, D. R. Douglas, and H. F. Dylla, “Selective photothermolysis of lipidrich tissues: a free electron laser study,” *Lasers in Surgery and Medicine*, 38(10): 913–919 (2006).
- [16] S. K. V. Sekar, I. Bargigia, A. D. Mora, P. Taroni, A. Ruggeri, A. Tosi, A. Pifferi, and A. Farina, “Diffuse optical characterization of collagen absorption from 500 to 1700 nm,” *Journal of Biomedical Optics*, 22(1):015006 (2017).
- [17] J. M. Schmitt, “Optical coherence tomography (OCT): a review”, *Selected Topics in Quantum Electronics, IEEE Journal of*, vol. 5, no. 4, pp. 1205–1215, (1999).
- [18] A. Lichtenegger, D.J. Harper, M. Augustin, P. Eugui, S. Fialová, A. Woehrer, C.K. Hitzenberger, and B. Baumann, “Visible light spectral domain optical coherence microscopy system for ex vivo brain imaging,” *Optics in the Life Sciences Congress, Optical Society of America* (2017).
- [19] J. Yi, Q. Wei, W. Liu, V. Backman, and H.F. Zhang, “Visible-light optical coherence tomography for retinal oxymetry,” *Opt. Lett.* (11):1796–1798 (2013).
- [20] C. S. Cheung, M. Tokurakawa, J. M. O. Daniel, W. A. Clarkson, and H. Liang, “Long wavelength optical coherence tomography for painted objects,” *Optics*

- for Arts, Architecture, and Archaeology IV, L. Pezzati and P. Targowski, Eds. (2013).
- [21] U. Sharma, E. W. Chang, and S. H. Yun, “Long-wavelength optical coherence tomography at 1.7 μ m for enhanced imaging depth”, *Optics Express*, vol. 16, no. 24, p. 19 712 (2008).
- [22] N.M. Isrealson, C.R. Petersen, A. Barh, D. Jain, M. Jensen, G. Hanneschläger, P. Tidemand-Lichtenberg, C. Pedersen, A. Podoleanu, and O. Bang, “Real-time high-resolution mid-infrared optical coherence tomography,” *Light:Science & Application*, 8(11) (2019).
- [23] E. N. Morel, N. A. Russo, J. R. Torga, and R. Duchowicz, “Interferometric system based on swept source-optical coherence tomography scheme applied to the measurement of distances of industrial interest”, *Opt. Eng.*, vol.55, no. 1, p. 014 105 (2016).
- [24] Z. Chen, Y. Shen, W. Bao, P. Li, X. Wang, and Z. Ding, “Identification of surface defects on glass by parallel spectral domain optical coherence tomography”, *Optics Express*, vol. 23, no. 18, p. 23 634 (2015).
- [25] M. Iwanicka, G. Lanterna, C. G. Lalli, F. Innocenti, M. Sylwestrzak, and P. Targowski, “On the application of optical coherence tomography as a complimentary tool in an analysis of the 13th century Byzantine Bessarion reliquary,” *Microchemical Journal*, vol. 125, pp. 75–84 (2016).
- [26] R. Su, M. Kirillin, E. W. Chang, E. Sergeeva, S. H. Yun, and L. Mattsson, “Perspectives of mid-infrared optical coherence tomography for inspection and micrometrology of industrial ceramics,” *Optics Express*, vol. 22, no. 13, p. 15 804 (2014).
- [27] C. S. Cheung, M. Tokurakawa, J. M. O. Daniel, W. A. Clarkson, and H. Liang, “Long wavelength optical coherence tomography for painted objects,” *Optics for Arts, Architecture, and Archaeology IV*, L. Pezzati and P. Targowski, Eds. (2013).
- [28] A. Mehreen, and J.S. Duker. “Optical coherence tomography--current and future applications,” *Current opinion in ophthalmology*, vol. 24,3 (2013): 213-21 (2013).
- [29] PubMed.<https://www.ncbi.nlm.nih.gov/pubmed/?term=OCT+and+ophthalmology> Accessed:2019.03.20.

- [30] PubMed.<https://www.ncbi.nlm.nih.gov/pubmed/?term=OCT+and+dermatology> Accessed:2019.03.20.
- [31] PubMed.<https://www.ncbi.nlm.nih.gov/pubmed/?term=OCT+and+technology> Accessed:2019.03.20.
- [32] PubMed.<https://www.ncbi.nlm.nih.gov/pubmed/?term=OCT+and+cardiology> Accessed:2019.03.20.
- [33] PubMed.<https://www.ncbi.nlm.nih.gov/pubmed/?term=OCT> Accessed:2019.03.20.
- [34] C. Baudouin, A. Labbé, A. El Maftouhi, and P. Hamard, “Application of anterior segment OCT to the study of glaucoma,” *Journal Fr ophtalmol.* 31(6):5-9.
- [35] S.B. Han, Y.C. Liu, K.M. Noriega and J.S. Mehta, “Applications of Anterior Segment Optical Coherence Tomography in Cornea and Ocular Surface Diseases,” *Journal of ophthalmology* vol. 2016 (2016): 4971572 (2016).
- [36] A. A. Nanji, F. E. Sayyad, A. Galor, S. Dubovy, and C. L. Karp, “High-resolution optical coherence tomography as an adjunctive tool in the diagnosis of corneal and conjunctival pathology,” *Ocular Surface*, vol. 13, no. 3, pp. 226–235 (2015).
- [37] S.H. Lim, “Clinical Applications of Anterior Segment Optical Coherence Tomography,” *Journal of Ophthalmology*, vol. 2015, Article ID 605729, 12 pages (2015).
- [38] R.M. Werkmeister, A. Alex, S. Kaya, A. Unterhuber, B. Hofer, J. Riedl, M. Brohagl, M. Vietauer, D. Schmidl, T. Schmoll, G. Garhöfer, W. Drexler, R.A. Leitgeb, M. Groeschl, L. Schmetterer, “Measurement of tear film thickness using ultrahigh resolution optical coherence tomography,” *Investigative ophthalmology & visual science*, 54(8):5578–83 (2013).
- [39] K. Bizheva, B. Tan, B. MacLelan, O. Kralj, M. Hajialamdari, D. Hileeto, L. Sorbara, L., “Sub-micrometer axial resolution in OCT for in-vivo imaging of the cellular structure of healthy and keratoconic human corneas,” *Biomed Opt Express*, vol.8, No.2 (2017).
- [40] R.M. Werkmeister, S. Sapeta, D. Schmidl, G. Garhöfer, G. Schmidinger, V. Aranha Dos Santos, G.C. Ashinger, I. Baumgartner, N. Pircher, F.

- Schwarzahns, A. Pantalon, H. Dua, L. Schmetterer, "Ultrahigh-resolution OCT Imaging of the human cornea," *Biomed Opt Express*, vol.8, No.2 (2017).
- [41] M. Wojtkowski, R. Leitgeb, A. Kowalczyk, T. Bajraszewski, and A.F. Fercher, "In vivo human retinal imaging by Fourier domain optical coherence tomography," *Journal of biomedical optics*, vol. 7, no. 3, pp. 457–463 (2002).
- [42] D.A Salz, and A.J Witkin, "Imaging in diabetic retinopathy," *Middle east afr. J Ophthalmol.*22(2):145-150 (2015).
- [43] J.M. Botto de Barros Garcia, D.L. Cruvinel Isaac, and M. Avila, "Diabetic retinopathy and OCT angiography: clinical findings and future perspectives," *International Journal of Retina and Vitreous* 3(14) (2017).
- [44] M. Wojtkowski, R. Leitgeb, A. Kowalczyk, T. Bajraszewski, and A.F. Fercher, "In vivo human retinal imaging by Fourier domain optical coherence tomography," *Journal of biomedical optics*, vol. 7, no. 3, pp. 457–463 (2002).
-

Chapter 2

A Structural modality: Ultrahigh resolution Optical Coherence Tomography (UHR-OCT)

2.1. Principle of Optical Coherence Tomography (OCT)

Author's note: Portions of this chapter are based on the theory chapter of the author's master thesis written in 2014. It has been submitted at the engineering school ENSSAT in France.

Author's note: A thorough discussion about OCT can be found in the chapter "Ultrahigh Resolution Optical Coherence Tomography" of the book Optical Coherence Tomography – Technology and Application written by W. Drexler and J.G. Fujimoto [1], parts of these chapter are based on it.

2.1.A Basics of OCT

2.1.A.1 Michelson interferometer

The incident beam emitted by a low temporal coherence light source is divided by a beam splitter, guiding one along a reference arm and the other along a sample arm. This is visualised in figure 2.1. In the general configuration of the Michelson interferometer, both arms are only composed of a mirror in order to reflect the beam back to the beam splitter [2,3]. The two reflected beams are then recombined and an interference pattern is measured by a detector.

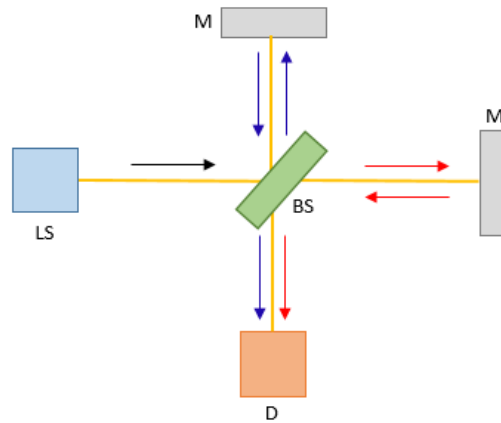


Fig.2.1. Michelson interferometer comprised of four parts: a light source (LS), beam splitter BS, two Mirrors M, and a detector D. The beam leaving the light source arrives at the beam splitter and it is divided into two beams, which are reflected by two mirrors. The reflected beams are then recombined by the beam splitter and finally collected by the detector.

If the optical path length difference (OPD) between both arms is smaller than the temporal coherence length of the light beam l_c , interference occurs. The intensity modulation detected is given by the formula:

$$I \propto I_1 + I_2 + 2\sqrt{I_1 \cdot I_2} \cdot \cos(2k \cdot \Delta L) \quad (2.1)$$

Here, I_1 and I_2 are the intensities corresponding to each arm. The last term is the interference between the two beams. The period of modulations depends on the optical path length difference ($OPD = \Delta L$) and the wavenumber $k = 2\pi/\lambda$.

To convert a Michelson interferometer to an OCT system, one of the mirrors is removed and replaced by the sample. A lens is added in the sample arm to focus the beam onto the target being imaged. This is not the case for imaging the retina because it is already focused by the lens (positioned in front of the vitreous body). A depth profile is achieved by sweeping the spectrum (using the source or the spectrometer) in FD-OCT or moving the mirror in TD-OCT.

Transversal scanning using galvanometer scanners (GS) added in the sample arm allows OCT to produce a 2D imaging (transversal plan). GS do not affect the mathematical discussion presented in the next section and are therefore not including in the figures for the purpose of clarity.

2.1.A.2 Mathematical description

A thorough mathematical discussion of OCT can be found in chapter 2 of the book “Optical Coherence Tomography - Technology and Applications” [1].

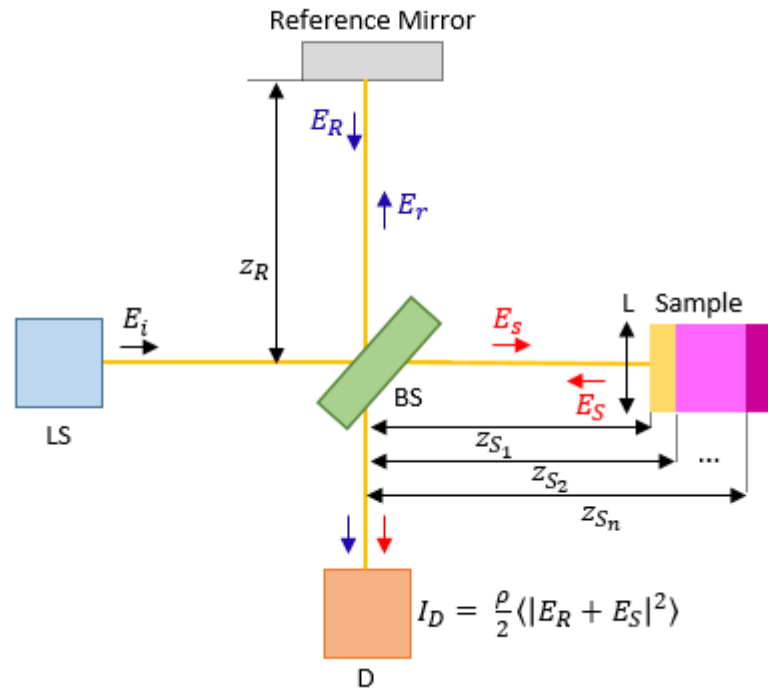


Fig.2.2. Michelson interferometer adapted for OCT. It uses the same configuration as that presented in figure 2.4 but the mirror from one of the arms is replaced by a sample and a lens (L) (to focus the beam onto the reflective sample).

If the time, the wavenumber, the position and the angular frequency are respectively, t , k , z and ω , the electric field before the interferometer is given by:

$$E_i = s(k, \omega). e^{i(kz - \omega t)} \quad (2.2)$$

with a spectral shape described by $s(k, \omega)$. As seen in Fig 2.2, the incident beam reaches the beam splitter which divides the intensities of the two waves as a function of its ratio. If the assumption that a 50:50 beam splitter is used, the intensity signal from the reference and sample arm is equal to half of the incident beam intensity. In air, the link between the intensity and electric field signal is given by: $I = \frac{c\epsilon_0}{2} |E|^2$. Thus, the

reflected fields for the sample arm (E_S) and reference arm (E_r), directly after the beam splitter, are given by:

$$E_S = E_r = \frac{s(k,\omega)}{\sqrt{2}} \cdot e^{i(kz-\omega t)} = \frac{E_i}{\sqrt{2}} \quad (2.3)$$

The sample arm and reference arm have lengths z_S and z_R respectively. There is a π shift in the phase of the optical signal after reflection from the sample and the mirror as well as an additional phase change equal to $2kz_R$ or $2kz_S$ when the beams arrive back at the beam splitter. The reflected beam's amplitude is reduced by a factor r_R in the reference arm and by a factor $r_S(z_{S_n})$ due to reflectivities of the different sample layers at different depths z_{S_n} in the sample arm. The two notations r_R and $r_S(z_{S_n})$ represent the reflection coefficients.

From there, the corresponding expression for the reference arm after the beam splitter is:

$$E_R = \frac{E_i}{\sqrt{2}} \cdot r_R \cdot e^{i2kz_R} \cdot e^{i\pi} \quad (2.4)$$

And for the sample arm, in the assumption of discrete reflectors:

$$E_S = \frac{E_i}{\sqrt{2}} \cdot \sum_n r_{S_n} \cdot e^{i2kz_{S_n}} \cdot e^{i\pi} \quad (2.5)$$

The detector response will be termed ρ . As the rate of detection is, for any practical detector, much smaller than the frequency ω , the detector effectively performs a time average. The intensity measured at the detector is:

$$I_D = \frac{\rho}{2} \langle |E_R + E_S|^2 \rangle$$

Using (2.4) and (2.5),

$$\begin{aligned}
I_D &= \frac{\rho}{2} \left\langle \left| \frac{s(k, \omega)}{\sqrt{2}} \cdot e^{i(kz - \omega t)} \cdot r_R \cdot e^{i2kz_R} \cdot e^{i\pi} \right. \right. \\
&\quad \left. \left. + \frac{s(k, \omega)}{\sqrt{2}} \cdot e^{i(kz - \omega t)} \cdot \sum_n r_{Sn} \cdot e^{i2kz_{Sn}} \cdot e^{i\pi} \right|^2 \right\rangle \\
&\quad \Leftrightarrow \\
I_D &= \frac{\rho}{2} \left\langle \left| \frac{s(k, \omega)}{\sqrt{2}} \cdot e^{i(kz - \omega t)} \cdot e^{i\pi} \left(r_R \cdot e^{i2kz_R} + \sum_n r_{Sn} \cdot e^{i2kz_{Sn}} \right) \right|^2 \right\rangle \\
&\quad \Leftrightarrow \\
I_D &= \frac{\rho}{2} \left\langle \left| \frac{s(k, \omega)}{\sqrt{2}} \right|^2 \cdot |e^{i(kz - \omega t)} \cdot e^{i\pi}|^2 \cdot \left| \left(r_R \cdot e^{i2kz_R} + \sum_n r_{Sn} \cdot e^{i2kz_{Sn}} \right) \right|^2 \right\rangle
\end{aligned}$$

Yet, $|e^{ix}|^2 = e^{ix} \cdot e^{-ix} = 1$ and if the expression of the light source spectrum is noted as $S(k) = \langle |s(k, \omega)|^2 \rangle$

$$I_D = \frac{\rho}{4} S(k) \cdot \left\langle \left| \left(r_R \cdot e^{i2kz_R} + \sum_n r_{Sn} \cdot e^{i2kz_{Sn}} \right) \right|^2 \right\rangle$$

By evaluating the modulus above, the equation becomes:

$$\begin{aligned}
I_D &= \frac{\rho}{4} S(k) \cdot \left[r_R^2 + \sum_n r_R r_{Sn} \cdot (e^{i2k(z_R - z_{Sn})} + e^{-i2k(z_R - z_{Sn})}) \right. \\
&\quad \left. + \sum_m \sum_n r_{Sn} \cdot r_{Sm} \cdot e^{i2k(z_{Sn} - z_{Sm})} \right]
\end{aligned}$$

The last term of the equation is a double sum and can be split into three different parts depending on the value taken by n compared to m: $n = m$, $n < m$ or $n > m$ and considering that $\forall n, m \sum_{n < m} r_{Sn} \cdot r_{Sm} \cdot e^{i2k(z_{Sn} - z_{Sm})} = \sum_{n > m} r_{Sn} \cdot r_{Sm} \cdot e^{-i2k(z_{Sn} - z_{Sm})}$

So, the expression of I_D becomes:

$$I_D = \frac{\rho}{4} S(k) \cdot \left[r_R^2 + \sum_n r_R r_{Sn} \cdot (e^{i2k(z_R - z_{Sn})} + e^{-i2k(z_R - z_{Sn})}) + \sum_n r_{Sn}^2 + \sum_{n < m} r_{Sn} \cdot r_{Sm} \cdot (e^{i2k(z_{Sn} - z_{Sm})} + e^{-i2k(z_{Sn} - z_{Sm})}) \right]$$

Involving the relationship between the exponential and cosine functions and introducing the power reflectivity defined as $R = |r|^2$, the equation above is further expressed by:

$$I_D = \frac{\rho}{4} S(k) \cdot \left[R_R + 2 \sum_n r_{Sn}^2 + \sum_n \sqrt{r_R r_{Sn}} \cdot \cos(2k(z_R - z_{Sn})) + 2 \sum_{n < m} \sqrt{r_{Sn} \cdot r_{Sm}} \cdot \cos(2k(z_{Sn} - z_{Sm})) \right]$$

Using the relation, $\forall n, m \sum_{n < m} X_{nm} = \frac{1}{2} \sum_{n \neq m} X_{nm}$ for $X_{nm} = X_{mn}$

$$I_D = \frac{\rho}{4} S(k) \cdot \left(R_R + \sum_n r_{Sn}^2 \right) \tag{a}$$

$$+ \frac{\rho}{2} S(k) \cdot \sum_n \sqrt{r_R r_{Sn}} \cdot \cos(2k(z_R - z_{Sn}))$$

$$+ \frac{\rho}{4} S(k) \cdot \sum_{n \neq m} \sqrt{r_{Sn} \cdot r_{Sm}} \cdot \cos(2k(z_{Sn} - z_{Sm})) \tag{b} \quad (2.6)$$

$$\tag{c}$$

Equation (2.6) can be seen as three independent terms: (a), (b) and (c).

The first term (2.6 (a)) is the DC component. This represents a path length independent offset to the detector current and depends on the light source wavenumber spectrum. Its amplitude is proportional to the power reflectivity of the mirror and of the different layers of the sample. It is typically the larger component of I_D and in SS-OCT and TD-OCT can be removed by using a high pass filter, before the signal above is employed

in the process of the creation of the images. This however represents a problem for spectrometer-based OCT, that can saturate the camera.

On the second line, the cross-correlation term (2.6 (b)) is the desired quantity for OCT imaging. It is defined as the correlation between the reference reflector and each sample reflector.

The third line is the auto-correlation term (2.6 (c)) which is the autocorrelation between different sample reflectors. It is linked to the power reflectivity of the sample reflections. It is considered as an artefact and it is, in most cases, negligible compared to the two other terms (reflected reference signal \gg reflected sample signal).

Now that the general basics of OCT have been reviewed, a more precise description of Fourier Domain Optical Coherence Tomography (FD-OCT) will follow, which is the system used throughout the rest of the manuscript.

2.1.B Fourier Domain Optical Coherence Tomography

2.1.B.1 Time Domain OCT (TD-OCT) vs Fourier Domain OCT (FD-OCT).

Two categories of OCT should be distinguished: Time Domain Optical Coherence Tomography (TD-OCT) and Fourier Domain Optical Coherence Tomography (FD-OCT) (Fig.2.3).

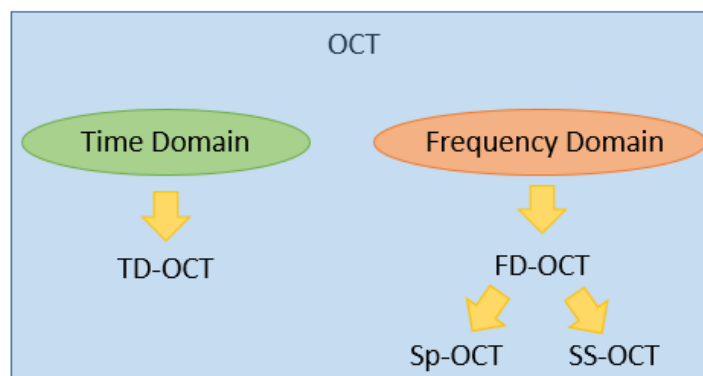


Fig.2.3. TD-OCT vs FD-OCT. FD-OCT subcategorised into Spectrometer based OCT (Sp-OCT) and Swept Source OCT (SS-OCT)

The information is not analysed in the same domain. In the case of the TD-OCT, the domain of the analysis is time whereas for FD-OCT, the domain is the optical frequency.

In both cases, a Fourier transform is applied to the signal delivered by the spectrometer in Sp-OCT and by the photodetector in SS-OCT to recover the depth resolved information coded in the sample.

Sp-OCT is usually named as Spectral Domain OCT (SD-OCT) for historical reason but because SS-OCT is also based on processing the spectrum information, it has been chosen in this thesis to refer to it by Spectrometer based OCT. The basic components of the OCT system are similar and the hardware is still made of three different parts: a light source, a Michelson interferometer and a detector. The main difference, from a hardware point of view, is whether or not the reference mirror changes position during the imaging process.

In TD-OCT, each point corresponds to one axial position of the reference mirror linked to one depth in the sample, when the lengths of the two match the zero OPD condition within the coherence-length. At each position of the mirror, the interference pattern is recorded by measuring the corresponding intensity with a photodetector. As seen in figure 2.4 (a), the two optical signals originating at the pairs of axial positions in the sample and reference arm respectively $(Z_{S1}; Z_{R1})$, $(Z_{S2}; Z_{R2})$, ... will interfere, where the OPD for each pair of coordinates is zero.

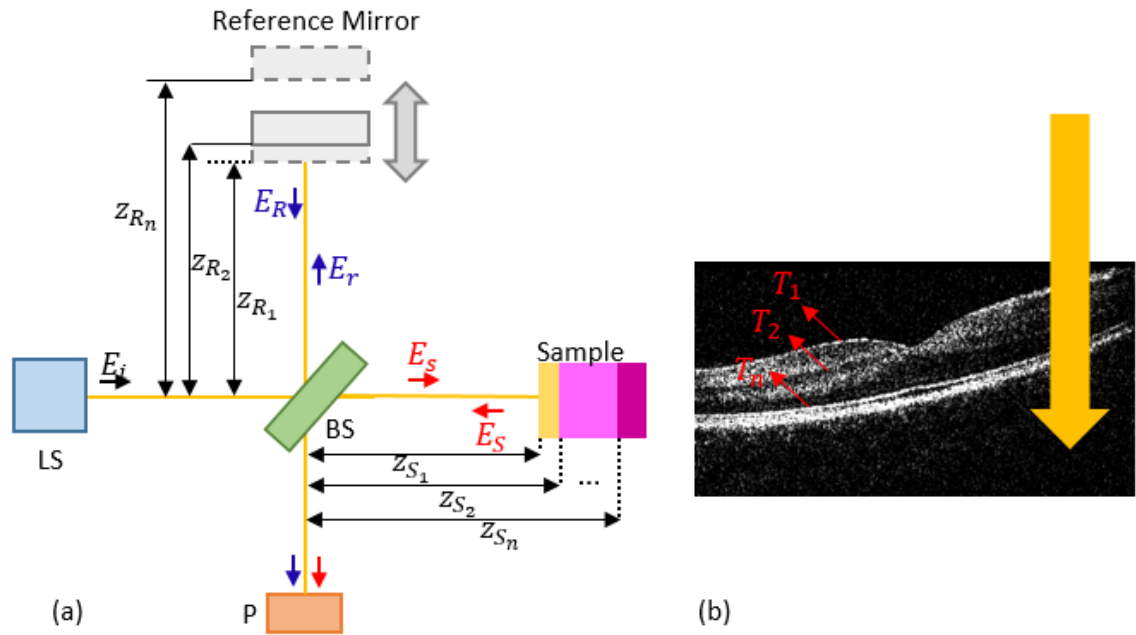


Fig.2.4. Time Domain Optical Coherence Tomography (TD-OCT) configuration. (a) LS: Light Source, BS: Beam splitter, P: Photodetector, E_i : the electric field of the incident beam, E_r and E_s : the electric fields after the BS in the reference arm and sample arm respectively, E_r and E_s : the electric fields after reflection from the mirror and the sample in the reference arm and sample arm respectively. The beam leaving the light source is divided and sent toward the sample and the reference arm using a beam splitter. After reflection, the beams are recombined and sent to the photodetector which acquires the optical signal. Interference between both arms occurs when $OPD = 0$, i.e when $z_R = z_S$. (b) Image of the retina. The yellow arrow shows the direction of the light beam.

Each depth is recorded by moving the mirror and therefore different points meet the zero-path length difference, which equates to scanning through the depth. Adding transversal scanning using GS then creates a B-scan image of the sample (Fig.2.4 (b)). Even if TD-OCT has the ability of achieving dynamic focus through moving the reference arm mirror position, FD-OCT has imposed itself as the most common form of OCT system in many applications due to its higher scanning speeds and higher sensitivity [4].

In FD-OCT, the reference mirror is fixed (Fig.2.5 (a)) and signals from all depths are acquired simultaneously $[T^1, \dots, T^x]$. There are two types of FD-OCT: Swept-Source OCT (SS-OCT) and Spectrometer based OCT (Sp-OCT). The main differences between the two modalities are the type of light source and detector used.

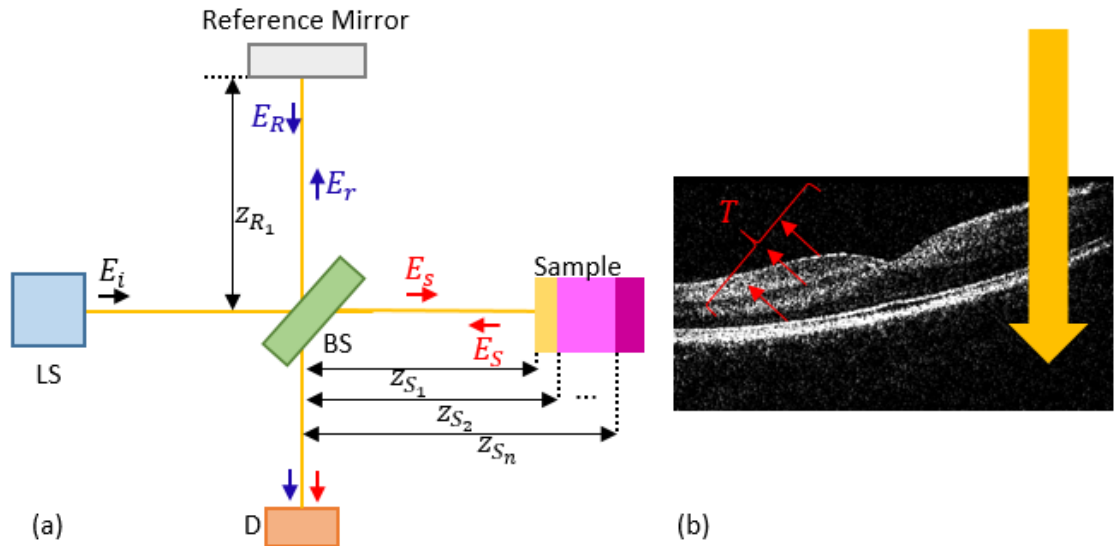


Fig.2.5. Frequency Domain Optical Coherence Tomography (FD-OCT) configuration. (a) LS: low temporal coherent light source, BS: Beam splitter, D: Detector, E_i : the electric field of the incident beam, E_r and E_s : the electric fields after the BS in the reference arm and sample arm respectively, E_R and E_S : the electric fields after reflection from the mirror and the sample in the reference arm and sample arm respectively. The beam leaving the light source is divided and sent toward the sample and the reference arm using a beam splitter. After reflection, the beams are recombined and sent to the detector, which is a spectrometer in the case of Sp-OCT and a balanced photodetector for SS-OCT. The interferences between both arms occurs along the depth of focus. (b) Image of the retina. The yellow arrow shows the direction of the light beam. All depth information is recorded in one acquisition.

As with TD-OCT, SS-OCT measures the resultant signal from the interferometer with a balanced photodetector whereas Sp-OCT measures the returning signal with a spectrometer. In both cases, the spectrum is interrogated over all wavelengths by using either the light source or the spectrometer. Although SS-OCT systems have some non-negligible advantages over Sp-OCT such as faster line scan rates and better roll-off [4], the work on ultrahigh resolution is for the moment limited to Sp-OCT technology because of the availability of light sources in the range required to achieve this goal and the unavailability of broadband swept sources.

2.1.B.2 Spectrometer based Optical Coherence Tomography (Sp-OCT)

The fundamental difference between Sp-OCT and the other OCT modalities is the use of a spectrometer as a detector. While using a spectrometer, the beams leaving the interferometer are transmitted through a diffraction grating or a prism. The grating disperses the beam according to wavelength which is then focused onto a line camera detector (Fig.2.6).

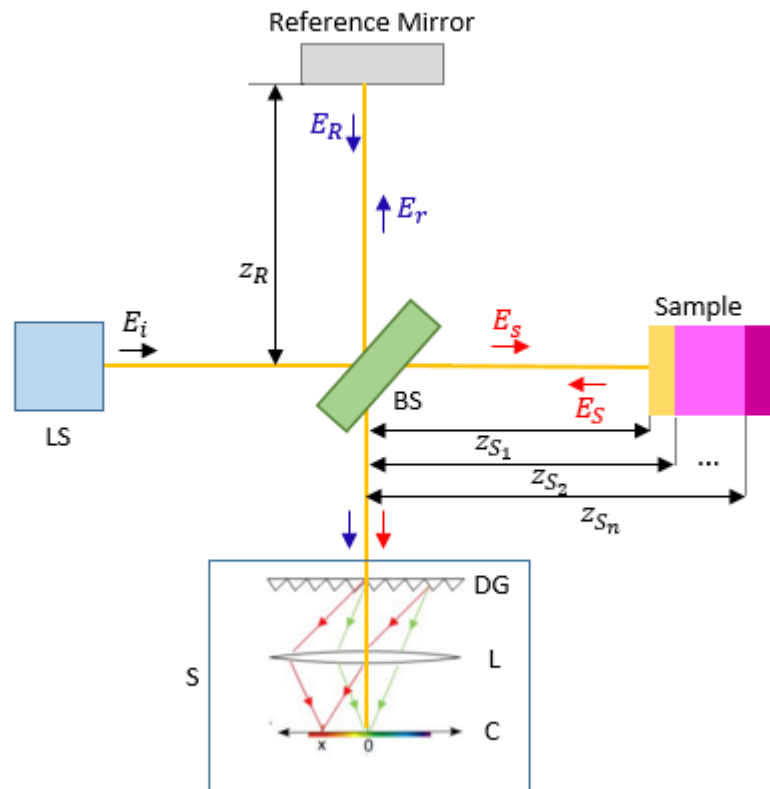


Fig.2.6. Spectrometer based Optical Coherence Tomography (Sp-OCT) system. LS: low temporal coherent light source, BS: Beam splitter, S: Spectrometer, DG: Diffraction grating, L: Lens, C: Line camera, E_i : the electric field of the incident beam, E_r and E_s : the electric fields after the BS in the reference arm and sample arm respectively, E_r and E_s : the electric fields after reflection from the mirror and the sample in the reference arm and sample arm respectively. The configuration is essentially identical to that previously shown in Fig.2.7. The only difference is the detection method being used. Information from all depths are acquired simultaneously using the spectrometer (S). The recombined beam meets the diffraction grating (DF) which spatially separates the light as a function of wavelength. A lens (L) is then used to focus each spectral component onto the line camera (C). The yellow line shows the optical axis.

The beam leaving the interferometer is composed of all interference patterns from the different layers of the sample (Fig.2.7). The frequency of the modulation has a direct link with the depth position of the layers in question. The larger the difference in the optical path length, the denser the spectral modulation (Fig.2.7. (a), (b) and (c)).

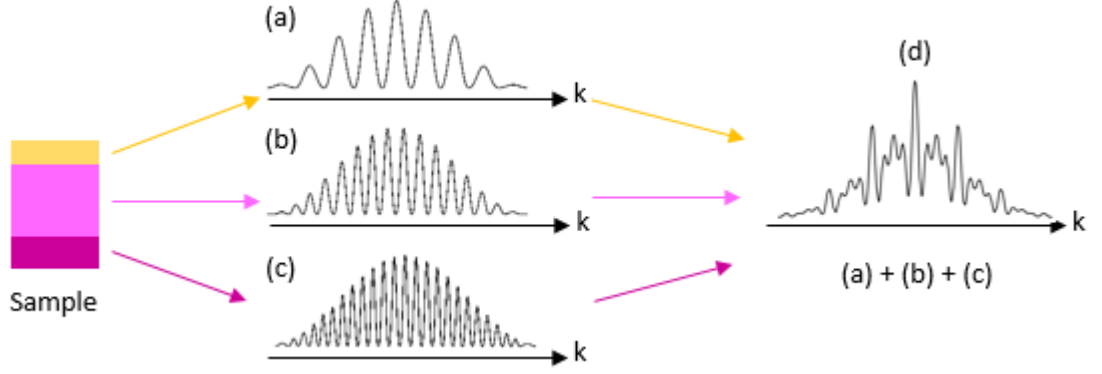


Fig.2.7. Signal detection on the line camera. Each layer of the sample reflects a signal with a certain modulation linked to the location in depth of the structure relative to zero OPD ((a), (b) and (c)). The signal detected on the line camera (d) is the summation of all the modulations produced by the different reflective layers in the sample.

The spectrum recorded by the camera is the summation of all modulation intensities from the reflecting layers (2.7 (d)). The information is then given by the detector current $I_D(k)$ as a function of the wavenumber k . To extract the depth information as a function of the axial position z , a Fourier transform is performed on the signal (Eq.2.7).

$$i_D(z) = FT(I_D(k)) \quad (2.7)$$

By introducing (2.6) to (2.7):

$$\begin{aligned} i_D(z) = & \frac{\rho}{4} FT(S(k)) \cdot \left(R_R + \sum_n r_{Sn}^2 \right) \\ & + \frac{\rho}{2} FT(S(k)) \cdot \sum_n \sqrt{r_R r_{Sn}} \cdot \cos(2k(z_R - z_{Sn})) \\ & + \frac{\rho}{4} FT(S(k)) \cdot \sum_{n \neq m} \sqrt{r_{Sn} \cdot r_{Sm}} \cdot \cos(2k(z_{Sn} - z_{Sm})) \end{aligned}$$

Using the properties of Fourier transforms and basic identities such as

$$\cos(k z_0) \stackrel{FT}{\leftrightarrow} \frac{1}{2} [\delta(z + z_0) + \delta(z - z_0)]$$

$$X(k).Y(k) \stackrel{FT}{\leftrightarrow} x(z) \otimes y(z)$$

where sign cross \otimes signifies convolution and where $\gamma(z)$ is the Fourier transform of $S(k)$, the previous equation becomes:

$$\begin{aligned} i_D(z) = & \frac{\rho}{4} \gamma(z) \cdot \left(R_R + \sum_n r_{Sn}^2 \right) \\ & + \frac{\rho}{4} \sum_n \sqrt{r_R r_{Sn}} (\gamma(z) \\ & \otimes [\delta(z + 2(z_R - z_{Sn})) + \delta(z - 2(z_R - z_{Sn}))]) \\ & + \frac{\rho}{8} \sum_{n \neq m} \sqrt{r_{Sn} \cdot r_{Sm}} (\gamma(z) \\ & \otimes [\delta(z + 2(z_R - z_{Sn})) + \delta(z - (z_R - z_{Sn}))]) \end{aligned}$$

However, $f(t) \otimes \delta(t - t_0) = f(t - t_0)$ so,

$$\begin{aligned} i_D(z) = & \frac{\rho}{4} \gamma(z) \cdot \left(R_R + \sum_n r_{Sn}^2 \right) \\ & + \frac{\rho}{4} \sum_n \sqrt{r_R r_{Sn}} [\gamma(z + 2(z_R - z_{Sn})) + \gamma(z - 2(z_R - z_{Sn}))] \\ & + \frac{\rho}{8} \sum_{n \neq m} \sqrt{r_{Sn} \cdot r_{Sm}} [\gamma(z + 2(z_{Sm} - z_{Sn})) \\ & + \gamma(z - (z_{Sm} - z_{Sn}))] \end{aligned} \quad (2.8)$$

Similar to equation (2.6), equation (2.8) can be seen as the combination of three different terms: DC, cross correlation and autocorrelation terms. As explained earlier, the three terms come from the combination of the different reflected optical signals inside the sample or from the sample and the reference arm. The second and the third terms of equation 2.8 have a positive term and a negative term for each different sample layers S_n . For the same modulus, two peaks, one for $OPD > 0$ and another one, symmetrically placed, for $OPD < 0$, can be observed. The term for $OPD < 0$ is usually called mirror image while the one for $OPD > 0$ is the desired images.

Figure 2.8 is a partial representation of the results obtained after the Fourier transform is carried out on the signal (d) (from Fig.2.7). For clarity, only the parts when OPD > 0 are displayed in Fig.2.8. Looking at Fig.2.8, the three terms from equation (2.8) can be identified.

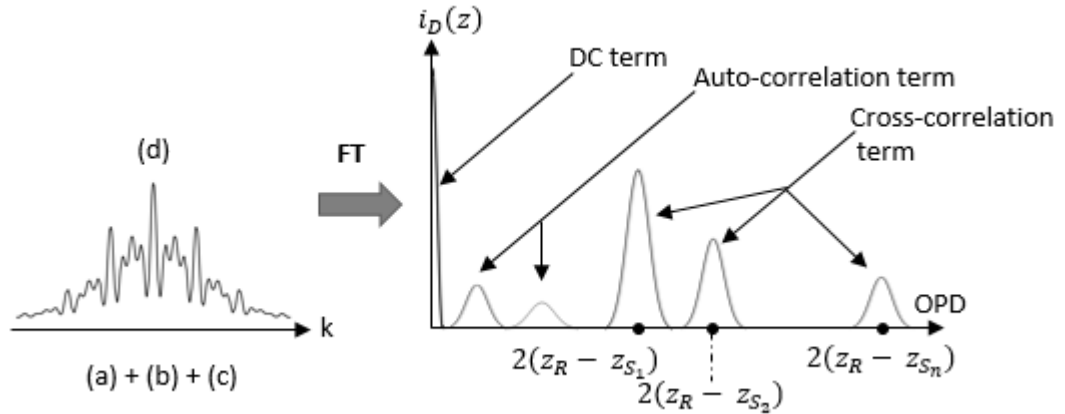


Fig.2.8 Recovery of the depth information. On the signal detected (d), a Fourier Transform (FT) is used to reconstruct the depth information. The recovered signal is composed of three terms: DC, auto correlation and cross-correlation terms. The depth information is given by the peak position of the cross-correlation term. For clarity, only the real part of the FT is shown.

The first peak is the DC component (first line in Eq.2.8) and has the highest amplitude. It can be removed by subtracting the reference signal on the assumption of having a stronger reflection signal from the mirror than from the sample (it is usually the case). In the case of the sample used here (superposition of three different layers), the cross-correlation term (eq.2.8) is composed of three different values representing the combination of the reflected beams from Z_R and Z_{S1} , Z_R and Z_{S2} and Z_R and Z_{S3} positioning at the OPD equal to $Z_R - Z_{S1}$, $Z_R - Z_{S2}$ and $Z_R - Z_{S3}$ respectively. These are on the right of Figure 2.8. It is this term that is essential to the reconstruction of the depth image. Finally, the last term (autocorrelation) is the interference produce by the superposition of the modulations from the different layers inside the sample. In our case (three layers sample), there will be signals due to the combination of three pairs, Z_{S1} and Z_{S2} , Z_{S1} and Z_{S3} , and Z_{S2} and Z_{S3} . On the assumption of higher reflected intensity from the reference arm than from the sample, these amplitudes are relatively small compared to the rest of the signal and will not be visible in the final image.

As explained above, an image is obtained with some features depending on the performance of the OCT system. The main parameters are the wavelength used, which depends on the sample imaged, the penetration depth (i.e. the largest distance along the axial direction where features can be seen from) and the resolution, which is the smallest distance between two resolved points. The last parameter can be separated into two; the axial resolution and the transverse resolution, depending on the direction of observation (along the axial or along the transversal axis). In the last section, our attention is focused on these two quantities.

2.1.C Resolution in OCT

In a B-scan image, several important parameters determine the performance of the system. All of them are represented in Fig.2.9 and depend on different physical properties.

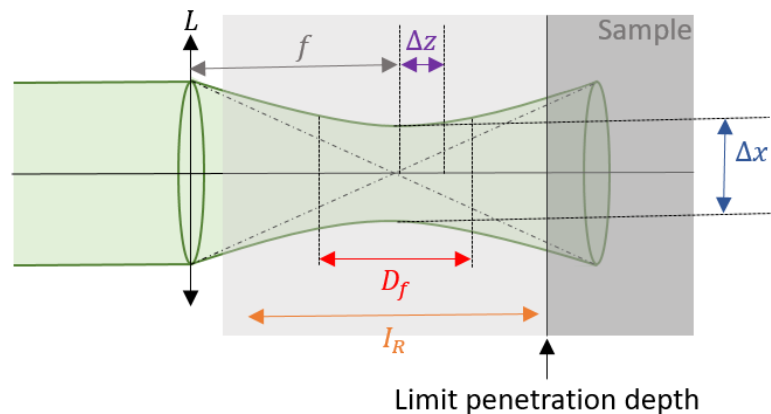


Fig. 2.9. Definition of relevant OCT parameters. L: lens, f: focal length of the lens L, Δz : axial resolution, Δx : transverse resolution, D_f : Depth of focus, I_R : Imaging range.

The focus position, the depth of field D_f and the transverse resolution Δx are linked to the confocal properties of the system while the maximum imaging range I_R and the axial resolution Δz to the coherence properties. To maximise interference, confocal and coherence gates need to be matched. The light beam, by interacting with the matter, is absorbed and scattered which limits the maximum penetration depth. It can be enhanced by increasing the power on the sample which is limited by the guideline of the maximum permissible exposure for a specific sample. The focal length, f is fixed

by the design of the lens but can be optimised by changing the lens itself. The imaging range, I_R is linked to the A-scan length determined by the spectrometer (number of pixels illuminated) and the light source (central wavelength and bandwidth) properties. Because of their different physical origin, in OCT (as opposed to e.g. light microscopy), the axial resolution is decoupled from the transversal resolution. As a consequence, they can therefore be improved independently from one another using different methods. In the following, the transversal and axial resolution are explained and how, by modifying the system parameters, it is possible to improve/optimize them.

2.1.C.1. Transversal Resolution

The transversal resolution of OCT is linked to the minimum beam waist of the focused beam on the object (focal spot size) and depends upon the numerical aperture of the lens (NA). As a first order approximation, the transverse resolution Δx can be defined as the smallest distance between two resolved points in the focus. It is equal to the first zero of the point spread function (PSF) which is defined as the radius of the first minimum of the Airy disc. The transverse resolution is defined as:

$$\Delta x = 0.37 \frac{\lambda_0}{NA} \quad (2.9)$$

where λ_0 is the central wavelength of the light source and NA the numerical aperture of the interface optics. If n is the refractive index of the medium and θ is the angle between the optical axis and the light beam focusing on the sample, NA is defined as:

$$NA = n \sin (\theta)$$

If the medium is considered to be air ($n = 1$) and assuming a small incidence angle θ , NA can be expressed as a function of the focal length f of the lens and the input beam diameter d :

$$NA = \frac{d}{2f} \quad (2.10)$$

By replacing (2.10) into (2.9), the transverse resolution equation becomes:

$$\Delta x = 0.74 \frac{f\lambda_0}{d} \quad (2.11)$$

Even if it is true that in OCT the axial and transverse resolution are decoupled and can be improved independently with different methods, it is not the case between Δx and the depth of focus, D_f because both are linked to the numerical aperture NA. If achieving a good transversal resolution is desirable, FD-OCT works with a fixed focus, hence it needs a large depth of focus to retrieve the depth information from the sample. Therefore, both parameters need to be optimised by finding a suitable balance between the two.

In the case of an illumination by a Gaussian beam, the depth of focus is equal to twice the Rayleigh length z_R . This length is defined as the distance from the focus where the diameter of the light beam reached twice the beam diameter in the focal position (equal to the transverse resolution). The Rayleigh length is a function of the central wavelength λ_0 and the numerical aperture NA, in case of a Gaussian light beam propagation in air this is given by the expression (2.12):

$$D_f = 2z_R \propto \frac{\lambda_0}{NA^2} \quad (2.12)$$

From equation (2.9) and (2.12), both parameters, the transverse resolution and the depth of focus, are inversely proportional to NA or to NA^2 respectively. However, to optimise the system performance, the transverse resolution needs to be maximised while the depth of focus is enlarged. In other words, while enhancing one, the other is worsened. A trade-off needs to be found between the improvements of these two parameters. Reaching a good transverse resolution is costly toward D_f because, as shown in equation 2.12, the depth of focus D_f is inversely proportional to the square

of NA so, a variation of NA leads to more changes to D_f than to Δx . Additionally, in most cases, samples are tissue and must be imaged in depth so it is essential to keep D_f reasonable (around 1-2mm). Therefore, several solutions have been evaluated to conserve the transversal resolution while enlarging the depth of focus. It can be considered to use a dynamic focus tracking system or a Bessel beam created with an axicon lens to extend it [5].

2.1.C.2. Axial Resolution

As mentioned before OCT is a low coherence interferometry method which uses the idea of finite temporal coherence to provide depth measurements. The axial resolution Δz depends on the spectral properties of the source and more exactly on the temporal coherence length l_c . This parameter is a function of the central wavelength λ_0 and the spectral bandwidth $\Delta\lambda$. Because of the two-way trip of the beam, the axial resolution is equal to half of the temporal coherence length l_c . For a Gaussian spectrum having a central wavelength λ_0 , it is given by:

$$\Delta z = \frac{l_c}{2} = \frac{2 \ln(2)\lambda_0}{\pi \Delta\lambda} \quad (2.13)$$

To enhance the axial resolution, two parameters can be maximised:

- decreasing the central wavelength λ_0 but this value is already determined according to the scattering coefficient of the tissue concerned and the penetration depth
- increasing the spectral bandwidth $\Delta\lambda$ which is equal to the full-width-half-maximum (FWHM) of the spectrum of the light source. This parameter is inherent to the source and cannot be improved afterwards. This is the reason why a supercontinuum source has been integrated in the setup to access a wider spectral bandwidth.

The curves shown in Fig. 2.10, represent the bandwidth $\Delta\lambda$ as a function of the central wavelength λ_0 for different resolutions. It is clear that, for shorter wavelengths, better axial resolution Δz is achievable for a smaller bandwidth than for a longer wavelength.

For example, to have a system running with an axial resolution of $1\mu\text{m}$, in theory, the light source needs at least a bandwidth equal to around 160 nm for a central wavelength equal to 600 nm . In contrast, for a longer central wavelength λ_0 , the axial resolution Δz is enhanced if the spectrum is distributed over a larger bandwidth $\Delta\lambda$. From Fig.2.12, an axial resolution approaching $1\mu\text{m}$ is achievable at $\lambda_0 = 1300\text{ nm}$ for $\Delta\lambda = 750\text{ nm}$.

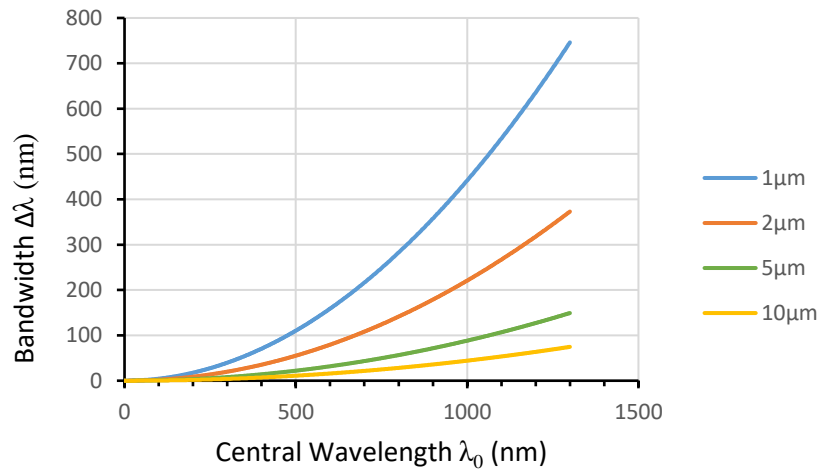


Fig.2.10. Bandwidth $\Delta\lambda$ as a function of the central wavelength λ_0 for different axial resolution values, Δz . These three parameters are linked by the equation (2.13).

From a technological point of view, it is complicated to create a light source with a large bandwidth and find optic components (lenses, gratings, couplers, etc...) suitable to accommodate such a large range of wavelengths. For this reason, achieving submicron resolution (around $1\mu\text{m}$) is for the moment not possible for longer wavelengths.

From this observation, it seems that to achieve ultrahigh resolution OCT system, it is easier to use a shorter wavelength. However, from 740 nm , the light beam is in the visible range for the human eye and this complicates the acquisition procedure for mainly two reasons. The first reason is that the maximum power applicable to the sample is much lower to be in the safety range and so, the penetration depth is limited. The second reason is that, when imaging the human eye, visible scanning light disturbs the fixation, i.e. it is more difficult for the patient to stay still.

A compromise is mandatory between the different parameters: the central wavelength which is chosen as a function of the application and the absorption properties of the sample, the bandwidth of the light source which is limited by its performance and the desired resolution. A suitable solution to perform ultra-high-resolution OCT in retina imaging is to choose a central wavelength around 850 nm with a bandwidth of at least 300 nm. This can be achieved by using a supercontinuum light source. Such a source also offers a variety of central wavelength and therefore the possibility to deviate away from 850 nm and choose a variety of other wavelengths. Accessibility to large bandwidth makes it possible to target any kind of application and sample type. In the next section, the use and challenges of this source are detailed.

2.2. OCT and Supercontinuum source

2.2.A Preamble

White light sources have been used from the beginning of biomedical imaging, with the use of oil lamps, candles or even the sun [6]. A large range of wavelengths makes it possible to highlight structural or functional information in any kind of sample. If, in addition to the natural large spectrum, filters are introduced, they offer flexibility in the choice of the wavelength and bandwidth used. In the last decade, supercontinuum sources (SC)s have become more attractive for biomedical imaging modalities such as fluorescence microscopy, photoacoustic or OCT.

The first reported supercontinuum generation was using a Q-switched pump at 532 nm [7,8]. The output source had a bandwidth equal to 300 nm emitting in bulk glass. Some years later, a SC was reported covering 0.7-2.1 μ m using a 1064 nm Q-switched Nd:YAG laser pumped into a long fibre [9]. The ability to have a broadband light emitted from the end of a flexible fibre is a turning point towards the use of SC as a potential source in biomedical imaging. The physical interpretation of phenomena such as modulation instability, also named four wave mixing, soliton self-frequency shift, self-phase modulation or zero dispersion wavelength were shown in 1991 [6] but it was necessary to wait for the invention of the photonic crystal fibre to see the first commercialisation of a SC by NKT Photonics in 2003.

In a few words, the supercontinuum generation can be seen as a pulsed laser at 1064 nm which is injected into a non-linear fibre (Fig.2.11). Due to interplay between dispersive effects and non-linear effects in the non-linear fibre, such as modulation instability, self-phase modulation and soliton fission, the bandwidth of the peak is enlarged and a broadband spectrum of several hundreds of nanometres is observed at the output of the fibre [6].

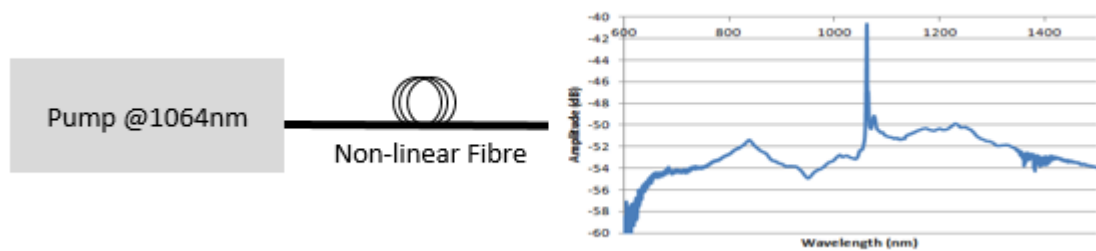


Fig.2.11. Schematic of supercontinuum generation principle.

Even if the first SC were commercialised in early 2000, they were considered too noisy for biomedical imaging. Indeed, the generation of SC is a stochastic phenomenon and the stability of the spectrum from one pulse to another is not ensured [10]. Researchers have tackled this issue and NKT Photonics launched a SC low noise source that is more attractive to biomedical applications.

Using the whole spectrum emitted by a SC through the optical and detection system is challenging. In our work, the detection of the optical signal is using a commercial spectrometer from Wasatch Photonic A/S (Cobra-S 800) and so, will not be approached in the following. Utilisation of the large spectrum requires precise dispersion control. A special section is dedicated on how the dispersion is minimised by introducing glass plates in one of the interferometer arms and employing a Split Spectrum Method (SSM) (2.2.C) to guide the correction. By the end of the chapter, section (2.2.D), a comparison is made of the noise properties and image quality between two broadband sources (Ti:Sa laser and SC).

2.2.B Supercontinuum laser in biomedical imaging

Early implementation of SC sources used a Ti:Sapphire laser for pumping the non-linear fibre [11]. Fluorescence microscopy [12], two-photon fluorescence [13] and Coherence Anti-Stokes Raman Spectroscopy [14] have all been demonstrated using this source. The disadvantages of such SC sources are the low power output and the limited spectral range in the visible wavelengths.

With the development of picosecond fibre SC sources, large bandwidth and high-power output are now available, which provides SC lasers with the potential to be used in several biomedical imaging systems. The option to select the wavelength and bandwidth, through the use of filters, combined with the ability to provide two wavelength bands simultaneously, makes the SC a suitable source for confocal fluorescence imaging [15], in particular Förster Resonance Energy Transfer, where two fluorescent dyes are excited simultaneously by different wavelengths to produce the donor and acceptor [16]. SC lasers have a pulsed nature that can be modified using a tuneable modulator, which can then be employed in Fluorescence Lifetime Imaging Microscopy. The pulse repetition rate is fixed to ensure that the time duration between two successive pulses is longer than the lifetime decay of the dye considered [17-21].

Another imaging modality is photoacoustic, which extracts sample information from its absorption properties. This modality requires a nanosecond pulse laser with a narrow bandwidth to target specific absorbers [22] and can be combined with an OCT system even though the longer pulse duration introduces higher noise since OCT favours picosecond timescales [22]. To assess the absorption information from the main tissue features, such as melanin or blood, the photoacoustic beam should present a wavelength in the visible range. However, the visible range presents several limitations for OCT imaging and therefore using the large bandwidth from the SC allows another wavelength range to be used simultaneously. Several publications already reported the use of such system to obtain structural and functional information from the sample [22- 24].

In the UBAPHODESA projects, 3 out of the 5 PhD researchers focused their work on using SC sources for OCT. Prior to this work, SC sources were considered too noisy

to be implemented in an OCT system compared to SLD or SS sources. With the improvements to the noise properties, SC sources became more and more attractive to the research community. Their wide spectral width permits the combination of different wavelength ranges and therefore a greater variety of samples can be imaged and characterized. The same source can be used to image in the visible, NIR and IR ranges and so structural imaging of the eye, brain and skin can be carried out [25- 27]. No other visible sources, fulfilling all these requirements, are available to be implemented in an OCT system whilst visible OCT research using SC lasers is thriving [25, 28- 32]. The abilities of the SC laser, via the wavelength selection and the large bandwidth, permits the improvement of the axial resolution and the design of sub-micron resolution OCT systems [28, 29]. The bandwidth can also be split into different spectral windows to retrieve the spectroscopic information from different features, allowing a new perspective on the sample [26, 32, 33]. SC sources have opened two main roads into the field of OCT – the use of the wider bandwidth improves the axial resolution, giving access to finer structural features, and the selection of specific wavelengths to retrieve more functional information.

2.2.C Superk from NKT Photonics

The first goal of this work was to achieve structural images with a good axial resolution (around 1 μ m). A SC from NKT Photonics A/S which covers wavelength from 450 up to 2400 nm is a perfect solution to achieve submicron resolution imaging. A part of the spectrum emitted by the SuperK Extreme from NKT Photonics A/S is displayed in Figure 2.12. In the OCT system assembled, the spectrum of the SC was centred at 840 nm and trimmed to a bandwidth of ~ 300 nm using a Superk Split from NKT Photonics A/S. The Superk Split is a passive filter splitting the spectrum into two bands: (i) in the visible and NIR range (600-1000nm) and (ii) in the infrared region. Using the values above in equation (2.13), the theoretical axial resolution is around 1 μ m.

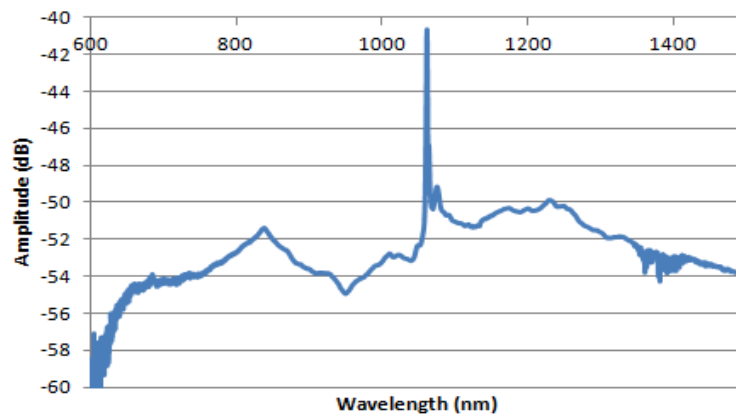


Fig.2.12. Spectrum of the SuperK EXTREME from NKT Photonics A/S from 600 nm to 1500nm

Using a broadband source as a light source is not enough to deliver ultrahigh resolution OCT images. To obtain an axial resolution as close as possible to the theoretical expected value, the components used need to be broadband (achromatic). Nevertheless, optical components have a limited acceptance wavelength range depending on their coating. Conventional lenses have a surface coating that ensures the maximum power transmission in a specific wavelength range and a precise focal point (depending of the wavelength of the propagated beam). Each wavelength is focused at slightly different axial locations. This phenomenon is called chromatic aberration which affects the bandwidth of the propagated beam and so, in the case of OCT system, the axial resolution. All lenses must be achromatic in order to maintain the advantage of ultra-broadband width and their coating has to be chosen wisely to reach the best performances possible. For this reason, a too large bandwidth cannot be used in the optical system (the interferometer and the spectrometer).

Another factor to consider when using a large bandwidth is dispersion. This has two origins; one is from the optical system and the other from the sample. In the next section, dispersion characterization techniques are explained based on hardware compensation. It is important to note that only dispersion from the optical system is tackled.

2.2.D Dispersion characterisation

The variation of phase velocity with wavelength is called dispersion [10]. In OCT, it is mainly introduced by the sample and by optical components of the interferometers. To minimize it, equal lengths of the same material should be secured in the sample and reference arms. The dispersion has a direct consequence on the pulse length. In case of normal dispersion, shorter wavelengths travel slower than longer wavelengths, and so, the temporal pulse gets wider. The same wavelength travelling in both arms will not arrive at the same time on the detector as can be seen in Fig.2.13. Therefore, polychromatic pulses travelling along dispersive material are therefore enlarged.

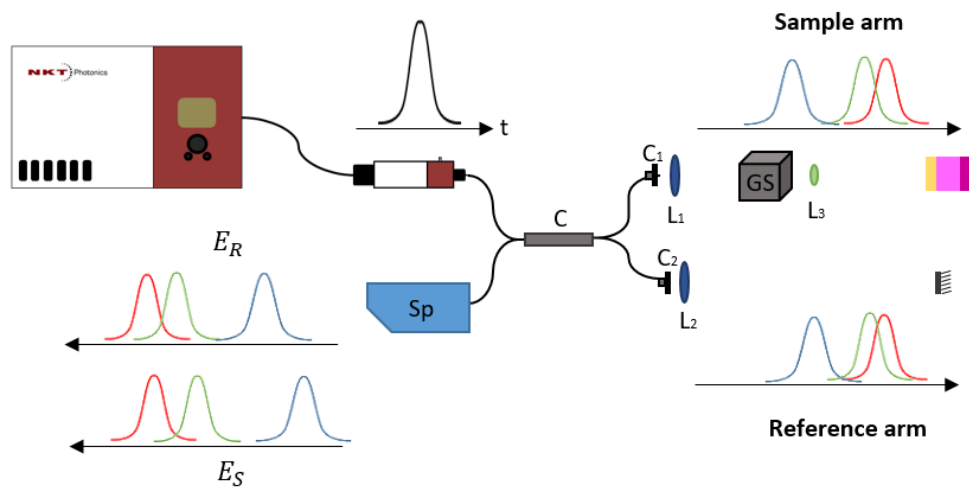


Fig.2.13. Dispersion through the OCT system. The blue pulse is the pulse at the output of the source. This propagates through the coupler which induces a separation in time of each wavelength. In the case of normal dispersion, shorter wavelengths are delayed more than the longer ones. If dispersion is not matched between the two arms, the pulses will not arrive at the same time at the output of the material.

Dispersion plays an important role in the quality of the image by impacting the axial resolution. It cannot be avoided but can be minimised. The solution is to balance the dispersion mismatch between both interferometer arms to achieve the same delay. The simplest way is to employ exactly the same optical components in both arms [34], but this will just compensate for the one induced by the material used in the interferometer and it is, in our case (large bandwidth), not enough to fully balance the dispersion. The effect of dispersion can also be reduced with some processing steps of the data as done

in the section 2.2.E. Another solution is to employ a method that is tolerant to dispersion in the interferometer, called complex Master Slave Interferometry (cMSI) as discussed in the next part of this chapter (2.3).

For now, it has been decided to use only hardware compensation by adding thin glass plates in one of the arms. Two approaches were adopted to evaluate the effect of addition of each plate: the first one consists of measuring the FWHM of the A-scan peak for different glass thicknesses introduced (section 2.2.D.1). In section 2.2.D.2, the relative position of the A-scan peak from a single layer sample (mirror) is measured.

2.2.D.1 Simple dispersion compensation

For this section, the sample is a mirror and so, the dispersion is balanced just for the interferometer and not for that introduced by the sample. Additional dispersion compensation characterization will be needed to balance the dispersion due to the sample. In the case of ultrahigh resolution applied to retinal imaging, the dispersion from the vitreous humour can simply be compensated by a cuvette of 25 mm of water introduced in the reference arm [35], water being considered sufficiently close in terms of dispersion to the vitreous [36].

The figure 2.14 presents the system used in this study. Light from a SuperK EXTREME Low noise, 320 MHz is spectrally filtered to obtain a range of 600 nm to 1000 nm that is conveyed towards a Michelson interferometer. Data are recorded with a commercial spectrometer from Wasatch Photonics A/S (Cobra-S 800). Some glass plates G_1 are added one by one to the sample arm to balance the dispersion. To keep the same modulation frequency in the interference pattern, i.e., to have the peak in the A-scan at the same position, the reference mirror is adjusted each time (translation of M_2 in Fig.2.14).

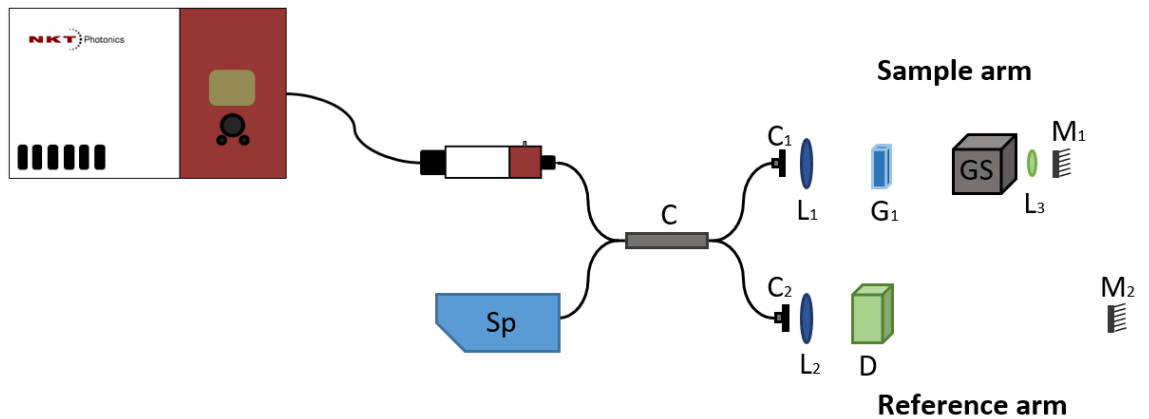


Fig.2.14. Setup configuration for simple dispersion compensation study. Sp: spectrometer, C: 50:50 coupler, $C_{1,2}$: collimators, GS: Galvanometer scanners, G_1 : Glass plate(s), $L_{1,2}$: Lenses, L_3 : Objective and $M_{1,2}$: Mirrors, D: Dispersion compensation block (for L_3)

To have a better overview, the measurement of the axial resolution is done at two different A-scan positions for each glass thickness. Position 2 is taken for a larger OPD than position 1. The axial resolution is, assuming a gaussian shape, equal to the FWHM of the A-scan peak. The results are displayed in Fig.2.15.

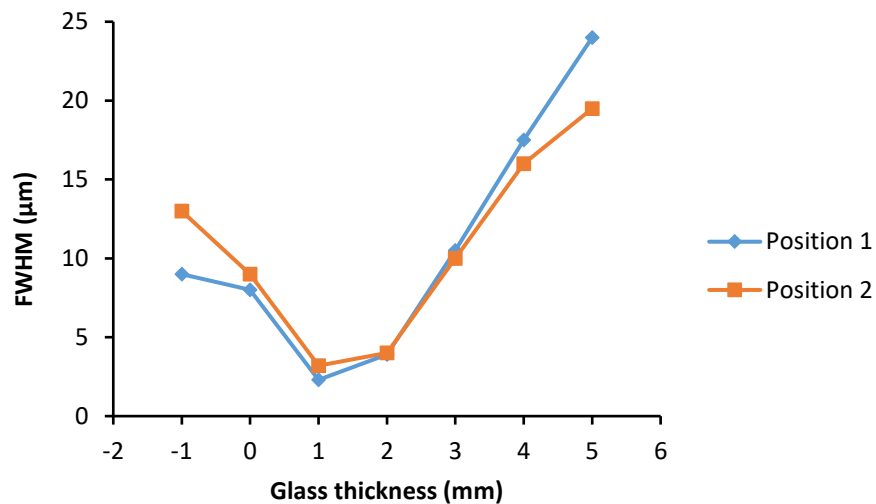


Fig.2.15. FWHM of the A-scan peak for different glass thickness. FWHM of A-line profiles obtained from two different OPD values as a function of the glass thickness added to the sample arm d_{G1} .

It is important to note that in Fig.2.15, negative glass thickness means that the glass plate is not introduced in the sample arm but in the reference arm. From Fig.2.15, the

best result is found for a glass thickness equal to 1 mm. The stock thickness value of a single glass plates is 1 mm, therefore it cannot be guaranteed that it is the optimum amount of glass to be introduced in the system. From this first measurement, it can be concluded that the optimum amount of additional glass thickness is between 1 and 2 mm. A finer step would have been desirable.

In the next section, another method is used based on tilting a glass plate. This allows for a continuous variation of glass thickness inserted. Instead of comparing the axial resolution between the different measurements, the relative A-scan position as a function of the central wavelength of the signal is used.

2.2.D.2 Split spectrum method (SSM) applied to dispersion compensation

The result of the previous section shows that the additional glass plate to compensate for the dispersion needs to be in the sample arm. To reach a finer dispersion compensation characterization, a tilted glass plate is used to introduce the right amount of glass. However, by tilting the glass plate, the optical beam is diverted from the optical axis. The glass is introduced, as shown in Fig.2.14 and Fig.2.16, before the galvanometer scanners (GS), and so diverting the beam from the optical axis by tilting the glass plate would cause issues in the scanning procedure.

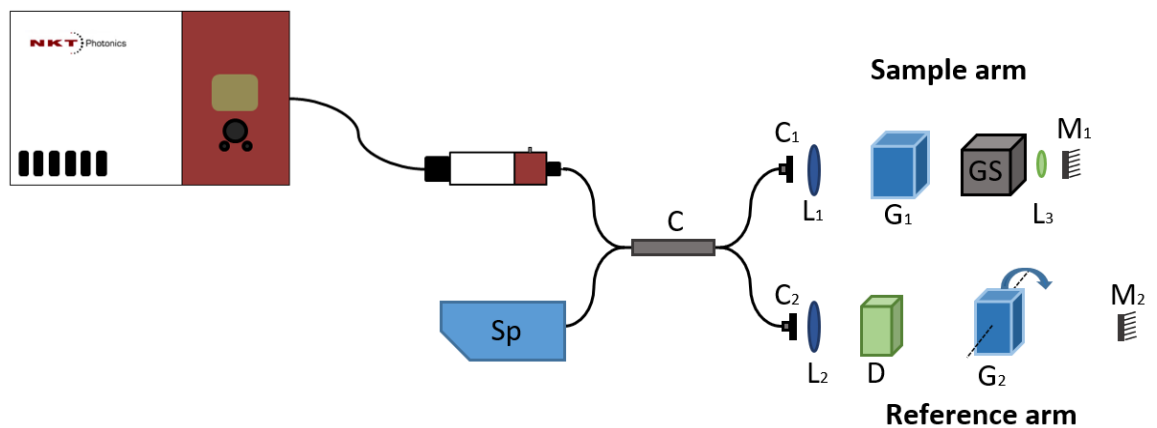


Fig.2.16. Set-up configuration for a more defined dispersion compensation. Some glass plate G_1 and G_2 have been introduced in the sample and reference arms, respectively equal to 7 and 5mm. G_2 can be tilted. Sp: spectrometer, C: 50:50 coupler, C_1 , C_2 : collimators, GS: Galvanometer scanners, L_1 , L_2 : Lenses, L_3 : Objective and M_1 , M_2 : Mirrors

To avoid that, the amount of glass thickness in the sample arm is fixed and kept perpendicular to the optical beam (case of $\alpha = 0$ in Fig.2.17), and in the case of our system equal to 7mm (G_1) and a 5 mm tilting plate (G_2) is placed in the reference arm. The plate (G_2) is tilted with an angle to change the amount of glass traversed by the optical beam (Fig.2.16 and Fig.2.17). Figure 2.17 shows the path taken by an incident light beam coming from a medium n_1 , traversing a medium n_2 and returning to the medium n_1 . It is a configuration $n_1/n_2/n_1$ where the terms n_1 and n_2 are the refractive indexes from the air and the glass equal to 1 and 1.4533 (fused quartz glass plates) respectively. The light beam has an incidence angle α and is refracted inside the glass plate (medium n_2) at an angle β . On the second surface (glass n_2 /air n_1), the ray arrives at an angle β and leaves at an angle α .

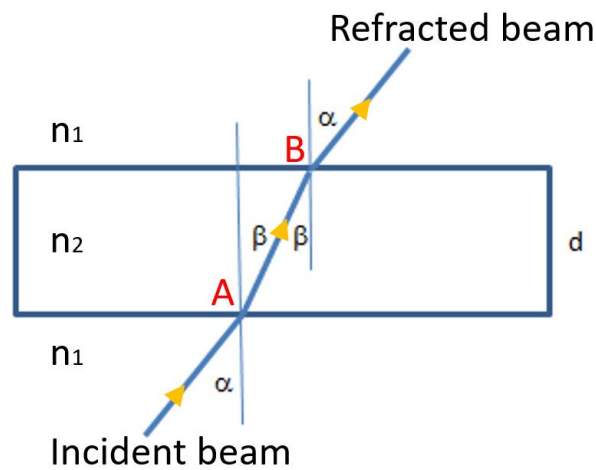


Fig.2.17. $n_1/n_2/n_1$ configuration. n_1 is the air refractive index and n_2 is the glass refractive index equal to 1.4533, α is the incidence angle of the light beam, β is the refracted angle from the glass plate surface and d is the thickness of the glass plate.

By tilting the glass plate, the thickness of traversed glass by the incident beam is adjusted to balance the dispersion in both arms. This method allows for a finer definition of the optimum glass thickness. Using the Snell-Descartes Law, also named the law of refraction, the effective glass thickness introduced in the incident beam path is given by:

$$n_1 \times \sin (\alpha) = n_2 \times \sin (\beta) \quad (2.14)$$

On the other hand, it can also be worked out that the distance between the point A and B (Fig.2.17), noted d_{AB} is equal to:

$$d_{AB} = \frac{d}{\cos(\beta)} \quad (2.15)$$

Combining eq.2.14 and eq.2.15, d_{AB} can be expressed as a function of the tilted angle, the refractive index and the thickness of the glass plate. The previous result in section 2.2.D.1 shows that the glass thickness needs to be between 0 and 2 mm to reach the best dispersion compensation. To cover this range, the tilted glass plate (with a maximum angle equal to 80°) must be 5 mm thick (G_2) in the reference arm and therefore a 7 mm thickness (G_1) is required in the sample arm. Figure 2.18 represents the effective thickness of the glass, d_{AB} traversed by the light beam as a function of the tilted angle α .

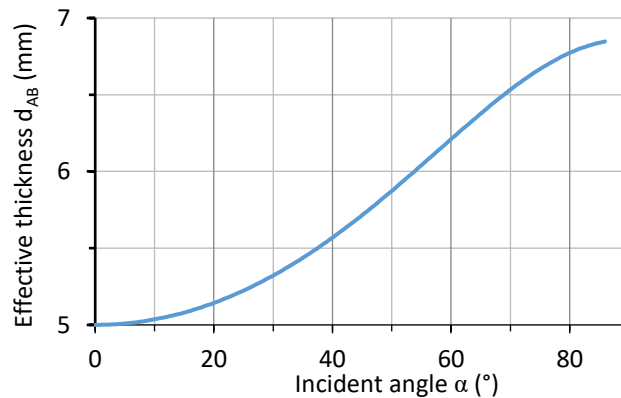


Fig.2.18. Effective Glass thickness d_{AB} as a function of the angle α .

This time, the measured values are not the FWHM of the A-scan peak but the relative position of the A-scan peak when using a mirror replacing the sample for different wavelengths. One solution to proceed is to use different narrow band light sources such as SLDs with different central wavelengths. However, for this, several light sources are needed to cover the full 300 nm bandwidth that the SC source has. Such a solution would be awkward. Another idea is to add a filter at the SC output and select just a part of the spectrum. The last method mentioned can be done in hardware but

using different filters or during the post processing steps of the raw data. It is the second solution that has been chosen to be applied in the following.

A similar procedure was developed for Optical Coherence Tomography Angiography (OCTA), under the name Split Spectrum Amplitude Decorrelation (SSAD) [37]. The principle is to split the spectrum into several spectral windows to enlarge the axial resolution in order to be less sensitive to motion in the depth direction, and average the N frames from the N divisions reducing the ratio between moving features over static ones.

This has the consequence of improving the continuity of vessels. Here, only the part about the split spectrum from this method is used and the amplitude decorrelation of the signal over time will not be calculated. In this way, the response from each wavelength through the system can be evaluated, dispersion-wise.

The interference pattern from a mirror, with a spectral extension BW , is multiplied by a Gaussian filter. The width of the filter was designed to match BW by adding zeroes before or/and after the Gaussian shape with a bandwidth of bw . The number of zeroes is determined by the relative position of the Gaussian function from the total spectrum length. If the full spectrum is divided by M , the number of windows, w is equal to $w = 2M - 1$. To correctly cover all parts, the central wavelength of the filter is shifted from $BW/2M$ between the m^{th} and $m+1^{th}$ windows with $0 \leq m \leq w - 1$. The number of zeros before and after the peak is equal to $mbw/2$ and $((w - 1) - m)bw/2$ with $0 \leq m \leq w - 1$. The function is defined, under the assumption of a normalized Gauss function, as:

$$G_m(x) = e^{-\frac{(x-\mu_m)^2}{2\sigma^2}} \quad (2.16)$$

where G_m is the Gaussian function for the m^{th} filter, μ_m the central wavelength of the m^{th} filter and σ , the standard deviation. The central wavelength is translated by $bw/2$, so $\mu_m = mbw/2$ with $0 \leq m \leq w - 1$. The standard deviation σ is extracted from the Gaussian distribution as a function of the central wavelength μ presented in Fig.2.19.

From Fig.2.19, to have the Gaussian window spread over the full division width bw , the standard deviation σ needs to be equal to $bw/6$.

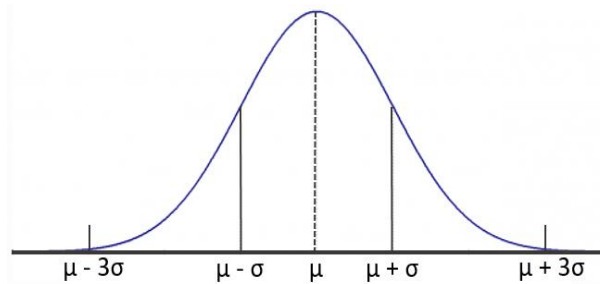


Fig.2.19. Gaussian distribution as a function of the central wavelength, μ and the standard deviation, σ .

Once the filters are created, the method can be applied as shown in Fig.2.20. The full spectrum from the raw data is used after linearization and multiplied by the Gaussian filter (Fig.2.20 (a)). As it can be seen in the figure 2.20 (b), all the areas of the spectrum are covered to be sure that the dispersion study is done over the full wavelength range. At each division (Fig.2.20 (c)), a Fourier transform is separately applied (Fig.2.20 (d)). If the dispersion is not properly balanced, the peak position of each A-scan for each division will differ (Fig.2.20 (e)). On the other end, if the dispersion is balanced between reference and sample arm, the different A-scan peaks will all be centred (Fig.2.20 (f)).

The glass plate was turned between 0 and 60°. The number of windows was set to 5 and the length of each one set to $BW/3$. Figure 2.21 presents the results. When the angle is 0 (Fig.2.21 (a)) i.e. as if 2 mm was introduced in the sample arm, the peak positions differ as with 30° (Fig.2.21 (c)). Both arms are balanced for a tilted angle equal to 50° (Fig.2.21 (b)).

This corresponds to an introduction of a glass thickness equal to 5.9 mm in the reference arm, in the addition of the 7 mm in the sample arm. This means that the equivalent glass plate thickness that should be introduced in the set-up should be 1.10 mm in the sample arm.

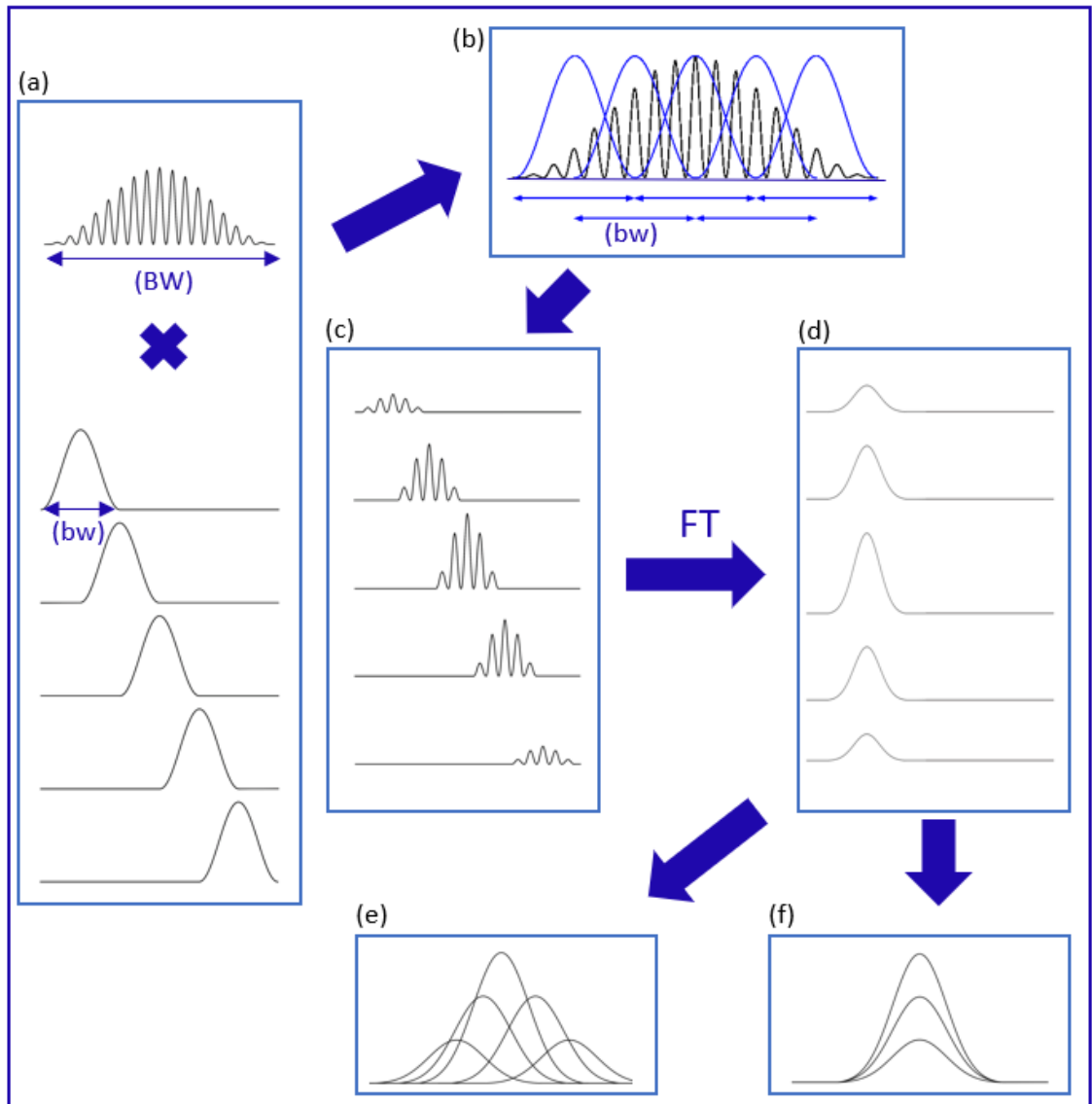


Fig.2.20. Split Spectrum Method (SSM) applied to dispersion compensation quantification. (a) the interference pattern from a mirror with a bandwidth equal to BW is filtered by a Gaussian shape with a size of bw , (b) superposition of the raw interference spectrum and the different Gaussian windows, (c) result of the filtering step, small interference pattern with a length of bw will be used to calculate the FT of the signal (d), (e) & (f) zoom on the peak position from each A-scan from each window in the case of dispersion compensated (f) and not (e).

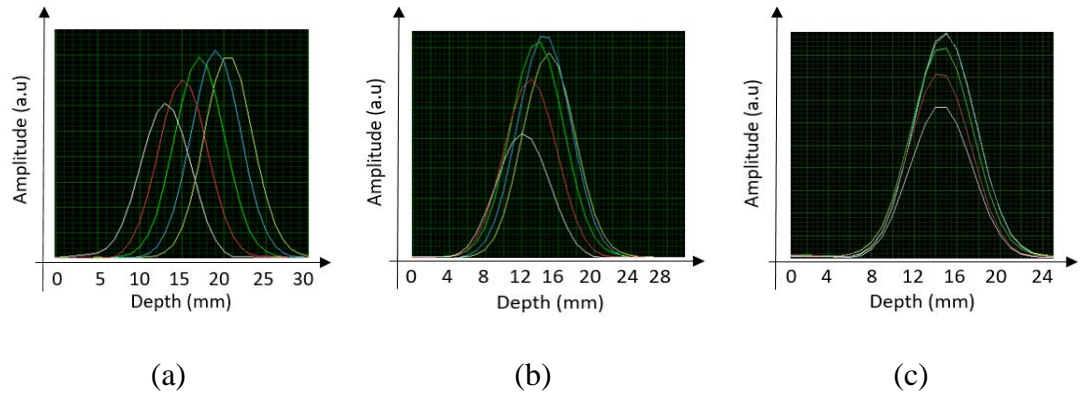


Fig.2.21. A-scan peak positions from a mirror for different tilted angles. 0° (a), 30° (b) and 50° (c)

This study is important in order to improve and optimize the image quality. Figure 2.22 presents several B-scan images from a mirror done with the full spectrum for different angles of the glass plate. It can be clearly seen that the resolution is worse in the case of tilted angles 0° and 30° (Fig.2.22 (a) and (b)) whereas the line is becoming finer when the dispersion is balanced (Fig.2.22 (c)). After the dispersion compensation is done, the axial resolution of the system is equal to $1.2 \mu\text{m}$ compared with $1 \mu\text{m}$ from theory.

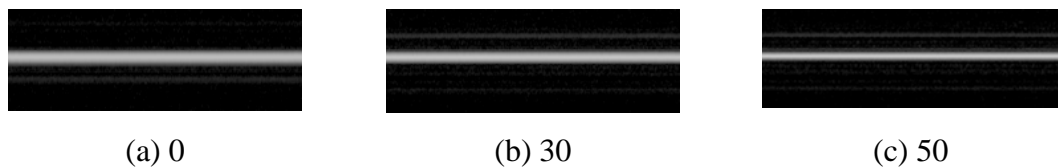


Fig.2.22. B-scan from a mirror for different tilted glass angle equal to 0° (a), 30° (b) and 50° (c)

Dispersion plays an important role in the quality of B-scan images. For further post-processing procedures such as spectroscopy or angiography, the functional information cannot be properly recovered if the dispersion is unbalanced. In this section, a study was run to evaluate the dispersion present in the system and to compensate using additional glass plates in one of the interferometer arms.

In the next section, a comparison between two broadband sources, a Ti:Sa laser and a SC source is performed as another step towards perfecting the method of achieving ultrahigh resolution.

2.2.E Broadband source in OCT: comparison between a Ti:Sa and Supercontinuum source for achieving ultrahigh resolution OCT – A case study

Author's note: This section is based on a study reported at the Bios conference hosted in Munich in June 2017 and published as a conference paper [15]. The research was performed at the Vienna Medical Centre.

2.2.E.1 Introduction and Methods

Two different light source, a Ti:Sa laser (Integral OCT, Femtolasers Produktions GmbH, Vienna, Austria) and a supercontinuum source (SuperK Extreme Low noise, 320 MHz, NKT Photonics, Birkerød, Denmark) were used in the same OCT system consisting of a free space Michelson interferometer and a broadband spectrometer [38- 40].

The source is connected to a 90:10 optical fiber coupler which splits the light between sample (10) and reference arm (90). In the sample arm, the beam leaves the coupler by a fibre collimator ($f=12$ mm; Schäfter+Kirchhoff GmbH, Hamburg, Germany) to go to the galvo-scanners head (GVS002; Thorlabs GmbH; Dachau/Munich, Germany), which scans the object in both directions, and is focused by a scan lens (LSM04-BB; Thorlabs; GmbH). The light scattered by the sample is directed to a spectrometer via the 90% transmission channel of the fiber coupler. In the reference arm, a neutral density filter was used to place the camera just before saturation and a dispersion compensation (LSM04DC; Thorlabs GmbH) rod to balance the dispersion in the object arm introduced by the sample and the optical components. The interference signal goes back to the coupler by a collimator ($f = 100$ mm; OZ Optics, Ottawa, Canada) and heads for the spectrometer. The spectrometer consists of a 50 x 50 mm transmission grating with 1200 lines per mm (Wasatch Photonics, Logan, UT) and is focused onto a high-speed line array CDD camera (Basler sprint spL4096- 140 kHz; Basler AG, Ahrensburg, Germany) by an objective ($f = 85$ mm, ZEISS PLANAR T 1,4/85 ZF-IR-I; Carl Zeiss AG, Oberkochen, Germany).

Figure 2.23 shows the different output spectra from the Ti:Sa laser and the SC operating at different percentages of the maximum power.

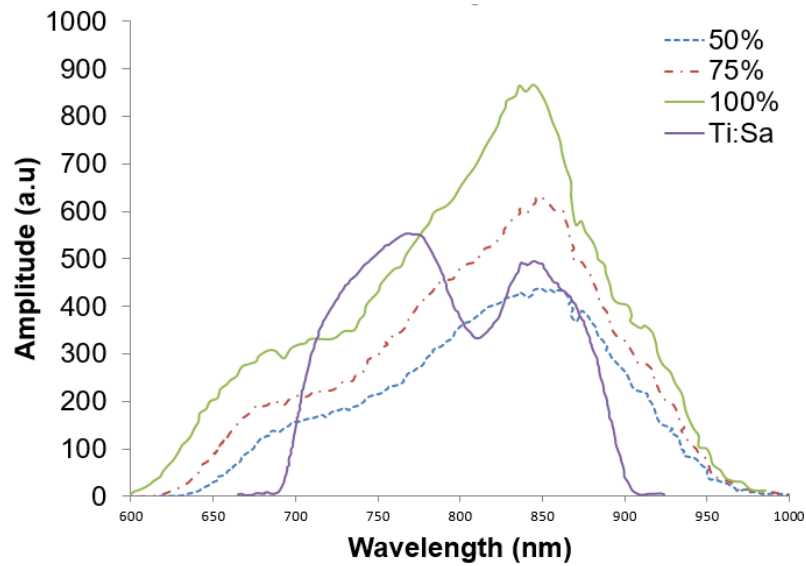


Fig.2.23. Spectrum at the output of the two broadband sources: SC running at different output powers (50%, 75% and 100%) and Ti:Sa laser.

The Ti:Sa laser emits at a central wavelength of 800 nm and covers a full width at half maximum (FWHM) spectral range of 175 nm. The theoretical axial resolution is equal to 1.7 μm in air and 1.2 μm in tissue (cornea).

The wavelength range covered by SC is from 600 to 2400 nm. The system used in this study has been designed to optimize the performance in the wavelength range of the Ti:Sa laser. To fit the same wavelength range, the output spectrum of the SC is spectrally filtered by a passive optical filter (SuperK Split from NKT Photonics, Birkerød, Denmark), which limits the spectrum to a FWHM bandwidth of 140 nm centered at 800 nm. The theoretical axial resolution is equal to 2 μm in air and $\sim 1.5 \mu\text{m}$ in tissue (cornea).

First, a comparison between noise performances of the SC has been conducted for different input power levels on a mirror serving as a reference sample. In a second measurement, the sample was a roll of sellotape and the SNR value was assessed from its returned signal. In both experiments, the sample arm power was adjusted using a neutral density filter implemented at the input of the Michelson interferometer to have a fixed incident power equal to 400 μW on the sample. A second neutral density filter was placed in the reference arm to reduce the power to not saturate the camera. The SC source was operated at different power outputs of 50%, 75% and 100% of full power capacity which influence the bandwidth and the shape of the spectrum as shown in Fig.2.26 and, thereby, the imaging parameters. The SC generation is more efficient at higher power where a broader spectrum is obtained. The depth information

was reconstructed using a Fourier Transform (FT) on the interference pattern. The comparison is performed by calculating the SNR. The SNR is defined by the formula:

$$SNR = 20 \times \text{Log}\left(\frac{\text{Signal}}{\text{RMS}}\right) \quad (2.17)$$

The signal considered in equation (2.17) is the amplitude value of the first peak in the A-scan. The RMS noise is expressed by:

$$RMS = \sqrt{\frac{1}{N} \sum_N x_i^2} \quad (2.18)$$

where x_i is the noise amplitude at position i . It is estimated by taking the amplitude values in a part of the image where no sample is present – more exactly before the first sample surface. In order to calculate the sensitivity, an additional neutral density filter was placed in the sample arm to attenuate the signal arising from the back reflection of the tape's front surface and had been considered as loss and added to the SNR value.

2.2.E.2 Results and Discussion

As mentioned, the first experiment was conducted using a mirror as a sample. The power on the sample was kept at 400 μ W. In Fig.2.24, the sensitivity is represented as a function of the SuperK output power level (%). The sensitivity was defined as the SNR value on which the loss value was added. The SNR is calculated using equation 2.17. The loss value corresponds to the intensity loss introduced by the neutral density filter in the sample arm. A mirror was placed in the sample arm at the focal position to measure the sensitivity. Two additional neutral density filters are also present to diminish the power and not oversaturate the camera, one in the reference arm and one in the input arm. The power from the reference arm should not be attenuated to be in the short noise regime. However, when using a SC source, the reflection from the reference mirror is enough to oversaturate the camera, even through a 90:10 coupler is

used. The level of attenuation is changed according to the percentage power output from the SuperK, which is held constant on the sample and equal to $400\mu\text{W}$. It was fixed to this value because it was the highest admissible power on the sample for a percentage output equal to 100% before saturating the camera. The sensitivity increases with the power outputs of the SC for the same power on the sample. This means that the noise is reduced as the power increases. This can be explained by the nature of the supercontinuum generation.

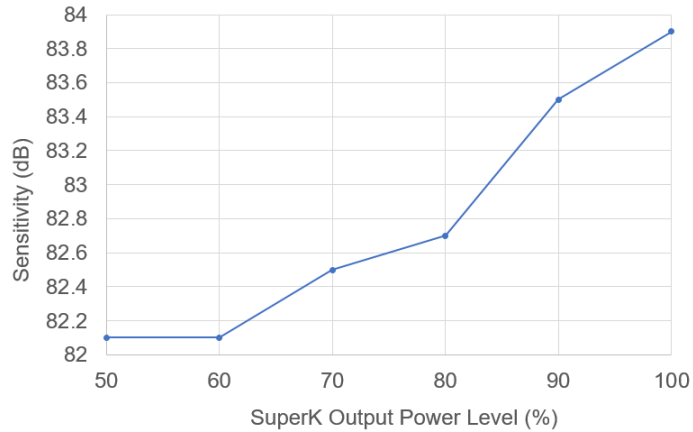


Fig.2.24. Sensitivity as a function of the percentage output from the SuperK. The power on the sample was set to $400\mu\text{W}$ [41]

The larger the input power of the pulsed laser, the larger the non-linear effects and the broader the spectrum. On the other hand, the intensity noise is most prominent at the edges of the SC spectrum. Increasing the pump power, which enlarges the width of the spectrum, leads to a reduction of the noise at a fixed wavelength (Fig.2.25) [42]. The relative intensity noise (RIN) of the SuperK has been measured using a spectrometer with 0.15 nm resolution and an integration time of 13 μs . The RIN is calculated as the standard deviation divided by the average value for each pixel. The sensitivity values exhibited by our experiment are quite low compared to the sensitivity from a state-of-the-art system, which is typically over 100 dB [43, 44], or even from the usual system sensitivity, which was stated at 97 dB [38]. The values shown in Fig.2.24 are more than 10 dB lower. A difference is expected because of the noise level being more significant in SC source than in the case of Ti:Sa laser. However, the difference is larger than expected, particularly when the images are compared. One explanation could be that the sample power had to be set especially low, $400\mu\text{W}$, instead of the 1.5 mW

used in the previous study [38]. In the formula, only the losses introduced in the sample have been taken into account but not those introduced before or in the reference arm.

From the second part of the study, the sample was a sellotape roll and both sources were used to perform measurements. The data on SNR performance are shown in Fig 2.26. For the SC source, the higher the pump power, the larger the bandwidth and therefore the lower the noise, as shown earlier. The SNR calculated from the OCT data produced with the SC running at 100% of the full power is 2dB lower than the measurements with the Ti:Sa laser.

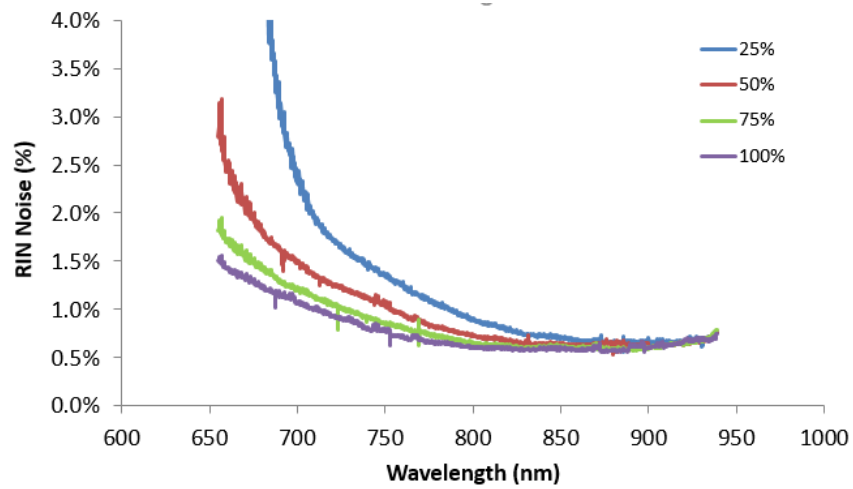


Fig.2.25. Relative Intensity Noise (RIN) as a function of the wavelengths for different output power levels of the SuperK. [41]

Source	Signal ($\times 10^5$)	RMS	SNR (dB)
SuperK at 50%	1.07	44.19	67.68
SuperK at 75%	1.35	47.20	69.14
SuperK at 100%	1.95	46.55	72.44
Ti:Sapphire laser	2.47	46.97	74.43

Fig.2.26. Calculations of the RMS noise and SNR for different output power of the SC and the Ti:sa laser [41].

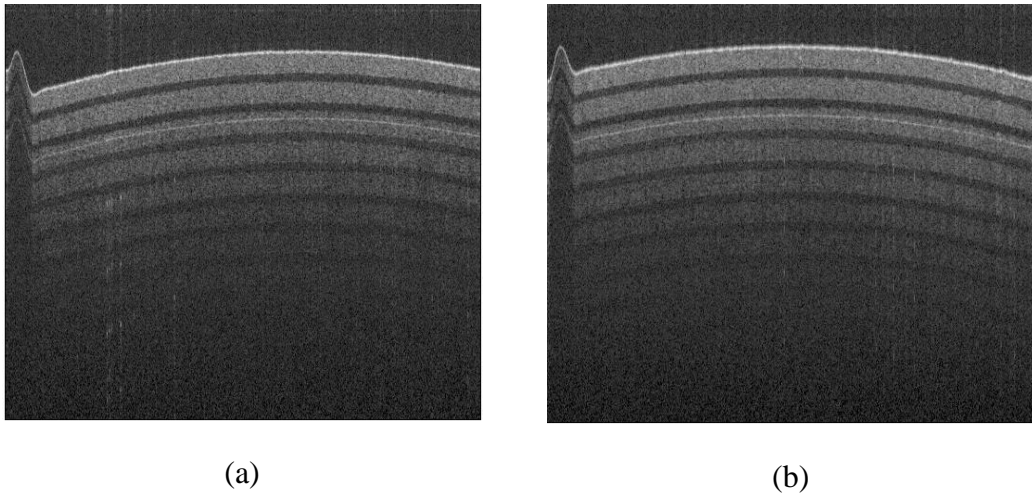


Fig.2.27. Performance comparison of the supercontinuum source from NKT Photonics running at 100% (a) and Ti:Sapphire (b) showing a B-scan with 512 A-scans on a sellotape sample after dispersion compensation at the post-processing stage. The power on the sample was 400 μ W [41].

Despite the difference in SNR calculated from the OCT data of the measurements with the different sources, the sellotape images shown in Fig.2.27 for a power output of 100% for the supercontinuum source (a) and Ti:Sapphire (b) reveal similar image features and the difference in image quality is barely noticeable. Both images present a fine bright line which is visible on the third layer of the sellotape. This line is not part of the sample and it is due to the presence of a glass plate placed in the sample arm. The thickness of the glass plate is fine enough to create a second image from the interference between the reference signal and the sample delayed signal.

To compare in a more realistic situation, images of the cornea from a healthy human volunteer have been acquired. The measurements were approved by the Ethics Committee of the Medical University of Vienna under the protocol number 1032/2015. The SC source was fixed at 100% power level. The power on the sample was set to 2 mW. This value is below the maximum permissible exposure (MPE) of 8.6 mW possible for this particular system given by the IEC 60825-1. LabView software was used for the data acquisition. Post processing steps were performed via a Matlab program, to compensate for the dispersion, and via ImageJ, to obtain images in

Fig.2.28 (a) and (b). Even though the sensitivity of the SC is worse, the precorneal tear film could be visualized using both the SC and the Ti:Sa laser. The reflection of the first layer from the SuperK appears brighter because the image was acquired closer to the central part of the cornea (where the reflection is higher) compared to that taken with the Ti:Sa which is more at the cornea periphery. By drawing an A-scan, the different layers can be resolved and measured in both cases. Even small variation between tear film measurements can be observed due to the fine axial resolution (Fig.2.28 (c) and (d)) by looking at the distance between the first two peaks, which is the thickness of the tear film.

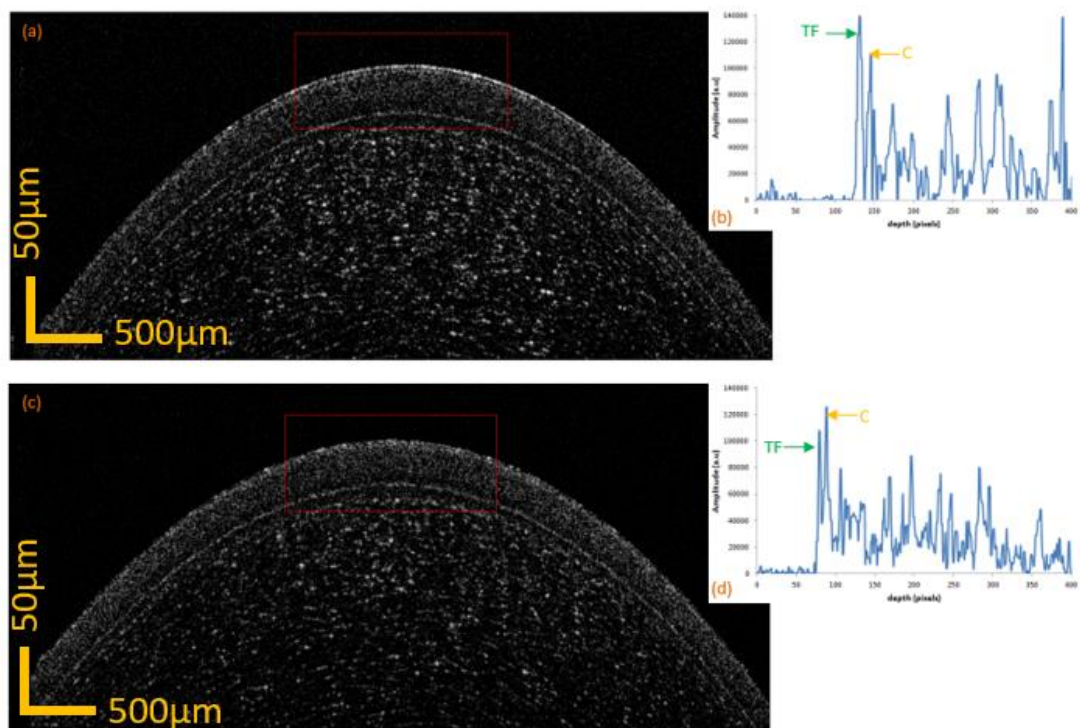


Fig.2.28. B-scans of human precorneal tear film using a supercontinuum source from NKT Photonics ((a), (b)) and the Ti:Sa laser ((c),(d)) acquired at different positions of the cornea. The power on the sample was 2 mW. (a) and (c) are the B-scans. Graphs (b) and (d) representative A-scan of the region indicated by the red rectangle shown in (a) and (c). TF, tear film front and C, cornea front surface.

2.2.E.3 Conclusions

In this section, high resolution OCT images of sellotape phantoms and *in-vivo* human cornea have been obtained using a supercontinuum source and a Ti:Sapphire laser. For the phantom, the signal to noise ratio performance was approximately 2 dB better for the Ti:Sapphire laser

than for the SuperK. The optimal performance of the SC was obtained when operating at the maximum power level, yielding an improvement in SNR of 4.8 dB when operated at 100% power compared to when operated at 50% power. However, despite the difference in SNR between the Ti:Sa laser and the Superk, the images from the sellotape, as well as the *in vivo* images of the precorneal tear film, appear to be similar. All corneal layers (Fig.2.29), as well as the tear film, can be resolved via both the Ti:Sapphire and the SC source. As in Fig.2.27, a curved line is visible in the middle of the first third of the corneal stroma. As explained earlier, this is because of the presence of a glass plate in the sample arm which creates a second image from the sample by combining the reference optical signal and the sample delayed optical signal.

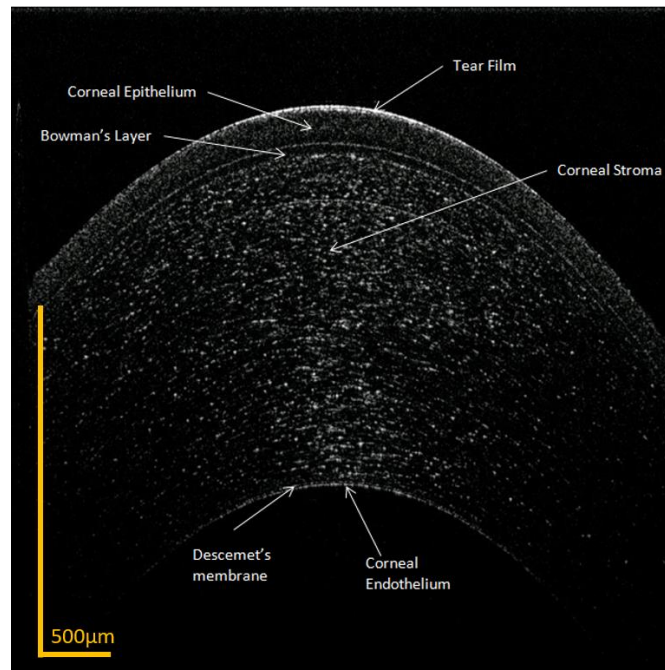


Fig.2.29. B-scan of human corneal eye with Superk running at 100%. Each structural layer is resolved: Tear Film, Corneal Epithelium, Bowman's Layer, Corneal Stroma, Corneal Endothelium and Descemet's membrane.

Both sources look suitable for ultrahigh resolution corneal OCT imaging, visualization of the precorneal tear film and evaluation of the tear film thickness and show potential for the diagnosis and treatment monitoring of various corneal pathologies [45, 46].

2.3. OCT and complex Master Slave Interferometry (cMSI) method

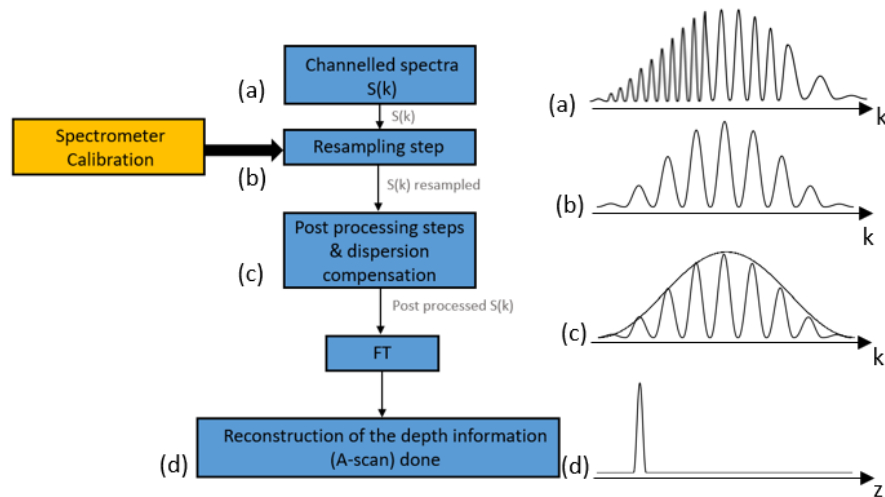
Compared with TD-OCT, only one acquisition is necessary to obtain the depth information collected by FD-OCT (Sp-OCT and SS-OCT). To separate the different information from each layer, the channelled spectra are recorded as a function of time for SS-OCT and as a function of pixel position on the spectrometer camera for Sp-OCT. The spectrum interrogation is done via the source, sweeping the different wavelengths in the SS-OCT case and via a spectrometer for Sp-OCT case, by reading its camera. Once the channelled spectra have been recorded, several processing steps are needed before recovering the depth information. Both post-processing methods present similar processing steps but the following will focus exclusively on Sp-OCT. Until now, the images shown have been processed using the most common processing method: the Fourier transform (FT). In the next section, the different steps employed to process the images with the FT method are explained, before moving to a different method developed at the University of Kent called complex Master Slave interferometry (cMSI).

2.3.A Fourier Transform vs Complex Master Slave interferometry

2.3.A.1 Fourier Transform

To separate the different optical frequencies, the detector in a Sp-OCT system is a spectrometer. Light from the interferometer output is sent towards a diffraction grating, working in transmission or reflection, before being focused on a CCD camera. The recorded signal is measured as a function of the camera pixel. However, to reconstruct the information from the different layers in depth before performing a Fourier transform, as shown in eq.2.9, data (the channelled spectra) must be resampled to ensure its uniform distributed in the k -space [46]. This is due to the fact that the pixel position in the camera is not linearly proportional to the optical frequency. Prior to the first measurement, a calibration step of the spectrometer is required and will be used to resample the raw data (before any further post-processing steps). The spectrum $S(k)$ is not linearly spaced with k and is denser for shorter wavenumbers (Fig.2.30 (a)). Using the information provided by the spectrometer calibration step, the channelled spectrum $S(k)$ can be resampled (2.30 (b)). An improper calibration of the

spectrometer leads to poor axial resolution, by enlarging the widths of the A-scan peaks and the drop off in sensitivity with depth [46]. Before calculating the Fourier transform of the resampled channelled spectra $S(k)$ (2.30 (d)), further post processing steps can be used such as apodization or normalisation. This step is not essential but it will ensure smoother final A-scan, improving the quality of the final image (2.30 (c)). Several window functions can be used for apodisation, such as for example Gaussian, Hamming, etc.



2.30 Recovery of the depth information using Fourier Transform. (a) the interference pattern mapped as a function of the wavenumber k . $S(k)$ is resampled using the spectrometer calibration (b) and post processed (c) before recovering the depth information by applying a Fourier transform (FT) (d).

It is important to note that the process just explained will reconstruct the information of a single A-scan line at one transversal position. To recover the full B-scan image, this process needs to be repeated at each transversal position of the sample scanned using a galvanometer scanner.

The explained process is the ideal case using the assumption of a dispersion free system. Under this condition, the propagation constant can be written as $\beta(\omega) = \frac{k}{2}$. As said earlier, even without considering the dispersion introduced by the sample, the system will still present some dispersion attributed to using couplers or other optical components, [47-49]. In this case, the propagation constant $\beta(\omega)$ cannot follow the relationship stipulated earlier and its second derivative needs to be considered. One

solution to this problem is to balance the dispersion in both arms, as seen in the previous section using hardware (2.2.C) or software methods.

Another solution is to analyse the data using an alternative method that does not require any Fourier transform and so therefore would not require the resampling step in k . This method has been developed by Professor Podoleanu of the Applied Optics Group at the University of Kent [50]. In the next section, a deeper explanation of this signal processing method is given. From now on, all the images presented will use this method and will not be processed using the Fourier transform.

2.3.A.2 Complex Master Slave interferometer (cMSI) method

Master Slave Interferometry (MSI) is a signal processing method to recover the depth information from the spectra recorded by the camera. As shown in previous publications [50, 51], MSI provides an improved strategy for processing the channeled spectra in frequency-domain interferometry. Instead of carrying out a FT on the acquired spectrum, it performs a comparison between the spectrum acquired and a previously saved set of spectra which fully incorporate the signature of the interferometer and of the process of coding the optical path difference into wavenumbers.

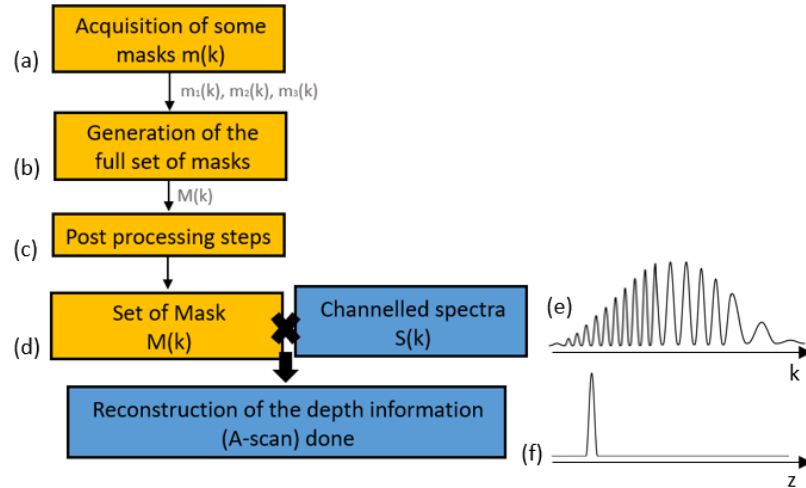
By employing this strategy, the system is immune to mismatches in the interferometer dispersion [51]. Moreover, it bypasses the requirement for linearization in the k -domain [51], which is a necessary step in all FT based conventional spectral (Fourier) domain OCT systems. An additional advantage of using the MSI method has also been identified, since the re-sampled FT method requires three steps to be completed (resampling, FT and numerical compensation) for each captured spectrum, whereas MSI requires only one step: the operation of comparison. Early implementations of the MSI algorithm were, however, intensity-based. Since the comparison algorithm was implemented using a cross-correlation function, all the phase information present in the channeled spectra was lost. Another disadvantage was that every single mask had to be recorded manually to create the full set of masks used later on. If for any reason the dispersion or the reference arm length changed, the masks set previously recorded were no longer optimum to reconstruct the depth information and another set of masks

was required. If the bandwidth is large, the axial resolution interval is small and this would have required collection of too many spectra.

Recently, an improved MSI technique has been reported called complex-domain MSI (cMSI) [52, 53]. Notably, spectra processed using the cMSI method have a complex-domain representation, which means that the phase can be extracted. It has been demonstrated that cMSI yields equivalent results in terms of amplitude and phase to those obtained by Fourier-transforming the k -linear spectra, without being affected by dispersion left uncompensated for in the interferometer [51]. Another advantage of this method is that the set of masks is now generated from at least 2 experimentally collected spectra recorded at different OPDs making this step much more efficient.

The different steps of using the cMSI method are shown in Fig.2.31, the procedure can be divided into two parts: Master and Slave. Prior to the first acquisition, several steps (operations in yellow boxes in Fig.2.31) being the Master part are needed to properly recover the depth information from the spectra. A mirror is used as a sample and placed in the focal plane to match the confocal gate. The mirror from the reference arm is moved until interference occurs and is positioned near $OPD = 0$. The reference mirror position of the first mask is not at $OPD = 0$ to be able to distinguish the signal of the cross-correlation term from the DC term. Three or more interference patterns are recorded for three or more equidistant positions of the reference mirror (Fig.2.31 (a)). They are done manually and are called “experimental calibration masks” and are noted, in the case of 3 experimental calibration masks, as $m_1(k)$, $m_2(k)$ and $m_3(k)$. From these experimental masks, the functions g and h , modeling the chirp affecting the channeled spectrum at the interferometer output, are extracted to build the full set of complex masks denoted as $M(k)$ (Fig.2.31 (b)). The matrix $M(k)$ can be developed into $M(k) = [m_1(k), m_2(k), \dots, m_p(k)]$ where p is the number of masks desired in the depth direction. The minimum number p is equal to the depth of imaging divided by the axial resolution. If some windowing function needs to be applied, it is instead applied to the set of masks $M(k)$ to minimize the number of steps done on the raw spectrum to obtain the depth information (Fig.2.31 (c)). Once this is done, the set of masks (Fig.2.31 (d)) is ready to be used with a sample and the next steps are included in the Slave part of the post processing procedure. The Master step only needs to be carried out once. However, in case of addition and replacement of optical components,

new experimental calibration masks are required to generate the new set of complex masks to properly balance the dispersion and the changed chirp in spectrum modulation of the optical system.



2.31 Recovery of the depth information using cMSI method. (a) acquisition of experimental masks, (b) generation of the full set of complex masks $M(k)$, (c) windowing of $M(k)$ to obtain the final set of complex masks (d). From a sample, the interference pattern is recorded named $S(k)$ (e) and then, $S(k)$ is correlated to $M(k)$ to recover the depth information (f).

Once the Master steps are done, the Slave part (blue step in Fig.2.31) can start by replacing the mirror from the sample arm with a sample and by running an OCT acquisition (Fig.2.31 (e)). During the Slave part, the set of masks $M(k)$ and the channelled spectra from the sample are correlated to reconstruct the depth information (Fig.2.31 (f)). Instead of the 5 steps presented in Fig. 2.30, only 2 steps are required with cMSI (Fig.2.31). The major advantages of cMSI in comparison with the previously implemented MSI method are: (i) any number of complex masks can be calculated from a relatively small number of experimentally collected calibration masks; (ii) opening novel avenues in phase processing and (iii) better stability in the delivered A-scan peak from the depth of the complex mask due to using both the cosine and sine components of the complex mask.

Both MSI and cMSI methods can work directly on the non-uniform distribution in wavenumber and conserves the expected theoretical axial resolution. As mentioned earlier, it is also possible to create enface images directly, which is not possible with

the FT method. During post processing, the enface information in the FT method is accessed via a transverse cut of a selected particular axial depth of the full volume created from the assembly of a large number of B-scan images. For cMSI, there is direct access by correlating the interference spectra with just one complex mask at the selected axial depth. If the action is repeated for different axial depth positions, a display of several direct enface images is possible. This ability is useful for monitoring a sample in real time, such as an embryo, making it possible to observe the sample simultaneously at several axial depths in addition to the confocal image and the depth information given by the display of the B-scan images (chapter 4).

As already mentioned above, the cMSI method, unlike the initial MSI method, is capable of recovering both amplitude and phase of the signal from the sample. The amplitude signal is essential for creating the structural images but for functional images, phase signal is also necessary. In the next section, a small study is conducted to compare cMSI and FT method for phase sensitive measurements.

2.3.B cMSI: phase information conservative method

Author's note: This section has been adapted from a study in collaboration with Manuel J.M. Marques reported at the international conference Photonics West, February 2017 (poster session).

2.3.B.1 Introduction

Phase-sensitive optical coherence tomography (PhS-OCT) can be employed to characterize the flow properties of a biological tissue by using methods such as phase variance or Doppler OCT [54], and also to measure additional polarimetric properties of a sample [55]. The structural information which is provided by OCT imaging is generally an intensity-based representation; it is known from microscopy that many objects yield poor contrast if the intensity is the only parameter considered. By taking the phase of the optical signal into consideration, additional information can be obtained, including flow quantification through Doppler OCT (D-OCT) [54], and

supplementary parameters in polarization-sensitive OCT such as the optic axis orientation or the degree of polarization uniformity (DoPU) [55].

Previously, experimental demonstrations have been carried out, showing that the two methods (cMSI and re-sampled FT) present comparable results in terms of amplitude. The cMSI method has the advantage to be implementable on raw data without the need to linearise the spectrum in k as is necessary in the FT method and being immune to the dispersion from the interferometer. In other studies, the processing time of both methods were also compared [53, 56]. To produce a B-scan, post-processed using cMSI, the processing time is equal to the time to multiply 2 matrices. If M and N are the number of points axially and laterally respectively, the number of operations that needs to be carried out to complete a full B-scan image is $M \times N (2M - 1)$ while in the case of the FT, it is equal to $M \times N \log_2 M$ [53, 56]. The FT method or FT with resampling is faster than the cMSI method. However, some optimisation in post-processing of the cMSI can be done using a high-performance toolbox from LabVIEW or by reducing the axial range or the digital axial resolution [53, 56].

In this section the phase-sensitive capabilities of the cMSI method is investigated. Several measurements on a flow phantom are performed and flow measurement are carried out for different flow rates. The same set of measurements is then post processed using the conventional FT based spectral interferometry (applied to resampled data sets) and cMSI. The complex-valued OCT data was obtained by carrying out the FT on the k -linear spectra and by using the cMSI method on the same spectra (with no linearization applied to it in the latter case).

2.3.B.2 Method

The experimental set-up, for this section and Chapter 3, is shown in Fig 2.32. Light from a SLD (super-luminescent diode from Superlum) with a central wavelength (λ_0) of 840 nm and a bandwidth $\Delta\lambda \sim 50$ nm, is sent via a fiber-based 50/50 coupler to divide the beam between a reference arm and a sample arm. In the sample arm, the beam is scanned using an 1D galvanometer scanner (SX) and focused into the sample by a microscope objective (MO) from Thorlabs. A dispersion compensation block (DCB), presenting the same dispersive properties as MO, is introduced in the reference

arm to match both arms. The reflected beams are then sent to a spectrometer consisting of a diffraction grating (TG, 1200 l/mm) operating in transmission from Wasatch Photonics and a lens (FL) that focuses the light onto a CMOS, line camera (Basler sprint spl4096-km). A peristaltic pump (Gilson minipuls 3) (PP) was added to the system to create the flow.

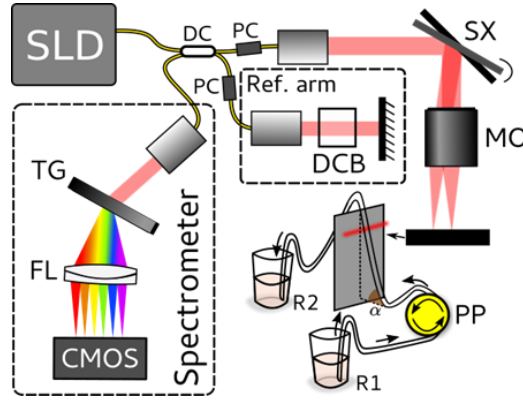


Figure 2.32. Set-up diagram for the experimental comparison of two phase-sensitive methods.

A phantom was assembled employing two PVC tubes of 1 mm internal diameter, oriented in such a way that the liquid (diluted milk) was flowing in opposite directions through them. The tubes and the liquid flowing through them were imaged for different pump speeds, and the resulting OCT data was processed with FT based and cMSI based software, as shown in Fig 2.33. For the processing of the FT, re-sampling was applied to correct non-linearities in the channeled spectrum caused by the spectrometer and residual uncompensated dispersion. For the cMSI method, 512 complex masks were generated from a set of 10 experimental channeled spectra taken at different OPD values before the data acquisition was carried out.

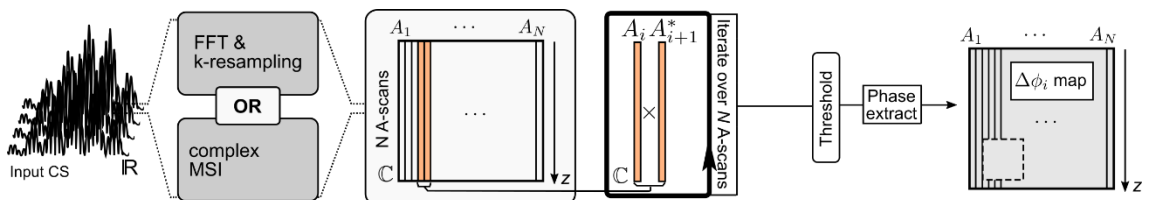


Fig. 2.33 brief summary of the data processing method to obtain the Doppler frequency shift map.

As shown in Fig. 2.33, the post-processing steps following the reconstruction of the A-scans are the same; these consist of applying a threshold to the amplitude in order to calculate the phase of the field of interest at each B-scan, followed by subtracting the phase of two adjacent A-lines. Since a fixed time period has elapsed between their acquisition, the ratio between the phase difference and that time period yields a Doppler frequency shift. For the comparison of phase reconstruction, an average of the phase differences were taken over a rectangular area of similar size, drawn over the center of each tube (as shown in Fig. 2.34 i.). The resulting values were then averaged together across 40 B-scans.

2.3.B.3 Results

Results from the experiments are shown in Fig. 2.34 and Fig. 2.35.

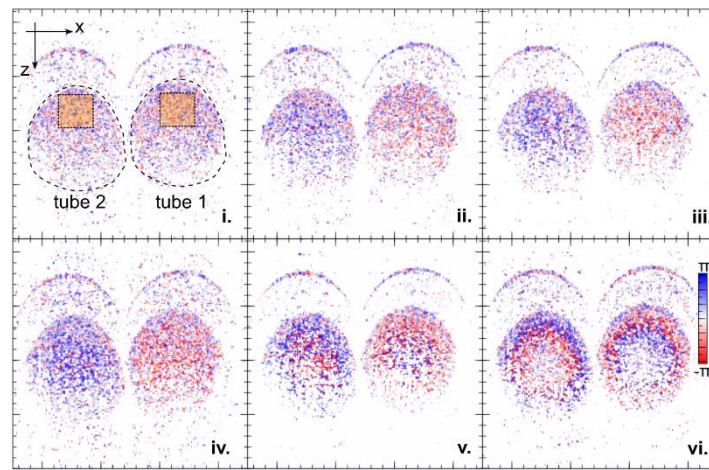


Figure 2.34 Adjacent phase difference $\Delta\phi$ (Doppler shift) as a function of pump speed. B-scan maps of $\Delta\phi$, obtained with the cMSI method, for different pump speeds: (i) 0 mL/s, (ii) 0.064 mL/s RPM, (iii) 0.096 mL/s, (iv) 0.224 mL/s, (v) 0.32 mL/s, and (vi) 0.48 mL/s.

Figure 2.34 shows the B-scan adjacent phase difference $\Delta\phi$ maps for different pump speeds, obtained with the cMSI method. When the pump speed is zero (Fig. 2.34 i.), the observed signal has a combination of positive and negative $\Delta\phi$ due to Brownian motion. However, the direction of movement cannot be inferred and both tubes appear of similar color (on average). The experiment was repeated for different pump speeds

(Fig. 2.34 ii - vi); as expected the higher the speed, the higher the phase difference. This can be seen in Fig. 2.34 ii. and iii, where the left-hand tube appears blue while the right-hand tube color shifts to red.

The Fig. 2.35 depicts the comparison of an average $\overline{\Delta\phi}$ of $\Delta\phi$ values between cMSI and the FT method for different pump speeds. These averages have been carried out along the (x,z) axis, within the shaded boxes in Fig. 2.34, and also over 40 B-scans.

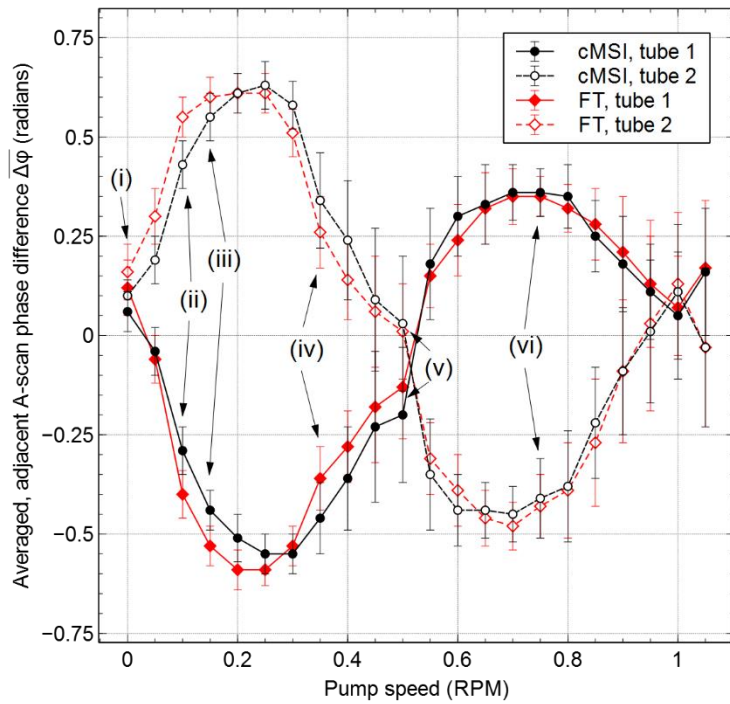


Figure 2.35 Comparison between the FFT and cMSI methods for an average $\overline{\Delta\phi}$ of $\Delta\phi$ values as a function of pump speed. The average has been carried out along the (x,z) axis, within the shaded boxes in Fig.2.37 (i), and also over 40 B-scans. The error bars represent the standard deviation associated to the calculation of $\overline{\Delta\phi}$.

In Fig. 2.35, the curves depicting the average $\overline{\Delta\phi}$ obtained with the cMSI or the FT method from the same raw data overlap within the error bars. A symmetrical behavior is observed between tube 1 (solid lines) and tube 2 (dashed lines) due to the reversal in the flow direction. For a sufficiently high pump speed, phase unwrapping effects are observed, introducing a reversal of signs for $\overline{\Delta\phi}$. This is also observed in Fig. 2.34, where regions of the opposite color are observed in the center of the tube.

The comparison of phase information extracted from both FT and cMSI on the same raw data shows similar results. The measurements suggest that cMSI can be used from now on to infer the phase information with less post-processing steps. It is important to note that this study was designed to see if FT and cMSI retrieved similar phase values after both post-processing methods are used. It should be remarked that the study was carried out on experimental data previously acquired by a third party. The only information provided about the fluid was that ordinary milk powder was used, diluted with an unknown quantity of water. But the dilution factor does not have an impact on the results since the same set of data was used for both methods. For the following study (Chapter 3), this limitation was overcome by selecting an intralipid solution with a known fixed dilution.

2.4 Conclusion

In this chapter, the fundamentals of OCT technology have been established. The different OCT modalities have been discussed, with a focus on FD-OCT and more specifically Sp-OCT. Sp-OCT, often referred as SD-OCT in the OCT field, allows for depth resolved imaging in one acquisition by the use of a low temporal light source. Some characteristics of OCT systems have been explained such as depth of focus as well as transverse and axial resolution. The last parameter is proportional to the central wavelength and inversely proportional to the bandwidth of the light source. Increasing the bandwidth for a fixed wavelength improves the axial resolution. With this in mind, a large bandwidth source from NKT Photonics A/S was chosen to enhance the axial resolution as much as possible. This source is based on supercontinuum generation, which, for a long time, was considered too noisy to be used in biomedical imaging.

In the second section, after explaining the different characteristics of this source and the challenge due to the large bandwidth, a study compared the noise performance based on the SNR calculation of two broadband sources, a Ti:Sa laser and the supercontinuum source. Imaging of the cornea was performed with each. Even though the SNR value shows a 2 dB difference between these two sources, in favor of the Ti:Sa laser, barely any difference can be observed on the *ex-vivo* sellotape or *in-vivo* cornea images. Both sources combined with an ultrahigh resolution OCT system were

able to distinguish all the different layers of the cornea and could also resolve the tear film.

In the last section, the feasibility of using the phase extracted from the OCT data, processed using the cMSI method has been studied. For this purpose, phase-sensitive measurements have been carried out on a flow phantom, with Doppler OCT being used to distinguish between several flow rates. By having access to the phase, cMSI can now be used for all phase-specific OCT imaging modalities such as optical angiography through phase variance, quantification of the orientation of the optical axis in polarization-sensitive OCT, among many others.

References

- [1] J.G. Fujimoto and W. Drexler, "Optical Coherence Tomography: Technology and Applications," Springer-Verlag, Berlin, Heidelberg (2008).
- [2] B.H. Bunch and A. Hellemans, "The history of Science and Technology," Houghton Mifflin Harcourt. p. 695. (2004).
- [3] P. Hariharan, "Basics of Interferometry," Elsevier Inc. (2007).
- [4] A. Podoleanu, "Optical Coherence Tomography," Journal of Microscopy, doi: 10.1111/j.1365-2818.2012.03619.x (2012).
- [5] F. Fleischhauer, "Optical coherence microscopy with extended depth-of-focus," Master thesis, Universität zu Lübeck, Institut für Biomedizinische Optik (2014).
- [6] H. Imam, C.L. Thomsen and O. Bang, "Broadband supercontinuum light sources for biophotonics application."
- [7] R.R. Alfano and S.L. Shapiro, "Emission in the region 4000 to 7000 Å via four-photon coupling in glass," PRL 24, 584-587 (1970).
- [8] R.R. Alfano and S.L. Shapiro, "Observation of self-phase modulation and small-scale filaments in crystals and glasses," PRL 24, 584-587 (1970).
- [9] C. Lin, V.T. Nguyen and W.G. French, "Wideband near-I.R. continuum (0.7-2.1 μm) generated in low loss optical fibres," Electron. Lett. 14, 822-823 (1978).
- [10] A. Unterhuber, "Development of compact broadband light sources for ultra-high resolution optical coherence tomography," PhD thesis, University Vienna, Vienna University of Technology (2006).
- [11] W.J. Wadsworth, A. Ortigosa-Blanch, J.C. Knight, T.A. Birks, T.O. Martin Man and P.S.J Russell, "Supercontinuum generation in photonic crystal fibers and optical fibers tapers: a novel light source," J. Opt. Soc. Am, B 19, 2148-2155 (2002).
- [12] G. McConnell, "Confocal laser scanning fluorescence microscopy with a visible continuum source," Opt. Express 12, 2844-2850 (2004).
- [13] C. McConnell and E. Riis, "Photonic crystal fibre enables short wavelength two-photon laser scanning fluorescence microscopy with fura-2," Phys. Med. Biol. 49, 4757-4763 (2004).

- [14] H.N. Paulsen, K.M. Hilligsoe, J. Thogersen, S.R. Keiding and J.J. Larsen, "Coherent anti-stokes Raman scattering microscopy with a photonic crystal fiber based light source," *Opt. Lett.* 28, 1123-1125 (2003).
- [15] E.A. Diaspro, "Confocal and two-photon microscopy: foundations, applications, and advances," Wiley-Liss. Inc. (2002).
- [16] D.M. Grant, W. Zhang, E.J. McGhee, T.D. Bunney, C.B. Talbot, S. Kumar, I. Munro, C. Dunsby, M.A.A. Neil, M. Katan and P.M.W. French, "Multiplexed FRET to monitor multiple signalling events in live cells", *Biophysical Journal: Biophysical Letters* 95 (2008).
- [17] D.M. Grant, J. McGinty, E.J. McGhee, T.D. Bunney, D.M. Owen, C.B. Talbot, W. Zhang, S. Kumar, I. Munro, P.M.P. Lanigan, G.T. Kennedy, C. Dunsby, A.I. Magee, P. Courtney, M. Katan, M.A.A. Neil and P.M.W. French, "High speed optically sectioned fluorescence lifetime imaging permits study of live cell signaling events," *Opt. Express* 15, 15656-15673 (2007).
- [18] C.B. Talbot, J. McGinty, D.M. Grant, E.J. McGhee, D.M. Owen, W. Zhang, T.D. Bunney, I. Munro, B. Isherwood, R. Eagle, A. Hargreaves, C. Dunsby, M.A.A. Neil and P.M.W. French, "High speed unsupervised fluorescence lifetime imaging confocal multiwell plate reader for high content analysis," *J. Biophoton.*, 1: 514-521 (2008).
- [19] S. Kumar, D. Alibhai, A. Margineanu, R. Laine, G. Kennedy, J. McGinty, S. Warren, D. Kelly, Y. Alexandrov, I. Munro, C. Talbot, D.W. Stuckey, C. Kimberly, B. Viellerobe, F. Lacombe, E.W.F. Lam, H. Taylor, M.J. Dallman, G. Stamp, E.J. Murray, F. Stuhmeier, A. Sardini, M. Katan, D.S. Elson, M.A.A. Neil, C. Dunsby and P.M.W. French, "FLIM FRET Technology for Drug Discovery: Automated Multiwell-Plate High-Content Analysis, Multiplexed Readouts and Application in Situ," *ChemPhysChem*, 12: 609-626 (2011).
- [20] D. Alibhai, D.J. Kelly, S. Warren, S. Kumar, A. Margineanu, R.A. Serwa, E. Thinon, Y. Alexandrov, E.J. Murray, F. Stuhmeier, E.W. Tate, M.A.A. Neil, C. Dunsby, and P.M.W. French, "Automated fluorescence lifetime imaging plate reader and its application to Förster resonant energy transfer readout of Gag protein aggregation," *J. Biophoton.*, 6: 398-408 (2013).

- [21] J. McGinty, H.B. Taylor, L. Chen, L. Bugeon, J.R. Lamb, M.J. Dallman and P.M.W. French, "In vivo fluorescence lifetime optical projection tomography," *Biomed Opt Express.*, 26;2(5):1340-50 (2011).
- [22] M. Bondu, M.J. Marques, P.M. Moselund, G. Lall, A. Bradu and A. Podoleanu, "Multispectral photoacoustic microscopy and optical coherence tomography using a single supercontinuum source," *Elsevier Photoacoustic*, 9:21-30 (2017)
- [23] M. Bondu, C.D. Brooks, C. Jakobsen, K. Oakes, P.M. Moselund, L. Leick, O. Bang, and A. Podoleanu, "High energy supercontinuum sources using tapered photonic crystal fibers for multispectral photoacoustic microscopy," *Biomedical Optics*, 21(6), 061005 (2016).
- [24] X. Shu, M. Bondu, B. Dong, A. Podoleanu, L. Leick, and H.F. Zhang, "High energy supercontinuum sources using tapered photonic crystal fibers for multispectral photoacoustic microscopy," *Biomedical Optics*, 21(6), 061005 (2016).
- [25] S. Caujolle, A. Unterhuber, T. Feuchter, A. Podoleanu and R.M. Werkmeister, "Comparison between a Supercontinuum Source and a Titanium Sapphire laser in achieving ultra-high resolution Spectral Domain Optical Coherence Tomography (SD-OCT)," in *Optical Coherence Imaging Techniques and Imaging in Scattering Media II*, M. Wojtkowski, ed., Vol. 10416 of SPIE Proceedings (Optical Society of America, 2017), paper 1041608.
- [26] A. Lichtenegger, D.J. Harper, M. Augustin, P. Eugui, S. Fialová, A. Woehrer, C.K. Hitzenberger, and B. Baumann, "Visible light spectral domain optical coherence microscopy system for ex vivo brain imaging," *Optics in the Life Sciences Congress*, Optical Society of America, p. JTU4A.16 (2017).
- [27] M. Maria, I.B. Gonzalo, T. Feuchter, M. Denninger, P.M. Moselund, L. Leick, O. Bang and A. Podoleanu, "Q-switch-pumped supercontinuum for ultra-high resolution optical coherence tomography," *Opt. Lett.* 42, 4744–4747, 10.1364/OL.42.004744 (2017).
- [28] P. Marchand, D. Szlag, A. Bouwens, and T. Lasser, "In vivo high-resolution cortical imaging with extended-focus optical coherence microscopy in the visible-NIR wavelength range," *Journal of Biomedical Optics*. 23(03):1, 10.1117/1.JBO.23.3.036012 (2018).

- [29] P. Marchand, A. Bouwens, D. Szlag, D. Nguyen, A. Descloux, M. Sison, S. Coquoz, J. Extermann, and T. Lasser, “Visible spectrum extended-focus optical coherence microscopy for label-free sub-cellular tomography,” *Biomedical Optics Express*. 8:3343-3359. 10.1364/BOE.8.003343 (2017).
- [30] J. Yi, Q. Wei, W. Liu, V. Backman, and H.F. Zhang, “Visible-light optical coherence tomography for retinal oxymetry,” *Opt. Lett.* (11), 1796–1798, doi:http:// dx.doi.org/10.1364/OL.38.001796 (2013).
- [31] X. Shu, L. Beckmann, and H.F. Zhang, “Visible-light optical coherence tomography: a review,” *Journal of Biomedical Optics*, 22(12), 121707 (2017).
- [32] D.J. Harper, M. Augustin, A. Lichtenegger, P. Eugui, C. Reyes, M. Glösmann, C.K. Hitzenberger, and B. Baumann, "White light polarization sensitive optical coherence tomography for sub-micron axial resolution and spectroscopic contrast in the murine retina," *Biomed. Opt. Express* 9:2115-2129 (2018).
- [33] F. Fleischhauer, S. Caujolle, T. Feuchter, R. Rajendram, L. Leick, and A. Podoleanu, “Spectroscopic low coherence interferometry using a supercontinuum source and an ultra broadband spectrometer,” *Proc.SPIE*, 9697 (2016).
- [34] M. Wojtkowski, S. Vivek, T. Ko, J. Fujimoto, A. Kowalczyk and J. Duker, “Ultrahigh-resolution, high speed, Fourier domain optical coherence tomography and methods for dispersion compensation,” *Opt Express*, vol.12, no. 11, pp. 2404-22 (2004).
- [35] W. Drexler, Y. Chen, A.D. Aguirre, B. Povazay, A. Untherhuber and J.G. Fujimoto, “Ultrahigh Resolution Optical Coherence Tomography,” in *Optical Coherence tomography: Technology and applications*, Drexler, W., Fujimoto, J.G., eds, 2nd ed., Springer, chapter 9 (2015).
- [36] W. Drexler, D. Hitzenberger, A. Baumgartner, O. Findl, H. Sattmann, and A.F. Fercher, “Investigation of Dispersion Effects in Ocular Media by Multiple Wavelength Partial Coherence Interferometry”, *Experimental Eye Research*, vol. 66, no. 1, pp. 25-33 (1998).
- [37] Y. Yali Jia, O. Tan, J. Tokayer, B. Potsaid, Y. Wang, J.J. Liu, M.J. Kraus, H. Subhash, J.G. Fujimoto, J. Hornegger and D. Huang, “Split-spectrum

- amplitude-decorrelation angiography with optical coherence tomography,” *Opt. Express*, no. 4, 4710-4725, vol.20 (2012)
- [38] R.M. Werkmeister, A. Alex, S. Kaya, A. Unterhuber, B. Hofer, J. Riedl, M. Brohagl, M. Vietauer, D. Schmidl, T. Schmoll, G. Garhöfer, W. Drexler, R.A. Leitgeb, M. Groeschl and L. Schmetterer, “Measurement of tear film thickness using ultrahigh resolution optical coherence tomography,” *Investigative ophthalmology & visual science*, 54(8):5578–83 (2013).
- [39] V. Aranha dos Santos, L. Schmetterer, M. Gröschl, G. Garhöfer, D. Schmidl, M. Kucera, A. Unterhuber, J.P. Hermand and R.M. Werkmeister, “In vivo tear film thickness measurement and tear film dynamics visualization using spectral domain optical coherence tomography,” *Optics Express*, Vol.23, Issue 16, (2015).
- [40] R.M. Werkmeister, S. Sapeta, D. Schmidl, G. Garhöfer, G. Schmidinger, V. Aranha dos Santos, G.C. Aschinger, I. Baumgartner, N. Pircher, F. Schwarzhans, A. Pantalon, H. Dua and L. Schmetterer, “Ultrahigh-resolution OCT imaging of the human cornea,” *Biomedical optics express* 1221, no. 2, Vol.8 (2017).
- [41] J.M. Dudley, “Supercontinuum generation in photonic crystal fiber, “Reviews of modern physics,” volume 78 (2006).
- [42] K. Bizheva, B. Tan, B. MacLellan, O. Kralj, M. Hajjalamdari, D. Hileeto and L. Sorbara, “Sub-micrometer axial resolution in OCT for in-vivo imaging of the cellular structure of healthy and keratoconic human corneas,” *Biomed Opt Express*, vol.8, No.2 (2017).
- [43] M. Choma, M. Sarunic, C. Yang and J.A. Izatt, “Sensitivity advantage of swept source and Fourier domain optical coherence tomography,” *Opt Express*. 11(18):2183-9 (2003).
- [44] M. Wojtkowski, V. Srinivasan, T. Ko, J. Fujimoto, A. Kowalczyk, and J. Duker, "Ultrahigh-resolution, high-speed, Fourier domain optical coherence tomography and methods for dispersion compensation," *Optics Express* 12, 2404-2422 (2004)
- [45] R.M. Werkmeister, S. Sapeta, D. Schmidl, G. Garhöfer, G. Schmidinger, V. Aranha Dos Santos, G.C. Ashinger, I. Baumgartner, N. Pircher, F.

- chwarzans, A. Pantalon, H. Dua and L. Schmetterer, “Ultrahigh-resolution OCT Imaging of the human cornea,” *Biomed Opt Express*, vol.8, No.2 (2017).
- [46] M. Wojtkowski, R. Leitgeb, A. Kowalczyk, T. Bajraszewski, and A.F. Fercher, “In vivo human retinal imaging by Fourier domain optical coherence tomography,” *Journal of biomedical optics*, vol. 7, no. 3, pp. 457–463 (2002).
- [47] M. Hughes, “Optical coherence tomography for Art Conservation and Archaeology: Methods and Applications,” PhD thesis, University of Kent (2010).
- [48] J.F. De Boer, “Spectral/Fourier Domain Optical Coherence Tomography,” in *Optical Coherence Tomography: Technology and Applications*, W. Drexler and J. Fujimoto, Eds., 2nd ed., Springer (2015).
- [49] W. Drexler, C.K. Hitzenberger, A. Baumgartner, O. Findl, H. Sattmann, and A.F. Fercher, “Investigation of dispersion effects in ocular media by multiple wavelength partial coherence interferometry,” *Experimental Eye Research*, 66 (1):25–33 (1998).
- [50] A.G. Podoleanu and A. Bradu, “Master–slave interferometry for parallel spectral domain interferometry sensing and versatile 3D optical coherence tomography,” *Opt. Express* **21**(16), 19324 (2013).
- [51] A. Bradu, M. Maria and A.G. Podoleanu, “Demonstration of tolerance to dispersion of master/slave interferometry,” *Opt. Express* **23**(11), 14148 (2015).
- [52] S. Rivet, M. Maria, A. Bradu, T. Feuchter, L. Leick and A. Podoleanu, “Complex master slave interferometry,” *Opt. Express* **24**(3), 2885 (2016).
- [53] A. Bradu, S. Rivet and A.Podoleanu, “Master/slave interferometry – ideal tool for coherence revival swept source optical coherence tomography,” *Biomed. Opt. Express* **7**(7), 2453 (2016).
- [54] R.K. Wang and L. An, “Doppler optical micro-angiography for volumetric imaging of vascular perfusion in vivo,” *Opt. Express* **17**(11), 8926 (2009).
- [55] C.K. Hitzenberger and M. Pircher, “MUW Approach of PS OCT,” in *Optical Coherence Tomography: Technology and Applications*, W. Drexler and J. G. Fujimoto, Eds. (2015).
- [56] A. Bradu, N.M. Israelsen, M. Maria, M.J. Marques, S. Rivet, T. Feuchter, O. Bang and A. Podoleanu, “Recovering distance information in spectral domain interferometry,” *Sci Rep* **8**, 15445 (2018).
-

Chapter 3

A functional modality: motion detection with FD-OCT

3.1. Introduction

3.1.A Definition

Optical Coherence Tomography (OCT) and more precisely Fourier Domain Optical Coherence Tomography (FD-OCT) has already been introduced in the previous chapters.

Motion is defined by the Oxford dictionary of English [1] as “the act or process of moving or of changing position over time”. It is linked with the notion of displacement, distance, velocity, acceleration and time. Motion of a body is observed by measuring the position as change relative to a reference frame.

Angiography comes from Ancient Greek where angio is “ἄγγειον” meaning vessel and -graphy “γράφω”, to draw or write[2-4]. In the medical field, angiography is used to define any procedure to view blood vessels. It can be performed with or without injection of a dye.

Optical Coherence Tomography Angiography (OCTA) is mainly used to map vessels from the retina without the injection of any dye. Several other applications were reported in neuroscience, gastroenterology and cancer biology [5-8]. OCTA highlights the vessels' position based on the motion created by the blood flow. Briefly, this method is based on comparing several successive frames. Usually, such frames are B-scans (X,Z) collected at the same coordinate Y. The comparison operation is sensitive to changes in the structure of the sample over time.

3.1.B Motivation

The three main diseases responsible for visual loss or blindness in developed countries are Age-related Macular Degeneration (AMD), glaucoma and diabetic retinopathy [9-

11]. They impact the blood vessels by reducing or complicating the retinal blood flow and are responsible for choroidal neovascularisation.

Currently, to diagnose these diseases, the gold standard methods are Fluorescein Angiography (FA) and Indocyanine Green Angiography (IGA) [12]. These contrast agents are injected intravenously into the bloodstream to highlight the blood vessel. For FA, blue light (465 – 490 nm) is used to excite the fluorescein which emits at ~ 540 nm. Indocyanine Green is excited at 790-805 nm and emits at 835 nm. Due to its longer excitation wavelength, IGA presents better depths penetration in the choroidal circulation compared to FA, but its fluorescence efficiency is only 4% that of the FA. FA and IGA present several drawbacks which limit their widespread use. Both technologies are invasive, as they require injection of a dye which is relatively expensive and time consuming. Also, the conventional angiography methods actually require an imaging window of up to 10-30 minutes from the dye injection. Some complications can occur such as nausea, vomiting or pruritus and in rare cases, more severe reaction as syncope or thrombophlebitis. Diseases typically require a frequent evaluation of the patient in order to monitor their evolution. However, their frequent use increases the probability of allergic reaction that can lead to counter-indication in case of pregnancy.

For these reasons, OCTA has been embraced by the ophthalmic community and continues to grow in popularity [13], helped by development of commercial systems. Some units combined OCTA with FA or IGA to achieve a better diagnosis. While OCTA extracts information from the backscattering light signal of the moving blood flow, leakages representing accumulation of static blood are detected with FA or IGA.

OCTA can be split into three categories depending on the physical quantity (phase or amplitude) of the signal used to evaluate the changes over time.

The first category, historically, is a method based on the phase of the signal. This method calculates the Doppler shift induced by the moving blood cells present in the vessels. Based on the phase parameter, different methods have been developed such as Doppler OCT [8, 14-21] where the difference in phase is calculated, or the Phase Variance where the variance of the phase difference is evaluated [8, 14, 17, 22-26 26-

28]. These techniques are sensitive to motion and phase noise induced by the light source predominant in swept-lasers and supercontinuum sources.

The second category includes amplitude-based methods such as Amplitude Decorrelation (AD) [8, 14, 17, 22, 23, 27, 28] and Speckle Variance (SV) [8, 14, 17, 22, 23, 27, 29, 30]. As the name suggests, these techniques use amplitude information at each pixel of the image to highlight changes.

The third category combines the changes in both amplitude and phase by using the complex signal from each point in the image [8, 14, 31-33].

Before presenting each method from the list detailed above, a short overview of the hemodynamic principles and the main scattering in blood is presented.

3.1.C Parameters for the moving backscattering centres

The hemodynamic principles explain the dynamics of blood flow. The first distinction that needs to be made is between the capillaries and arteries (Fig.3.1) [34]. Both are part of the microcirculation which comprise the whole network of blood vessels supporting tissue and organ viability, by supplying them with oxygen and nutrients. The flow of red blood cells (RBC) present different hemodynamic parameters in the case of capillaries or arteries.

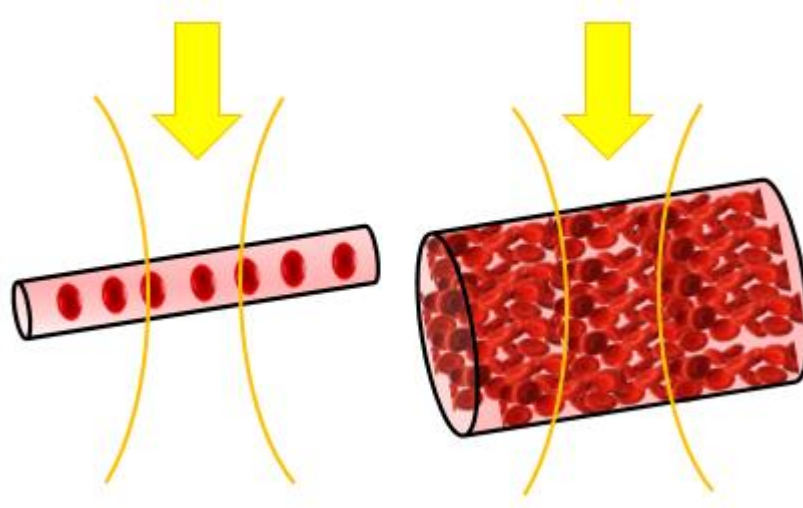


Fig.3.1. Capillary vs Artery. In capillaries, RBCs flow in a line separated by plasma whereas in arteries or veins, the flow is laminar. The yellow arrow indicates the incident beam and the yellow lines limit the coherence volume, adapted from [34].

The capillary in the left sketch in Fig.3.1 has a diameter below 10 μm , where the RBCs flow in a single line separated by plasma [34-36]. The speed is evaluated by counting the number of RBCs over time.

On the other hand, arteries present a much larger size in the range between 10-100 μm . Across a section of the vessel, the profile of the velocity is laminar, i.e. each scattering centre in the cross section moves without any interaction from its neighbours making the flow oriented in one direction [37]. The velocity is lower at the edges and exhibits a maximum in the centre [38]. The velocity of the RBCs in arteries depends on several parameters such as flow rate and hematocrit which is the density of RBCs. This changes over time with the respiration and heartbeat of the subject and some characteristics such as their gender, age and health condition [38].

OCTA highlights scattering, moving objects. Scattering intensity depends on the size of the scatterer relative to the wavelength and the refractive index difference between the scattering features and the surrounding environment.

The main scatterer from RBCs is the haemoglobin [39, 40], whose refractive index is in the range between 1.41 to 1.48 in visible and short IR, whereas for the plasma, the index of refraction is ~ 1.35 [41, 42] (Fig.3.2). So, the plasma has a close refractive index to the surrounding tissue. For a vein or a capillary, the ratio of the refractive index between the RBC and the surrounded plasma is $\sim 3\text{-}6\%$ [39, 41-44] making the haemoglobin the main refractor inside the blood vessel.

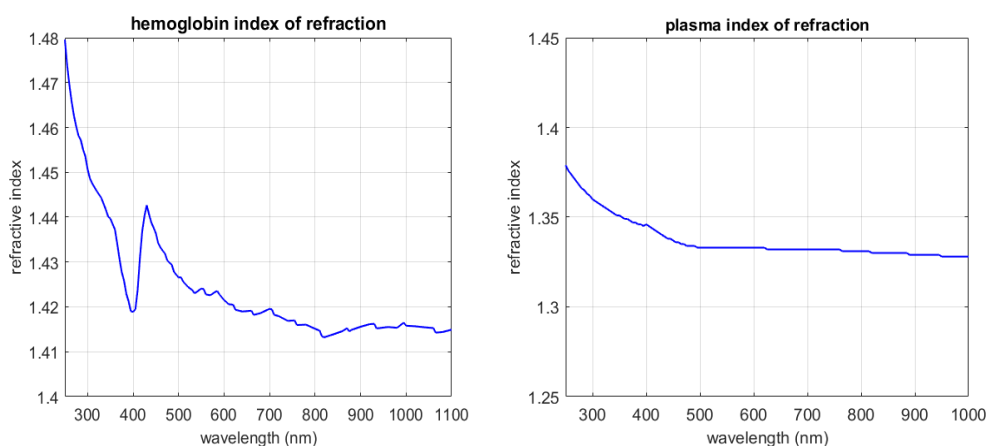


Fig.3.2. Refractive index as a function of the wavelength in the case of the haemoglobin [41] and plasma [42]

The index of refraction is one factor to consider, in addition to the volume (size and shape) and the orientation of the RBC [45, 46]. Knowing that RBCs move parallel to the blood flow, the backscattered light depends on the relative orientation of the vessel from the incident beam.

To summarize, RBCs are the main scattering centres in blood considering their density and their mismatch in refractive index compared to the surrounding plasma. These scatterers are influenced by several parameters such as the blood vessel direction or their shape. It is also important to note that the OCTA procedures extract the position of moving features from the structural images and so, the image penetration, transverse and axial resolutions and the backscattering signal detected, all depend on the sample optical properties and on the performance of the OCT system used.

The main motivation of the next section is to develop methods to distinguish between the moving and static scatterers. These methods will be based on the amplitude or the phase of the backscattered optical signals.

3.2. Optical Coherence Tomography Angiography (OCTA)

3.2.A Preamble

3.2.A.1 Principle

Optical Coherence Tomography Angiography (OCTA) detects motion by comparing several successive B-scan (X,Z) frames collected at the same transversal coordinate Y. The transversal position between these successive frames must deviate by less than the size of a pixel in the direction of change [13, 17, 22, 23, 34].

Figure 3.3 explains the concept of OCTA. The signal from static tissue (in red) stays the same over time while a moving blood cell passing through a vessel or an artery, induces a fluctuation in the field (signal in green).

By comparing the value of the phase or the amplitude of each pixel along the A-scan from time T_n to that at T_{n+1} , the moving part is detected. By repeating this procedure at each point of the B-scan, temporal changes between successive scans are visualised that create an angiography image.

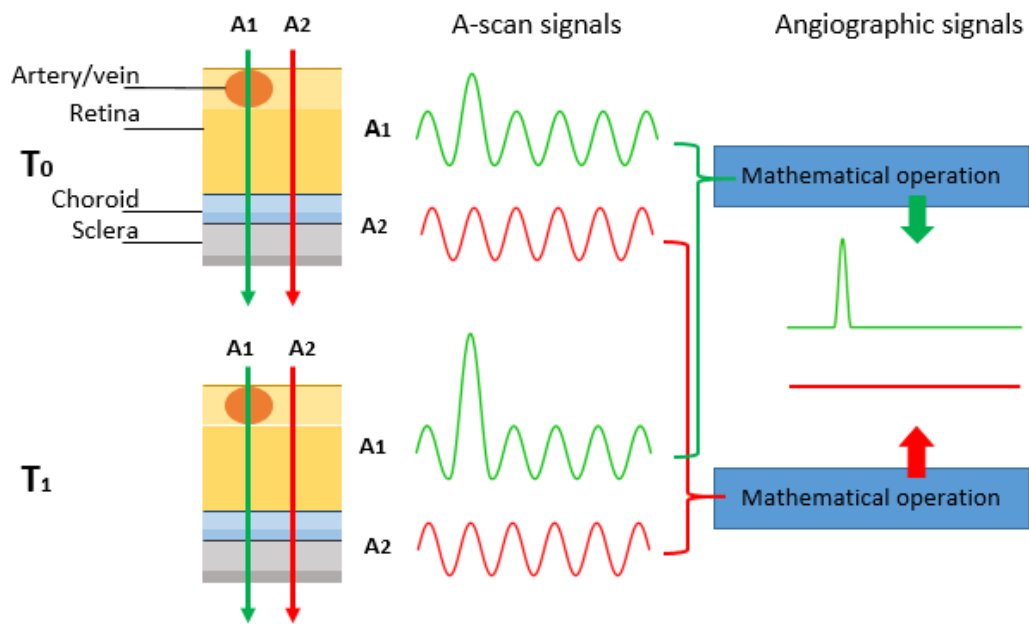


Fig.3.3. OCTA principle: the backscattered OCT signals at T_0 from two different positions are compared to those at T_1 . If the tissue being imaged is static, no difference is observed in the optical signal (A_2) while the motion caused by the red blood cells distorts it (A_1). An amplitude variation is illustrated, but equally the green signals could be of the same shape but only slightly out of phase (not shown) adapted from [8].

3.2.A.2 Decorrelation vs Doppler effect

The direction of the scattered motion has a strong impact on the OCT signal. In most cases a Doppler shift and decorrelation are present [47].

If the scattering object has an axial motion towards or away from the incident beam, the OCT signal present a linear phase shift over time, which produces a Doppler effect. Alternatively, if the scattering object has a lateral motion along the coherence volume the intensity and phase of the OCT signal changes with time, which is known as decorrelation. The Doppler effect is associated with a change in the phase of the OCT signal while the decorrelation is a change in the amplitude of the OCT signal over time [16]. Both effects are typically present in vasculature system.

The Doppler effect is only sensitive to motion along the incident beam (axial direction) so it is a main component in vessels that are going from one layer to another. For this reason, this method gives access to a partial vessel map [34]. On the other hand, the decorrelation is present in the majority of vessels with transversal flow, which is the

most common situation. The OCTA method, based on decorrelation, offers a more complete vessel map [47].

3.2.A.3 OCT system and Phantom parameters

The SD-OCT system used throughout this chapter was the same as that from section 2.3.B.2 above (Fig 2.32.). To reiterate, a beam leaving an SLD source from Superlum travels toward a fiber-based coupler (50/50) to be divided between the reference arm and the sample arm. The reference arm is composed of a dispersion compensation block, matching the dispersion properties introduced in the sample arm by the objective lens, and a reflective mirror, reflecting the beam back to the beam splitter. In the sample arm, the beam scans the sample using an 1D galvanometer scanner (SX) and a microscope objective (Thorlabs), which focuses the beam at the right position. The reflected beam from the sample and the reference mirror are then sent to the spectrometer. In this system, the spectrometer consists of a transmissive diffraction grating (TG, 1200 l/mm, Wasatch Photonics) and a lens to focus the line onto the CMOS line camera (Basler).

This system was specifically design to image the human eye and therefore operates with a central wavelength (λ_0) of 840 nm using a bandwidth of $\Delta\lambda \sim 50$ nm. The theoretical optical axial resolution was 6.2 μm and the experimental was 8.5 μm . The theoretical and experimental optical, transverse resolution was 12 μm and 14 μm respectively. Throughout the experimental work, the CMOS camera was used in the range of 20 to 70 kHz. As demonstrated in the previous Chapter, the post processing using the FT and cMSI methods can recover the amplitude and the phase of the signal. All images from this point were post-processed using cMSI. If it is not specified otherwise, all analyses are run over 100 images, taken along the slow axis, and every calculation is performed on two successive structural images.

Experiments were conducted on a phantom composed of one or two silicon tubes glued to a piece of cardboard, which was fixed to a mounting stage with adjustment to the x-axis and y-axis. This ensured stability whilst the fluid was pumped through the tubes and allowed control over the angle of the incident rays on the sample. An example image of a single tube phantom is shown in Fig. 3.4 below.

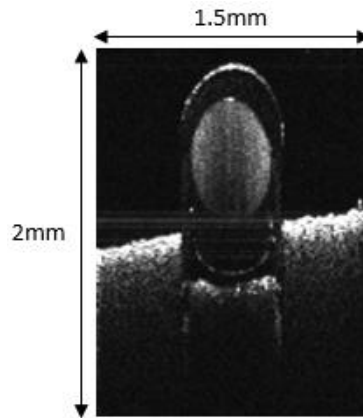


Fig.3.4 OCT image of the silicon tube glue to a piece of cardboard.

The tube had an internal diameter of 1 mm and was connected to a peristaltic pump (Gilson minipuls 3) to create the fluid flow. An 5% dilution intralipid solution was used as a reflective liquid to match the typical SNR from inside the vessel [Boy reference]. This liquid was forced to flow through the tubes by the pump to perform the several different experiments that follow.

3.2.A.4 Structural images vs functional images dimension

Let us consider consecutive B-scan images separated by the same distance. In this case, the total number of angiography frames produced is equal to $N - (n - 1)$ where “ N ” is the total number of B-scans images and “ n ” is the number of oversampled frames used in the calculation to create each angiography image (Fig.3.5). The minimum oversampling number is equal to 2 for all methods except for the phase variance method where a minimum of 3 frames is required. The reason for this will be explained in the next section.

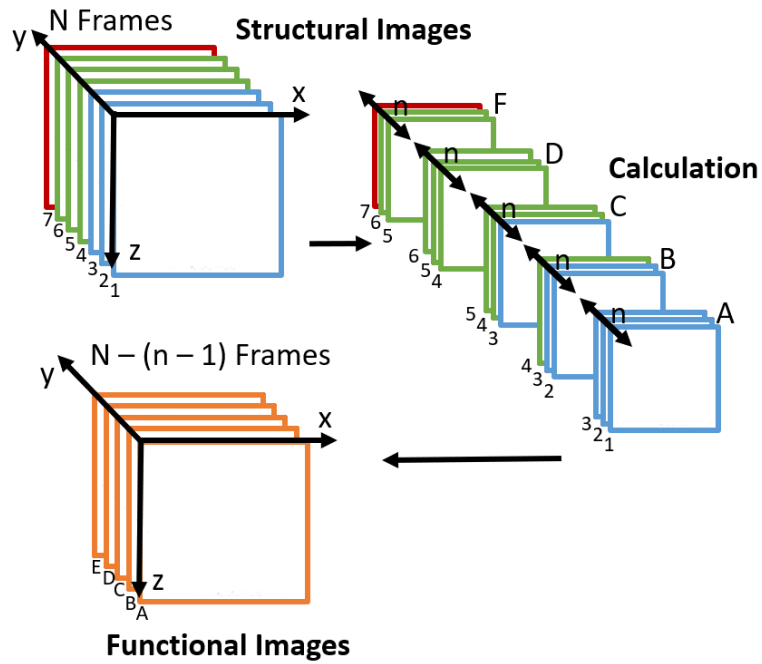


Fig.3.5. Functional vs structural frames dimensions. In the referential (x, y, z) , the structural image has a size (X, N, Z) , the calculation is done over n where n is the number of oversampled frames. At the end, the dimension of functional volume (angiographic image in our case) is $(X, N - (n - 1), Z)$.

In the case of discontinuous scanning signal (last part of this chapter), each set of n frames used in the calculation is acquired at the same y position and separated from the next set and so, the number of angiographic images is given by the ratio between the total number of frames, N and the number of oversampled frames, n . By using the same notation in Fig.3.5 and considering an oversampling equal to 3, the functional image A is created using the structural frames 1,2, and 3, B using 4,5, and 6 and so on over the N images.

All functional images in the following are obtained from a data set of 100 images taken at the same position (slow axis disabled). The image size is 1.5 mm (transverse) x 2 mm (axial) measured in air.

3.2.B Amplitude based method

Intensity based methods such as Speckle Variance (SV) have been included in this section. The intensity values are directly linked to the amplitude of the optical signal.

For this chapter, the optical signal is denoted with “S”, while its amplitude is “A” which is the absolute value of S ($A = |S|$) and the intensity by “I” which is the square of the amplitude value ($I = |S|^2$).

3.2.B.1 Speckle Variance (SV)

Due to the limited spatial frequency bandwidth of the interference signal detected, a granular pattern can be observed, historically called “granularity” [49], which is now more commonly known as speckle. Several parameters modulate this signal, such as optical properties of the optical system or those of the sample (multiple scattering and phase aberration in the interface optics), motion of the investigated object, temporal coherence length of the light source and aperture of the detector [49]. Speckle has a double function, as “signal-degrading”, and as “signal-carrying” of the coherence pattern (phase and amplitude) created by a sample [50]. It is considered as a source of noise, making images look blurred, resulting in an inability or difficulty to separate the different layers of the sample, and leading to a reduction of the contrast. Studies have been conducted to reduce it by using polarization, spatial and frequency combination, or digital signal processing [50]. However, speckle also transports essential information from the sample examined and it is used in some applications such as laser speckle contrast imaging to measure blood detection [51, 52]. Speckle is a random phenomenon and needs to be evaluated statistically. An important feature of speckle is that for static tissue, the mean intensity and the standard deviation of the intensity variation are equal [53] which is not the case for moving tissue. So, even if the speckle pattern of a static object varies in time, it is possible to make a distinction within the sample between static and moving parts. The SV method evaluates the deviation of the speckle pattern from a diffuse object over a period of time and highlights the part with the higher fluctuation where motion takes place. To characterise it, the variance function is used.

From the Cambridge dictionary on statistics [54] for the variable x , the k^{th} moment about the origin noted $\mu_{k,\text{origin}}$ is defined as:

$$\mu_{k,\text{origin}} = E(x^k)$$

where $E(x)$ represents the expectation of the variable x . For a population of N samples, the variance (noted “ s^2 ”) is defined as the second moment about the mean μ , denoted as

$\mu_{2,\text{mean}}$ and can be written as:

$$s^2 = \mu_{2,\text{mean}} = E[(x - \mu)^2]$$

where

$$s^2 = \frac{1}{N} \sum_{i=1}^n (x_i - \mu)^2 \quad (3.1)$$

SV is defined from the equation (3.1) for the population of N B-scan images. In practice, SV is the variation of the speckle and more exactly, its intensity. For this purpose, several structural B-scan images are acquired at the same position (slow axis of the galvanometer scanner disabled) and then post-processed as shown in the flow diagram (Fig.3.6).

After the acquisition of several spectra, raw data are processed using cMSI (explained in the previous chapter). N B-scan images are acquired and the intensity of each pixel is compared amongst each group of n frames with the mean intensity from the same pixel over n B-scans. The calculation sv_{ijk} is performed n times and averaged to give a single variance image SV [17, 22, 23, 27, 29,30]. The process is repeated $N - (n - 1)$ where N is the total number of B-scan images and n the number of oversampling frames used. The equation derived from (3.1) to describe this operation is given by:

$$SV_{ik} = \frac{1}{n} \sum_{j=1}^n (I_{ijk} - \frac{1}{n} \sum_{j=1}^n I_{ijk})^2 \quad (3.2)$$

where n is the number of oversampled B-scan or frames and i the index for the transverse pixels, j the frame considered and k the axial pixel index. Equation (3.2) can also be written as:

$$SV_{ik} = \frac{1}{n} \sum_{j=1}^n (I_{ijk} - I_{mean(ik)})^2 \quad (3.3)$$

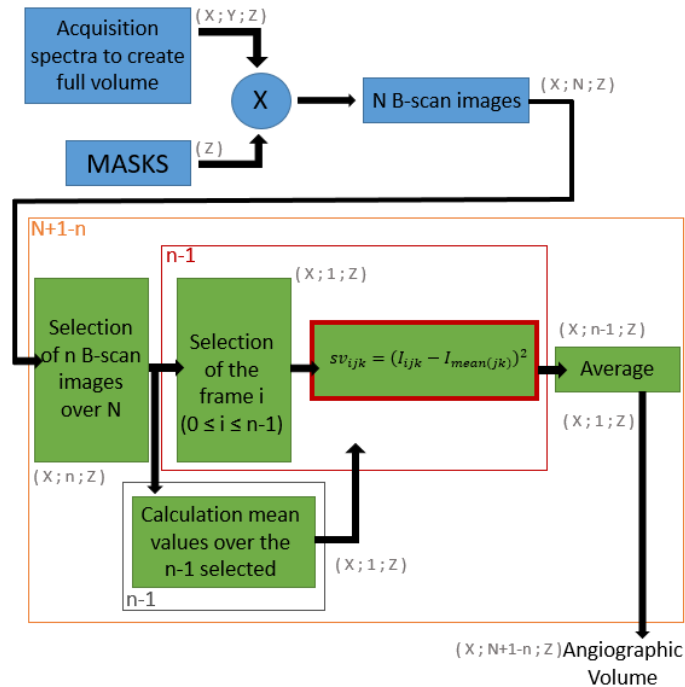


Fig.3.6. Flow diagram showing the operations to evaluate angiography volumes from acquired spectra using SV method. The blue parts are performed in real time whereas the green parts follow some post-processing steps.

3.2.B.2 Amplitude Decorrelation (AD)

As with speckle variance, amplitude decorrelation (AD) is just using the real part of the optical signal detected. AD evaluates the amplitude and not the intensity of the signal ($I = A^2$). Furthermore, the calculations of angiography images are normalized i.e. the intensity values are divided by the highest value and so, adjusted into a common scale which is between 0 and 1. The question is not anymore how much variation there is in each pixel in the n images, but more on how similar the corresponding pixels are in the n images. Pixels which are dissimilar are considered as moving, such as fluid.

In probability and statistics, the correlation is a measure of the link between two random variables. From the Cambridge dictionary of statistics [54], the correlation is “a general term for interdependence between pairs of variables”. It can also be seen as

a normalised form of the covariance. The covariance is defined as the expected value of the product of two random variables.

The protocol associated with the AD is similar to that used in the SV method (Fig.3.7). This starts with the acquisition of X spectra for each B-scan, for a total of N B-scans, where each spectrum acquired is subject to a cMSI operation with the storage of masks (Chapter 2, section 3).

Afterwards, the calculation is performed over the pixels of n successive B-scan images that are averaged over the $n - 1$ angiographic calculations to deliver a single angiography image at a precise lateral position. The process is repeated $N - (n - 1)$ times at each transverse position along the slow axis (the y -axis in this case) to create an angiographic volume. The equation describing this operation is given by [17, 22, 23, 27, 28]:

$$AD = 1 - \frac{1}{n-1} \sum_{j=1}^{n-1} \frac{A_j(x, z) A_{j+1}(x, z)}{\frac{1}{2} (A_j(x, z)^2 + A_{j+1}(x, z)^2)} \quad (3.4)$$

where n is the number of oversampled B-scan frames and x the transverse position, j the frame and z the axial pixel. This can also be seen as:

$$AD = 1 - AC$$

where “AC” is the amplitude correlation defined as:

$$AC = \frac{1}{n-1} \sum_{j=1}^{n-1} \frac{A_j(x, z) A_{j+1}(x, z)}{\frac{1}{2} [A_j(x, z)^2 + A_{j+1}(x, z)^2]}$$

It is important to note that, in this instance, the value is normalized to reduce the impact of large intensity value pixels. The drawback is that noisy pixels which are randomly distributed, exhibit a high decorrelation amplitude similar to that created by the moving pixels. This issue has not appeared before with the SV method because, even if the noise is having a higher variance relative to its amplitude, the backscattered signal strength is so strong compared to the noise that it does not go through to the angiographic images. By normalising the amplitude value of the optical signal, the

amplitude decorrelation value becomes independent on the relative amplitude of each pixel considered and noise makes it through to the angiographic image. To cancel or at least to reduce the noise, a threshold is applied to the amplitude variable and fixed to a value equal to the average of the pixel noise values. If the amplitude is lower than the threshold, the AD value is set to 0. If not, it will enter into the calculation loop.

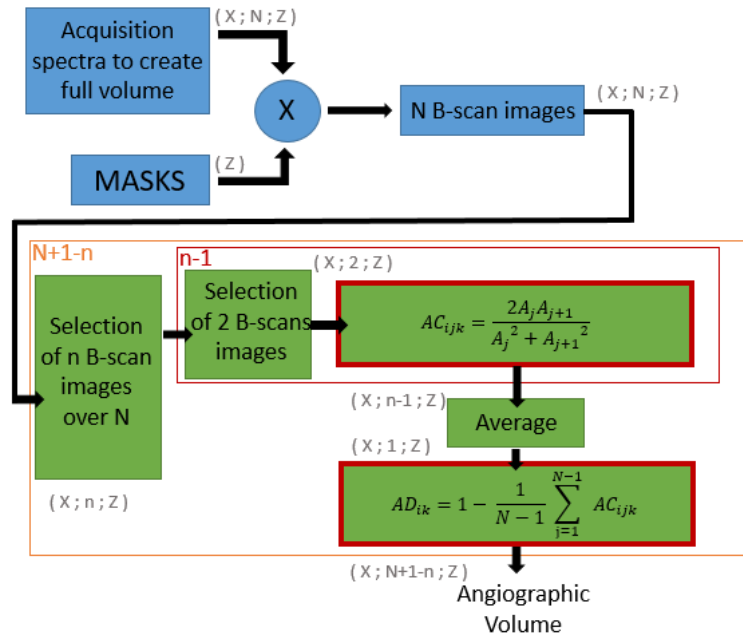


Fig.3.7. Flow chart of steps from acquisition to final angiographic volume

3.2.B.3 Amplitude Difference (D)

The third method tackled in this thesis is the amplitude difference (D). The amplitude values extracted from two successive images are subtracted at each pixel within the plane of axial and transversal coordinates. If the process is done over more than a pair of frames, each final angiographic image is the result of the average of the $n - 1$ images (where n is the number of oversampled frames). The equation describing this method is given by [27]:

$$D(x, z) = \frac{1}{n-1} \sum_{j=1}^{n-1} |A_{j+1}(x, z) - A_j(x, z)| \quad (3.5)$$

where j is the frame index. The process is repeated $N - (n - 1)$ times. The different steps followed are shown in Figure 3.8. Once again, the procedure is similar to that employed by the SV method.

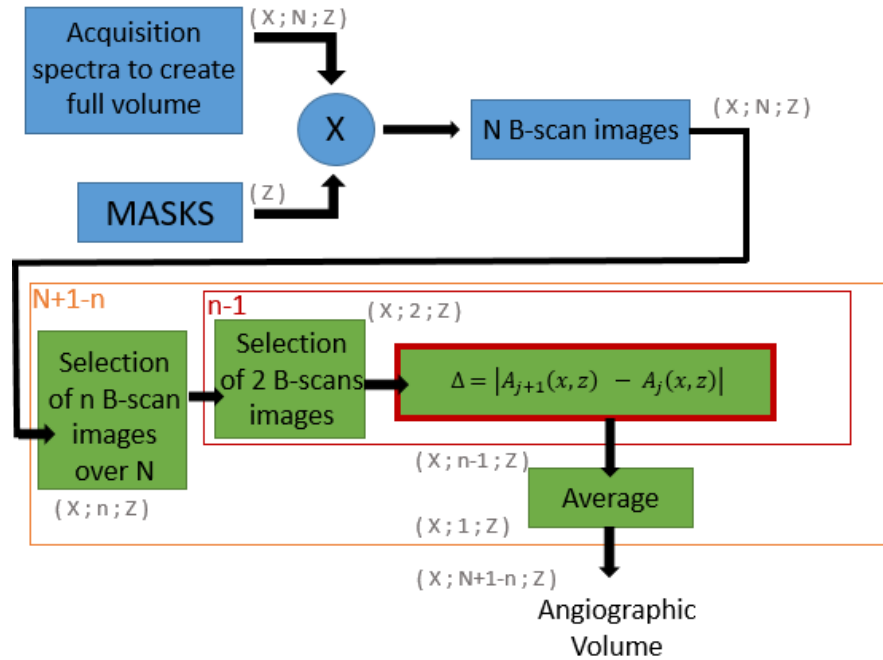


Fig.3.8. Amplitude Difference organigram showing processing steps from acquisition spectra to final angiographic volume

3.2.C Phase based method

In the previous section of this chapter, the focus was placed on methods using the amplitude/intensity of the optical backscattered signal. In this section, I will refer to methods based on phase. The Doppler method, requiring calculation of the Doppler frequency difference, can be applied to detect flow and allows a quantification of the flow rate but is just sensitive to the parallel direction of the optical beam. As said earlier, vessels are mainly in a perpendicular plane to the direction of the scanning beam, making the detection of the blood stream partial.

In the following, two techniques based on phase are presented: Phase Difference (PD) and the Phase Variance (PV) [17, 22-26, 34]. Throughout the rest of this thesis, the PV method will be renamed Phase Difference Variance (PDV). The reason for this is to

clarify that the variance function is not applied on the phase values but on the phase difference amplitudes.

As in Doppler OCTA [8, 14-21], the angiography image displays a phase variation map over time, where the amplitude OCT signal is lost. Furthermore, phase-based methods are more sensitive to any type of variations which can be motion as well as noise. For this reason, a threshold is applied to the angiographic amplitude displayed but also, to select on which pixel the calculations are run. As previously explained, pixels presenting an amplitude below the average of pixels considered as noise are set to 0 and do not enter in the loop calculation.

In this section, φ represents the phase of the backscattered optical signal and $\Delta\varphi$ the phase difference between several pairs of B-scans.

3.2.C.1 Phase Difference (PD)

As explained in the section 3.1.C (Amplitude Difference), the calculation uses two successive B-scan images where the phase values φ for each pixel are subtracted. First a threshold is applied for selecting the pixels involved in the calculation. This is done on the amplitude values from the structural image. A threshold is set to the average value of the pixels identified as noise. The phase of each pixel presenting a lower amplitude value than the threshold is set to 0 and no calculation is conducted on these pixels. Otherwise, the following equation is used:

$$\Delta\varphi = \frac{1}{n-1} \sum_{j=1}^{n-1} (\varphi_{j+1}(x, z) - \varphi_j(x, z)) \quad (3.6)$$

where, as before, φ represents the phase of the optical signal at the given pixel, $\Delta\varphi$ the average phase difference calculated over several pairs of B-scan images and n is the number of oversampled frames.

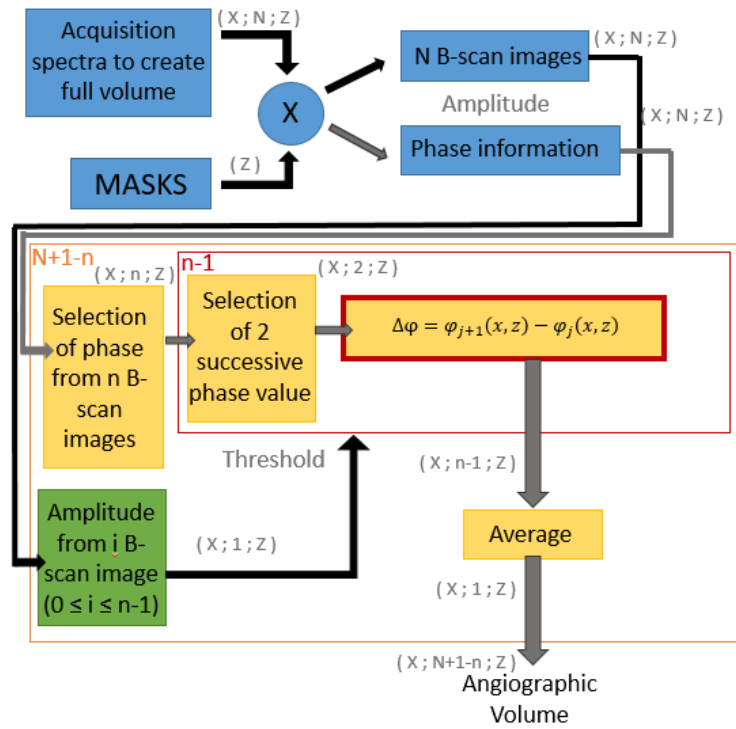


Fig.3.9. Stages of implementation for the Phase Difference method from acquisition spectra to final angiographic volume. This angiographic method takes into account the amplitude (in green) to select the pixel where the calculation is run using the phase value of the signal (indicated in yellow). All the steps in yellow and green are done in post-processing.

In Figure 3.9, all the different steps are explained. The acquisition of the images and the post processing steps using cMSI to retrieve the depth information are the same as those for amplitude/intensity methods beside the fact that in addition to the amplitude, the phase information is extracted from the complex optical field. While the amplitude from each B-scan frame is compared to the threshold, the phases from the oversampled n B-scans are used in pairs in the calculation. For each selected pixel, the phase value in the current frame is subtracted from the phase corresponding to the frame that immediately follows. This calculation step is conducted when the amplitude is above the threshold determined by the noise average value. After this process has been repeated $n - 1$ times, the phase difference map is averaged to give a unique phase map at the position j with $0 \leq j \leq N - (n - 1)$ along the frame direction.

3.2.C.2 Phase Difference Variance (PDV)

Until now, the evaluated quantities were directly obtained from the backscatter signal (amplitude and phase) but in this section the resultant value is calculated from the variance of the phase difference $\Delta\varphi$ between two successive B-scan frames. Once again, the detection of the moving parts is performed using the notion of variance, which is the second moment about the mean. The minimum number of frames used in the earlier methods was two but in this case three are used because of the variable used. Before starting the process of the variance calculation, an array of phase difference amplitude is created by subtracting the phase values of two successive frames. If we introduce two phase arrays from the y^{th} and $y+1^{th}$ B-scan frames, noted φ_y and φ_{y+1} and expressed by:

$$\varphi_y = \begin{bmatrix} \varphi_{1,y,1} & \cdots & \varphi_{x,y,1} \\ \vdots & \ddots & \vdots \\ \varphi_{1,y,z} & \cdots & \varphi_{x,y,z} \end{bmatrix} \quad \varphi_{y+1} = \begin{bmatrix} \varphi_{1,y+1,1} & \cdots & \varphi_{x,y+1,1} \\ \vdots & \ddots & \vdots \\ \varphi_{1,y+1,z} & \cdots & \varphi_{x,y+1,z} \end{bmatrix}$$

then the phase difference array is given by

$$\Delta\varphi = \begin{bmatrix} \varphi_{1,y+1,1} - \varphi_{1,y,1} & \cdots & \varphi_{x,y+1,1} - \varphi_{x,y,1} \\ \vdots & \ddots & \vdots \\ \varphi_{1,y+1,z} - \varphi_{1,y,z} & \cdots & \varphi_{x,y+1,z} - \varphi_{x,y,z} \end{bmatrix}$$

where y is the number of B-scan images ($0 \leq y < N-1$), x is the transverse pixel along the fast axis and z is the axial pixel (depth coordinate).

This step adds a new loop in the process as shown in Fig. 3.10. Then, the new array $\Delta\varphi$ is used to calculate the variance between the phase difference from the B-scan image y ($0 \leq y < n$) and the mean value of the phase difference over the n frames. After repeating this process $N - n$ times, the angiographic volume is created. All these steps are summarized in the flow chart presented in Fig. 3.13, including calculation of the phase difference $\Delta\varphi_{ijk}$ [17, 22-26, 34]:

$$PDV = \frac{1}{N} \sum_{j=1}^N (\Delta\varphi_{ijk} - \frac{1}{N} \sum_{j=1}^N \Delta\varphi_{ijk})^2$$

Or

$$PDV = \frac{1}{N} \sum_{j=1}^N (\Delta\varphi_{ijk} - \Delta\varphi_{mean})^2 \quad (3.7)$$

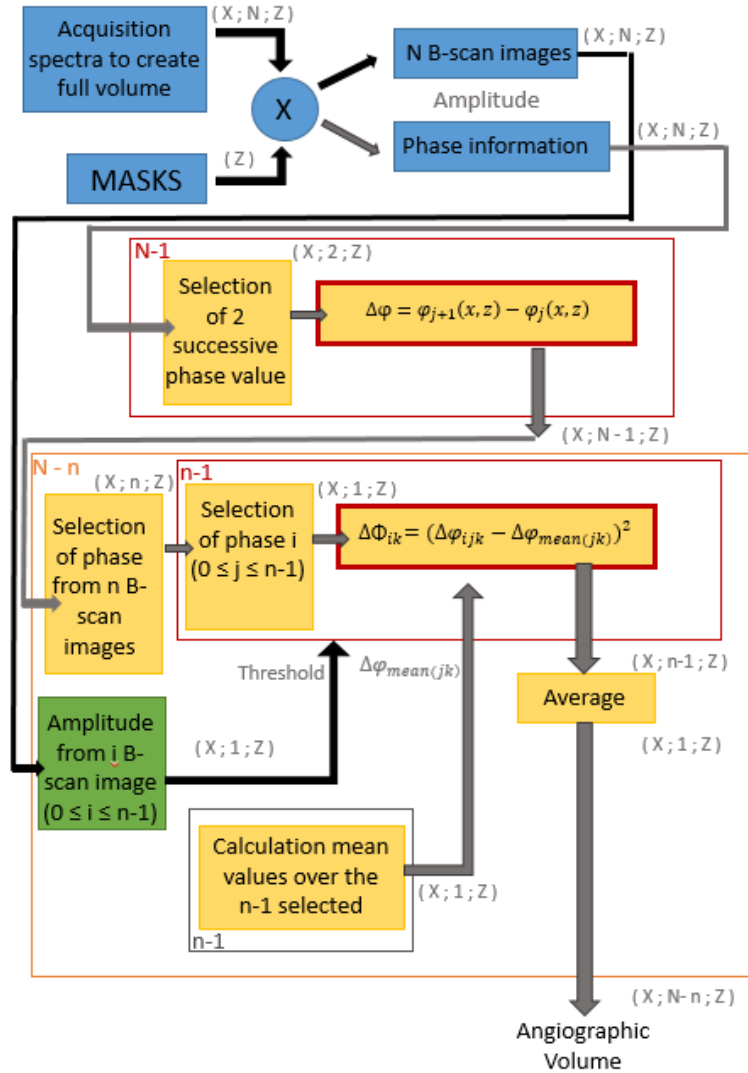


Fig.3.10. Processing steps to implement the PDV method from acquisition of spectra to final angiographic volume

3.2.D Application

Before going into the following study to quantify the flow using the different methods, Figure 3.11 shows an example of angiography images processed using the different amplitude or phase methods explained in the first part of this chapter. Figure 3.11 (a) is the structural image over 4 B-scan images using a single silicon tube phantom.

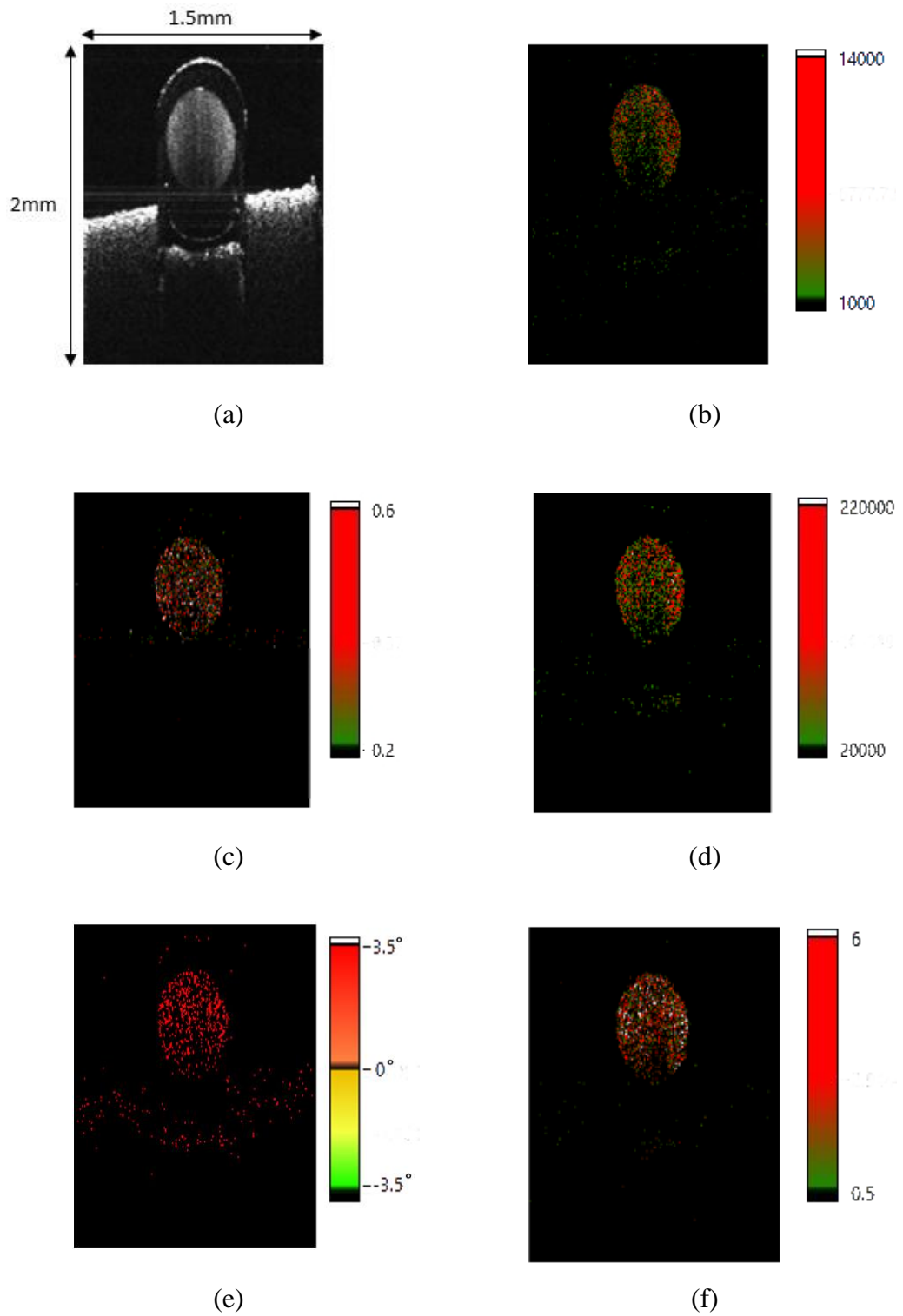


Fig.3.11. (a) Average of 4 OCT structural images; (b) SV-OCTA image with no threshold on intensity signal. Process has been carried out on one pair of B-scan images. Red points present the higher SV values and the lower limit is fixed at 1000.

Figure 3.11 (b), (c) and (d) are the angiographic images processed using the amplitude methods, SV, AD and D respectively. The number of oversampling steps for the calculation of the angio-amplitude, n , was fixed to 2. The flow area is highlighted and static features have been removed.

In the case of SV (Fig.3.11(b)), a threshold was applied on the SV values to remove some leftover static pixels. However, the threshold is 14 times lower than the highest value of SV values and the majority of SV amplitudes from the flow presents a larger variance that preserves the information of the area in motion.

For the AD method, two thresholds were applied on the image, one prior to the angio-amplitude calculation on the amplitude itself and one after on the angiographic image making possible to eliminate the static features and to keep only the information from the pixels demonstrating the flow. For the case of Fig.3.11 (b), all AD values are within the range 0.2 – 0.6.

When considering the D method, no threshold is applied on the amplitude values to remove the noise for the same reason explained earlier in the SV section (amplitude of the noise \lll amplitude of the signal). Nonetheless, the highest static, reflective pixels can be observed on the angiographic frame and so, a threshold on the angiographic values is applied. For example, colour is given to values between 20,000 and 220,000 only in the angiographic image and for the rest of the values, D is set to black.

A comparison is made for the AD method in Fig.3.11 (b), (c) and (d). It demonstrates a disadvantage of being more sensitive to noise. However, by considering the covariance of the intensity/amplitude values, static pixels presenting high reflectivity are discarded and only moving features are selected in the image. Furthermore, the flow information recovered in the bottom centre part of the tube is higher for the AD method. This area presents lower amplitude values, which can be explained by the partial loss of the backscattered signal along the propagation of the beam. In the AD method, the decrease of the amplitude of the optical signal does not have a big impact because of the normalisation but in the case of SV the variance of these points is similar to the variance of static, highly reflective pixels, and so are cancelled after the use of the threshold. On the other hand, the D method shows a good result in recovering the

flow but some leftover static pixels are visible below the tube. If a higher threshold is applied, the flow information is heavily impacted.

Figure 3.11 (e) and (f) show the angiographic images resulting from phase-based methods. For the PD method, as with the amplitude methods, the angio-amplitude calculation is applied to pair of B-scan images while for the PDV over 3 B-scan images (acquired in 3 frames of the initial array (ϕ) or 2 in the created one ($\Delta\phi$)). Because the phantom with the pipe used is static, no bulk motion removal method is needed. For any of the phase-based method, two thresholds, in the same way than with the AD method, are applied. The first one is to filter the intensity value considered as noise and the second one is to remove the last static features present in the angiographic image by assigning a zero value to the pixels having a relatively lower PD or PDV amplitudes than those from moving pixels. Even after applying both threshold, static features are still visible on the PD images. For the PDV method, the flow information is recovered and static pixels, here the tube and the carboard, are not appearing on the angiographic image. From fig. 3.11 (f), the full flow information from the structural images is recovered. By comparing PD to PDV, the static features removal and the moving features highlight is better done with the PDV calculation. This can be explained by the fact that the PDV calculation is based on the variance of the PD amplitudes. Values presenting the highest variance are considered to be moving and the rest as static acting like an additional threshold.

A more general comparison of the SV, AD and PDV methods can be carried out by looking at fig. 3.11 (a), (b) and (f), which appear to show that the flow information is better recovered using the phase method rather than the amplitude methods. This suggests that the phase methods are more sensitive.

However, unlike Doppler OCT or PD methods, where flow speeds can be calculated, PDV values do not have a direct link to the physical quantity (phase). Similar to the SV method, the PDV method just gauges how much the phase difference of the same pixel varies over time and so the final calculated value has no real link to the initial phase quantity.

Through this section, several methods for flow visualisation based on the amplitude and phase information have been explained and compared from a theoretical

viewpoint. In the next part, the focus is made on SV, AD and PDV. Until now, just the identification of the moving part was the target information, however, having the flow speed could be an important key for early diagnosis and better understanding of the mentioned disease (AMD, Glaucoma or diabetic retinopathy). Can the blood velocity be recovered from SV, AD and PDV? Does either of the SV, AD and PDV amplitude present any relation to the flow speed? What is the effect of the windowing function or of the focus position on the recovery of the functional information? All these questions are approached in the next section.

3.3. Qualitative or quantitative method

The visualisation of the vessels gives access to a vascular map and information on its architecture. In this way, the clinicians are informed of neovascular area (presence of vessel ramification or proliferation) or alteration of the vessel network (occlusion and part of the vasculature system lost). OCTA is an essential tool for diagnosis of retinal and skin diseases, although there is no quantification of the blood velocity. By drawing a more quantitative map of the blood flow, a better understanding, follow-up and early diagnosis becomes possible.

In opposition to Doppler shift-based method that deliver quantitative measurements of flow velocity, SV, AD and PDV techniques do not present a direct link to the flow speed. This is because these methods highlight moving areas by calculating the variance or the decorrelation between successive image.

A first thought could assume that by increasing the flow speed, the signal from the moving parts of the image are less correlated over time and so, the AD, SV and PDV amplitudes increase. Several reports on SSAD (Split-Spectrum Amplitude Decorrelation) already evaluated this assumption and tried to find a relation between flow speed and AD values [27, 55-57]. However, despite investigation for the past several years, no precise quantitative relationship between flow and decorrelation (or variance) values have been established. In the following, the PDV, SV, and AD amplitude will be studied in different configurations and the following questions will be tackled: How does the decorrelation or variance value evolve when the velocity of

the scattering centre varies? Doppler methods are dependent on the sample angle. Are the SV and AD, (amplitude/intensity based) methods, totally independent of this angle? Is this also the case for PDV techniques and what is the impact on the angio-amplitude (decorrelation or variance) values as a function of the tilted angle? And finally, how the SV, AD and PDV amplitude changes if the tube is in focus or not?

All data was processed using cMSI. The raw spectra were windowed using a Hamming function. The size of the image in the transversal plane, along the slow axis, is always the same and equal to 3 mm and, homogeneously distributed, over 200 points. In the case of the phantom with one tube, the image depth is fixed at 2 mm measured in air whereas for two tubes it is adjusted to 3 mm in air. In this section, the gain of all images, which is a multiplier factor to rescale the image to the representation format chosen, is fixed to 0.3. All the angiographic methods used the same set of data, composed of 100 images acquired at the same vertical position (scanning along the slow axis is disabled). This choice was purposely made to draw a more general conclusion and try to validate a model, if possible. The error bars on each experimental point correspond to 4 times the standard deviation which is defined as the amount of dispersion of the angio-amplitudes values from 99 calculations. Assuming a normal distribution, 95% of the values are permitted within this range. To ensure a fair comparison, the results (decorrelation or variance values) were normalised by dividing all decorrelation or variance values by the maximum angio-amplitude value of the method concerned, from the set used. In this way, the impact on the target parameters can be compared. For the rest of this chapter, the focus will be just on three methods: SV, AD and PDV and the value calculated from each of the three methods will be referred as “angio-amplitude”.

3.3.A Flow rate vs flow speed

As described earlier the phantom is composed of one or two silicon tubes on a cardboard filled with a 5% intralipid solution, which was pumped through one of the tubes and static in the other. The pump used was a Minipuls 3 from Gilson (LT801121-16). A PVC tube (reference F117949) (tube A in Fig.3.12) with an internal diameter ~ 3.16 mm, filled with the intralipid solution is compressed under the action of several

rollers creating a flow. The tube supplied with the pump is too large to have 2 tubes present at two distinct depths in the same image (imaging range of our setup is around 2mm) as is used in the case of the more complex phantom (section 3.3.D). Therefore, it was connected to a smaller tube with an internal diameter $\sim 0.5\text{mm}$ (tube B in Fig.3.12).

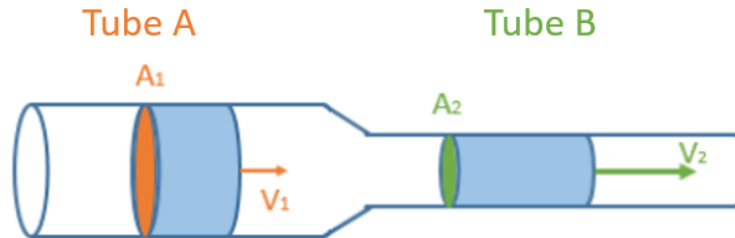


Fig.3.12. Flow rate vs speed in the case of the reduction of a tube. A_1 is the area of the larger tube noted “tube A” associated with the vector velocity \vec{v}_1 and A_2 and \vec{v}_2 are the equivalent quantities for the smallest tube, “tube B” respectively.

The datasheet from the pump gives access to the flow rate as a function of the RPM (revolutions per minute) for tube A and the corresponding flow speed (Fig.3.13). To verify the value given by the manufacturer, experimental values were obtained for several pump speeds by measuring the time required to flow a fixed fluid volume through tube A. As seen in Fig. 3.13, there is a good correlation between experimental and theoretical values. From now on, the speeds from tube A are the theoretical speeds (blue curve in Fig.3.13).

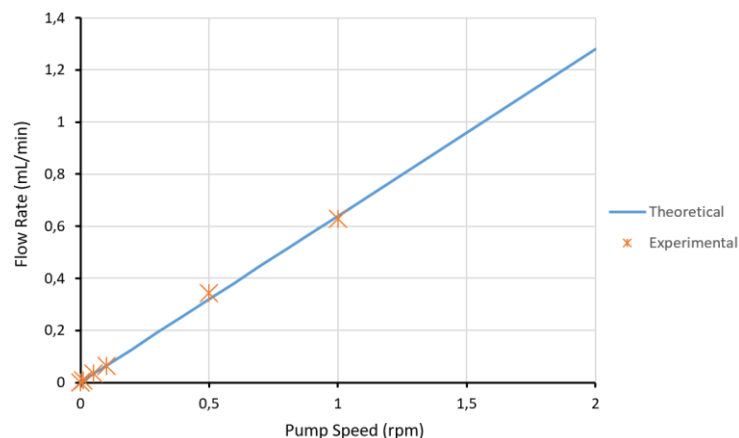


Fig.3.13. Theoretical flow rate as a function of the pump speed for tube A with an internal diameter of 3.16 mm. Blue curve: theoretical values; Orange crosses: experimental values.

A distinction needs to be made between flow rate and flow velocity. Even if one can be expressed as a function of the other, flow rate and velocity represent two different notions. The flow rate is the volume of fluid flowing through an area during a time period. The SI unit is $\text{m}^3.\text{s}^{-1}$ or $\text{L}.\text{s}^{-1}$. The velocity is a rate which measures how much an object changes its position over time and is expressed in units of $\text{m}.\text{s}^{-1}$. The link between them is given by:

$$Q = A v \quad (3.8)$$

where Q denotes the flow rate, A the area of the tube and v the velocity vector. In the assumption of an incompressible fluid flowing through the tube, the flow rate is conserved even in the case of a reduction of diameter while the speed is increased.

$$Q_1 = Q_2$$

$$\text{so, } Q_1 = \pi \times \frac{d_2^2}{4} \times v_2$$

In the case of tubes A and B configuration, the velocity amplitude v_2 is equal to:

$$v_2 = \frac{4Q_1}{d_2^2 \times \pi} \quad (3.9)$$

In this way the relation between the velocity in the tube B and the pump speed (Eq.3.9) can be worked out and is represented in Fig.3.14, by using theoretical Q values.

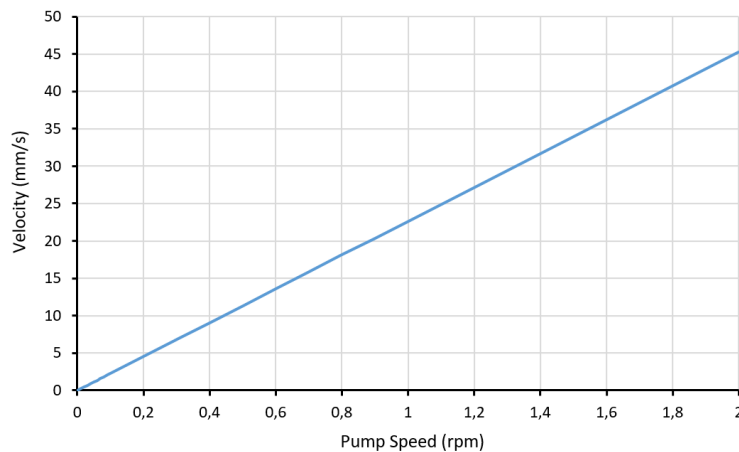


Fig.3.14. Theoretical velocity (mm/s) as a function of the pump speed in the case of tube B with an inner diameter equal to 0.5mm.

For all studies, the pump speed was driven between 0 rpm (static situation) to 2 rpm covering a wide range of typical blood flows corresponding [58, 59]. In the following experiments the pump speed will be displayed in mm/s.

3.3.B Decorrelation or variance values vs speed

The first experiment is to try to see if there is a link between the decorrelation/variance value and the velocity. The protocol followed is explained in Fig. 3.15. Briefly, after focusing the beam inside the tube, the acquisition of several sets of data each of 100 B-scan images at the same position (slow axis disabled) is done. Each cross-section image has 200 A-scans oriented perpendicularly to the lateral size of the image of 1.5 mm length. Once a set of data is saved for a given speed, the velocity is increased to the next value. The time between two acquisitions is sufficiently long, over 5 minutes, to ensure that the flow is in a stable state. After the collection of all data sets, each set was used and processed to create structural and functional images. The angiographic images were produced using SV, AD and PDV methods explained earlier to extract the angio-amplitude.

An area on the structural image, has been identified as the inside of the tube and have been used to calculate the mean of the angio-amplitude values (fig.3.16). These results have been averaged over the 99 B-scan images and the mean and standard deviation over the identified area have been extracted.

Fig. 3.17 and Fig. 3.18 present the results. The curves are using 99 angiograms from the selected area in Fig.3.16. The first observation is that there are two different trends depending on velocity, taking place below and above $5 \text{ mm}\cdot\text{s}^{-1}$. Briefly, below $5 \text{ mm}\cdot\text{s}^{-1}$, a linear trend is presented. Above $5 \text{ mm}\cdot\text{s}^{-1}$, the higher pump speed leads to larger intervals without signal and so, the lower decorrelation values.

For parts with a velocity $> 5 \text{ mm}\cdot\text{s}^{-1}$, the three methods lead to decreasing angio-amplitude values. The reason can be visually demonstrated in Fig. 3.18. While the speed increases, fringe washout is observed. This happens because the flow speed is much higher than the acquisition speed of the camera. As stated earlier, the distribution of the fluid speed follows a Gaussian trend. The maximum velocity is located in the middle of the tube, where the black area due to the washout is seen (Fig. 3.18 (b))

whereas parts closer to the edges exhibit smaller speed values and hence the signal is still strong.

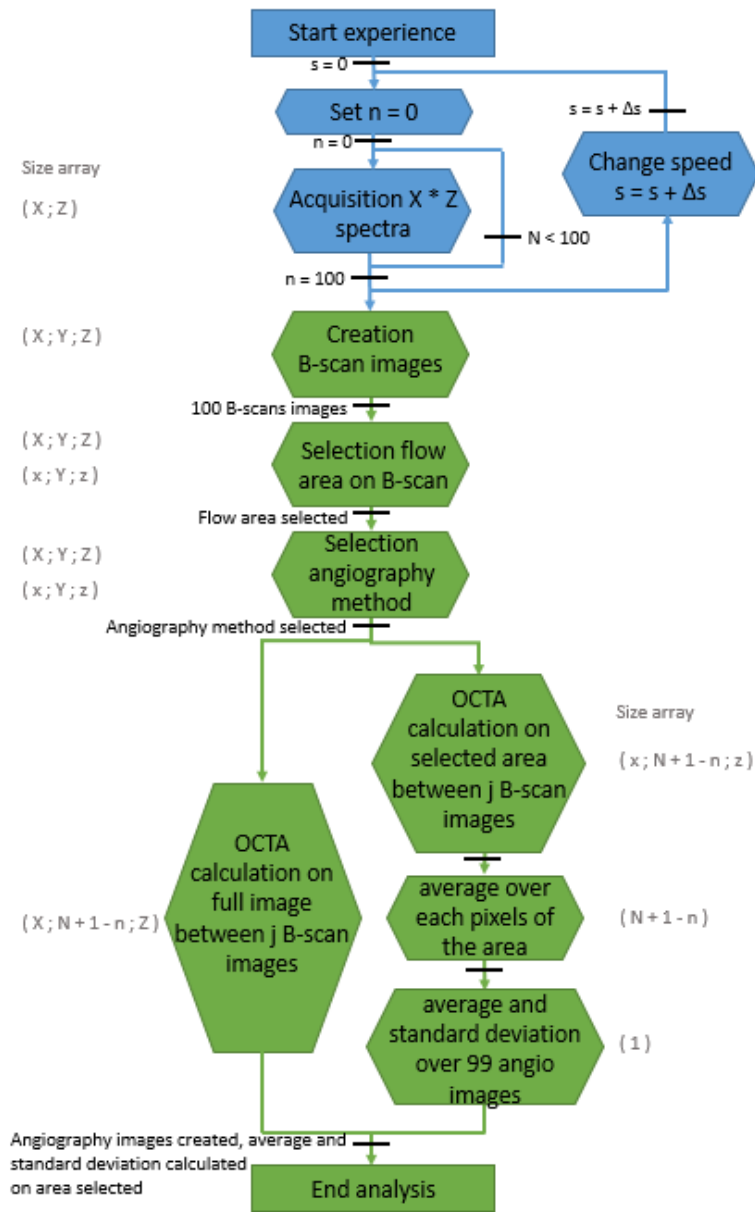


Fig.3.15. Organigram of the experiment. The sample is fixed on a translation stage that is used to move the phantom through the focus. Blue operations are done in real time while operations in green are done in post-processing.

Therefore, the larger the pump speed, the larger the regions without any signal and therefore the lower the decorrelation/variance values calculated by all three methods. The flow speed detection is therefore limited in this case by the camera performance and not by the characteristics of the angiographic method used. The angio-amplitude

information of the moving scattering centres in the washed out area, indicated by a yellow arrow in Fig.3.18, is lost before entering into the angiography process, leading to the observation that the quality of the structural images, and by extension the systems performance, are essential for the reconstruction of the flow signal in the functional images.

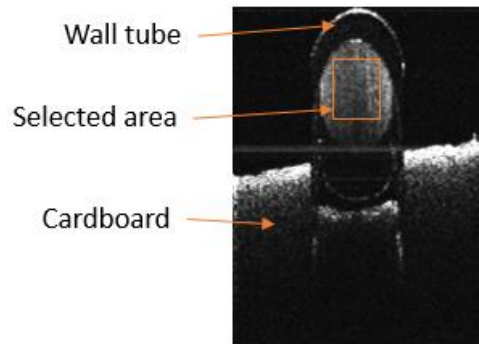


Fig.3.16. Structural image of one of the tubes and of the cardboard in the phantom. The beam is focused inside the tube. Orange rectangle delimits the area used to average the decorrelation/variance values in each OCTA image processed by SV, PDV or AD method.

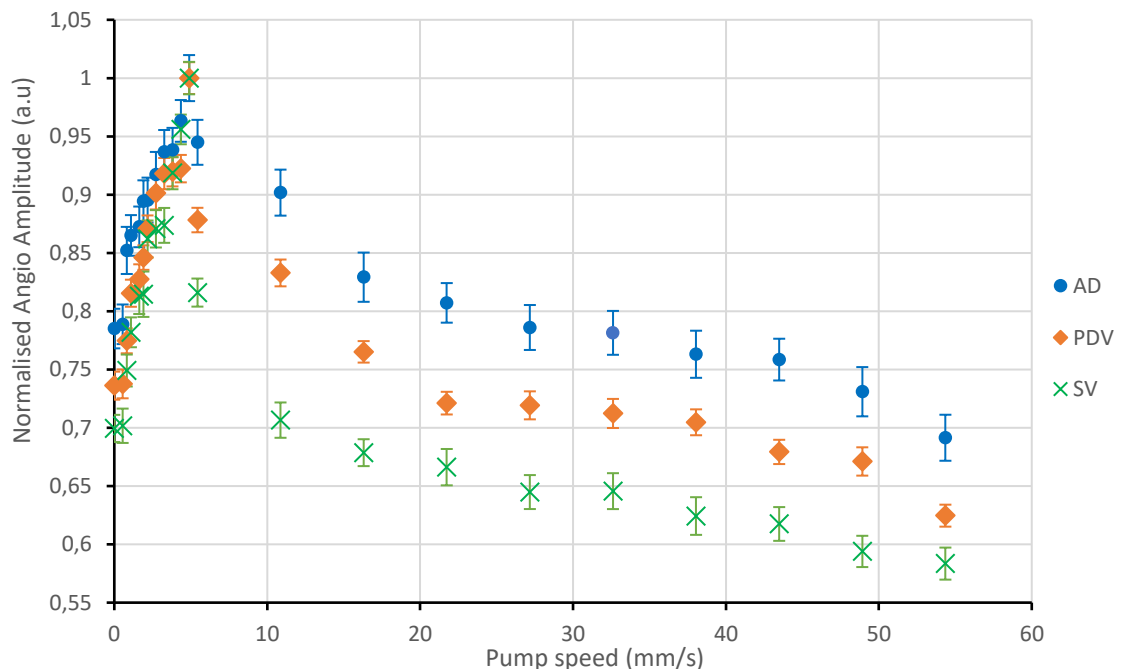


Fig.3.17. Average of normalised angio-amplitude versus pump speed. Inset shows the angio-amplitude: AD: blue dots, PDV: orange diamonds and SV: green cross.

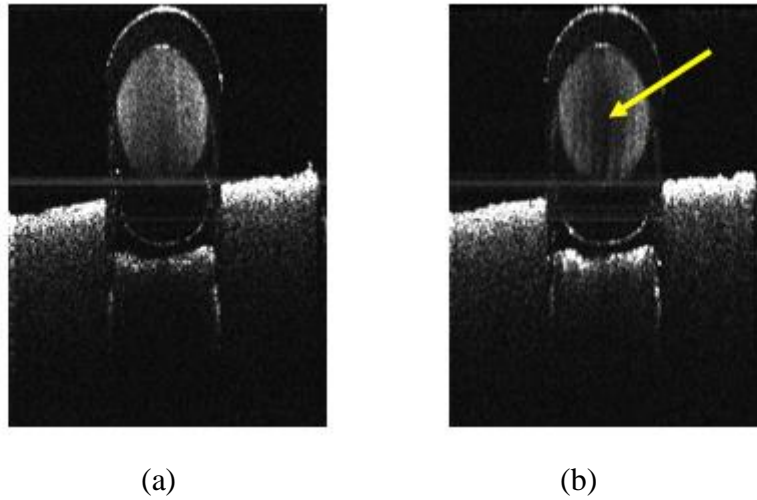


Fig.3.18. Comparison of structural B-scan images with fluid flowing at low speed (a) and at high speed (b).

On Fig. 3.19, a zoom into the area for speeds below 5 mm.s⁻¹ in the graphs in Fig.3.17 is shown. The larger the speed, the larger the angio-amplitude. This result was already shown for AD and SSAD [27, 55-57].

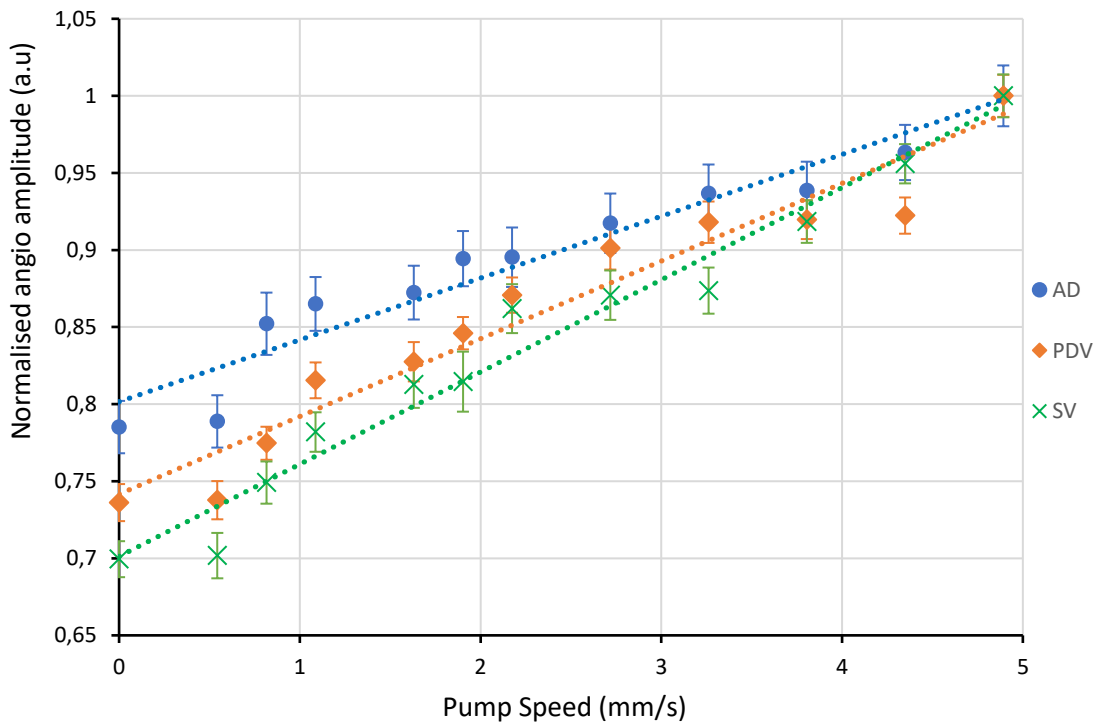


Fig.3.19. Zoom from fig.3.20 for the range 0 to 5 mm.s⁻¹.

A linear relationship between the fluid velocity and the pump rate can be speculated. By linearizing the experimental values, some comparison between the 3 methods can be made. It seems that SV method is more sensitive to the pump rate variation than the two others. Indeed, from 0 to $\sim 5 \text{ mm.s}^{-1}$, the SV amplitude has increased by 30% whereas the PDV by 27% and AD by 20% only. This means that the distinction between two different velocity values is clearer with the SV method than with the PDV and the AD methods.

However, in reality, the determination of flow rate is not so straightforward. The first reason is that the experimental data does not perfectly follow a linear trend. For example, for all methods, the angio-amplitude values do not show any increase between the static fluid and the fluid flowing at 0.54 mm.s^{-1} . Furthermore, the experiment was run over 100 B-scan images and standard deviation from the mean was noted. By looking at the standard deviation of the set of data values, in the case of no averaging, decorrelation or variance values for two different speeds are not different enough to quantify them.

Although a relationship between angio-amplitudes and displacement of scatterers over time exists, it is not possible to establish a precise and rigorous quantification of the flow. Under some assumptions, a relative quantification may be established but no absolute value can be rigorously derived, as is possible with the Doppler method.

However, the main disadvantage of the Doppler method is its strong dependence on the angle. The signal detected (Doppler shift) is a function of the angle between the light beam and the direction of the vessel (cf. Parameter for the moving backscattering centres [3.1.C] and Decorrelation vs Doppler effect section [3.2.A.2]). For this reason, the amplitude of the Doppler shift of some vessels is less strong or non-existent. It is a legitimate question to ask if SV, PDV and AD techniques are angle dependent. In the following, the angle dependence of the SV, PDV and AD method is studied.

3.3.C Angio-amplitude vs angle

An experiment is conducted to see the impact of the angle on the angio-amplitude from SV, AD and PDV. This has been divided into two small studies. In both studies the sample is the same as in the previous section but its inclination is changed. To collect data from the same position, each time the translation stage was moved to keep the inside of the tube in focus.

Prior to the start of the first study, the sample is set on a fixed inclination. The evolution of the angio-amplitude is then measured for different pump rates. The same process was conducted for three different inclinations equal to 0° , 5° , and 15° , measured between the surface normal and the incident beam direction (Fig.3.20).

The results from the three experiments are shown in Figure 3.21. As expected, and as already observed in the previous section, the angio-amplitude values increase linearly with the pump rate. For each method, a linear trend is assumed as a good first approximation to describe the normalised angio-amplitudes as a function of the pump speed. The experimental angio-amplitudes take the form of $y = gx + h$. The value “g” is the gradient and can be calculated for the angles $A = 0$, $B = 5^\circ$, and $C = 15^\circ$ and noted respectively a, b and c. It is on these values that the comparison will be done between AD, SV and PDV but also between the angio-amplitudes taken by a specific method for different angle values.

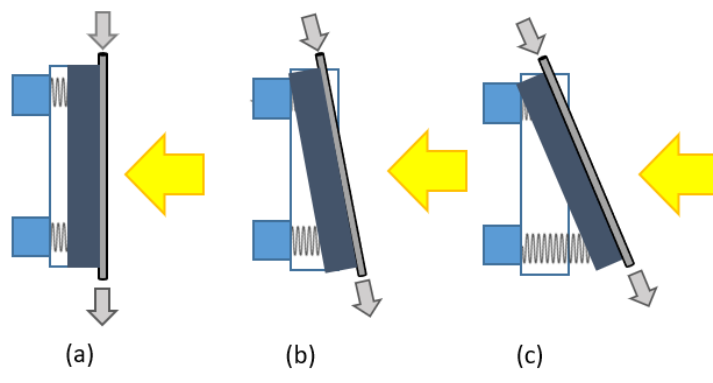


Fig.3.20. Sample inclination. From left to right, angle (a) equal to 0° , the sample is perpendicular to the beam, (b) with a small tilted angle equal to 5° and (c) with a large one equal to 15° . The yellow arrow symbolises the direction of the incident light beam.

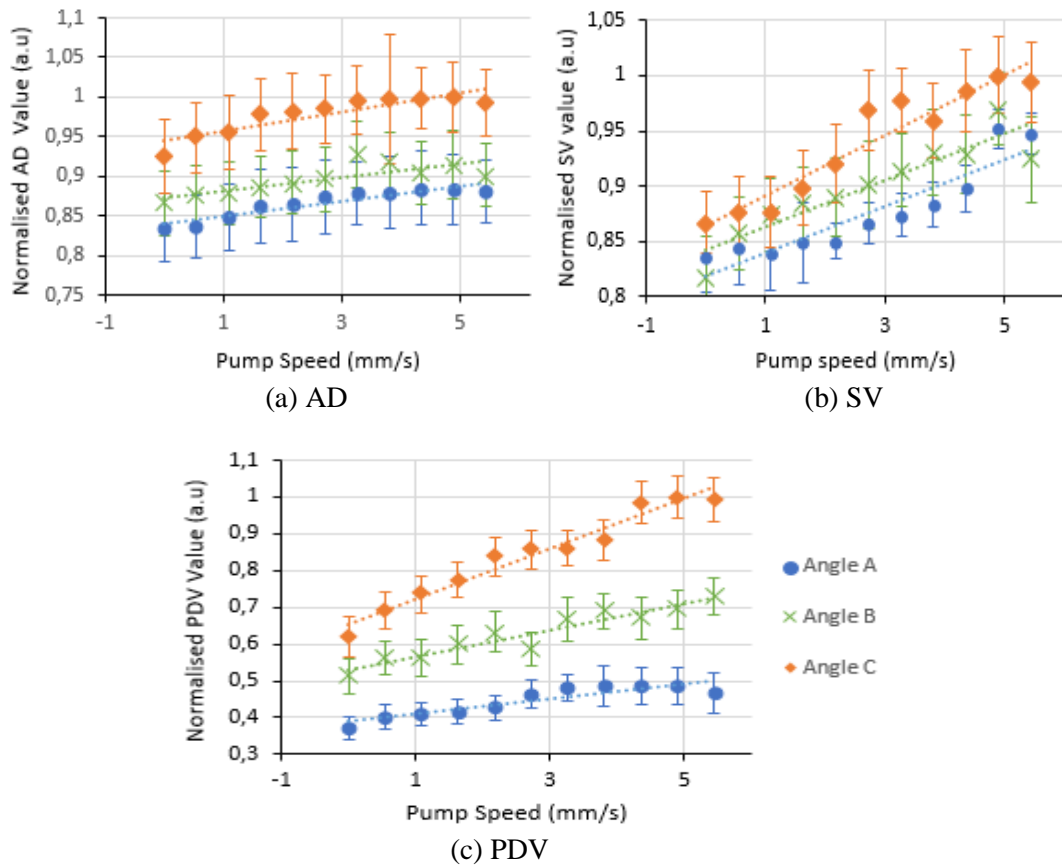


Fig.3.21. Normalised angio-amplitudes for (a) AD, (b) SV and (c) PDV versus the pump speed for three different angle of the tube, angle A = 0 (blue round), angle B = 5° (green cross) and angle C = 15° (orange diamond).

The slope variation, noted “s”, is introduced, which defines how much the gradients from the linear trends vary for different angle values (A = 0, B = 5° and C = 15°). It is given by the relation: $s = 100 \frac{(X-Y)}{(X+Y)}$ where X and Y are the gradients from the linear trends a, b and c.

The first interpretation is comparing the result of each method separately for the different angle values.

Using the amplitude methods (SV and AD), over small angles, the linear trends A_{AD} and B_{AD} are the same. Similarly, A_{SV} and B_{SV} are also the same i.e., the gradient values are approximately equal $a_{AD} \approx b_{AD}$ and $a_{SV} \approx b_{SV}$. The slope variation coefficient s_{AD} or s_{SV} between A and B is near zero. Nevertheless, once the sample is tilted with a higher angle (in the case of the angle C), the slope of linear trend, c_{AD} and c_{SV} , is steeper

($a_{SV} < c_{SV}$ or $a_{AD} < c_{AD}$). In other words, the difference between angio-amplitudes of two different speed values is larger. The slope variation between angles A and C is 12.5% for SV method and 12% for the AD method. The change is small but not negligible so, SV and AD are angle dependant methods.

PDV is based on the phase information of the signal. As with the Doppler method, the inclination of the object has a greater impact on the PDV angio-amplitude. Unlike when using the amplitude methods, small or large angle changes both have a large effect, whereby the larger the angle, the steeper the linear trend ($a_{PDV} < b_{PDV} < c_{PDV}$). The slope variation rate, s_{PDV} , is around 26% between the angle A and B and 53% between the angle A and C.

The second interpretation from this experiment is to take the results found for each method and compare them with each other. PDV is clearly angle dependent where even small inclinations of the sample produce an effect on the angio-amplitudes. There is a greater impact on the PDV angio-amplitude (phase method) than on the angio-amplitude extracted from AD and SV methods (amplitude method) for equal angles. On the other hand, if AD and SV can be considered as insensitive to small angle inclinations of the sample, it is not the case for large angle inclinations. The difference of slope variation s_{AD} and s_{SV} (between angle A and C) is so small that, as a first approximation, it can be speculated that the angle dependency is similar for both techniques.

A second experiment was conducted to better evaluate the impact on the angio-amplitudes by changing the inclination of the sample over a wider range of angles between -25° and $+25^\circ$.

The pump rate is fixed at 4 mm.s^{-1} and the angle is changed between each acquisition. The procedure followed is explained by the flow chart in Figure 3.22, where the angle α is changed in steps $\Delta\alpha$. As before, the sample is translated axially to ensure that the laser beam is focused inside the tube. Results can be seen in Fig. 3.23.

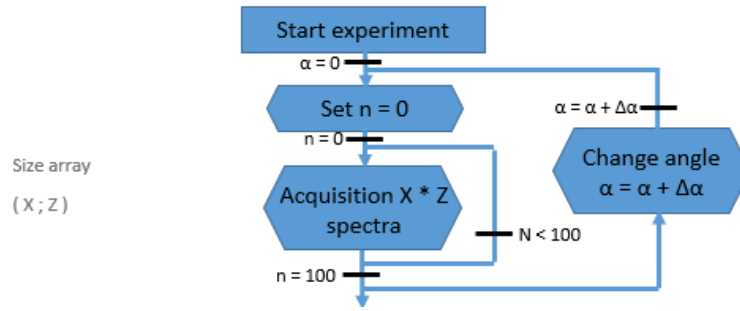


Fig.3.22. Organigram of the protocol followed. The sample is placed on a translation stage which can move the tube through focus. After each acquisition, the sample is more tilted.

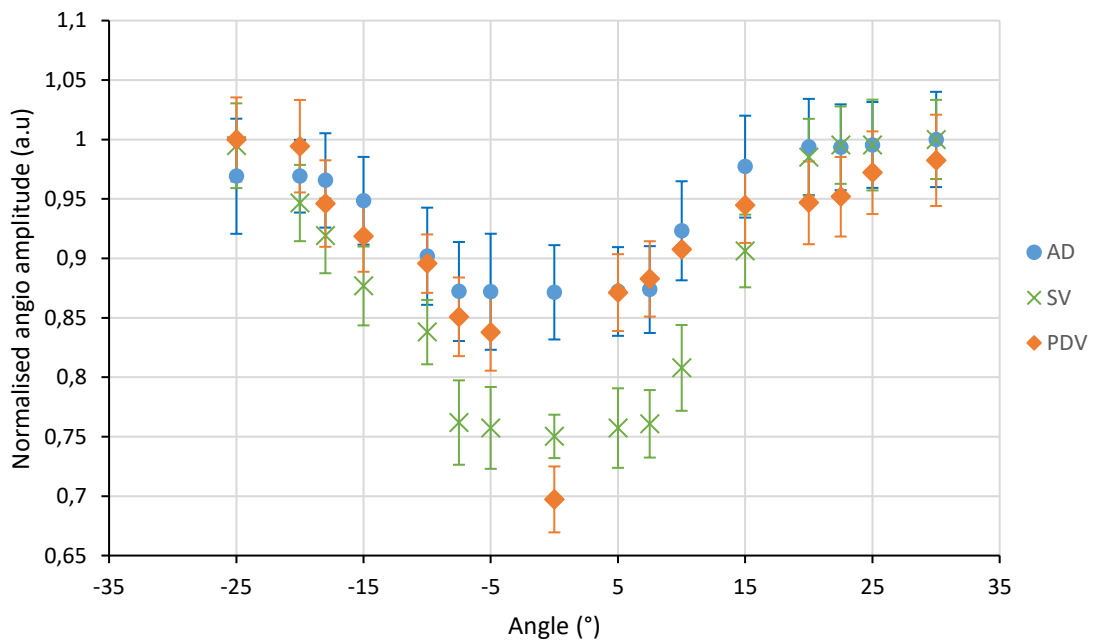


Fig.3.23. Angio-parameters vs sample tilted angle for a fixed pump rate equal to 4 mm.s^{-1} .

By looking at the PDV values, for the different tilting angles, the same conclusion can be drawn as before. PDV is angle dependant. As another feature, the gradient between 5° and the horizontal is higher than the gradient for the other angles of the graph.

For AD and SV methods, there are two zones where the slope variation rate is near 0. These are located in intervals where the angle presents a small or a high value. For positive angles, the data plateaus from 0° to 7.5° , then after 7.5° , the normalized angio-amplitudes increase until 20° and then become stationary again. As previously observed, the SV depends more on the angle than compared to AD. The experiment

was conducted on both positive and negative values to see if the behaviour differs and as expected, the trend is symmetric on either side.

The results above demonstrate that all angio-amplitudes extracted from the three methods depend on the incident pipe angle. Therefore, to interpret the results, the angle value should be known, as in the case of Doppler based methods.

3.3.D Dependence of angio-parameters on the focus position

Until now, a basic sample was used made of a single tube attached to a piece of cardboard. In each experiment, the beam was focused on the flowing intralipid solution. However, this is not realistic. In the real case of tissue, rich in vessels and capillaries, some will be in focus and some will be out of focus. To evaluate the effect of defocus on real samples, a more sophisticated phantom was assembled, using two tubes (1 and 2), one on top of the other, with perpendicular orientation direction fixed to the cardboard plate acting as a static background feature (Fig.3.24) (drawing a cross as seen from the top).

The image presents some artefacts where the flow for tube 2 or the cardboard look discontinued. It can be also noticed that the signal from these areas is less strong. Both observations can be explained by the fact that the light beam does not go through the same succession of media in each case. On each side of the image, the optical signal crosses air/wall of tube 2/intralipid solution/second wall of tube 2 and reaches the cardboard. However, by the time the signal reaches the cardboard, in the case of the two tubes, it has crossed through several layers (air/wall of tube 1/intralipid solution/second wall of tube 1/wall of tube 2/intralipid solution/second wall of tube 2 and the cardboard). The multiple layers crossed contribute to the optical path length and make the cardboard depth appear deeper than it is, as shown in figure 3.24.

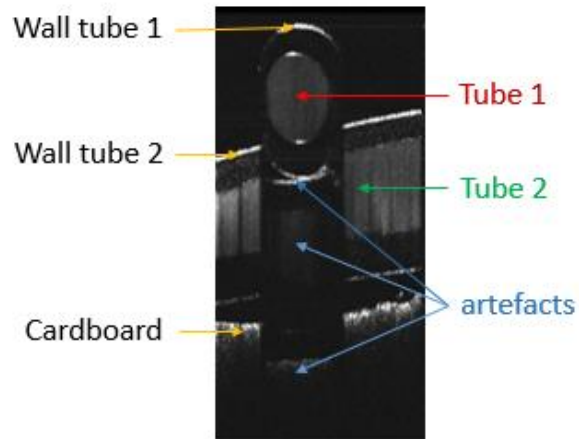


Fig.3.24. B-scan OCT image through the two tubes phantom.

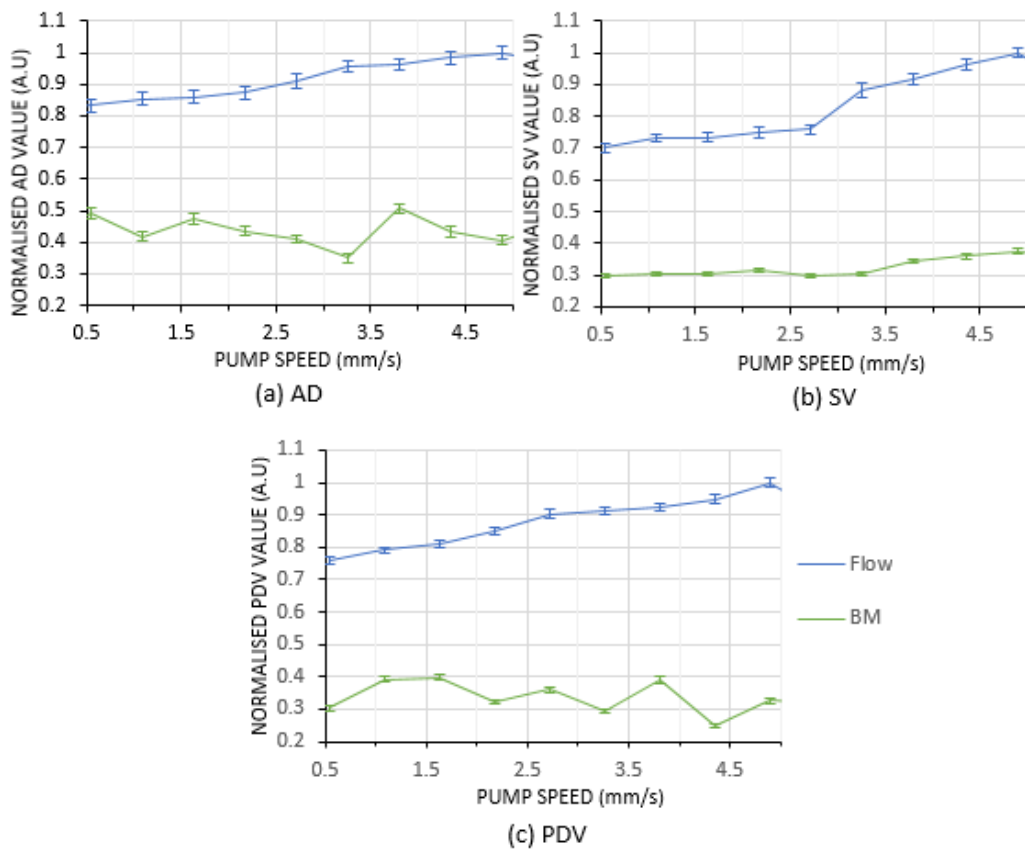


Fig.3.25. Normalised angio-amplitude for intralipid in tube 1 (blue curve), versus the pump speed. Tube 2 (green curve) is filled with stationary intralipid. (a) AD, (b) SV and (c) PDV.

Throughout this study, the two tubes were filled with the same intralipid solution previously used and tube 1 was kept in focus. One of the tubes was connected to the

pump to flow the solution while the second tube had not external stimulation besides its own motion otherwise known as Brownian Motion (BM).

The graphs in Fig. 3.25 are obtained from the intralipid flowing in tube 1, connected to the pump (not shown), and represented by the blue curve. Angio-amplitudes from AD, SV and PDV were evaluated for both tubes, showing larger values in comparison with the BM in tube 2. The blue curve, presenting the evolution of the angio-amplitudes as a function of the pump speed flowing the intralipid solution in tube 1, is, as expected, similar to that shown in figure 3.19. The angio-amplitude for tube 2 exhibiting BM (green curve) is 1.5 - 2 times less than in the blue curves for tube 1. This shows that the tube with flow can be discriminated from the quasi-static tube if a suitably adjusted threshold is applied, as shown in Fig. 3.26.

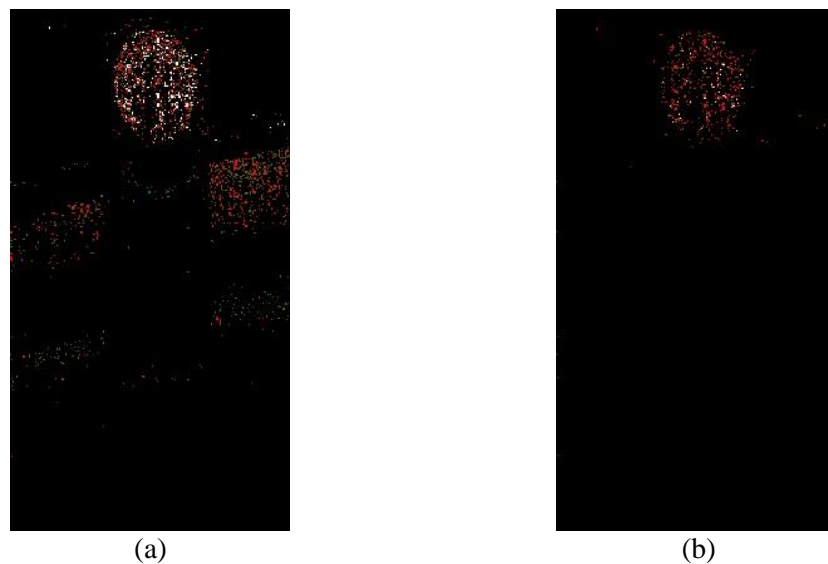


Fig.3.26. Brownian motion (tube 2) vs flowing fluid (tube 1). (a) OCTA image made with the AD method. Threshold applied just on the amplitude of the optical signal. The scale is set between 0 and 0.7, (b) OCTA image with the same parameter as in (a) but with a threshold on the AD value too, equal to 0.4. This time, the range is 0.4 to 0.7.

Data used for graphs in Fig.3.27 were obtained using the roles of the two tubes inverted. Tube 1 exhibits BM and is in focus while tube 2 is connected to the pump flowing the intralipid solution. The curves have kept similar shapes as in Fig.3.25. However, below a certain intralipid speed, it is not possible to differentiate flowing

fluid from liquid with just BM. Indeed, below such a level, the angio-amplitudes for pumped fluid are lower than those for the BM, making it impossible to separate moving from “static” liquid. These levels do not have the same values for the three methods, making them more or less sensitive to static liquid.

It seems that PDV is the best method to separate a moving fluid from BM even at low flow speeds. This method is less sensitive because of the information used to detect motion (phase in this case). The change in focus impacts less on the phase values of the optical signal and so neither the PDV amplitudes.

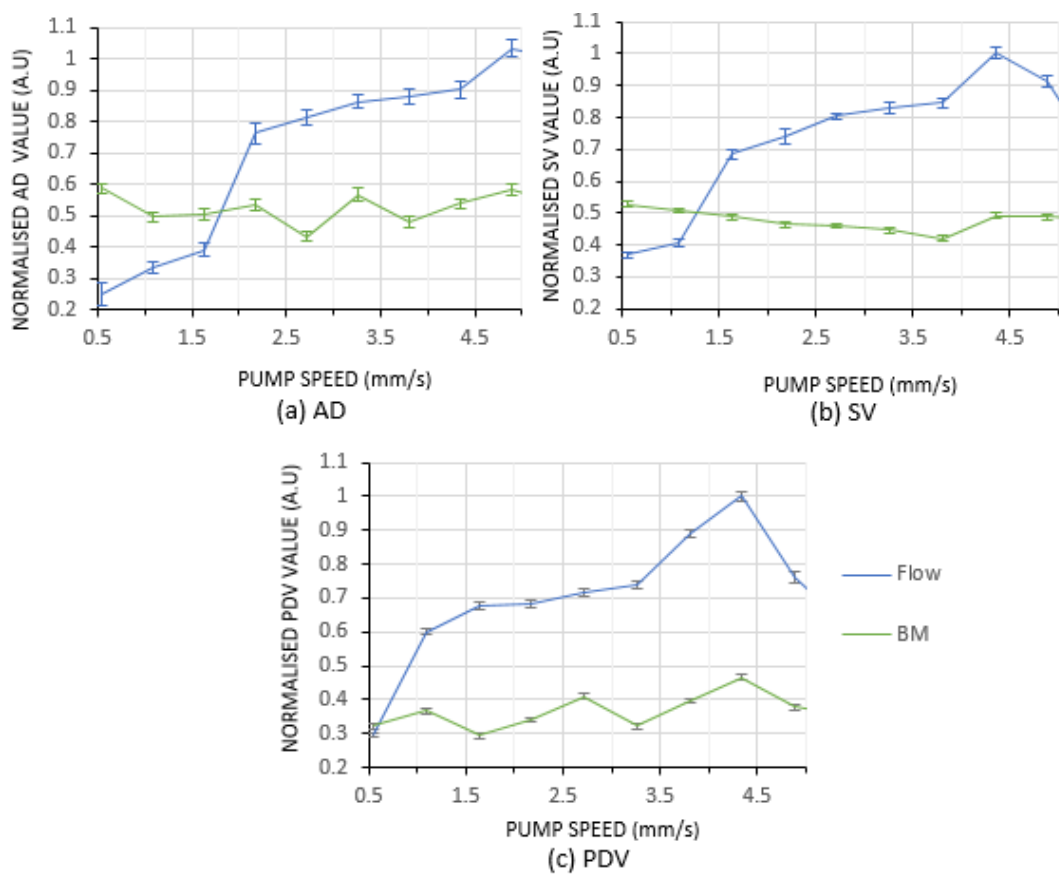


Fig.3.27. Normalised angio amplitude versus pump speed applied to the intralipid in tube 2. Tube 1 contains stationary intralipid and is in focus. (a) AD, (b) SV and (c) PDV. Each subinterval on the horizontal is 0.5.

The angio-amplitude from the AD and SV methods have a lower strength than the BM for some small flow speeds. The turning point where strength is larger than that of BM is $\sim 1.6 \text{ mm}\cdot\text{s}^{-1}$ for AD and $\sim 1 \text{ mm}\cdot\text{s}^{-1}$ for SV. Below these values, BM can be confused

with moving features. These points are larger from the angio-amplitude extracted from the PDV method because the focus position has a direct impact on the quantity used for the angio-amplitude. Indeed, features in focus would have a stronger reflected intensity signal influencing the angio-amplitude. For the same reason, the green curve describing the angio-amplitude from tube 1, this time not connected to the pump, exhibits a higher average value than the average of the angio-amplitude from tube 2 when it is not connected to the pump in the previous configuration from figure 2.28.

3.3.E Conclusion

In the settings of our study, the quantification of the flow by PDV, SV and AD methods seems compromised. Decorrelation and variance amplitudes increase with the velocity of scatterers. However, the angio-amplitude is not reliable and presents a large standard deviation on a set of data acquired under the same conditions. One solution is to increase the number of points where the calculation is done and calculate the average as it was done in the next section 3.4 of this chapter. Nevertheless, OCTA is mainly applied in ophthalmology and requires a compromise between the integration time and the patient investigation time. The larger the integration time, i.e. the time between the frames involved in calculations, the longer it takes for the whole imaging process.

Furthermore, PDV, SV and AD methods are angle dependent. This means that correct quantification requires knowledge of the angle value. Once this is calculated, a link between the inclination of the sample and the angio-amplitudes needs to be established to determine the relationship between the flow velocities and the values extracted from the AD, SV and PDV calculations. To address the angle dependence of AD and SV, it would be acceptable to assume that the imaged vessels present an inclination smaller than 10° . In this case, the angio-amplitudes are similar and a relative approximate velocity can be found. Another way to tackle the angle dependence is to find the inclination of the moving object from the incident light beam direction and afterwards, study the relationship between the angle value and the angio-amplitude. Some studies have been conducted to work out the value of this angle by using a two or three beam illumination on the sample [60-61]. Each beam is oriented towards the object at a

certain angle. These techniques allow to infer the angle of the sample top surface and so can lead to a better approximation of the velocity value using the Doppler method. However, these are complex and expensive to implement.

Not only parameters from the functional images such as the inclination of the sample or the angio-amplitude are important but also the relative placement of the object in the structural image with respect to the focus point. The angio-amplitude is a function of the distance from the tube to the focus. In the case of a single tube sample, this has no consequence, because the tube is the only feature being imaged and so, in focus. However, for more elaborate samples, it is not so trivial. The tube subjected to BM (not connected to the pump) and in focus presents larger angio-amplitude values than the tube flowing intralipid solution for smaller speeds. The discrimination between BM and flow is not ensured for all flow speeds. The relative position of the moving scatterers from the focus point influences the angio-amplitude and so, the recovery of the speed value from it. The only way to be sure that the “moving” solution is discriminated against the static solution is to apply a threshold on the angio-amplitude to remove the too low values from the functional images. This impacts the quality of the retrieval of the flow information.

To conclude, under the conditions of our study, SV, PDV and AD techniques are qualitative methods, i.e. they cannot provide quantitative data on the flow. This study was conducted on a static phantom (no bulk motion beside that of the intralipid flowing by the pump) and strict quantification is already complicated. With more elaborate or *in vivo* samples, the chance to find a relationship linking the flow velocity to the angio-amplitude, taking into account the angle and the object position from the focus position, is unlikely.

The reader should keep in mind that the presented studies have some limitations. The first limitation is from the scattering media used in the tubes. A reflective, 5% dilution, intralipid solution was used throughout the different experiments to replicate the same conditions reported in the literature [62, 63]. However, the scattering properties depend upon the size and the shape of the particles. The RBCs have a concave shape whereas intralipid particles are spherical. The difference in shape changes the reflected signal

and the result previously observed. One solution would be to use actual blood with anticoagulant as the fluid phantom, which was done by Tokayer *et al* [64] and Su *et al* [65]. Furthermore, the concentration of RBCs in the human body is variable and so the experiment should have taken into account this parameter to examine the impact. In addition, the phantom used, with one or two tubes, is not realistic since it only used one size diameter. Other studies have covered the full range of vessel sizes using microfluidic chips [2]. Additionally, a more recent study was carried out using two microfluidic channels to mimic the superficial and deep retinal vessels [66]. To be the closest to retina morphology, multi-layered thin film was synthesized to correspond to the ganglion cell layer, inner plexiform layer and the inner nuclear layer. The phantom is the composition of the microfluidic channel and the multi-layered thin film in addition to an optical lens, water chamber and an aluminium tube base. Other experiments have been conducted in vivo and try to relate the velocities found to the function of their nature (vein or artery) and the diameter of the vessels [60, 67]. Uncertainty and variation of the measurements, as exposed in our study, made the interpretation difficult and even show contradictory results under similar conditions [68]. Even if the knowledge of blood speed has already been demonstrated as clinically relevant, and that different techniques or models have been developed [68-70], the retrieved quantification measurement cannot currently be considered reliable [69-74].

3.4. Improvement of the angiography image

Up until this point, all the functional images have been created using a pair of frames from two successive OCT scans. However, using just one pair of structural frames does not give the optimum result. The flow visualisation, or the ratio of angio-amplitudes between moving and static parts, can be improved by averaging over several frames. In this section, two averaging techniques are explored: one based on time and the other based on spectral dimensions. Later on, we report a study conducted to evaluate the impact on structural imaging parameters such as the gain or the bandwidth of the filter used to sample the spectrum.

3.4.A Temporal averaging

In the capillaries, the main cause of backscattering is from the red blood cells (RBC). There are gaps between successive RBCs in their flow and therefore a pair of images may not suffice to capture one at each pixel giving a discontinuous line in the drawing of the vessels. Therefore, more images are required to ensure continuity. Furthermore, on the functional images, a threshold is applied to the angio-amplitudes for all methods and on the intensity values for AD and PDV. By increasing the number of oversampling “ n ” (number of frames at the same lateral position), better separation of moving targets from static targets is obtained, however at the cost of increasing the overall acquisition time, T . A trade-off between T and n needs to be found to keep the value of T small whilst improving the reduction in the strength of static features while highlight the flow. Therefore, a minimum number of n is targeted that is sufficient to cancel the static features and highlight the flow.

The OCTA images shown in Fig.3.28 (a), (b) and (c) demonstrate the impact of oversampling using the AD method for different values of n , equal to 2, 5 and 10. The same scale range was used in all images. Clearly, the larger the n value, the less visible the static features. In the regions showing flow, denser flow information is reconstructed. This observation is less obvious on the image (c), just because the scale is kept the same in all images (Fig.3.28 (a), (b) and (c)) and so, some angio amplitudes of pixels presenting flow are below the threshold applied on the AD amplitudes and are therefore set to 0. If the scale is adjusted, better visualisation of the flow area is observed. Graphs showing the different angio-amplitudes using the AD method as a function of the transversal pixel position for each depth are presented in Fig.3.28 (d), (e) and (f)). On all these curves, a threshold was applied on the intensity values prior to calculation to remove the pixels considered to be noise. Subsequently any further thresholding is applied to the angio-amplitudes at the difference of the images (a), (b) and (c). The same observation can be made upon examination of each graph, increasing the oversampling improves the differentiation between static and moving scattering elements in the sample. No high AD amplitudes are visible outside of the flow area on the images (e) and (f) compared with image (d) in figure 3.31.

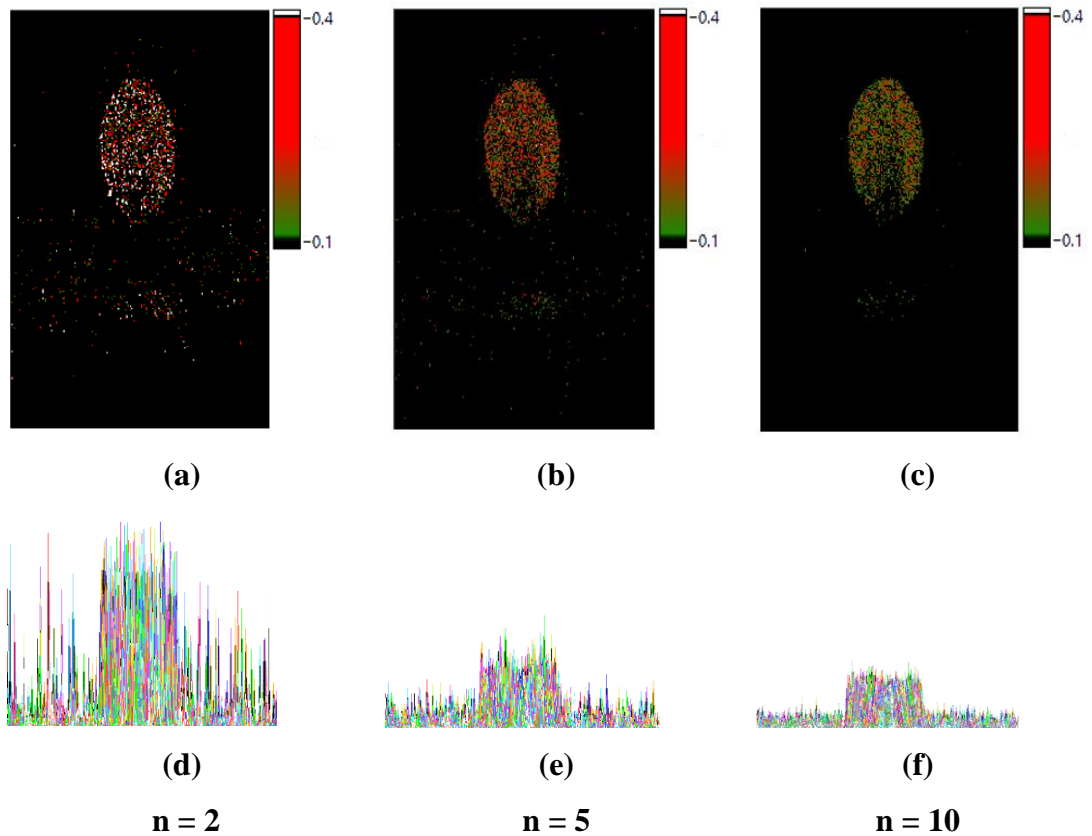


Fig.3.28. OCTA images using the AD method for different oversampling values: (a): $n = 2$, (b): $n = 5$ and (c) $n = 10$. The same threshold was applied to all cases and only values above 0.1 are displayed on the functional images. (d), (e) and (f) are the angio-amplitudes extracted from the calculation with the AD method as a function of the transverse pixel position overlaid for each depth. A threshold has been used on the intensity values prior to the calculation.

Taking this further, a quantity “ r ” was introduced to quantify the average angio-amplitudes from the moving pixels over the static pixels. This ratio is calculated using the angio-amplitudes from two different areas selected in the structural images. The first area is delimited by the orange square in Fig.3.29, inside the tube. The second area, with the same dimension, is composed of static features, such as the cardboard and some noisy pixels, delimited by the blue square in Fig. 3.29. The ratio r was calculated for several oversampling numbers (variable n) and for the different OCTA methods implemented here (AD, SV and PDV) and is shown in Fig. 3.29. The ratio r is calculated for all three methods.

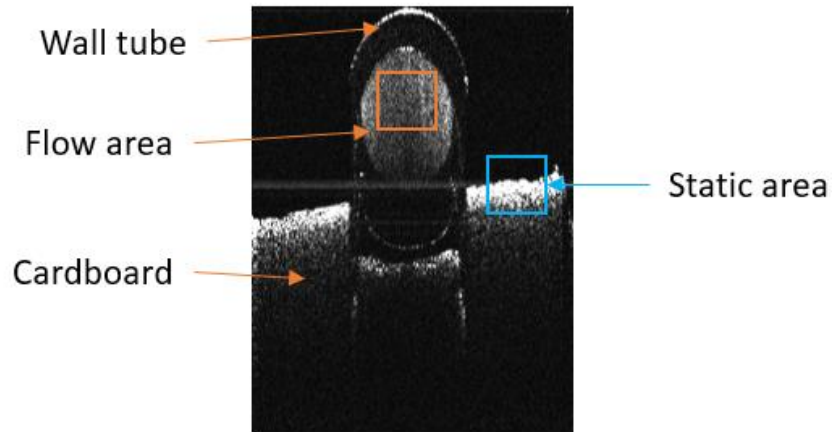


Fig.3.29. Flow vs static area. Delimitation of both areas in the case of the ratio r calculation. The orange square shows the flow area used whilst the blue square shows the static area.

As expected, the results from Fig.3.30 confirm the observation made in relation to Fig.3.31. By increasing the number of oversampling, i.e. the number of B-scan images taken into account in the calculation, the ratio r follows a logarithmic trend until approximately $r = 20$. Then, it becomes constant afterwards. From Fig.3.30, a maximum value for n can be extracted. The evolution of r reaches a plateau around $n = 20$. Using a larger value of n will not impact significantly the quality of the angiography images, nor the differentiation between static and moving features.

Even if all methods exhibit the same trend in the evolution of the ratio r as a function of the oversampling number n , the gradient between two successive points is larger for the PDV technique. In other words, the differentiation between static and moving features is improved for the same variation of n .

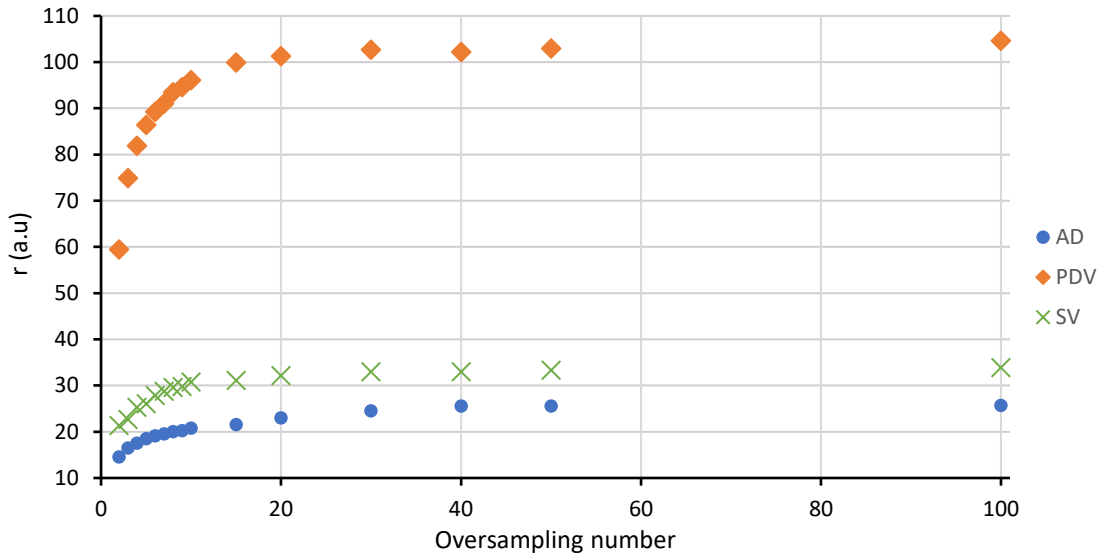


Fig.3.30. The ratio r between the average angio amplitudes from moving and static pixels for different OCTA methods using SV, AD and PDV.

The disadvantage with using the time averaging method is that the acquisition time is elongated to create a volume (with fixed dimensions). This increases the chance of disturbances due to extra motions during *in vivo* imaging and therefore requires further post processing to correct them and/or the use of a tracker. For a volume of size X , N , Z and recording a B-scan image in $T_{B\text{-scan}}$, the 3D acquisition time, T_{3D} , is equal to $N \times T_{B\text{-scan}}$ for a structural volume and at least, $2N \times T_{B\text{-scan}}$ for a 3D angiography volume scan using AD and SV and $3N \times T_{B\text{-scan}}$ for PDV. For the functional volume with no time averaging, the acquisition time is therefore 2 or 3 times longer compared to the T_{3D} required to generate a structural volume. By applying temporal averaging, multiple B-scan images are taken at the same position and T_{3D} becomes $n \times N \times T_{B\text{-scan}}$ (where n is the number of oversampling and N is the number of transversal positions along the slow axis). This means that by using the optimum $n \sim 20$ found in Fig.3.30, T_{3D} is 20 times longer than that for a 3D structural volume with the same dimensions, making any kind of *in vivo* imaging impossible. It is clear that such a high number of oversampling events is not currently possible with the acquisition parameters from the OCT systems available. As mentioned at the beginning of this section, a trade-off between quality of the functional images and acquisition time needs to be found.

In this study, the oversampling acquisition is easy to implement because the volume was a succession of 2D images (the slow axis of the galvanometer scanner being

disabled and taking all images at the exact same position). However, when this is applied to a real sample, it is necessary to scan in both directions. Implementation of the scanning pattern is more complex. In order to maintain the beam at the same position for a number of acquisition events, requires that the signal applied to the galvanometer scanners takes the form of a stair. This makes it possible to acquire the signal from the same position of the sample each time. Another possibility consists of acquiring several frames from approximately the same position to maintain a continuous galvanometer scanner signal and overestimate the number “ n ” to observe the Nyquist Shannon sampling condition. This will be explained in more detail in section 3.5.

Because of the reasons listed above, n is, most of the time, kept below 10 in the literature [7, 8, 17, 30]. An alternative method that can be used to replace or even combine with time averaging (to reduce the number of oversampling) is to employ averaging over the spectral dimension.

3.4.B Spectral Average

Another way to reduce the noise impact on the image is to apply spectral averaging. This method is known in the literature as the split spectrum method (SSM) [27, 28, 55-57]. The idea of SSM is to average the signal in the spectral domain and keep the number of oversampling “ n ” small.

As seen in a previous chapter (2.2.C.2), this method can also be used to characterize the dispersion present in the OCT system. Initial reports employed FFT. Equally, we can continue using the FFT method, however here we implemented a method developed in the AOG, termed as complex Master Slave Interferometry (cMSI) explained more in details in the section 2.3 of chapter 2.

Typically, an A-scan is produced using the full spectrum detected by a camera (Fig.3.31(a)). In the case of the SSM, the spectrum is divided into M equal parts using a Gaussian filter. If BW is the bandwidth of the full spectrum, the bandwidth of each Gaussian peak is bw . The filter is moved each time by half of the FWHM of the filter window ($bw \div 2$) to ensure that all the interference pattern is covered. The number of small divided spectrum windows, w is equal to $w = 2M - 1$ (Fig.3.31(b)).

Furthermore, zero values have been added before and/or after the Gaussian peak (zero padding) to maintain the same number of pixels in the A-scan as in the structural frame. The number of zeroes before or after the Gaussian peak depends on the relative filter position with respect to the full bandwidth (BW). Each divided spectrum window, w has a bandwidth bw equal to $bw = BW \div M$. Two successive windows are distanced by $BW \div 2M$. The length of added zero values before is $mbw \div 2$ where m is the index of the Gaussian filter between $[0; w-1]$ and after is $((w - 1) - m)bw \div 2$.

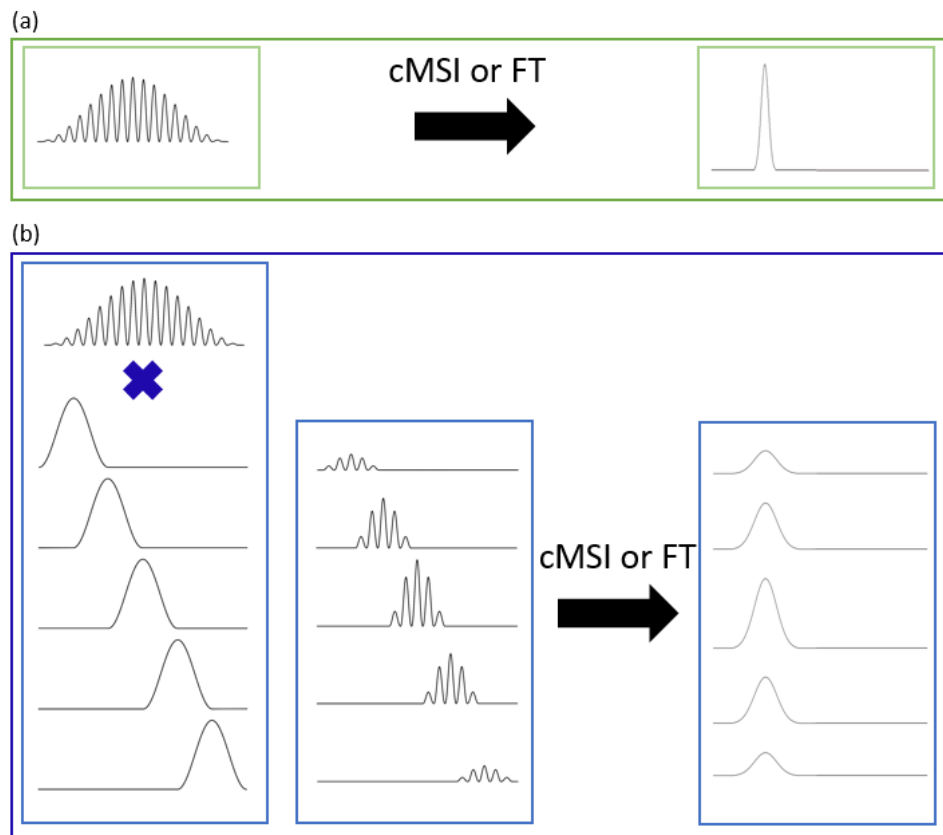


Fig.3.31. From spectrum to A-scans. (a) the full spectrum gives a unique A-scan line. In the case of the SSM, the interference pattern is split by multiplying the data acquired with a Gaussian filter. “w” spectral windows of channelled spectra are processed by FT or cMSI to obtain w A-scan profiles.

The reconstruction of the information from all layers is made, this time using cMSI. The first thought is, as it is done with the FFT in section 3.2.C.2, to split the interference pattern for each depth with the Gaussian filters created and repeated for each transverse position along the fast axis. For each w spectral window, an A-scan is

calculated. The group of w A-scans is compared with the group of w A-scans from the next B-scan at the same depth and afterwards an average is produced (fig.3.31 (b)). In this case, the spectral division needs to be done each time for each new set of data obtained.

To simplify the operation, one solution is to not apply the division on the raw data spectrum but instead, on the masks. One set of masks is acquired to analyse all the data afterwards; by splitting the masks and not the data, there is no need to repeat this action each time and it can be done separately before any further analysis. The process is explained graphically in figure 3.32. Each mask has two parts: a real part and an imaginary part. Each portion is then, multiplied by the filter (exactly the same used in the case of the data filtering) and the result is the creation of two separated split mask arrays.

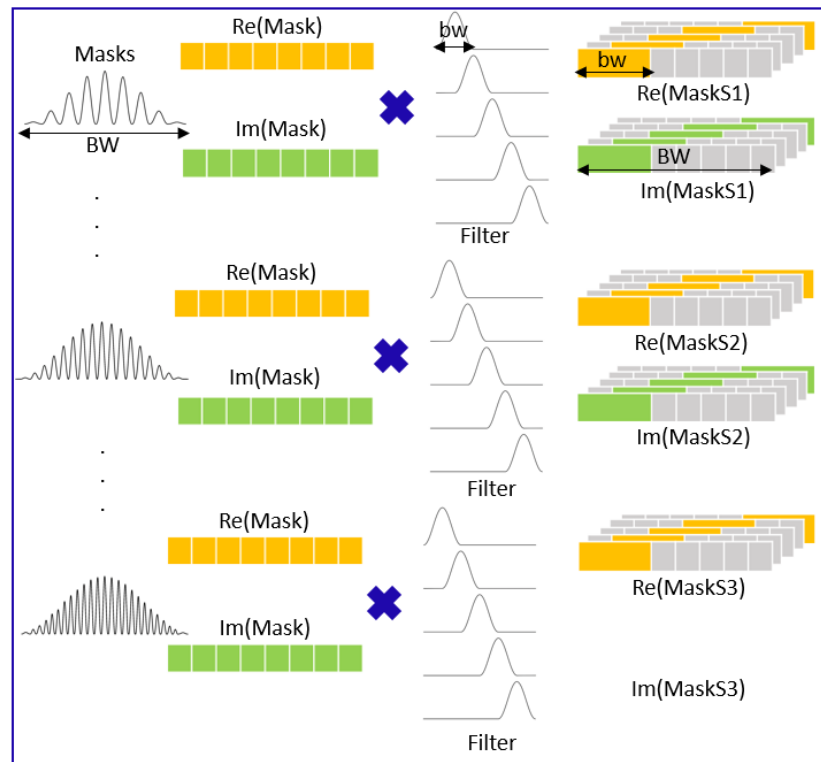


Fig.3.32. From masks to split masks. Masks have a real and imaginary part at each depth. Both parts are multiplied by a Gaussian filter of length bw . The array of original size $(x, 1)$ becomes (x, w) . This is repeated for each z and gives a mask array with a size of (x, w, z)

Once this is repeated for all depths, the masks volume is extracted (Fig.3.33 (a)). When the image is reconstructed using the full spectrum, the masks array (imaginary or real) is two dimensional, i.e. $(x, 1, z) = \text{number of pixels} \times \text{full spectrum} \times \text{number of depths}$. When applying the SSM method, the masks array (imaginary or real) has a three-dimensional size $(x, w, z) = \text{number of pixels} \times \text{number of divided spectrum windows} \times \text{number of depths}$.

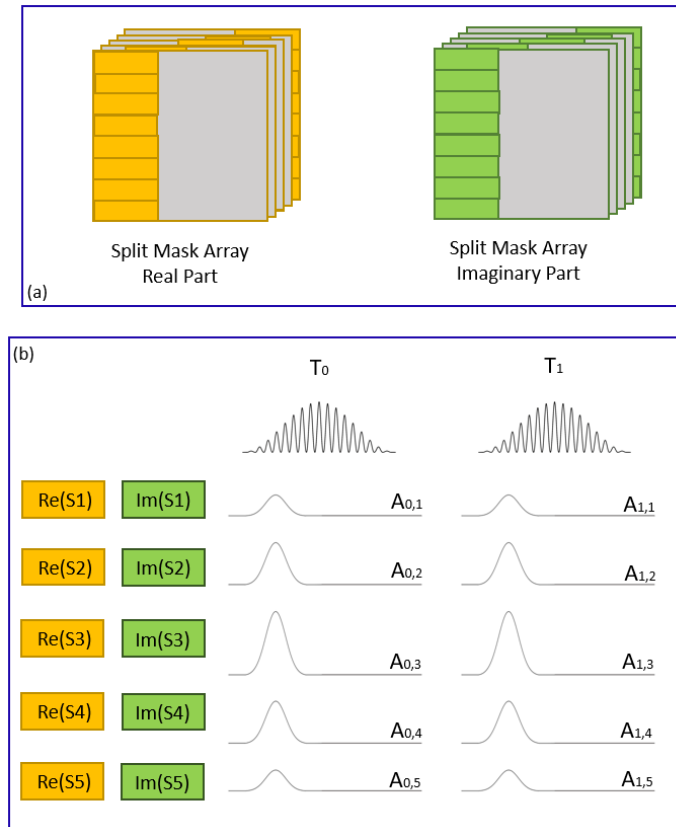


Fig.3.33. SSM vs angiographic calculation. (a) split mask volume computed with a size of $(x, 2M-1, z)$. (b) Each split A-scan line is compared to the same depth and split number A-scan profile but separated in time.

Afterwards, the arrays are used to create an A-scan profiles at each depth and for each spectrum windows (Fig.3.33 (b)). Once the w structural images have been processed, the angiographic calculation is run on two or more successive B-scan frames, for example between the pairs $(A_{0,1}; A_{1,1}), \dots, (A_{0,5}; A_{1,5})$ from Fig. 3.33 (b) giving the angio-amplitude array $(a_1(p,x), a_2(p,x), a_3(p,x), a_4(p,x), a_5(p,x))$. The notation “a” denotes the angio-amplitude extracted from the applied method (AD, SV or PDV) for the depth p and the transversal position x for w windows (in the case of Fig.3.33 $M=3$

so, $w=5$). The final angio-amplitude which is used in the final angiographic frame is the average of all values from the angio-amplitude array and noted $a(x,p)$. It can be expressed as: $a(x,p) = \sum_{m=0}^w a_m(p,x)$. This is repeated along all depths and for each transversal position until the full volume is obtained.

To see the impact on the quality of the detection of moving features, the SSM was applied to the three methods: PDV, AD and SV. For the remainder of this chapter, the followed notation is used: SS-PDV (Split Spectrum Phase Difference Variance), SS-AD (Split Spectrum Amplitude Decorrelation) and SS-SV (Split Spectrum Speckle Variance). All subsequent work from here onwards was performed using the cMSI method.

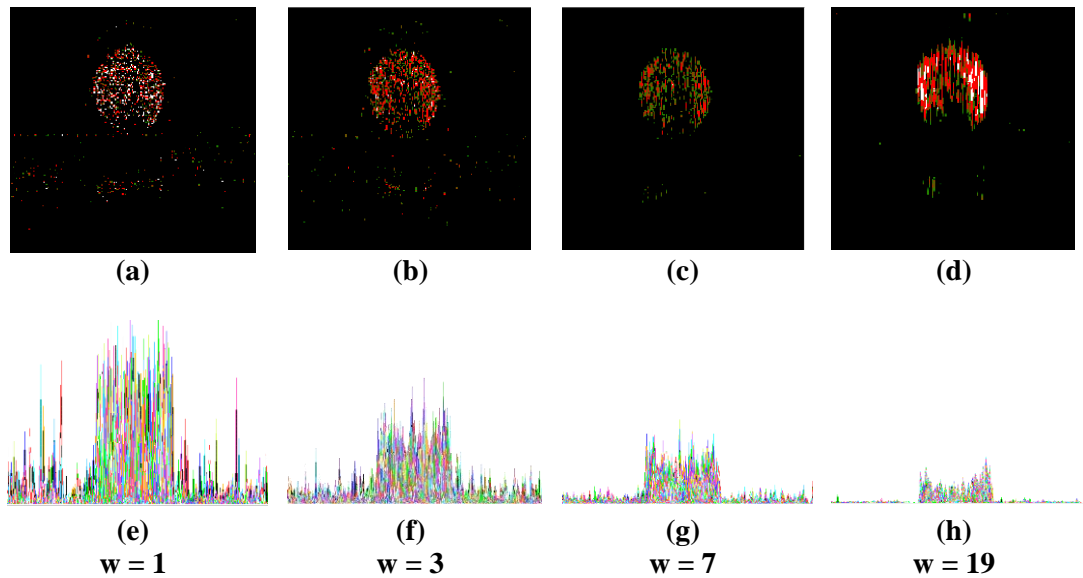


Fig.3.34. Functional images for different numbers of divided spectrum windows, w . (a)-(d) Angiographic images taken with SS-AD for $w = 1, 3, 7$ and 19 respectively. The colour scale is in the range from 0.1 to 0.4 except for (d), which is from 0.025 to 0.1 (e)-(h) Transversal profile of the SS-AD values superimposed for each depth. All graphs have been scaled to the range between 0 and 1 . For all the curves and images, the number of oversampling is kept at $n = 2$.

In Figure 3.34, the first line (image (a), (b), (c) and (d)) shows the functional images created using a different number of divided spectrum windows (w): 1 (full spectrum), 3, 7 and 19 for the SS-AD method. In each case, calculations are done over two

successive B-scans images. Each one has a bandwidth equal to BW , $BW \div 2$, $BW \div 4$ and $BW \div 10$ respectively. The resulting image is the average of the angio-amplitudes calculated for each window. An improvement can clearly be seen when the number of divisions is increased whereby fewer static features are present. This is confirmed by the four graphs, (e)-(h), from line 2 in figure 3.34, which represent the angio-amplitudes as a function of the transversal position (along a horizontal line in the images from (a), (b), (c) and (d)) displayed as the total combined stack of every transversal profile, overlaid on top of each other, representing all depths at once). On either side of the tube, where the static features are situated, the angio-amplitudes diminished, further highlighting the moving parts. However, due to averaging over a larger number of split windows, the averaged angio-amplitude of the flow area is also decreased.

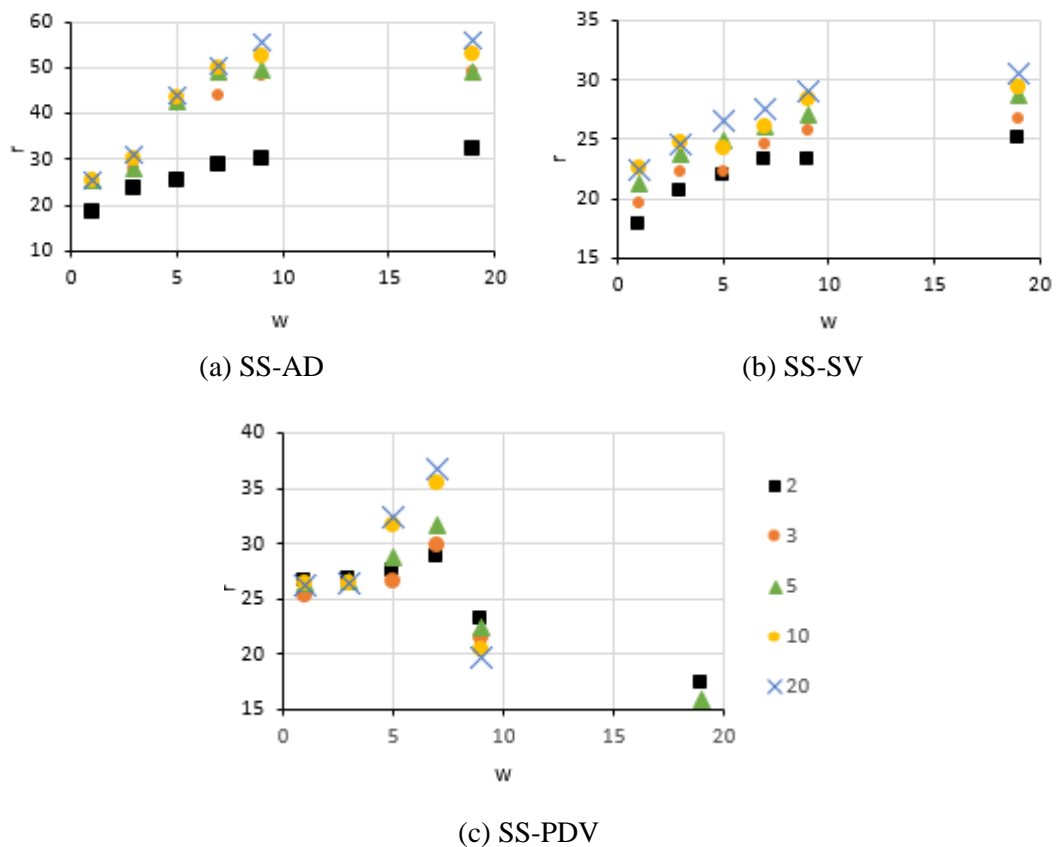


Fig.3.35. Ratio between the average angio-amplitudes of the moving and static pixels, r , as a function of the number of divided spectrum windows, w . Each type of data point corresponds to the number, n , of oversampling used where $n=2, 3, 5, 10$ and 20 . (a) SS-AD, (b) SS-SV and (c) SS-PDV.

To evaluate the improvement, characterised by the reduction of the static angio-amplitude over the flow angio-amplitude, the ratio r , introduced in the last section (3.4.B), is calculated as a function of the number of windows w for different methods and oversampling values (n). Figure 3.35 represents the evolution of r , defined as the ratio between the average angio-amplitude values of the moving and static pixels. This was plotted against the number of spectrum windows w or $(2M+1)$ and for the different number of oversampling (n). The top two charts ((a) and (b)) from Figure 3.35 are concerned with the amplitude/intensity methods. As expected, the value r increases with the number of w and n with an almost linear trend for the first portion where $w < 10$ and presents a plateau afterwards. This means that moving features can be differentiated from static ones more precisely and therefore a threshold can be applied.

Using the PDV method (Fig.3.35 (c)), there is an improvement until a certain point ($w = 7$) and afterwards, the ratio r drops. When w is larger, some information from the fluid area is not recovered on the angiographic image (Fig.3.36 (a), (b) and (c)). One reason for this is because the threshold applied on the intensity values (before calculation) is set too high and so the calculation excludes several data points from the beginning. Furthermore, the graphs depicting the angio-amplitudes, horizontal stacked profiles in Figure 3.36 (d), (e) and (f) show that the central flow area reduces in amplitude whilst the sides remain virtually the same, which is different to the graphs showing the AD method in Figure 3.34 (d), (e) and (f). For this reason, the threshold value applied on the angio-amplitude SS-PDV had to stay the same for all calculation configurations (for all w and n) to remove the static features. However, from a certain point, the moving pixels with a lower amplitude, due to the spectrum splitting, are lower than the threshold and therefore are set to zero. This has a negative impact on the recovery of the flow information. Applying SSM to PDV technique improves the differentiation between moving and static features for small numbers of spectrum windows w . From a certain value ($w \sim 9$, as seen in Fig.3.35), the larger the value of w , the less flow information is recovered, which is caused by a threshold that is too strong.

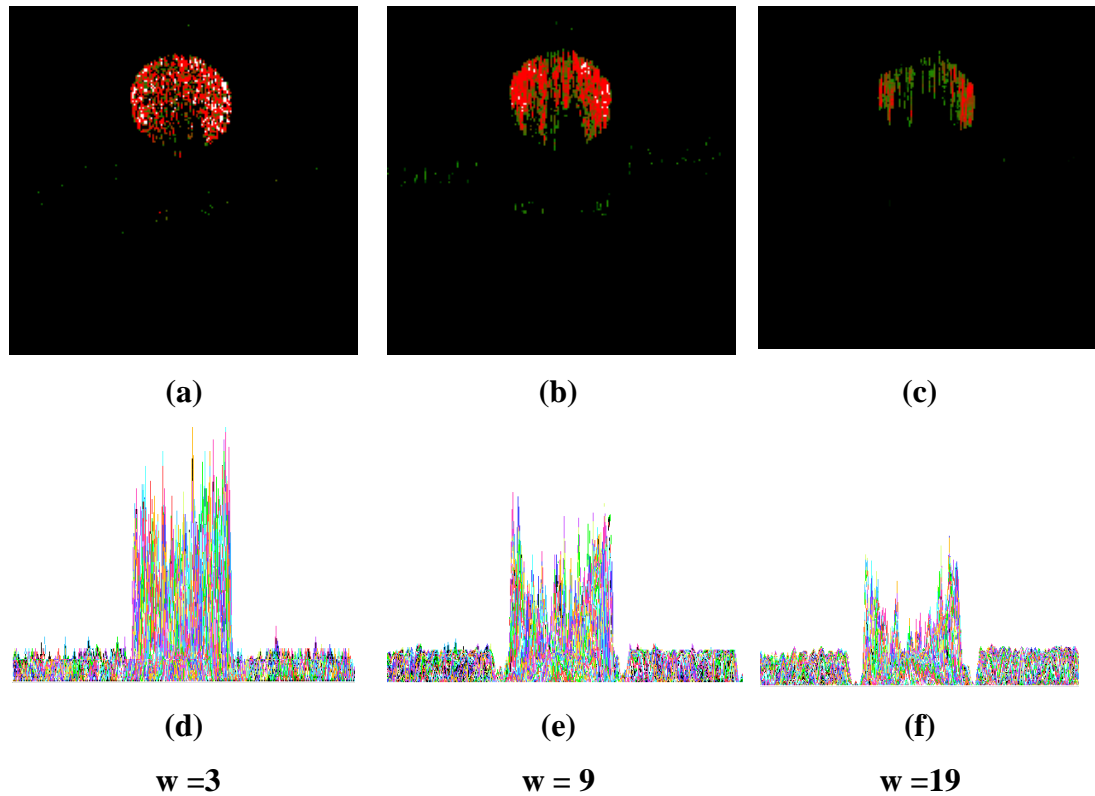


Fig.3.36. SS-PDV images for different number of spectrum windows w . The number of oversampling n is kept at 2. (a), (b) and (c) are functional images for $w=3$, 9 and 19 spectrum windows. The same colour scale is used across the 3 images, in the range from 1 to 10. (d), (e) and (f) are the graphs representing the angio-amplitudes from the SS-PDV method as a function of the transverse position over all depths. They are the SS-PDV horizontal line profile of (a), (b) and (c).

The Split Spectrum method presents the advantage to make a better distinction between moving and static parts of the image without increasing the acquisition time and enhance the continuity of vessels over depth. However, by dividing the full spectrum into smaller windows, the axial resolution is dramatically impacted with increasing values of M (Fig.3.37). Multiplying the axial resolution by the factor M has a direct repercussion on the detection of small moving features. The axial definition of the image is less precise (less details can be observed) and information from tiny vessels such as capillaries can be missed. It is for this reason that most articles from the literature keep this number relatively small, around $M=3$ [27, 28, 55-57].

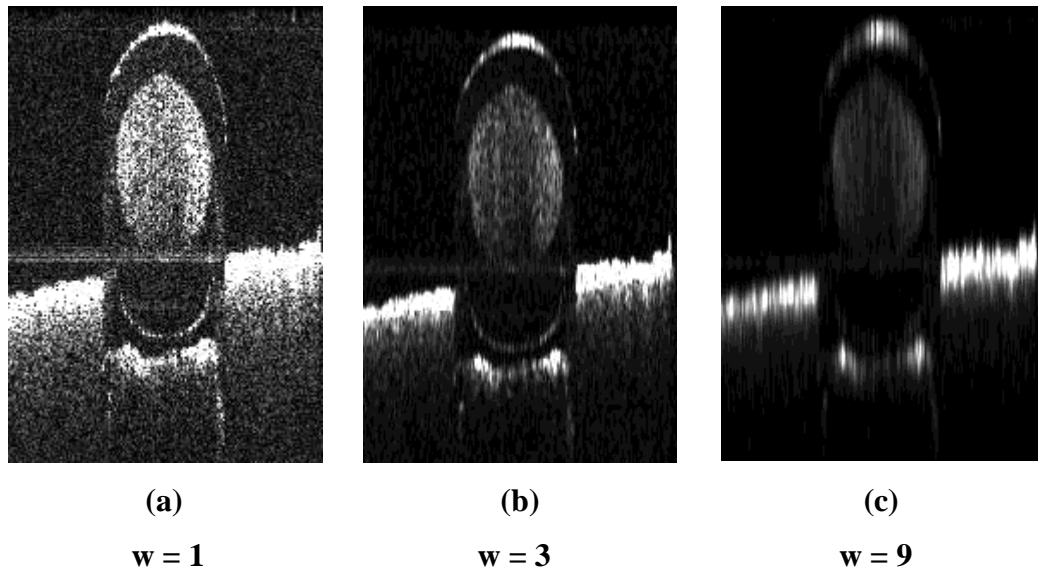


Fig.3.37. Structural images for different number of divisions $w = 1$ (full spectrum), 3 and 9 corresponding to $M = 1, 2$ and 5.

To conclude, both temporal and spectral methods need to be carefully employed to be beneficial. It is possible to achieve a better result, whilst keeping the axial resolution and reasonable acquisition time by combining temporal and spectral averaging. As shown in Figure 3.35, having a larger n and w simultaneously, improves the ratio between the moving and static features. A trade-off needs to be found between the number of divisions vs. axial resolution as well as the number of oversampling vs. acquisition time.

Structural and functional images are two different entities that highlight different features from the sample, however they are intrinsically linked: the functional image being the result of the correlation calculation between two structural images. The quality of the structural image is an important parameter of the reconstruction of the flow information. This is a key point to access a good angiographic image. While the structural image is processed, most of the time, to improve its quality, a filter is applied. How the measurement is done and how the raw data and masks are used, impacts the quality of the functional images. A natural question is to evaluate how much the filter performance affects the quality of the angiographic images.

3.4.C Impact of the windowing function applied on the structural images: Gaussian vs Hamming

Before applying the FT or cMSI methods on the raw data, filters can be applied in post-processing to achieve a better structural image. They can take the shape of different windows such as the Gaussian or Hamming function. Using these filters, the quality of the structural image is improved with a reduction of noise and/or smoother rendering. If the FT or cMSI is directly carried out on the raw spectrum, which is unlikely to have a perfect Gaussian shape, the A-scans present several sidelobes damaging the reconstruction of the image. However, as said earlier, functional images are made from this reconstructed information so, considering that filter function has an impact, it seems normal to consider that this parameter will also change the quality of the functional image. The question tackled in this section is to see what the repercussions are on the angiographic images when the reconstruction is done with a Gaussian or a Hamming filter.

For this purpose, the same set of raw data has been filtered by a Gaussian and a Hamming filter before being processed using the cMSI method. Both filters have been generated using LabVIEW software. The Hamming function associates the windowed array Y to an array X . If the array X is defined as $X = x_0, \dots, x_{n-1}$ where n is the number of elements of the array, the associated windowed element Y is for $i = 0, \dots, n - 1$:

$$y_i = x_i \left[0.54 - 0.46 \cos \left(\frac{2\pi i}{n} \right) \right] \quad (9)$$

The associated windowed Y array for the Gaussian filter follows the formula:

$$y_i = x_i e^{-\frac{(i-m)^2}{2(\sigma n)^2}} \quad (10)$$

where the coefficient $m = \frac{n-1}{2}$ acts to centre the filter for any length array and σ is the standard deviation of the Gaussian window.

The single tube phantom was used to evaluate how the ratio r between moving and static features is impacted. For this study the full bandwidth is used and r is calculated for the AD, SV and PDV methods as functions of the number of oversampling n with both filters. For this first study the value of the standard deviation used on the Gaussian filter is set at 2.

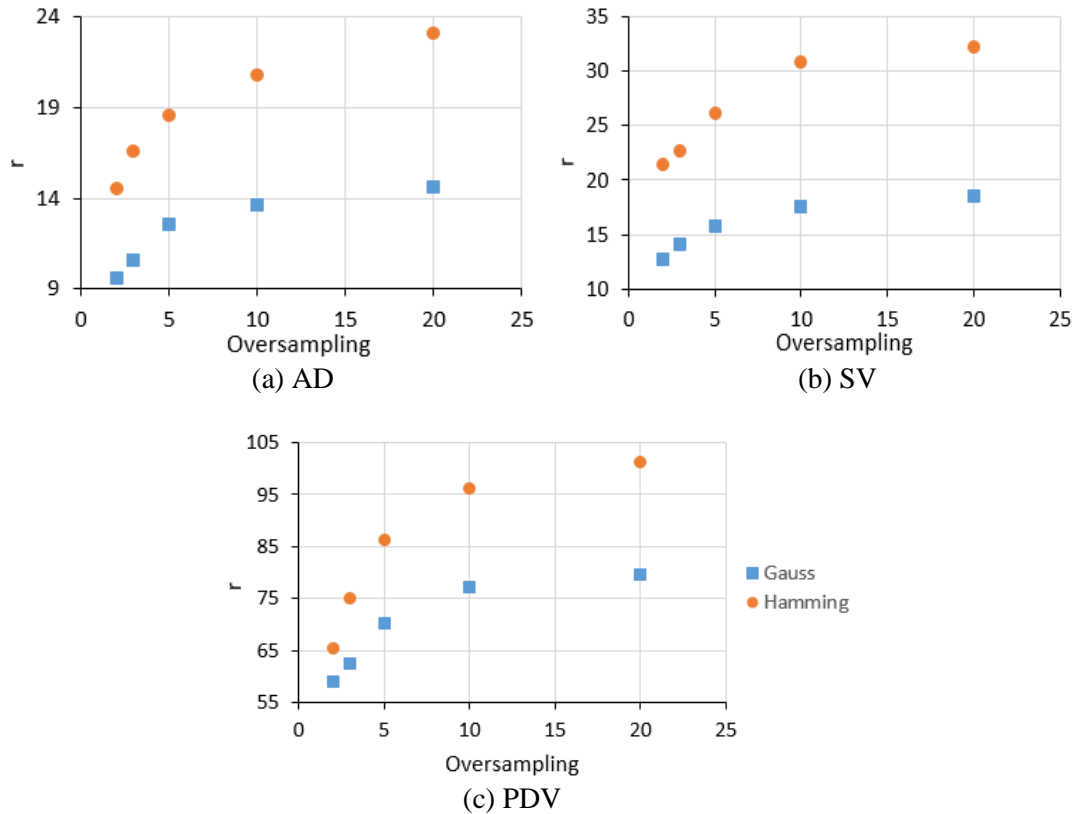


Fig.3.37. Gaussian vs Hamming filtering. Ratio between average angio-amplitudes of moving and static features, r as a function of the number of oversampling for Gaussian (blue points) and Hamming (orange points) filters on the different angiographic methods: (a) Amplitude Decorrelation, (b) Speckle Variance and (c) Phase Difference Amplitude.

Results are presented in Figure 3.37. It is clear that the filter applied on the raw, structural information has a direct impact on the quality of the functional images. Of the two windows applied, the ratio is highest for the Hamming filter, indicating that the distinction between moving and static features are better perceived. Figure 3.38 shows the various profiles for the Gaussian filter at different values of the standard deviation compared to the Hamming filter. For $\sigma = 2$, the bandwidth of the filter is much larger and so nearly no amplitude value is filtered as seen in Fig. 3.41(a). On the

other hand, the Hamming function has a narrower bandwidth, which restricts the spectrum and cuts the edges where the low amplitude modulations occur (Fig.3.41(d)). It is over this part of the modulation that the signal is the most unstable making the image noisier.

However, the FT of a Gaussian shape is another Gaussian whereas for the Hamming filter the resulting signal presents sidelobes on each side of the main peak. Gaussian windowing should therefore give the best resulting image.

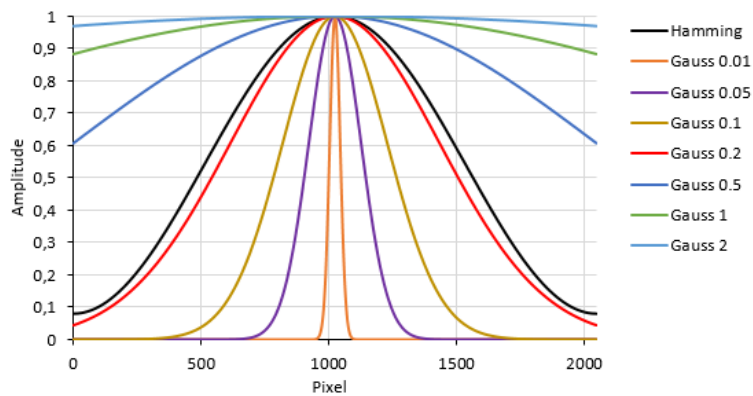


Fig.3.38. Window profiles for different filter configurations. Hamming filter and Gaussian filter for several different standard deviations (0.01, 0.05, 0.1, 0.2, 0.5, 1 and 2) using the equation (10)

To verify this assumption, the ratio r is calculated for the different window functions presented in Figure 3.38. The Gaussian window functions have been plotted for several standard deviations, σ equal to 0.01, 0.05, 0.1, 0.2, 0.5, 1 and 2. The Hamming function is also displayed on the same graph for comparison. The smaller the standard deviation σ , the narrower the bandwidth covered by the filter. Therefore, a Gaussian window with a smaller standard deviation is more selective than a larger one. The different values of the ratio r for different σ values are presented in Figure 3.39 as a function of the oversampling number n .

Before any further explanation of the results, it should be noted that in Figure 3.37 the three methods show the same trend on the impact of the window function used on the ratio r . It is for this reason that the result from the AD method are displayed for clarity in Figure 3.39 and 3.40. As usually done with the AD method, a threshold is still

applied to the intensity values before any angio-amplitude calculations but also another one on the angio-amplitude itself.

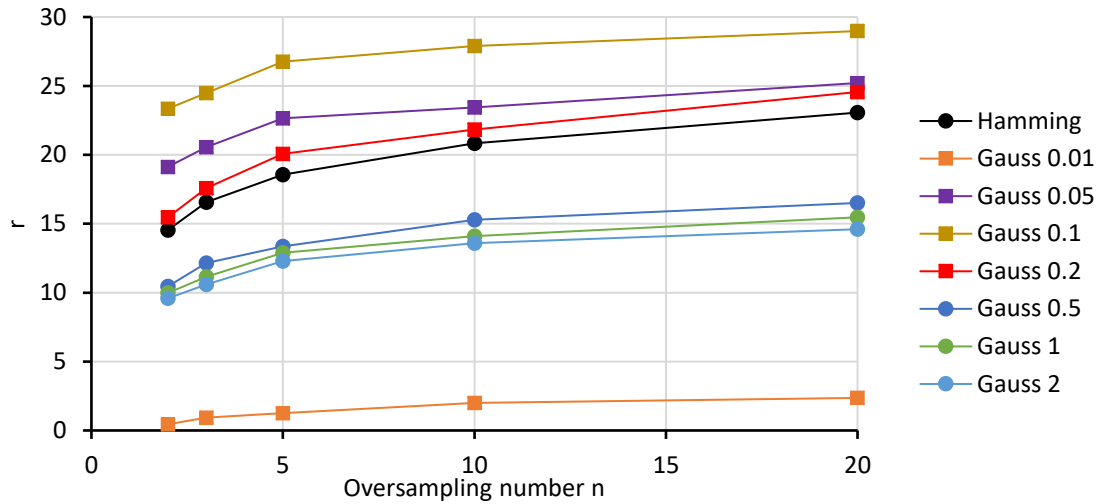


Fig.3.39. Ratio between the average value of the moving pixels over the static pixels for the different window shapes (Fig.3.41) using the Amplitude Decorrelation method.

For larger standard deviations, i.e. when $\sigma \geq 0.5$, the ratios calculated for the Gaussian windows are worse than when using the Hamming function. As explained earlier and as shown in Figure 3.38 and 3.41.(a), the window function has such a large bandwidth that it has barely any impact on the raw spectrum. Unstable modulations present at the edges of the raw spectrum are still taken into account in the calculation, making the image noisier. This can be observed in Figure 3.40(a), (d) and (g). The structural image (Fig.3.40(g)) is noisier than the one displayed for $\sigma = 0.2$ and 0.1 in Figure 3.40(h) and 3.40(i) respectively. However, it is not really affecting the visualisation of the structural features. In the case of the functional image (Fig.3.40 (a)), the distinction between static and moving features is compromised by the remaining high angio-amplitudes for static pixels (attributed to noise). This can be observed in Figure 3.40(d) where the angio-amplitude profiles are displayed for all depths. Angio-amplitudes from moving pixels are as high as the other parts of the image.

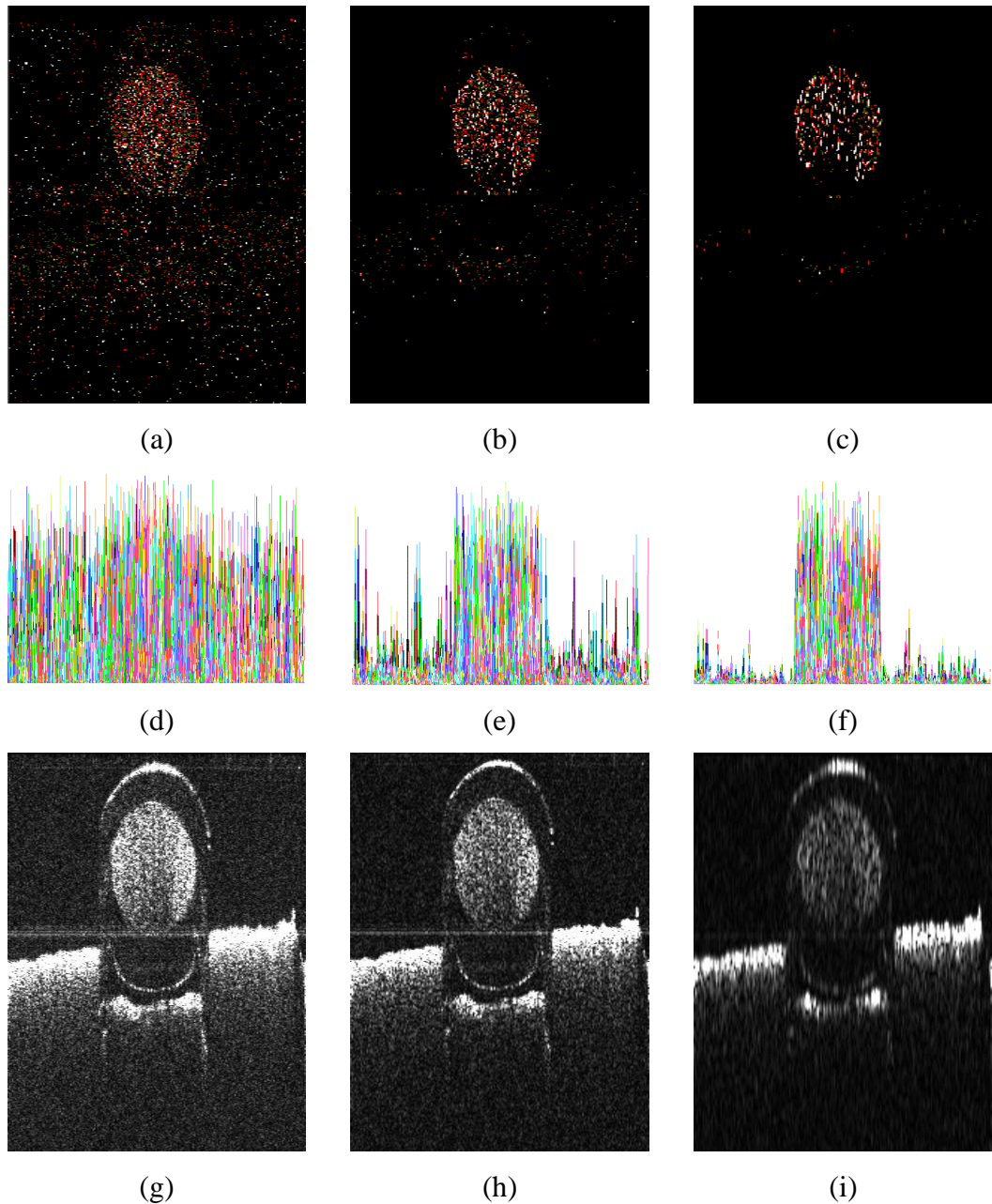


Fig.3.40. Comparison of the functional and structural images for Gaussian window with different standard deviation values. The first column (a, d and g) is for a standard deviation equal to 2, the second is 0.2 and the third is 0.1. (a), (b) and (c) are Angiographic images for the different standard deviations. The same colour scale has been used in the three images in the range from 0.1 to 0.4. (d), (e) and (f) are the Angio-amplitudes from the AD method as a function of the transversal pixel positions for all depths. (g), (h) and (i) are the structural images created from the raw spectrum windowed by the Gaussian filter with a standard deviation equal to 2, 0.2 and 0.1 respectively.

It is not the same situation for the smallest values of σ . The ratio is better in the case of $\sigma = 0.2, 0.1, 0.05$ with a maximum performance for $\sigma = 0.1$ compared with the Hamming function. However, if σ is too small, the ratio drops, which is the case when the ratio curve for $\sigma = 0.01$ in Figure 3.39. The trend can be interpreted by looking at Figure 3.38, 3.39 and 3.41. When σ is small, the data will be filtered by cutting the edge of the spectrum (Fig.3.41 (b)). The image is less noisy (Fig.3.40 (i)) but the axial resolution is impaired by the reduction of the spectral bandwidth and some of the information is not recovered in the structural and angiographic images. It is important to maintain a high resolution and therefore the window function used from now on, in all the calculations, is the Gaussian function with $\sigma = 0.2$. Indeed, the figure 3.40(h) shows that the structural image is less blurry, even if there is a reduction of the bandwidth (as shown in Fig. 3.41) and on the functional image (Fig.3.40 (b) and (e)), the distinction from moving to static pixel is possible.

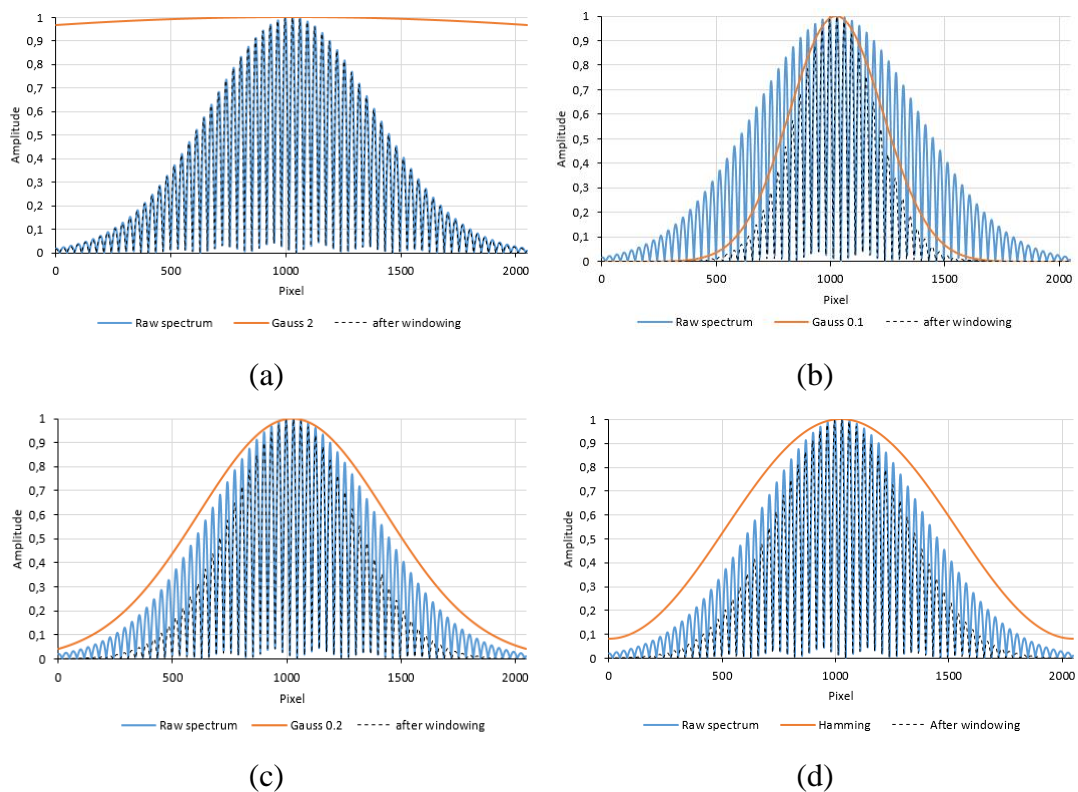


Fig.3.41. Raw spectrum, filter function and windowed spectrum. Amplitude as a function of the pixel position showing the raw channelled spectrum (blue curve), the filter function (orange curve): Gaussian filter with a standard deviation equal to 2 (a), 0.1 (b) and 0.2 (c) and Hamming filter (d) and their associated windowed output spectrum (black dashed curve).

To conclude, the angiographic images are made from the successive structural frames. Post-processing steps to reconstruct the image plays an important role in the recovery of information from the moving features within the sample. Before calculating the A-scan profile extracted from the signal modulations with the FT or cMSI method, parameters such as gain, normalisation or windowing can be applied on the raw data to improve the image quality. In this section, the question of how the windowing function affects the visualisation of moving features and the distinction of them over the static features has been tackled. It can be concluded that the best performance was observed using a Gaussian function with a standard deviation equal to 0.2 even if the ratio introduced earlier is better for $\sigma = 0.1$.

3.4.D Conclusion

Threshold on the amplitude values, oversampling number, number of splits, windowing function on the raw spectra and angio-amplitude scale of the functional image are all variables that must be taken into account while the angiographic image is processed. They cannot just be maximised and minimised to enhance the visualisation because of their impact on the other features of the system such as the time acquisition or axial resolution. A trade-off needs to be found to balance between the detection of low amplitudes from flow pixel / noise, noise reduction / acquisition time, axial resolution / number of division and low angio-amplitude from moving parts/ high angio-amplitude from static ones. While the parameters to reconstruct the angio-amplitude from the flow are important, it can be observed that structural parameters also have a strong repercussion on the distinction between moving and static features. The choice of the windowing function is one of them and has an impact on the amount of flow information recovered vs the noise. The Gaussian window with a standard deviation equal to 0.1 shows the best result from the point of flow reconstruction. However, the reduction of the bandwidth impacts the quality of the structural image and therefore, the Gaussian function with a standard deviation equal to 0.2 is chosen rather than that with $\sigma = 0.1$.

3.5. Angiographic Volume – Scanning procedure

The last section is about scanning procedures used to image the sample. The scanning procedure plays a key role in the distinction of moving from static features. In all the previous sections, the images were taken at the same transversal position i.e. without any scanning along the slow axis. This option is not realistic but was chosen to be able to statically study the angio-amplitudes extracted from SV, AD and PDV methods as a function of the object inclination and flow speed. However, when using a sample and not a phantom, it is preferable to render a full volume scan, which complicates the acquisition data process for case of functional analysis. As said before, the comparison is between two or several successive images. It is essential that the images are taken at the same location or at least in the same area from the point of view of the transversal optical resolution. The following is a description of the different parameters involved and the procedures used in order to ensure the images are taken at the same location. Two control signals are applied to the galvanometer scanners and studied: a ramp and a step signal. Firstly though, it is important to establish the difference between the concept of transverse optical resolution and digital resolution along the slow axis.

3.5.A Transverse optical resolution (Δy) vs Digital resolution (D_R) along the slow axis.

Before going any further, it is important to understand which entities are used and along which dimensions. While scanning the sample to create the full volume along both axes, the fast scanning axis is defined as the one that gives a full B-scan, which is along the “x” axis (Fig.3.42(b) black dash line). The slow scanning for building the full volume proceeds along the “y” axis. It is the scanning procedure along the slow axis that matters for angiographic imaging. More specifically, it is the distance between two successive points along the red dashed line (Fig 3.42(b)). The two dimensions along the y axis (slow axis) defined and used here are the Transverse optical resolution (Δy) and the Digital resolution (D_R).

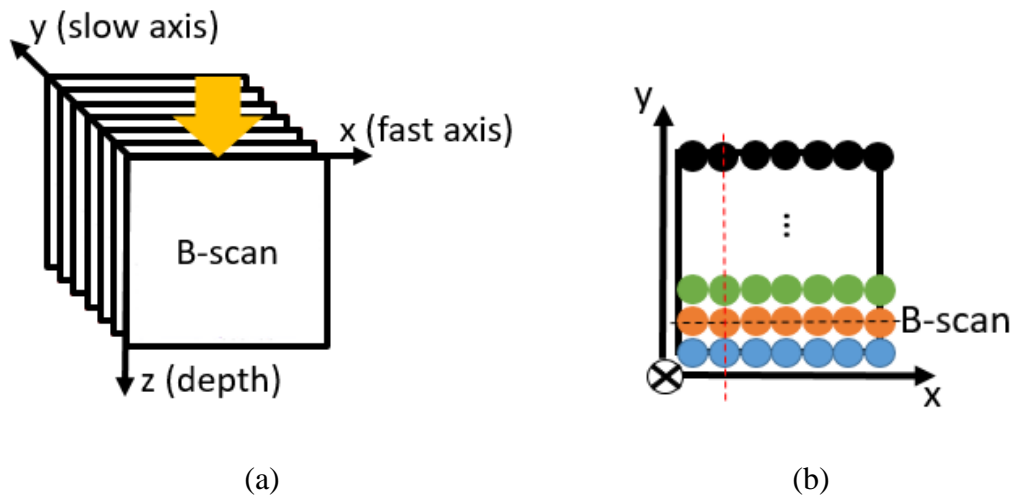


Fig.3.42 Fast vs Slow axis. (a) volume representation showing the different dimension. The light beam is indicated by the yellow arrow. The x (fast scanning axis) and z (depth) axis make up the B-scan images. By using the slow axis, a volume is created. (b) Top view from the volume (a). Each circle represents the light beam while the fast scanner is working. The same dots colour is used as if they are part of the same B-scan image. The black dash line shows the direction of B-scan image. It is along the red dash line that entities are from in this section.

The sample is illuminated using flying spot illumination. In the assumption of small astigmatism, the spot light is a dot and so the transverse optical resolution is isotropic in both directions along the fast and slow axes i.e. $\Delta x = \Delta y$. As previously mentioned in Chapter 2, Δx is linked with the central wavelength (λ_0), the focal length of the objective (f) and the diameter of the light beam D, as Δy . On the assumption that the beam propagates in air, the refractive index is equal to 1 and Δy is defined as:

$$\Delta y = \frac{1.22 \times \lambda_0 \times f}{D}$$

This parameter does not depend on the scanning procedure and only depends upon the optical performance of the system.

As with the transverse resolution, there are two different digital resolutions involved in the imaging procedure; one along the fast axis and the other along the slow axis. In this section, only the digital resolution (D_R) along the slow axis is tackled, being the resolution important to determine the sufficient number of oversampling to retrieve the flow information. The digital resolution D_R can be defined as the distance between two successively acquired B-scan images. It depends on the voltage applied to the galvanometer scanners (GS) and the number of data points used along the y axis.

Having the value of the digital resolution for each parameter (number of points and the voltage applied) of the GS is really important to establish a volumetric angiographic protocol that will respect the Nyquist-Shannon sampling condition. The signal from the GS is a discrete signal rather than continuous. At the end of the acquisition, the optical beam needs to have covered all the size of the sample and extracted all information from every resolvable point without any discontinuity. The Nyquist-Shannon sampling theorem establishes a rule on the sample frequency to be able to correctly sample a continuous signal, by producing a discrete succession of digital values.

To respect this condition, the digital resolution D_R is required to be smaller than half of the transverse optical resolution, Δy . This ensures that two or more successive images are practically acquired from the same position. In this way, they are not completely decorrelated and roughly imaging the same part of the sample. This is explained further in figure 3.43.

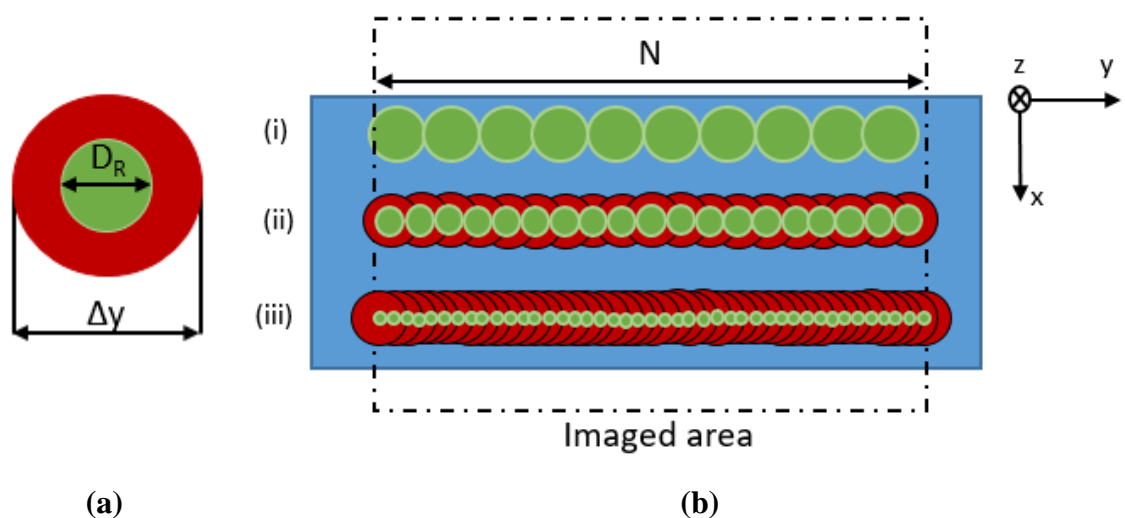


Fig.3.43 Digital Resolution (D_R) vs Transverse resolution (Δy) along the slow axis. The red circles represent the transverse resolution Δy and the green circles are the digital resolution D_R . (a) To respect the Nyquist condition, D_R needs to be at least two times smaller than Δy . (b) scanning procedure along the slow axis (y -axis) in the case of $\Delta y = D_R$ (i), $\Delta y = 2D_R$ (ii) and $\Delta y \gg D_R$ (iii).

In the case (i), the digital resolution is equal to the transverse resolution along the slow axis (green and red dots are superposed, $\Delta y = D_R$). The position of the two successive

B-scan images (minimum number to run the angiographic calculation) are optically too far apart to be considered at the same position. When $\Delta y = 2D_R$ (case (ii)), there is an overlap between two successive points (superposition of some parts of the red dots). The area is quite small and the angiographic calculation can only be run between two frames. If now, $\Delta y \gg D_R$, the overlap area is larger making it possible to consider more frames to obtain the angio-amplitudes at each point.

The experimental transverse resolution in the setup used is equal to $14 \mu\text{m}$ so, D_R needs to be at least $7 \mu\text{m}$. Figure 3.44 shows the evolution of digital resolution as a function of the number of points used to scan the sample. The dash/dots black horizontal line represents the case where the digital resolution is equal to $7 \mu\text{m}$. Any point below this curve respects the Nyquist Shannon condition. For example, by looking at figure 3.44 and by fixing the number of points in the transversal plane along the slow axis to 200, the amplitude voltage needs to be less than or equal to 0.2V .

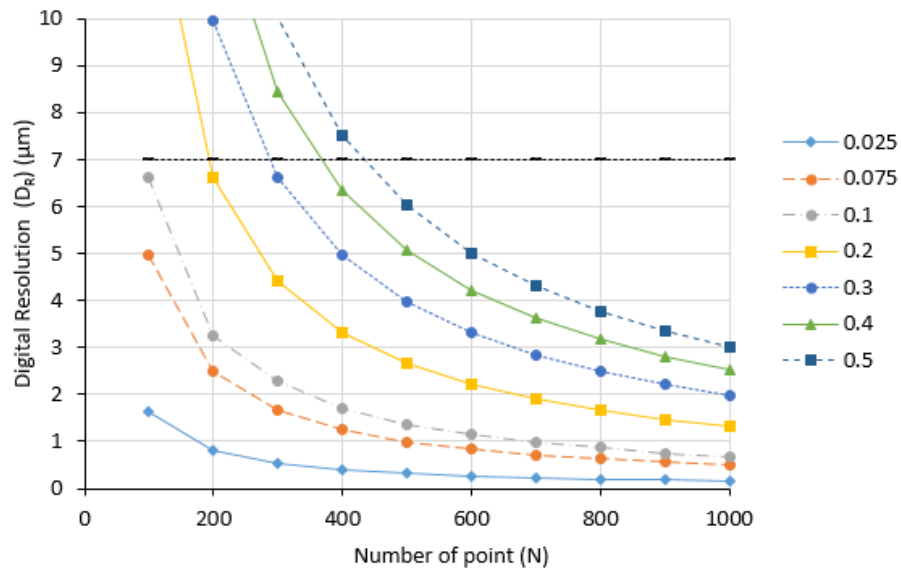


Fig.3.44. Digital resolution as a function of the transverse number of points along the slow axis (y axis) for different GS voltage amplitudes. Black dash line is $\Delta y = 7 \mu\text{m}$

3.5.B Ramp signal control

The first signal uses the ramp function and is the easiest to implement. The protocol stays the same as in the case of the creation of a structural 3D image but including

more points to oversample each position. It presents the advantage of not stopping the GS and so, reduces the chance of having any spatial discontinuity in the acquisition of the image.

For this particular signal, the Nyquist-Shannon sampling condition needs to be strictly respected. If not, the images used in the angiographic calculation are not spatially at the same place and present high angio-amplitudes even on static features. The phantom with two tubes was imaged. For this part only, the second tube is empty and used as extra static features. One hundred images were taken on the slow axis and each B-scans is 200 x 512 pixels (number of points along the fast axis x number of points along the depth). The angiographic calculations were performed over two successive images. The number of angiographic images is equal to 99 for AD and SV and 98 for PDV.

In Figure 3.45, three different GS amplitudes along the slow axis are used to scan the sample and create the 3D array. To compare the different cases, a GS voltage amplitude was set above the theoretical value found in the previous section and two others were set below the theoretical value, at 0.2V, 0.1V and 0.075V respectively.

The first conclusion drawn is that the Nyquist-Shannon sampling condition needs to be respected to recover the flow information correctly. By using a value higher than the limit value, static features are highlighted as much as the moving parts of the image. It is impossible to distinguish clearly between them as can be seen in Figure 3.45(a). The wall of the tube or the cardboard presents angio-amplitude values as high as the flow. If a threshold is applied, nearly all the flow information is lost.

The Nyquist-Shannon sampling condition is respected by setting the GS voltage equal to 0.1V in the case of using 100 points along the slow axis. Nevertheless, it can be observed from the experiment that static features are still highlighted in the functional images. The separation of moving from static pixels is not possible presenting angio-amplitudes that are too high, even after applying a threshold.

It is for voltages below 0.075V that the spatial distance between two successive points in the scanning process is small enough to be considered at the same optical position. For this voltage amplitude (Fig.3.45(c) and (f)), a clear distinction is possible and, by applying a threshold on the angio-amplitude, static features are set to 0 on the final

functional image. The ratio between Δy and D_R , to distinguish between moving and static features, is then around 5 and not 2 as used earlier in this section.

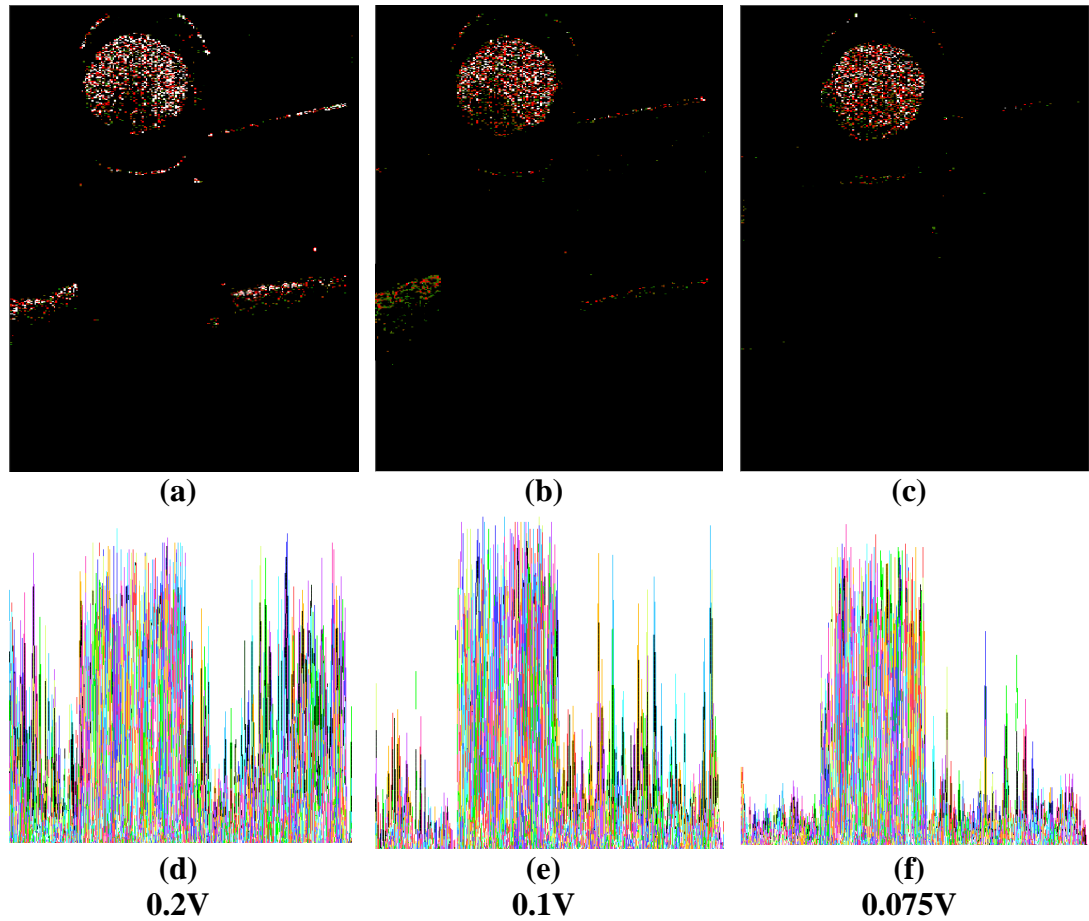


Fig.3.45 Angiographic images with a ramp signal applied to GS equal to 0.2V, 0.1V and 0.07V along the slow axis. A threshold was applied on the intensity value prior to the calculation to remove the pixels considered to be noise. (a), (b) and (c) are the angiographic frames calculated with the AD method. The values are scaled between 0.1 and 0.4. (d), (e) and (f) are the transverse profiles. Each horizontal line in the images (a), (b) and (c) is displayed as a function of the angio-amplitudes. The amplitude scale is between 0 and 1.

By using 100 points, the size of the sample scanned in the transverse dimension (y axis) is around 0.5 mm for a GS voltage equal to 0.075V. This is too small for the reconstruction of functional features such as the detection of vessels. One solution is to increase the number of points taken along the slow axis. With the system parameters used here, the voltage needs to be around 0.5V to scan the sample over 3 mm. Using the graph in Fig.3.44, the total number of acquisition points N needs to be at least 500 points if the calculation is run over just 2 frames. In most cases, the number of

oversampling n is around 4 and the total amount of points is larger than $500 \times n$. For example, if $n = 4$, the number of points required needs to be over 1000. Increasing the number of points has the disadvantage of making the acquisition time longer and therefore increasing the deleterious effect of movement in images acquired in-vivo.

Another solution is to change the scanning protocol by using a stair function to generate the GS signal. Generation of such a signal is more difficult but it ensures that several successive images are taken at the same position.

3.5.C Stair signal control

In the case of a stair signal control, the GS determines scanning along the slow direction by stopping at each Y position to acquire several images (Fig.3.46). Nothing else is changed on the B-scan parameters. The acquisition time to acquire a B-scan image stays the same. The only change is in the time interval that the optical beam sits at the same Y position. The amplitude of the stair signal is given by the voltage applied on the GS along the slow axis. In Figure 3.46, T_n is the time taken to produce n B-scan images. It is equal to n times the acquisition time for a single B-scan. T_N is the total acquisition time to produce the full volume and can be expressed as $T_N = N \times T_n$.

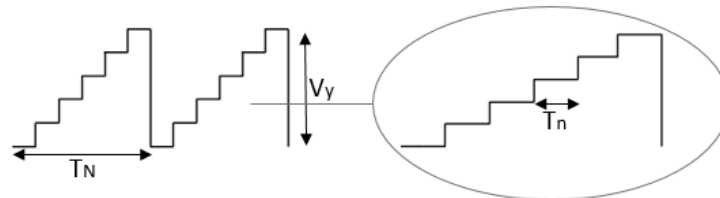


Fig.3.46 Stair signal. T_N is the acquisition time for the full acquisition volume with N B-scans along the fast axis and T_n is the time for the n images at the same spatial position.

The distinction between static and moving features is the same as in the case of the disabled slow axis, reported in the previous sections. There is no limitation on the voltage applied in order to have it. However, to generate an image presenting no discontinuity, it is essential to respect the Nyquist-Shannon condition (Fig.3.46). If the spatial position between two successive points given by the digital resolution is larger than the optical resolution (Fig.3.46 (a)), the sample is subsampled. If the digital resolution D_R is equal to the optical resolution Δy (green and red dots are superposed,

Fig.3.46 (b)), the image is not properly rebuilt and information is lost. To operate with the right sampling rate, the Nyquist-Shannon sampling condition has to be respected (Fig.3.46 (c)).

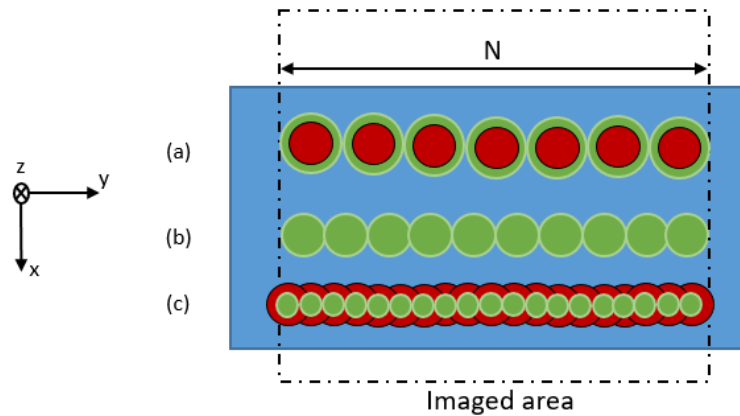
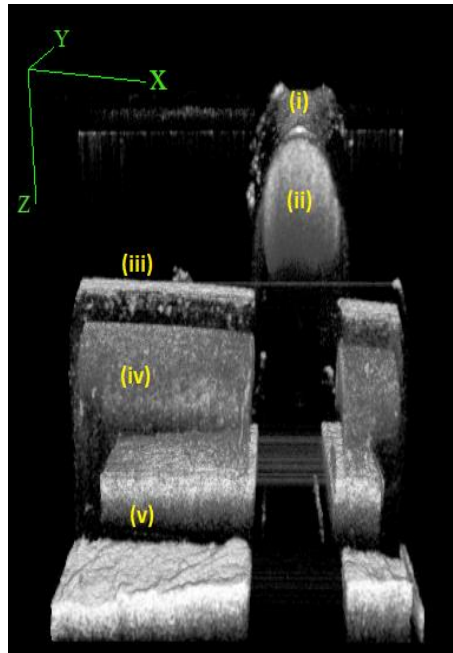


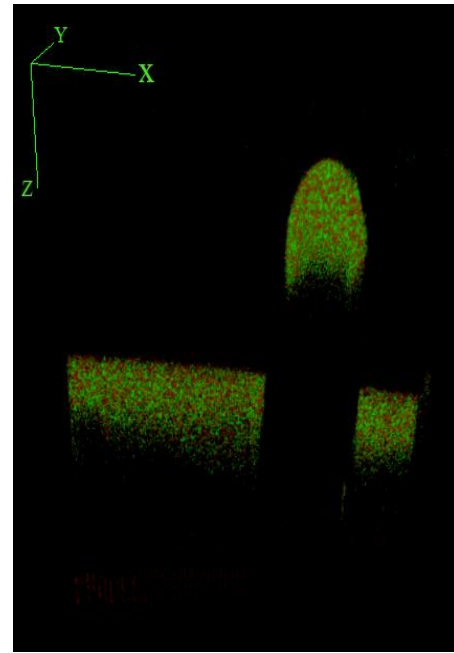
Fig.3.46 D_R vs Δy in the case of the stair signal. Sampling rate needs to be sufficient to cover all the parts of the sample (a) $\Delta y < D_R$, the spatial position between two successive points are too far away and the sample is subsampled, (b) $\Delta y = D_R$ limit case, (c) $\Delta y = 2D_R$, the sample scanning rate respects the Nyquist-Shannon sampling condition.

Once the digital resolution is set to respect the Nyquist-Shannon sampling condition, the volume acquisition of the sample can be carried out. To examine more features, a two-tube phantom attached to a piece of cardboard has been imaged. At each position, n B-scan images are rebuilt, where the total number of B-scan images is equal to 400. At each Y position of the stairs, 4 B-scan images are taken. The number of positions along the slow axis is so equal to 100.

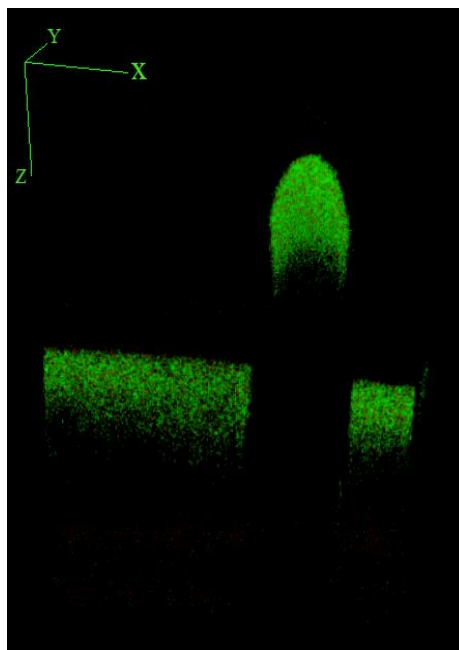
To obtain the structural volume (Fig.3.47 (a)), the n images (equal to 4) are averaged to give a unique B-scan image at each location and repeated at each position along the slow axis (100 points). The angiographic volume is created from the structural oversampled volume. To create the angiographic images, the angio-amplitudes are calculated from the information extracted from each set of 4 structural B-scan images. A threshold on the intensity values from the structural images is selected for AD and PDV methods. Another threshold is also used to remove the last static pixels present in the functional images for all the methods (AD, SV and PDV).



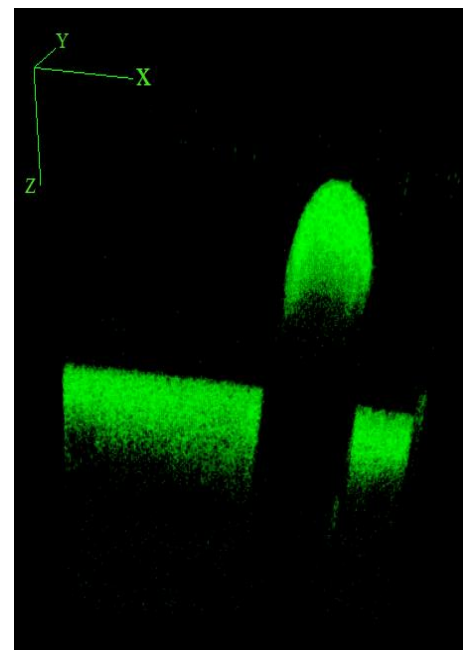
(a) structural volume



(b) PDV



(c) AD



(d) SV

Fig.3.48 3D angiographic volumes. The GS was controlled by a stair signal. (a) structural volume (i) first wall of tube 1, (ii) moving fluid, (iii) first wall of tube 2, (iv) liquid under Brownian motion in tube 2, (v) cardboard, (b), (c) and (d) angiographic volumes using PDV, AD and SV respectively. The voltage along the slow axis is equal to 0.4V.

From Figure 3.48 (b), (c) and (d), the flow information clearly appears on the functional images for the 3 methods and the distinction between static and moving features is possible. The wall of the tubes and the cardboard are not present in any of the functional 3D reconstructions making the scanning protocol valid. The stair signal has the advantage of distinguishing static from moving features independently, whether or not the Nyquist-Shannon condition is respected. The only risk is to miss information if the sample is subsampled. In this case, the 3D reconstruction will not contain all the information from the sample, even if the detection of the flow area in the B-scan plane is conserved. This is even more problematic in the case of *enface* visualisation of the moving area. For example, in the case of the tube, the flow line is not continuous and a dashed line is drawn. To avoid this, the Nyquist-Shannon sampling condition needs to be respected, $\Delta y = 2 \times D_R$. In other words, the number of points used to image the sample must be equal to twice the ratio between the distance covered along the slow axis and the transverse resolution.

3.5.D Conclusion

The functional volume cannot be created from any structural volume. The scanning protocol must be adapted to ensure that the frames, where the calculation is run, are optically at the same location. Here, two scanning signals have been considered to be applied to the GS. The first, the ramp signal, is the most straightforward to create an angiographic volume from the structural volume. The GS signal is not changed from the structural to functional volume and it is just the number of acquisition points that is increased to ensure to have an oversampled volume along the slow axis. The digital resolution D_R needs to be carefully chosen by comparing it to the optical transverse resolution Δy . It has been shown that working at the limit of the Nyquist-Shannon sampling condition is not enough and that the D_R needs to be 5 time smaller than Δy . The time acquisition of a full volume is increased by a factor of 5 making the process too long to perform in-vivo imaging.

The other scanning protocol considered uses a stair signal. The GS along the Y axis is not working continuously, as in the ramp function, and stops at each transversal position to acquire several structural images. In this protocol, all B-scan images from

the same set are at the same spatial position. The performance of the angiographic methods (AD, SV and PDV) are identical to the case when the slow axis is disabled. It ensures the differentiation of the moving over the static features. In the case of cross-sectional visualisation, no further considerations need to be taken into account. However, if the observation of the moving features is in the transversal plane, it is important to keep the continuity of the enface images. In which case, the Nyquist-Shannon sampling condition needs to be respected and $\Delta y = 2D_R$. This protocol presents the advantage of requiring less acquisition of B-scan images however it is more complicated to implement and more time consuming by the use of a discontinuous signal.

3.6. Final Conclusion

Amplitude and phase-based software have been demonstrated and characterised in this chapter. Each method was able to separate flow from static features in the sample. Phase based methods (PD and PDV) and AD use a threshold on the structural intensity amplitude to discriminate the noise values from the rest of the image. To help separate the moving over static features, a second threshold is applied on all the methods, this time to kill the last static pixels showing a larger angio-amplitude. From the five methods explained at the beginning, the focus is on AD, PDV and SV techniques to know if they can be qualified as quantitative methods. For this purpose, an experiment using two different phantoms consisting of one or two rubber tubes fixed to cardboard has been carried out. 5% diluted, intralipid solution was flowing in one of the tubes with the help of a static pump. Even if there is undoubtedly a link between angio-amplitudes and speeds, a clear quantification, in the condition of our experiment, is not possible especially when some parameters, such as the relative position of the beam from the focal plane or the inclination of the sample, are taking into account. The replacement of intralipid solution by whole blood or a more complex and realistic sample or even in vivo measurements should be implemented before the generalisation of our conclusions.

Techniques allowing a better distinction of moving from stationary features are then introduced. The initial approach is to use averaging methods in the “time dimension”. The calculation is not run over 2 successive images but over 3 or more. All resultant angiographic images are averaged and a reduction of noise is observed leading to a better reconstruction of the flow information. However, this method requires the GS to image a particular location for a longer period of time or acquire a larger number of points along the slow axis, which is therefore more time consuming and also increases the chance of recording motion artefacts. Another approach is to use spatial averaging. The acquisition process stays the same as before and it is only the data processing that is changed. Each interference pattern from each depth is split into several spectrum window divisions. Each window is processed separately to create the angiographic images and then averaged over all sub-windows to create a unique frame at the end. The major issue is that the axial resolution is affected, making the detection of small features less achievable. It can also be noted that temporal averaging methods improve the angiographic image until a turning point where the evolution presents a plateau and the difference is not observed anymore. The choice of the number of oversampling n or windows w is a trade-off between reducing the noise and highlighting the moving and static feature versus keeping an acceptable acquisition time and axial resolution. Each angiographic image is the result of the comparison between successive structural images. The quality of the functional image is interlinked with the quality of the structural image. The axial and transverse resolution, as well as the imaging depth, will be the same or worse than on the structural images. Hardware performance is also important in the detection of the flow area as well as the parameters from the data processing, such as the type of filter being used, and has an impact on the quality of the angiographic images. In this chapter, we saw that the use of a Gaussian windowing with $\sigma=0.2$ is the best trade-off to match the best performance of the structural and functional images.

Lastly, two protocols to create angiographic volumes are explained. The GS control signal uses a ramp or a stair function. The scanning protocol, based on a ramp function, is the same as that used to produce a structural volume with the difference being that the number of points along the slow axis, N , is increased to have two successive frames optically at the same position. If N is too small, the angio-amplitudes from the static

pixels is large and the distinction between moving from static features is impossible. On the other hand, the stair signal stops at each position and therefore the process of detection of the flow area is exactly the same as in the case when the slow axis is disabled. Even if the value of N does not impact the performance of the detection of the flow, it needs to be carefully chosen to extract information from each resolved point in the transversal plane by keeping the GS signal continuous. To ensure the separation between moving and static features and the continuity between successive frames, the Nyquist-Shannon sampling condition has to be observed. The ratio between transverse and digital resolution is equal to 2 for the stair signal and 5 for the ramp.

In the next chapter, a direct application of the software developed is used to follow the evolution of the vitality of a bovine embryo. The software is not used to highlight flow areas but instead used to detect motion inside the embryo and add more information from the structural images about its ability to become a successful foetus.

References

- [1] Oxford Dictionary of English (2019). Motion [online] Available at: <https://en.oxforddictionaries.com/definition/motion> [Accessed 20 May 2019]
- [2] En.wiktionary.org. (2019). angiography - Wiktionary. [online] Available at: <https://en.wiktionary.org/wiki/angiography> [Accessed 20 May 2019].
- [3] En.wiktionary.org. (2019). angio - Wiktionary. [online] Available at: <https://en.wiktionary.org/wiki/angio> [Accessed 20 May 2019].
- [4] En.wiktionary.org. (2019). graphy - Wiktionary. [online] Available at: <https://en.wiktionary.org/wiki/graphy> [Accessed 20 May 2019].
- [5] U. Baran, and R.K. Wang, "Review of optical coherence tomography based angiography in neuroscience," *Neurophotonics* vol. 3,1 (2016): 010902. doi:10.1117/1.NPh.3.1.010902 (2016).
- [6] A.C.S. Tan, G.S. Tan, A.K. Denniston, P.A. Keane, M. Ang, D. Milea, U. Chakravarthy and C.M.G. Cheung, "An overview of the clinical applications of optical coherence tomography angiography." *Eye (London, England)* vol. 32,2 (2018): 262-286. doi:10.1038/eye.2017.181 (2018).
- [7] M. Ang, A.C.S. Tan, C.M.G. Cheung, P.A. Keane, R. Dolz-Marco, C.A.S. Chelvinet, and L. Schmetterer, "Optical coherence tomography angiography: a review of current and future clinical application," *Graefes Arch Clin Exp Ophthalmol* 256: 237 (2018).
- [8] A.H. Kashani, C.L. Chen, J.K. Gahm, F. Zheng, G.M. Richter, P.J. Rosenfeld, Y. Shi and R.K. Wang, "Optical coherence tomography angiography: A comprehensive review of current methods and clinical applications," *Prog Retin Eye Res.* (2017).
- [9] Blindness and vision impairment – World Health Organisation Available at: <https://www.who.int/news-room/fact-sheets/detail/blindness-and-visual-impairment> <http://www.who.int/blindness/causes/en/> [Assessed 30 May 2019].
- [10] R.P.A. Bourne, J.B. Jonas, S.R. Flaxman, J. Keeffe, J. Leasher, K. Naidoo, M.B. Parodi, K. Pesudovs, H. Price, R.A. White, T.Y. Wong, S. Resnikoff, and H.R. Taylor, "Prevalence and causes of vision loss in high-income countries and Eastern and Central Europe: 1990-2010," *British Journal of Ophthalmology* 98:629-638 (2014).

- [11] I. Kocur, and S. Resnikoff. "Visual impairment and blindness in Europe and their prevention," *The British journal of ophthalmology* vol. 86,7 (2002): 716-22. doi:10.1136/bjo.86.7.716 (2002).
- [12] E. Nikolopoulou, M. Lorusso, L. Micelli Ferrari, MV. Cicinelli, F. Bandello, G. Querques and T. Micelli Ferrari, "Optical Coherence Tomography Angiography versus Dye Angiography in Age-Related Macular Degeneration: Sensitivity and Specificity Analysis," *BioMed Research International*, vol. 2018, Article ID 6724818, (2018).
- [13] C.L. Chen and R.K. Wang, "Optical coherence tomography based angiography [Invited]," *Biomed. Opt. Express* 8, 1056-1082 (2017)
- [14] Z. Chen, T.E. Milner, S. Srinivas, X. Wang, A. Malekafzali, M.J. van Gemert and J.S. Nelson, "Noninvasive imaging of in vivo blood flow velocity using optical Doppler tomography," *Opt Lett.* 1997 Jul 15; 22(14):1119-21 (1997).
- [15] J.A. Izatt, M.D. Kulkarni, S. Yazdanfar, J.K. Barton and A.J. Welch, "In vivo bidirectional color Doppler flow imaging of picoliter blood volumes using optical coherence tomography," *Opt Lett.* 1997 Sep 15; 22(18):1439-41 (1997).
- [16] R.A. Leitgeb, R.M. Werkmeister, C. Blatter and L. Schmetterer, "Doppler optical coherence tomography," *Prog Retin Eye Res.* 2014 Jul; 41():26-43 (2014).
- [17] A. Zhang, Q. Zhang, C.L. Chen and R.K. Wang, "Methods and algorithms for optical coherence tomography-based angiography: a review and comparison," *J Biomed Opt.* 2015 Oct; 20(10):100901 (20115).
- [18] R. Leitgeb, L. Schmetterer, W. Drexler, A. Fercher, R. Zawadzki and T. Bajraszewski, « Real-time assessment of retinal blood flow with ultrafast acquisition by color Doppler Fourier domain optical coherence tomography," *Opt Express.* 2003 Nov 17; 11(23):3116-21 (2003).
- [19] J.G. Fujimoto and W. Drexler, "Optical Coherence Tomography: Technology and Applications," Chapter 21, Springer-Verlag, Berlin, Heidelberg (2008).
- [20] H.C. Hendargo, RP. McNabb, A.H. Dhalla, N. Shepherd, and J.A. Izatt, "Doppler velocity detection limitations in spectrometer-based versus swept-source optical coherence tomography," *Biomed. Opt. Express* 2, 2175-2188 (2011).

- [21] R.A. Leitgeb, R.M. Werkmeister, C. Blatter, and L. Schmetterer, "Doppler optical coherence tomography," *Progress in retinal and eye research*, 41(100), 26–43. (2014).
- [22] I. Gorczynska, J.V. Migacz, R.J. Zawadzki, A.G. Capps and J.S. Werner, "Comparison of amplitude-decorrelation, speckle-variance and phase-variance OCT angiography methods for imaging the human retina and choroid," *Biomed. Opt. Express* 7, 911-942 (2016).
- [23] M. Mahmud, D.W. Cadotte, David, B. Vuong, C. Sun, T. Luk, A. Mariampillai and V. Yang, "Review of speckle and phase variance optical coherence tomography to visualize microvascular networks," *Journal of biomedical optics*. 18. 50901. 10.1117/1.JBO.18.5.050901. (2013).
- [24] B. Hyle Park, M.C. Pierce, B. Cense, S.H. Yun, M. Mujat, G.J. Tearney, B.E. Bouma and J.F. de Boer, "Real-time fiber-based multi-functional spectral-domain optical coherence tomography at 1.3 μm ," *Opt. Express* 13, 3931-3944 (2005).
- [25] J. Fingler, D. Schwartz, C. Yang, and S.E. Fraser, "Mobility and transverse flow visualization using phase variance contrast with spectral domain optical coherence tomography," *Opt. Express* 15, 12636-12653 (2007).
- [26] J. Fingler, R.J. Zawadzki, J.S. Werner, D. Schwartz and S.E. Fraser, "Volumetric microvascular imaging of human retina using optical coherence tomography with a novel motion contrast technique," *Opt. Express* 17, 22190-22200 (2009).
- [27] D. Ruminski, B.L. Sikorski, D. Bukowska, M. Szkulmowski, K. Krawiec, G. Malukiewicz, L. Bieganowski and M. Wojtkowski, "OCT angiography by absolute intensity difference applied to normal and diseased human retinas," *Biomed. Opt. Express* 6, 2738-2754 (2015).
- [28] Y. Jia, O. Tan, J. Tokayer, B. Potsaid, Y. Wang, J.J. Liu, M.F. Kraus, H. Subhash, J.G. Fujimoto, J. Hornegger, and D. Huang, "Split-spectrum amplitude-decorrelation angiography with optical coherence tomography," *Opt. Express* 20, 4710-4725 (2012).
- [29] A. Mariampillai, B.A. Standish, E.H. Moriyama, M. Khurana, N.R. Munce, M.K.K. Leung, J. Jiang, A. Cable, B. C. Wilson, I.A. Vitkin, and V.X. D. Yang,

- "Speckle variance detection of microvasculature using swept-source optical coherence tomography," *Opt. Lett.* 33, 1530-1532 (2008).
- [30] A. Mariampillai, M.K.K. Leung, M. Jarvi, B.A. Standish, K. Lee, B.C. Wilson, A. Vitkin and V.X.D. Yang, "Optimized speckle variance OCT imaging of microvasculature," *Opt. Lett.* 35, 1257-1259 (2010).
- [31] K. Wang, S.L. Jacques, Z. Ma, S. Hurst, S.R. Hanson and A. Gruber, "Three-dimensional optical angiography," *Opt Express*. 2007 Apr 2; 15(7):4083-97 (2007).
- [32] R.K. Wang, L. An, P. Francis and D.J. Wilson, "Depth-resolved imaging of capillary networks in retina and choroid using ultrahigh sensitive optical microangiography," *Opt Lett*. 2010 May 1; 35(9):1467-9 (2010).
- [33] R.K. Wang, "Optical Microangiography: A Label Free 3D Imaging Technology to Visualize and Quantify Blood Circulations within Tissue Beds in vivo.," *IEEE J Sel Top Quantum Electron*. 2010 May; 16(3):545-554 (2010).
- [34] J. Zhu, C.W. Merkle, M.T. Bernucci, S.P. Chong and V.J. Srinivasan, "Can OCT Angiography Be Made a Quantitative Blood Measurement Tool?," *Appl Sci (Basel)*. 2017 Jul;7(7):687 (2017).
- [35] D. Kleinfeld, P.P. Mitra, F. Helmchen, and W. Denk, "Fluctuations and stimulus-induced changes in blood flow observed in individual capillaries in layers 2 through 4 of rat neocortex," *Proceedings of the National Academy of Sciences* Dec 1998, 95 (26) 15741-15746 (1998).
- [36] W.S. Kamoun, S.S. Chae, D.A. Lacorre, J.A. Tyrrell, M. Mitre, M.A. Gillissen, D. Fukumura, R.K. Jain and L.L. Munn, "Simultaneous measurement of RBC velocity, flux, hematocrit and shear rate in vascular networks," *Nature methods* vol. 7,8 (2010): 655-60 (2010).
- [37] C. Desjardins and B.R. Duling, "Microvessel hematocrit: Measurement and implications for capillary oxygen transport," *American Journal of Physiology-Heart and Circulatory Physiology* 1987 252:3, H494-H503 (1987).
- [38] T.P. Santisakultarm, N.R. Cornelius, N. Nishimura, A.I. Schafer, R.T. Silver, P.C. Doerschuk, W.L. Olbricht and C.B. Schaffer, "In vivo two-photon excited fluorescence microscopy reveals cardiac- and respiration-dependent pulsatile blood flow in cortical blood vessels in mice," *American journal of physiology. Heart and circulatory physiology* vol. 302,7 (2012): H1367-77 (2012).

- [39] D.J. Faber, M.C.G. Aalders, E.G. Mik, B.A. Hooper, M.J.C. van Gemert and T.G. van Leeuwen, "Oxygen saturation dependant absorption and scattering of blood," *Phys. Rev. Lett.* 93, 028102 (2004).
- [40] M.C. Meinke, G.J. Müller, J. Helfmann and M. Friebel, "Optical properties of platelets and blood plasma and their influence on the optical behavior of whole blood in the visible to near infrared wavelength range," *J. Biomed. Opt.* 12(1) 014024 (2007).
- [41] M. Friebel and M. Meinke, "Model function to calculate the refractive index of native hemoglobin in the wavelength range of 250-1100 nm dependent on concentration," *Appl. Opt.* 45, 2838-2842 (2006).
- [42] J. Vörös, "The density and refractive index of adsorbing protein layers," *Biophysical journal* vol. 87,1 (2004): 553-61 (2004).
- [43] M.C. Meinke, G.J. Müller, J. Helfmann and M. Friebel, "Optical properties of platelets and blood plasma and their influence on the optical behavior of whole blood in the visible to near infrared wavelength range," *J. Biomed. Opt.* 12(1) 014024 (2007).
- [44] O. Sydoruk, O. Zhernovaya, V. Tuchin and A. Douplik, "Refractive index of solutions of human hemoglobin from the near-infrared to the ultraviolet range: Kramers-Kronig analysis," *Journal of biomedical optics.* 17. 115002. 10.1117/1.JBO.17.11.115002. (2012).
- [45] N. Bosschaart, G.J. Edelman, M.C. Aalders, T.G. van Leeuwen and D.J. Faber, "A literature review and novel theoretical approach on the optical properties of whole blood," *Lasers Med Sci.* 2014;29(2):453–479 (2014).
- [46] A.N. Yaroslavsky, I.V. Yaroslavsky, T. Goldbach and H.J. Schwarzmaier, "Optical properties of blood in the near-infrared spectral range," *Proc. SPIE* 2678, *Optical Diagnostics of Living Cells and Biofluids* (1996).
- [47] J.D. Briers, "Laser doppler, speckle and related technique for blood perfusion mapping and imaging," *Physiological Measurement*, Volume 22, Number 4 (2001).
- [48] J. David Briers, "Laser Doppler and time-varying speckle: a reconciliation," *J. Opt. Soc. Am. A* 13, 345-350 (1996).

- [49] J.D. Rigden and E.I. Gordon, "The granularity of scattered optical maser light," Proc. IRE, 2367-2368.
- [50] J.M. Schmitt, S.H. Xiang and K. Man Yung, "Speckle in optical coherence tomography: an overview," Proc. SPIE 3726, Saratov Fall Meeting '98: Light Scattering Technologies for Mechanics, Biomedicine, and Material Science (1999).
- [51] D. Briers, "Laser Speckle Contrast Imaging for Measuring Blood Flow," Optica Applicata. 37 (2007).
- [52] M.D. Stern, "In vivo evaluation of microcirculation by coherent light scattering," Nature. 254. 56-8. 10.1038/254056a0 (1975).
- [53] J. Goodman, "Statistical Properties of Laser Speckle Patterns. Laser Speckle and Related Phenomena," 9. 57. 10.1007/BFb0111436 (1963).
- [54] B.S. Everitt and A. Skrdal, "The Cambridge dictionary of statistics," Fourth edition, Cambridge University Press (2010).
- [55] J. Tokayer, Y. Jia, A.H. Dhalla, and D. Huang, "Blood flow velocity quantification using split-spectrum amplitude-decorrelation angiography with optical coherence tomography," Biomed. Opt. Express 4, 1909-1924 (2013).
- [56] W.J. Choi, W. Qin, C.L. Chen, J. Wang, Q. Zhang, X. Yang, X., B.Z. Gao and R.K. Wang, "Characterizing relationship between optical microangiography signals and capillary flow using microfluidic channels," Biomedical optics express, 7(7), 2709–2728 (2016).
- [57] J.P. Su, R. Chandwani, S.S. Gao, A.D. Pechauer, M. Zhang, J. Wang, Y. Jia, D. Huang and G. Liu, "Calibration of optical coherence tomography angiography with a microfluidic chip," Journal of biomedical optics, 21(8), 86015 (2016).
- [58] C.E. Riva and L. Schmetterer, "Microcirculation of the ocular fundus," in Comprehensive Physiology, Wiley-Blackwell, pp. 735–765 (2011)
- [59] T.J. Fallon, P. Chowienczyk and E.M. Kohner, "Measurement of retinal blood flow in diabetes by the bluelight entoptic phenomenon," Br. J. Ophthalmol. 70(1), 43–46 (1986).
- [60] V. Doblhoff-Dier, L. Schmetterer, W. Vilser, G. Garhöfer, M. Gröschl, R.A. Leitgeb, and R. M. Werkmeister. Measurement of the total retinal blood flow using dual beam Fourier-domain Doppler optical coherence tomography with

- orthogonal detection planes. *Biomedical Optics Express*, 5(2):630–642, (2014).
- [61] G. Aschinger, R. M. Werkmeister, V. Doblhoff-Dier, R. Leitgeb, G. Garhöfer, M. Gröschl, and L. Schmetterer, "Blood flow velocity vector field reconstruction from dual-beam bidirectional Doppler OCT measurements in retinal veins," *Biomed. Opt. Express* 6, 1599-1615 (2015).
- [62] G. Liu, A.J. Lin, B.J. Tromberg and Z.A. Chen, "Comparison of Doppler optical coherence tomography methods," *Biomed Opt Express*. 2012 Oct 1;3(10):2669-80. doi: 10.1364/BOE.3.002669. Epub 2012 Sep 26. PMID: 23082305; PMCID: PMC3469988,
- [63] W.J. Choi, W. Qin, C.L. Chen, J. Wang, Q. Zhang, X. Yang, B.Z. Gao and R.Z. Wang, "Characterizing relationship between optical microangiography signals and capillary flow using microfluidic channels," *Biomed Opt Express*. 2016 Jun 20;7(7):2709-28. doi: 10.1364/BOE.7.002709. PMID: 27446700; PMCID: PMC4948624.].
- [64] J. Tokayer, Y. Jia, A.H. Dhalla and D. Huang, "Blood flow velocity quantification using split-spectrum amplitude-decorrelation angiography with optical coherence tomography," *Biomed Opt Express*. 2013 Sep 3;4(10):1909-24. doi: 10.1364/BOE.4.001909. PMID: 24156053; PMCID: PMC3799655
- [65] J.P. Su, R. Chandwani, S.S. Gao, A.D. Pechauer, M. Zhang, J. Wang, Y. Jia, D. Huang and G. Liu, "Calibration of optical coherence tomography angiography with a microfluidic chip," *J Biomed Opt*. 2016 Aug 1;21(8):86015. doi: 10.1117/1.JBO.21.8.086015. PMID: 27557344; PMCID: PMC4995373.
- [66] H.J. Lee, N.M. Samiudin, T.G. Lee, I. Doh and S.W. Lee "Retina phantom for the evaluation of optical coherence tomography angiography based on microfluidic channels," *Biomed Opt Express*. 2019;10(11):5535-5548. Published 2019 Oct 3. doi:10.1364/BOE.10.005535
- [67] R. Haindl, W. Trasischker, A. Wartak, B. Baumann, M Pircher and C.K. Hitzenberger, "Total retinal blood flow measurement by three beam Doppler optical coherence tomography," *Biomed Opt Express*. 2016;7(2):287–301.
- [68] C.J. Pournaras and C.E. Riva, "Retinal blood flow evaluation," *Ophthalmologica*. 2013;229(2):61–74.

- [69] A. Harris, H.S. Chung, T.A. Ciulla and L. Kagemann, "Progress in measurement of ocular blood flow and relevance to our understanding of glaucoma and age-related macular degeneration," *Prog Retin Eye Res.* 1999;18(5):669–87.
- [70] A. Harris, L. Kagemann, R. Ehrlich, C. Rospigliosi, D. Moore and B. Siesky, "Measuring and interpreting ocular blood flow and metabolism in glaucoma," *Can J Ophthalmol.* 2008;43(3):328–36.
- [71] J. Flammer, S. Orgül, V.P. Costa, N. Orzalesi, G.K. Krieglstein, L.M. Serra, J.P. Renard and E. Stefánsson, "The impact of ocular blood flow in glaucoma," *Prog Retin Eye Res.* 2002;21(4):359–93.
- [72] T. Nakazawa, "Ocular blood flow and influencing factors for glaucoma," *Asia Pac J Ophthalmol (Phila).* 2016;5(1):38–44.
- [73] L. Schmetterer and M. Wolzt, "Ocular blood flow and associated functional deviations in diabetic retinopathy," *Diabetologia.* 1999;42(4):387–405.
- [74] D.S. Ting, G.C. Cheung and T.Y. Wong, "Diabetic retinopathy: global prevalence, major risk factors, screening practices and public health challenges: a review," *Clin Experiment Ophthalmol.* 2016;44(4):260–77.
-

Chapter 4

OCTA for depth resolved assessment of the viability of bovine embryos – A case study

Author's note: The work in this paper was a collaboration between the Applied Optics Group (AOG) and the School of Bioscience from the University of Kent. Several embryos were fertilized by Dr. Silvestri to run this study. The image acquisition and the analysis of the data was carried out by myself using the OCT system build by Dr. Cernat.

As mentioned in chapters 2 and 3, OCT is a non-invasive, structural and functional imaging modality. To characterize the evolution of the 7-days embryo, the observation was conducted during a short (10min) and a long (18hrs) period on several embryos. Structural and functional images were used to assess its viability. The depth information was retrieved using the cMSI method explained in Chapter 2, section 2.3.

Structural imaging

After positioning the blastocyst in the sample arm of the OCT system, the number of masks was selected to cover the full embryo depth. To follow the evolution of the sample in real time, 9 direct enface images from different depths were displayed by the software (Fig.4). By analysing the data afterwards with Dr. Silvestri, the different structural entities were identified. Visualisation of the inner structures at each depth and of the 3D shape reconstruction of the blastocyst was achieved. From the structural information collected over the long period, the embryo collapsed during the 12th hour, and was considered to be “dead”. In addition to the structural images, functional imaging was carried out by producing motion maps.

Functional imaging

Functional imaging was done by displaying motion maps which highlight the portion of the embryo in motion (Fig.7). From Chapter 3, three methods could be employed; Speckle Variance (SV), Amplitude Decorrelation (AD) and Phase Variance (PV). The SV method was chosen over AD and PV because the intensities from the structural enface images are not homogeneous, which makes it impossible to set a unique threshold for the whole embryo (Fig.4). Applying a threshold is desirable since the blastocyst is kept in a synthetic ovarian fluid and was therefore subjected to Brownian motion. Compared with AD and PV, SV only needs a threshold applied to the angio-amplitudes. The threshold applied on the intensity prior to the angio-amplitude calculation is not necessary. This can be explained by the fact that in SV method, the angio-amplitude is a function of the amplitude values, and so the difference between noise and other part of the images in amplitude is large enough to have a discrimination between the angio-amplitudes of the noise and moving features. The threshold was set with reference to the average angio-amplitude values of several dead embryos, considered to be motionless, since these amplitudes were 5 time smaller than those seen from moving features.

From the angio-amplitudes of the motion maps, a quantity of movement value has been extracted over time and presented in Figure 8. It is defined as the summation of all angio-amplitudes from the motion map. From the motion maps and the quantity of movement taken over a long period, the presumed “death” of the blastocyst is declared after 18 hrs, which is when all the motion has stopped.

Speckle Variance OCT for depth resolved assessment of the viability of bovine embryos

S.Caujolle^{*,1,3,+}, R.Cernat^{1,+}, G.Silvestri^{2,+}, M.J.Marques¹, A.Bradu¹, T.Feuchter³, G.Robinson², D.K.Griffin², A.Podoleanu¹

¹ Applied Optics Group, School of Physical Sciences, University of Kent, Canterbury, CT2 7NH, UK

² School of Biosciences, University of Kent, Canterbury, CT2 7AF, UK

³ NKT Photonics A/S, Blokken 84, 3460 Birkerød, Zealand, Denmark

*smcc4@kent.ac.uk

+ contributed equally to this work.

Abstract: The morphology of embryos produced by *in vitro* fertilization (IVF) is commonly used to estimate their viability. However, imaging by standard microscopy is subjective and unable to assess the embryo on a cellular scale after compaction. Optical Coherence Tomography is an imaging technique that can produce a depth-resolved profile of a sample and can be coupled with Speckle Variance (SV) to detect motion on a micron scale. In this study, day 7 post-IVF bovine embryos were observed either short-term (10 minutes) or long-term (over 18 hours) and analyzed by swept source OCT and SV to resolve their depth profile and characterize micron-scale movements potentially associated with viability. The percentage of *en face* images showing movement at any given time was calculated as a method to detect the vital status of the embryo. This method could be used to measure the levels of damage sustained by an embryo, for example after cryopreservation, in a rapid and non-invasive way.

© 2017 Optical Society of America

OCIS codes: (110.4500) Optical coherence tomography; (170.1420) Biology; (110.4153) Motion estimation and optical flow; (170.3880) Medical and biological imaging; (030.6140) Speckle.

References

1. P. Holm, N. N. Shukri, G. Vajta, P. Booth, C. Bendixen and H. Callesen, "Developmental kinetics of the first cell cycles of bovine *in vitro* produced embryos in relation to their *in vitro* viability and sex," *Theriogenology*, **50**(8), 1285-1299 (1998).
2. I. Boiso, A. Veiga and R.G. Edwards, "Fundamentals of human embryonic growth *in vitro* and the selection of high-quality embryos for transfer," *Reprod. Biomed. online*, **5**(3), 328-350 (2002).
3. G.M. Lindner and R.W. Wright, "Bovine embryo morphology and evaluation," *Theriogenology*, **20**(4), 407-416 (1983).
4. A. Van Soom, B. Mateusen, J. Leroy, A. De Kruif, "Assessment of mammalian embryo quality: what can we learn from embryo morphology?" *Reprod. Biomed. online*, **7**(6), 664-670, (2003).
5. G.A. Bo and R. J. Mapletoft, "Evaluation and classification of bovine embryos" *Anim. Reprod.*, **10**(3) 344-348, (2013).
6. M. Alikani, J. Cohen, G. Tomkin, G.J. Garrisi, C. Mack and R.T. Scott "Human embryo fragmentation *in vitro* and its implications for pregnancy and implantation," *Fertil. Steril.*, **71**(5), 836-842, (1999).
7. T. Somfai, Y. Inaba, Y. Aikawa, M. Ohtake, S. Kobayashi, K. Konishi and K. Imai, "Relationship between the length of cell cycles, cleavage pattern and developmental competence in bovine embryos generated by *in vitro* fertilization or parthenogenesis," *J. Reprod. Develop.*, **56**(2), 200-207, (2010).
8. C. Racowsky, P. Kovacs and W.P. Martins, "A critical appraisal of time-lapse imaging for embryo selection: where are we and where do we need to go?" *J. Assist. Reprod. Gen.*, **32**(7), 1025 (2015).
9. M.R. Hee, C.A. Puliafito, C. Wong, J.S. Duker, E. Reichel, J.S. Schuman, E.A. Swanson and J.G. Fujimoto, "Optical coherence tomography of macular holes," *Ophthalmology*, **102**(5), 748-756, (1995).
10. D. Ruminiski, B.L. Sikorski, D. Bukowska, M. Szkulmowski, K. Krawiec, G. Malukiewicz, L. Bieganowski and M. Wojtkowski, "OCT angiography by absolute intensity difference applied to normal and diseased human retinas," *Biomed. Opt. Express*, **6**(8) (2015).
11. A. Federici, H.S. Gutierrez da Costa, J. Ogien, A.K. Ellerbee and A. Dubois, "Wide-field, full-field optical coherence microscopy for high axial-resolution phase and amplitude imaging," *Appl. Optics*, **54**(27) (2015).
12. I. Górczyska, J.V. Migacz, R.J. Zawadzki, A.G. Capps and J.S. Werner, "Comparison of amplitude-decorrelation, speckle variance and phase-variance OCT angiography methods for imaging the human retina and choroid," *Biomed. Opt. Express*, **7**(3) (2016).
13. M.S. Mahmud, D.W. Cadotte, B. Vuong, C. Sun, T.W. Luk, A. Mariampillai and V.X. Yang, "Review of speckle and phase variance optical coherence tomography to visualize microvascular networks," *J. Biomed. Opt.*, **18**(5) (2013).
14. A. Mariampillai, M.K.K. Leung, M. Jarvi, B.A. Standish, K. Lee, B.C. Wilson, A. Vitkin and V.X.D. Yang, "Optimized speckle variance OCT imaging of microvasculature," *Opt. Lett.*, **35**(8), (2010).
15. Y. Huang, Q. Zhang, M.R. Thorell, L. An, M.K. Durbin, M. Laron, U. Sharma, G. Gregori, P.J. Rosenfeld and R.K. Wang, "Swept-source OCT angiography of the retinal vasculature using intensity differentiation-based optical microangiography algorithms," *OSLI Retina*, **45**(5), 382-389, (2014).
16. W. Drexler, U. Morgner, F.X. Kärtner, C. Pitris, S.A. Boppart, X.D. Li, E.P. Ippen, and J.G. Fujimoto, "In vivo ultrahigh-resolution optical coherence tomography," *Opt. Lett.*, **24**(17), 1221-1223, (1999).

17. I.V. Larina, K. Furushima, M.E. Dickinson, R.R. Behringer and K.V. Larin, "Live imaging of rat embryos with Doppler swept-source optical coherence tomography," *J. Biomed. Opt.*, **14**(5), (2009).
18. K. Karnowski, A. Ajduk, B. Wieloch, S. Tamborski, K. Krawiec, M. Wojtkowski and M. Szkulmowski, "Optical coherence microscopy as a novel, non-invasive method for the 4D live imaging of early mammalian embryos," *Scientific Reports*, **7**, 4165, (2017).
19. J.G. Zheng, D. Lu, T. Chen, C. Wang, N. Tian, F. Zhao, T. Huo, N. Zhang, D. Chen, W. Ma, J.L. Sun and P. Xue, "Label-free subcellular 3D live imaging of preimplantation mouse embryos with full-field optical coherence tomography," *J. Biomed. Opt.*, **17**(7), (2012).
20. P. Holm, P.J. Booth, M.H. Schmidt, T. Greve and H. Callesen, "High bovine blastocyst development in a static *in vitro* production system using SOFa medium supplemented with sodium citrate and myo-inositol with or without serum-proteins," *Theriogenology*, **52**(4), 683-700 (1999).
21. R. Cernat, A. Bradu, N. Møller Israelsen, O. Bang, S. Rivet, P.A. Keane, D.G. Heath, R. Rajendram and A. Podoleanu, "Gabor fusion master slave optical coherence tomography," *Biomed. Opt. Express*, **8**(2), 813-827 (2017).
22. A. Podoleanu and A. Bradu, "Master-slave interferometry for parallel spectral domain interferometry sensing and versatile 3D optical coherence tomography," *Opt. Express*, **21**(16), (2013).
23. S. Rivet, M. Maria, A. Bradu, T. Feuchter, L. Leick and A. Podoleanu, "Complex master slave interferometry," *Opt. Express*, **24**(3), 2885, (2016).
24. I.V. Larina, S. Ivers, S. Syed, M.E. Dickinson and K.V. Larin, "Hemodynamic measurements from individual blood cells in early mammalian embryos with Doppler swept source OCT," *Opt. Lett.*, **34**(7), 986-988 (2009).
25. N. Sudheendran, S.H. Syed, M.E. Dickinson, I.V. Larina and K.V. Larin, "Speckle variance OCT imaging of the vasculature in live mammalian embryos," *Laser Phys. Lett.*, **8**(3), 247(2011).
26. K.S. Richter, D.C. Harris, S.T. Daneshmand and B.S. Shapiro, "Quantitative grading of a human blastocyst: optimal inner cell mass size and shape," *Fertil. Steril.* **76**(6), 1157-116 (2001).
27. A. Van Soom, M.T. Ysebaert and A. De Kruif, "Relationship between timing of development, morula morphology, and cell allocation to inner cell mass and trophectoderm in *in vitro*-produced bovine embryos," *Mol. Reprod. Dev.* **47**(1), 47-56 (1997).
28. A.H. Handyside and S. Hunter, "A rapid procedure for visualising the inner cell mass and trophectoderm nuclei of mouse blastocysts *in situ* using polynucleotide-specific fluorochromes." *J. Exp. Zool. A.* **231**(3), 429-434 (1984).
29. G. A. Thouas, N.A. Korfiatis, A.J. French, G.M. Jones and A.O. Trounson, "Simplified technique for differential staining of inner cell mass and trophectoderm cells of mouse and bovine blastocysts." *Reprod. Biomed. Onl.* **3**(1), 25-19 (2001).
30. K. Hardy, A.H. Handyside and R.M. Winston, "The human blastocyst: cell number, death and allocation during late preimplantation development *in vitro*," *Development* **107**(3), 597-604 (1989).
31. H. Stinshoff, S. Wilkening, A. Hanstedt, K. Brünig and C. Wrenzycki, "Cryopreservation affects the quality of *in vitro* produced bovine embryos at the molecular level," *Theriogenology*, **76**(8), 1433-1441(2011).
32. L. Zarnescu, M. Abeyta, T.M. Baer, B. Behr and A.K. Ellerbee, "Assessment of imaging parameters correlated with the effects of cryopreservation on embryo development," *Optical Methods in Developmental Biology II, Proc. SPIE 8953*, 89530F (2014).
33. L. Zarnescu, M.C. Leung, M. Abeyta, H. Sudkamp, T. Baer, B. Behr, A.K. Ellerbee, "Label-free characterization of vitrification-induced morphology changes in single-cell embryos with full-field optical coherence tomography," *J. Biomed. Opt.* **20**(9), 096004-096004 (2015).

1. Introduction

After fertilization, mammalian zygotes undertake a series of rapid mitotic divisions known as cleavage events which bring them from the original 1 cell to 16-32 cells. In cattle, this phase has a duration of approximately 4 days, after which the embryo undergoes the process of compaction during which it appears as a tight cluster of cells with hardly any distinguishable inter-cellular borders. Between day 6 and 7 after fertilization, as the embryo continues to grow, a liquid filled cavity develops, termed as blastocoel, whilst the embryo is referred to as the blastocyst. By the time the embryo reaches the blastocyst stage, its cells have formed two distinct populations: a thin outer layer known as trophectoderm and a compact cluster known as the inner cell mass [1]. A normal bovine blastocyst is presented in Fig. 1.

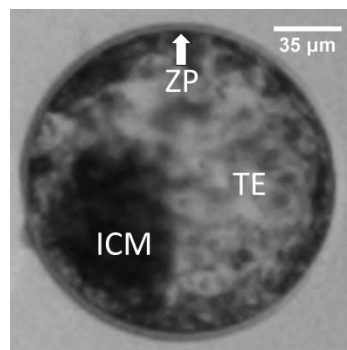


Fig. 1 A typical bovine blastocyst produced *in vitro* using the same method described under section 2.1. ICM: inner cell mass, TE: trophectoderm, ZP: zona pellucida. The embryo can be imagined as a liquid filled sphere. The ICM forms a discrete unit and is attached to the sphere's internal surface, while the surface itself is formed by the thin TE cell layer. Additionally, an outer

proteic shell, the ZP (arrow), encapsulates the whole embryo. The image was acquired by a Nikon Eclipse TE200 inverted modulation contrast microscope at x200 total magnification and by using an RI DC2 camera and its dedicated software RI Viewer.

In order to establish a pregnancy, bovine blastocysts produced by *in vitro* fertilization (IVF) are transferred into recipient animals, but the eligibility for transfer requires assessment of the viability of each candidate embryo. Evaluation of the embryo morphology, as a method to estimate its viability, has found wide use in human IVF [2] and the principle that the transfer of embryos of better morphology leads to higher pregnancy rates has long been validated in cattle [3]. One of the most substantial differences between human and bovine embryos, however, is that the latter are made opaque by the accumulation of lipid droplets in their cytoplasm, which makes the embryo harder to assess through conventional methods [4]. Commonly, bovine blastocysts produced by IVF are screened morphologically at x50 to x100 magnification using a stereomicroscope [5]. Whilst this level of investigation is simple and non-invasive, it is also highly subjective, gives little indication of intracellular activity [4], and is unable to quantify accurately the percentage of fragmentation (amount of sub-cellular, non-viable material) in the embryo which is known to affect its viability [6].

To support the morphological assessment of embryos and in an attempt to provide a better prediction of viability, time-lapse systems have been introduced [7]. Although widespread, the use of these systems has failed to produce obvious benefits due to the lack of a stringent correlation between the morphokinetic parameters measured and clinical pregnancy outcomes [8]. Time-lapse systems also present the disadvantages of a long time required to complete an assessment and of a poor depth of view. The second problem is made worse in post-compaction embryos like blastocysts and in bovine embryos generally due to their unfavourable lipid distribution [4]. An example of these limitations is given in Fig. 2, showing that protracted time-lapse observation is likely required to detect any changes in embryo morphology while at the same time, information on the different optical planes of the embryo is likely lost.

Therefore, there is scope for the development and application of new imaging modalities able to resolve the embryo structure in full depth and provide for a rapid and non-subjective assessment of viability.

Optical Coherence Tomography (OCT) is a non-invasive optical method developed in the 1990s that has historically found most applications in ophthalmology [9]. It can create structural images of biological tissues with high axial and transverse resolution providing cross-sectional 2D maps in the (x,z) or (y,z) planes (B-scans) and *en face* 2D maps in the (x,y) plane (C-scan), where x and y coordinates are measured along the lateral directions of the sample and z coordinate is measured along its depth.

Moreover, recent advancements have also allowed for the acquisition of functional images, one example being Optical Coherence Tomography Angiography (OCTA) which is used to differentiate moving blood cells from stationary features. The detection is possible due to algorithms like Speckle Variance (SV) analysis which can quantify the changes in the speckle pattern of a sample associated with movement [10-15].

OCT has already found some limited application in developmental biology in model organisms like *Xenopus laevis* [16], and *Rattus norvegicus* [17]. Recently, high-resolution intracellular imaging on live mouse and pig oocytes and embryos has been reported [18]. In this context, the fundamental advantages of OCT are its ability to image embryos without labels, and its use of low power light sources as compared to confocal systems. The use of low power optical beams reduces the chance of damaging the embryo during observation [18, 19]. However, no study so far has applied the motion detection principles of OCTA to early stage embryos, like blastocysts, to assess their viability.

In this study, an OCT system was used to produce a full depth structural characterization of a day 7 post IVF blastocyst and display its 3-D models. Moreover, to test whether kinetic differences could be measured between live and dead embryos, micron-scale movements were measured with the SV method to enable quantitative analysis of embryo viability over time.

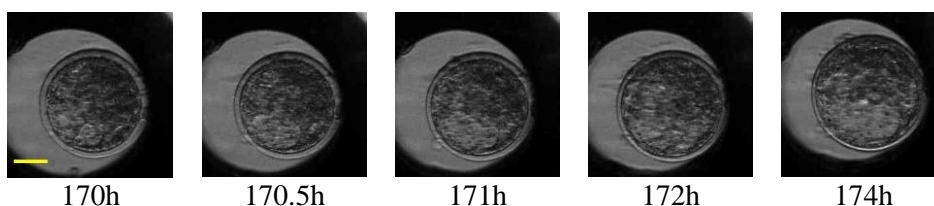


Fig. 2 Images of a day 7 bovine blastocyst at different time points after insemination. The images were acquired by phase contrast microscopy at x200 magnification using a time-lapse system PrimoVision Evo (Vitrolife). Completing a viability assessment is likely to require protracted observation as the general morphology of the embryo changes very little over time. Scale bar = 50 μm .

2. Materials and Methods

2.1 Preparation of bovine embryos

Bovine blastocysts were produced *in vitro* following a previously described method [20]. Briefly, oocytes were collected from abattoir material and *in vitro* matured, then fertilized with frozen/thawed sperm (Semex). The resulting embryos were then cultured in Synthetic Ovarian Fluid (SOF) medium droplets until they reached the blastocyst stage 7 days post-IVF. Five of the resulting blastocysts were monitored by OCT over short-term observation of several minutes whereas one embryo was monitored over long-term observation (exceeding 18 hours).

2.2 Set-up

The OCT system used is schematically presented in Fig. 3. A swept source at 1310 nm center wavelength (Axsun Technologies), 100 kHz sweep rate, 12 mm coherence length, 106 nm FWHM bandwidth in the range (1256.6 nm–1362.8 nm) [21] is used. The source is connected to a 2×2 fiber coupler (C1) with an 80:20 ratio which splits 80% of the power towards the reference arm and 20% towards the sample arm. In the sample arm, light is collimated through lens L1 and directed to a pair of galvanometer scanners which, via the imaging lens L2, scan the beam laterally in the (x,y) plane. Light from the reference and sample arms are combined in the 50:50 fiber coupler C2. The output ports from C2 are routed to a balanced photo-detector (Thorlabs Model PDB460C, DC 200 MHz). A 12-bit waveform digitizer (AlazarTech ATS9350 - 500 MS/s) digitizes the output signal which is processed using an “in-house” acquisition software written in LabVIEW (National Instruments). This software calculates 500 *en face* images from 500 depths and delivers a real-time compound display of two cross section OCT images, 9 *en face* OCT images and a summed voxel projection (SVP) image, all made possible due to the use of Master-Slave interferometry protocol [21, 22, 23]. The combined rendering of the 12 such images is updated every 0.8 s. The depth interval between the 9 selected depth positions is chosen to cover the axial range of the full embryo. Images are produced from 200x200 lateral pixels. The axial resolution was measured to be approximately 15 μm in air and the transverse resolution approximately 4.2 μm .

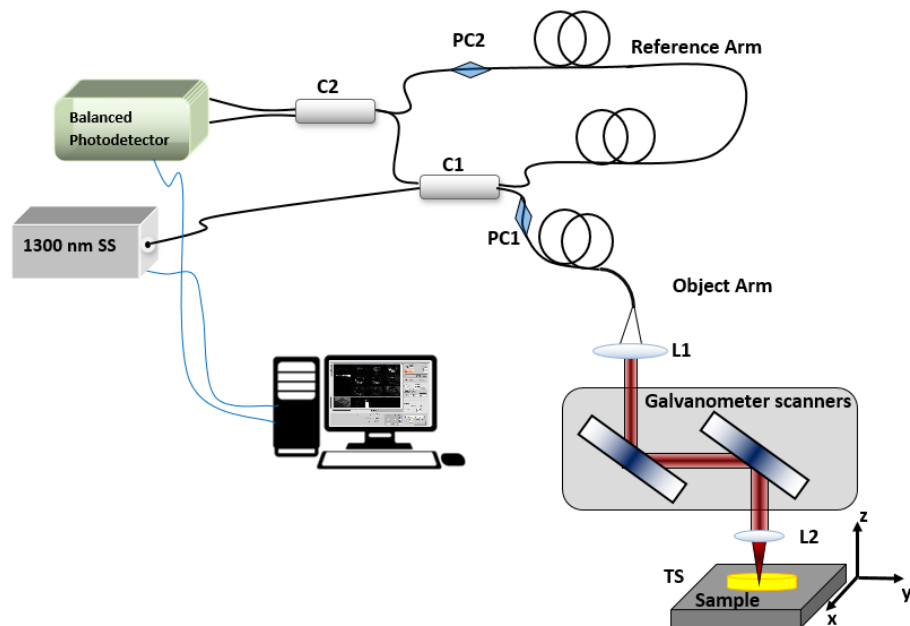


Fig. 3 OCT set-up. SS: swept source; C1, C2: directional optical couplers, PC1, PC2: polarization controllers, L1, L2: lenses, TS: x,y,z translation stage to position the sample.

2.3 Image acquisition and Speckle Variance (SV) analysis

The embryos are placed on a Petri dish. Then the dish is adjusted laterally and vertically, using the translation stage, TS, by monitoring the SVP image. Initially, the differential distance between the 9 *en face* images in the display is adjusted approximately based on an estimated embryo thickness. While monitoring the two cross section OCT images, the reference arm length is adjusted in order to position the cross sections of the embryos in their central region.

To characterize the structure and the progressive loss of viability of the embryos, cross section images and *en face* images were acquired over short and long-term observation. For short-term observation, 5 embryos were observed for 10 minutes and a full set of data was acquired every minute. For long-term observation, the embryo was observed until it ceased all motion (18 hours), acquiring a set of data every minute for 10 min followed by 20 min of rest; the no-motion measurement was confirmed by another observation performed after a further 8 hours. The SV analysis was performed as described before [10-14] on successive *en face* images at 1 min intervals. The Speckle Variance for each lateral pixel (j,k) is defined as:

$$SV(j, k) = \frac{1}{N} \sum_{i=1}^n \left(I(i, j, k) - \frac{1}{N} \sum_{i=1}^N I(i, j, k) \right)^2 \quad (1)$$

In (1), I is the strength of the OCT signal at each pixel, N is the total number of *en face* images considered for the calculation which in our case is N = 2 and the index i is the *en face* image concerned, respectively. The calculation was over j and k, i.e. over 200 by 200 pixels, leading to a 2D motion map of similar size. The lateral size of *en face* images is 230 μm by 230 μm. The SV values represent the variance calculated over two successive images with a time lapse equal to 1 min. The larger the variability, the larger the SV. A SV value equal to 0 means that images are identical and no motion is detected. To compensate the effects of Brownian motion, image sets from a dead embryo were also acquired and used to establish a minimum speckle variance value (threshold) for each pixel. In the final display of motion maps, all pixel values whose SV was below this threshold were assigned zero values. Moreover, to produce a quantitative assessment of motion, a parameter “quantity of movement” was calculated as the summation of all pixel values from the motion map.

3. Results

Overall, 5 live bovine blastocysts were observed for 10 minutes (short-term observation) and 1 bovine blastocyst was observed for over 18 hours (long-term observation). During the assessment, 12 structural images were displayed in real time in the form of SVP, 2 x cross sectional images and 9 x *en face* images. In Fig. 4, an example of the acquisition display is given.

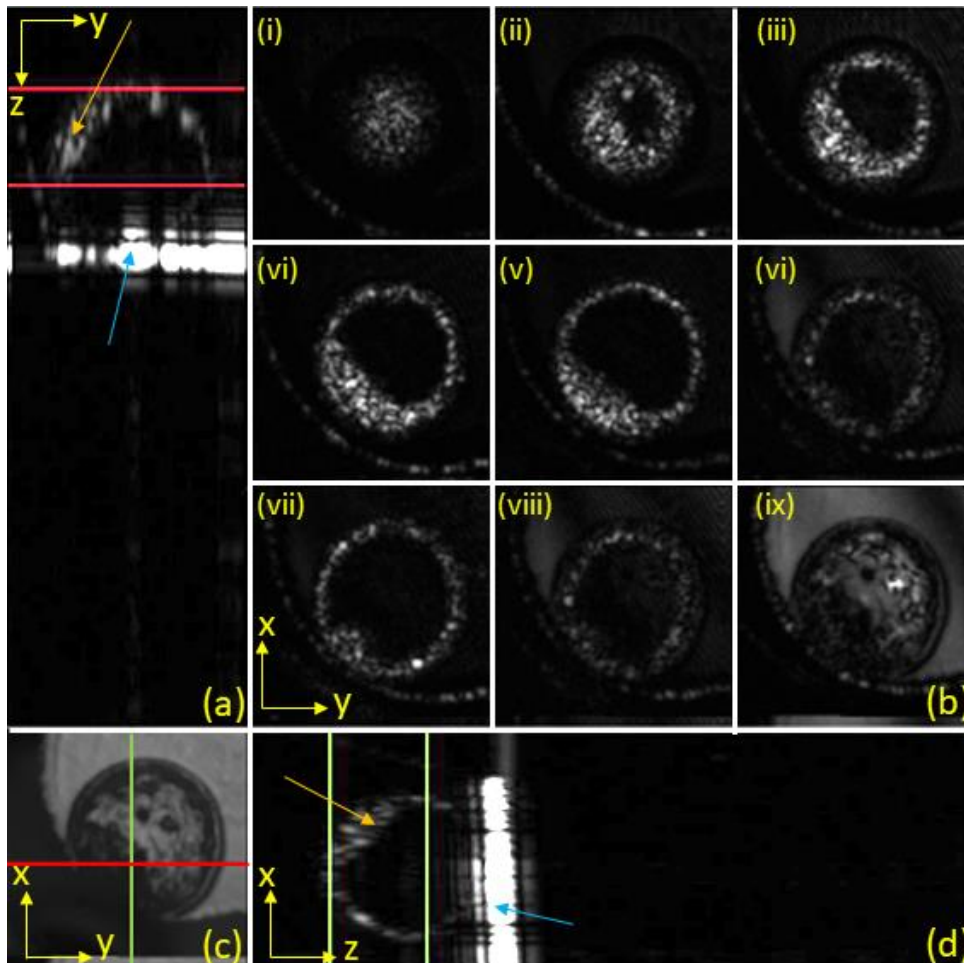


Fig. 4 Screen-shot of the “in-house” Master/Slave software used for image guidance. Three categories of images are displayed simultaneously and in real time in each raster: 2x cross section images, 9x *en face* images and a SVP. (a) Cross section along the red line (plane (z,y)) in the SVP image, (b) (i-ix) *en face* images, (c) SVP and (d) cross section image along the green line (plane (x,z)) in the SVP image. To cover the whole depth of the embryo, 9 *en face* images (i – ix) are shown over a total depth of 225 μm , separated by a depth interval of 25 μm (measured in air). All images are represented on a linear scale. Blue arrows indicate the glass plate and the orange arrow indicates the embryo shape. The lateral size of images is 230 μm and the axial range of the cross sections is 1 mm (measured in air).

3.1 Blastocyst 3D reconstruction and structural imaging

En face images were used to create a 3D volume of the embryo as shown in Fig. 5 and could be used to identify two separate structural entities forming a blastocyst, namely a ring of outer cells (trophoblast) and a discrete mass of cells in the inside (inner cell mass). The volume allowed by the “in-house” acquisition software written in LabVIEW software extends over a voxel size of 200x200x500 pixels.

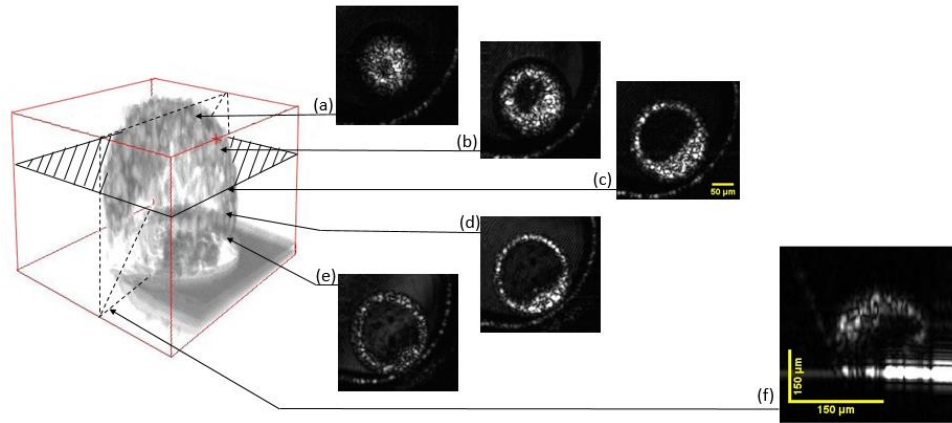


Fig. 5 3D display of a day 7-post *in vitro* fertilization bovine embryo. *En face* images at different depths from the top embryo surface (a) 25µm, (b) 75µm, (c) 150µm, (d) 225µm and (e) 300µm (all measured in air) at the beginning of the experiment, scale bar = 50µm. (f) cross section view over 500 µm in depth (measured in air), scale bar = 150 µm x 150 µm.

By varying the differential distance between the depths, the axial range was adjusted as such, that the embryo covers 300 depths. Therefore, the size of the volume displayed in Fig. 5 is 200x200x300. Moreover, the shape of the inner cell mass could be clearly distinguished in the 3D reconstruction potentially providing information on its compactness, size and distribution. As described in the introduction (and also in Fig. 2) a blastocyst stage embryo does not necessarily display large morphological changes over a time period of a few hours when observed by standard microscopy, but it can sometimes display a pulsating behavior whereby the embryo collapses on itself and then re-expands to its full size. In this analysis, the blastocyst appeared to maintain its normal structure over the first 12 h; however, by the 13th hour it started to collapse on itself. From this point on, a faint halo of the same size as the original embryo could be detected by OCT indicating that the blastocyst's zona pellucida maintained its shape and position while the rest of the embryo collapsed. Interestingly, the complete collapse of the blastocyst's inner cavity was observed between 15 and 16 h of culture and this detail would have been impossible to notice with standard microscopy. After this point, however, the embryo failed to re-expand, an observation consistent with an embryo approaching the end of its life. A selection of images acquired over long-term observation is given in Fig. 6 A, showing the first 18 h of culture and an additional image acquired 8 h after complete cessation of embryo motion.

3.2 Micron-scale movement detection by SV and quantity of movement calculation

The SV algorithm was applied to obtain motion maps at each embryo depth to highlight the portions of the embryos in motion during each 1 min interval considered. The analysis could also indicate when the embryo ceased all motion (Fig. 6B).

For the 5 embryos selected for the short-term observations, motion maps were calculated using *en face* images from a depth approximately in the middle of each embryo.

Figure 7 shows the maximum speckle variance registered in such maps. Usefully, the maximum value calculated for the dead control embryo was found to be at least 5 times smaller than the average maximum value of any live embryo.

For the next evaluations, a threshold was calculated to differentiate the live embryos from the dead one. This was obtained as the maximum SV extracted from the motion maps evaluated over the whole embryo volume.

In Fig. 8, quantity of movement was calculated at 5 different depths (as indicated) in the same embryo over long-term observation and it was possible to pinpoint at which depth the embryo maintained movement over time. The calculation included only those pixels out of the 200x200, where the SV exceeded the threshold evaluated above.

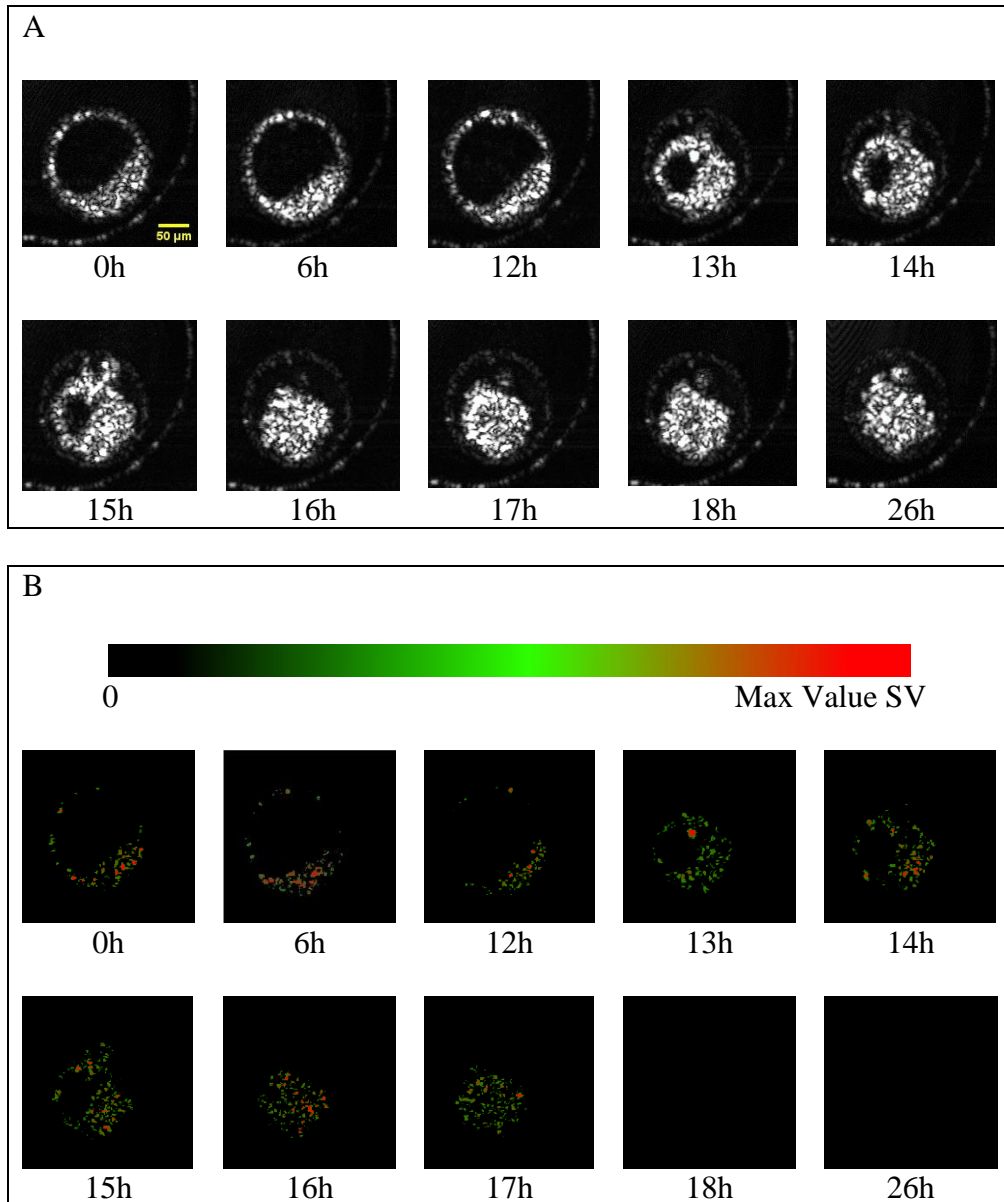


Fig. 6 *En face* images (A) of the embryo over 26 h (actively monitored over the first 18 h) and their SV *en face* display/Motion Map (B) at a fixed depth (150 μm from the top embryo surface measured in air). Scale bar = 50μm. SV value are displayed Red/Green scale. Red represents higher value.

An alternative representation of this information is given in Fig. 9, showing the percentage of *en face* images from the same embryo in which movement could be detected at any given time. The calculation was performed over 300 *en face* images obtained from different depths covering the embryo thickness (i.e. using the same adjustment of axial range as in Fig. 5).

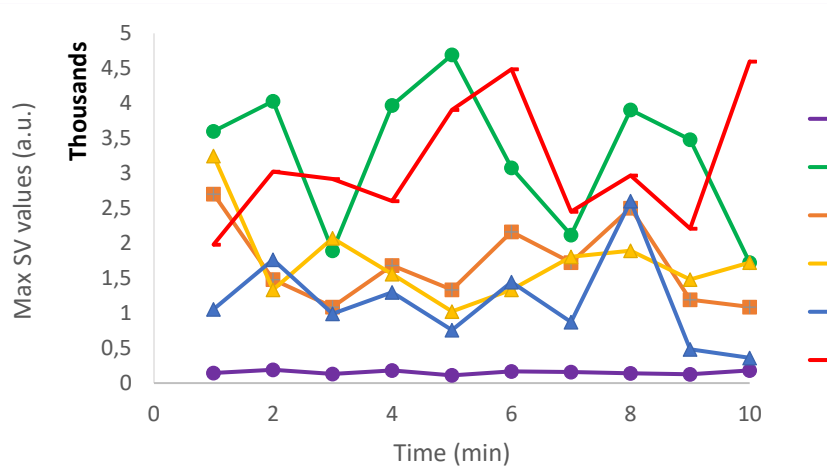


Fig. 7 Maximum value of the Speckle Variance for different embryos over 10 minutes. Embryo 1 – Embryo 5 (E1-E5): Curves representing the quantity of movement for live embryos, DE: Curve for dead embryo.

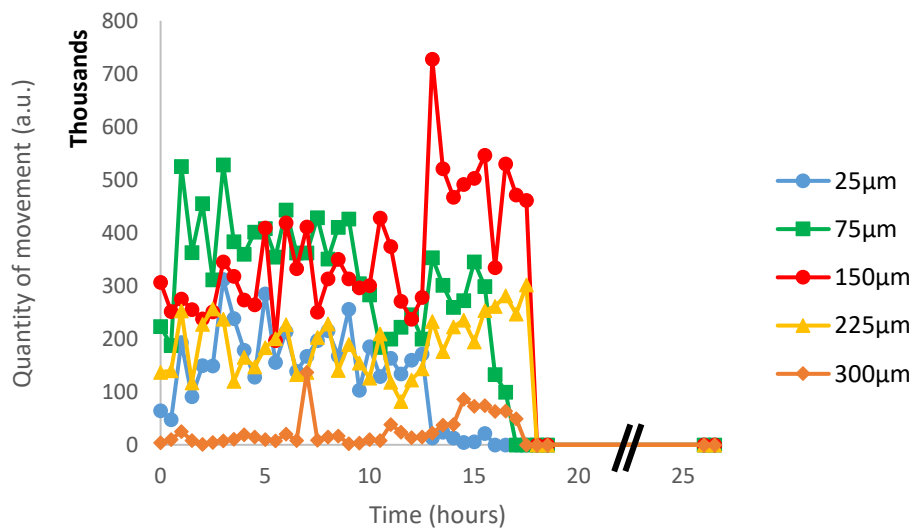


Fig. 8 Quantity of movement (for the embryo 5 in Fig. 6) at superficial (25 µm and 300 µm, middle (75 µm and 225 µm) and central depth (150 µm) over long-term observation.

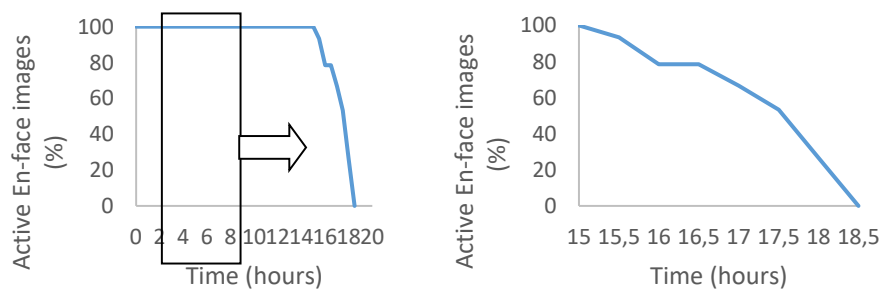


Fig. 9 Percentage of number of *en face* images displaying SV values above threshold at any given time for an embryo (number 5 in Fig.7) over long-term observation. The downward trend is expanded on the right hand to better display the decreasing motion of the embryo over time.

4. Discussion

To date, a limited number of reports have focused on applying functional OCT imaging to study early mammalian embryos [18, 24, 25]. However, to our best knowledge, this is the first time OCT and SV have been applied to a day 7 post-IVF mammalian embryo to resolve its 3D structure and quantify micron-scale movement.

As seen in Fig. 5, OCT can be successfully used to identify the key structures within the bovine blastocyst. Additionally, motion maps can be produced (Fig. 6b) to detect motion in the areas of the blastocyst which are populated with cells.

Over short-term observation, all live embryos consistently displayed higher SV values (Fig. 7) when compared with dead controls suggesting that a live embryo is likely to possess levels of intracellular activity detectable by OCT.

However, the interpretation of the motion measurement became more complex during long-term observation. As shown in Fig. 6A, the embryo had collapsed on itself after 12 h of culture. This is an expected behavior for a blastocyst approaching the end of its life. As shown in Fig 8, this was associated with a surge in movement around the median portion of the embryo at a depth of 150 μm . One possible explanation for this behavior is that the SV measurement is sensitive at the same time to both genuine intracellular movement and to mechanical movement of the blastocyst's tissues caused by the deflation of its internal cavity and that the summation of these two movements caused the spark detected. Indeed, while the embryo could safely be declared dead after 18 h of culture, the actual cessation of biochemical activity within it could have happened at an earlier time point between 15 and 18 hours. On one hand, non-blank motion maps were obtained between 17 and 18 hours of culture after the complete disappearance of the embryo's blastocoel when mechanical motion seemingly came to an end, suggesting that the embryo more likely ceased all biochemical activity around the 18th hour mark. On the other hand, this might not be the only possible interpretation as spontaneous decaying processes, not necessarily linked with intra-cellular activity, could have been detected instead. However, these type of movements were not present in the dead controls. Therefore, based on the comments above, whilst the decaying trend in Fig. 9 expresses the attenuation of motion inside the embryo, it cannot be used to predict the exact time of the embryo's death.

As portrayed in Fig. 8, the embryo did not behave consistently across its depth from a kinetic point of view over long-term functional observation. This finding is not necessarily surprising since it is known that cells or cell groups in a blastocyst can become fragmented or even die [30]. This is also known to happen in embryos that are cryopreserved. Indeed, the cryopreservation of an embryo in liquid nitrogen is a standard procedure, however not all embryos survive the freeze thawing process and those that do are likely to suffer from various levels of damage [31]. Cryodamage assessment on a per embryo basis is very challenging due to the invasive nature of the tests available. Very few papers have used OCT to investigate cryodamage in embryos [32, 33] and none of them studied blastocyst stage embryos which are widely cryopreserved in both human and animal IVF systems. The SV analysis here described could become a useful tool to quantify the level of damage sustained by cryopreserved embryos within minutes of thawing and without a need for extended culture. The results of this assessment would be easy to interpret since they would simply take the form of percentages of *en face* images in motion, as shown in Fig. 8.

5. Conclusions

We anticipate that in future studies, OCT, due to its potential submicron axial resolution, could be used to obtain precise measurements of the shape and volume of a blastocyst's inner cell mass, since these parameters have been shown to correlate well with implantation rates when measured by conventional microscopy [26]. In a similar way, OCT can be used to measure non-invasively the volume of a blastocyst's trophectoderm to obtain another metric of embryo quality: the trophectoderm/inner cell mass ratio [27], an assessment that currently implies the destruction of the embryo with standard methods [28, 29].

The assessment of the percentage of *en face* images in active motion could also be expanded to take into account that, due to the spherical nature of the embryo, not all the *en face* images contain the same number of cells so that a proportion of actively moving embryo volume could be calculated instead. This refinement can be conducted to accurately measure the percentage of fragmentation (intended as non-viable material) present in an embryo, a metric closely associated with viability which is currently estimated subjectively [6].

In conclusion, OCT and SV analysis hold promise to become useful tools for the rapid identification of embryos with poor viability for example after freeze/thawing. The proper adjustment of the embryo prior to measurements based on the *en face* direct view of the Master Slave OCT method further facilitates the procedure.

Funding

S. Caujolle, A.Podoleanu and T. Feuchter acknowledge the UBAPHODESA Marie Curie European Industrial Doctorate 607627. M. J. Marques and A. Podoleanu acknowledge the ERC Proof-of-Concept 'AMEFOCT' 680879. R. Cernat and A. Podoleanu are supported by the NIHR Biomedical Research Centre (BRC) at Moorfields Eye Hospital NHS Foundation Trust, UCL Institute of Ophthalmology. G. Silvestri acknowledges the University of Kent for his PhD support. M. J. Marques and A. Bradu acknowledge the EPSRC 'REBOT' EPN0192291 project. A. Podoleanu is also supported by the Royal Society Wolfson Research Merit Award. D.K. Griffin acknowledges the Innovate UK grant 10189.

Disclosures

(P) A. Podoleanu and A. Bradu are co-inventors of Master Slave patents assigned to the University of Kent.

Disclosures

The authors declare that there are no conflicts of interests related to this article.

Chapter 5

Summary and Conclusion

Optical Coherence Tomography can be considered as a mature technology. Already several commercial systems from different companies are on the market offering structural and functional images (OCTA images). While there is no doubt about the clinical relevance of the structural images, better resolution and deeper penetration depth are required to go further in the interpretation of the images. For functional/physiological features, OCTA images are judged interesting by the medical community but are still under investigations. OCTA images are not enough and the missing link to see it prospering is to add more quantitation based on the speed of the blood or the vascular density.

The work presented in this thesis has two aims. The first is to demonstrate ultrahigh axial resolution OCT system using a supercontinuum source and achieve structural imaging to resolve fine details of an *in-vivo* sample. The second aim is to add some functional information to the structural imaging and see if it is possible with the different actual OCTA methods to quantify it.

OCT, a structural modality

In this chapter 2, the theory of OCT technology was presented and parameters such as depth of focus and axial and transverse resolution were defined. Axial resolution is directly linked to the light source used and more exactly with the central wavelength and the bandwidth.

To achieve ultrahigh resolution, shorter wavelength and/or larger bandwidth need to be combined. In this work, a supercontinuum source from NKT Photonics A/S was used to enhance the axial resolution by using a large bandwidth. However, using this type of source presents several challenges. One is to keep the large bandwidth through

the system and to minimize the dispersion. For this purpose, components of the system were chosen wisely and the dispersion in the system was fully characterized using a split-spectrum method, and then successfully compensated for by using a tilted glass plate. A second challenge is the noise properties of this source because of the origin of the supercontinuum generation. This is a stochastic phenomenon and for several years has meant this source was considered too noisy for use in biomedical imaging. By comparing a low noise SC with a Ti:Sa laser, a SNR difference of 2dB (in favor of the Ti:Sa laser) can be observed that it is barely noticeable on the cornea images. Every layers of the cornea were resolvable using both sources, proving that SC is a suitable light source solution for OCT imaging.

The scattering signal from the sample is conveyed via an optical wave with an amplitude and phase. The structural images are based only on the amplitudes of the signal ie the information carried out by the phase is discarded. The functional image is having an increasingly large impact in biomedical imaging research, so phase values can no longer be ignored and need to be extracted, and we show this here using both with FT and cMSI. Parts of this work demonstrates that phase values have been equally retrieved from both methods, thus opening the door to a full new range of applications based on the functional features.

OCT, a functional modality

In chapter 3, the focus is made on how the OCT technology can be seen as a functional modality and more exactly on a motion detection technique (OCTA). OCTA can be based on the amplitude and/or phase of the detected optical signal. Several software using these values were used to separate moving from static features in the sample. The OCTA images are improved using spectral or temporal averaging, but a trade-off needs to be found between reducing the noise and better highlighting the moving and static feature versus keeping an acceptable acquisition time and axial resolution of the functional images.

Over the years, a large variety of OCTA methods have been proposed but the question stays the same: how can the angio-amplitudes be associated to a physiological meaning and give additional information of the motion parameters such as the blood speed?

Based on the results of our research, OCT as a functional modality for motion detection (OCTA) is a qualitative method. There is indubitably a link between the angio-amplitudes and speeds, but this depends on several parameters (the inclination or the relative position of the sample from the focal plane) making the link not straight forward. Our study presents some limitations that should be taken into account while reviewing this work. Essentially, the sample was too simple. A more complex sample mimicking the layered structure of the retina, integrating the superficial and deep plexus, would have offered a more realistic approach if in vivo measurements were impractical by presenting too many constraints [1]. Another limitation is in the scattering media used. In this study a 5% diluted intralipid solution was used. However, the shape and size of its particles are not comparable to typical RBCs. This impacts the reflected signal and, therefore, the measurements. Other studies were conducted with blood with anticoagulant [2,3], providing more realistic results. Furthermore, current models are very simple and can take into account just single scattering events [4-8]. More complex models based on the orientation of RBCs and multiple scatterers should be developed [9,10] and adapted to the nature of the vessel (vein or artery). The phantoms could also be replaced by in vivo measurements to have a more realistic result whilst taking into account, for example, the cardiac cycle or underlying movements from the patients. Even if a speed quantification is not possible on just the angio-amplitude, a “quantity of motion” parameter can be defined as in the case study presented in chapter 4.

OCT, structural and functional modality

Characterizing the full sample is required in order to recover the structural and functional information. Usually different systems are needed or in the best cases, a multimodal imaging platform with different modalities to achieve it. Here, we have presented an OCT system combining structural images and functional images. The finest structural images make it possible to have an inner look into the embryo at different depths. In addition, the motion detection, via a motion map (functional images), informs on the active parts of the embryo at a precise time. By processing the structural and functional images over time, the bovine embryo was characterized. This

study can lead to a grading on the survival rate of embryos after insemination. This clearly shows that both types of information are necessary to understand and achieve a full assessment of any living sample.

Outlook

An OCT system was built that was centred around 800 nm for eye imaging, driven a supercontinuum source. In principle, OCT could be designed towards shorter or longer wavelength to achieve even finer axial resolution or enhance the penetration depth respectively [11-15]. Another idea can be to implement a parallel OCT system, in addition to the main one, using another wavelength to observe, for example, the difference in contrast from the different tissue layers (absorption) or to combine finest resolution and deepest penetration depth for a full assessment of the different structure of the eye. This type of source can also be used in a multimodal platform combining PAM and OCT, work presented by one of the other researchers of the project UBAPHODESA [16-18]. Even if no commercial system is available at this stage with this source, its versatility makes it a premium choice to advance OCT technology to its limits and several publications have been reported by different research groups [11-13, 17, 19-21].

Speed quantification is not accessible with the current methods, but OCTA remains the central focus of ophthalmologic clinical research and its potential to diagnose early diseases as glaucoma or AMD show a lot of promise. Clinicians start to feel that speed is, perhaps, not the most relevant parameter to quantify but to have access to the vessel density is more important [22-28]. From a more technological point of view, combining OCTA with spectroscopic OCT will allow the clinician access to oxygenation vessel maps [29-33].

To conclude, even if OCT can be considered as a mature technology, new innovations are certainly on the way. The gap between OCT systems present in the OCT research lab and those used by the clinicians is huge. To enable the full potential of OCT for biomedical imaging, quicker translation of technology is needed to allow the clinicians or biologists to provide feedback on the utility of the new features added by research.

For example, applying the same protocol presented in chapter 4 but with an OCT inside an incubator will allow a full characterization at different stage of the embryo evolution permitting the biologist to have an inside look never achieved before.

References

- [1] H.J. Lee, N.M. Samiudin, T.G. Lee, I. Doh and S.W. Lee, “Retina phantom for the evaluation of optical coherence tomography angiography based on microfluidic channels,” *Biomed Opt Express*. 3;10(11):5535-5548 (2019)
- [2] J. Tokayer, Y. Jia, A.H. Dhalla and D. Huang, “Blood flow velocity quantification using split-spectrum amplitude-decorrelation angiography with optical coherence tomography,” *Biomed Opt Express*. 2013 Sep 3;4(10):1909-24. doi: 10.1364/BOE.4.001909. PMID: 24156053; PMCID: PMC3799655
- [3] J.P. Su, R. Chandwani, S.S. Gao, A.D. Pechauer, M. Zhang, J. Wang, Y. Jia, D. Huang and G. Liu, “Calibration of optical coherence tomography angiography with a microfluidic chip,” *J Biomed Opt*. 2016 Aug 1;21(8):86015. doi: 10.1117/1.JBO.21.8.086015. PMID: 27557344; PMCID: PMC4995373.
- [4] J. Zhu, C.W. Merkle, M.T. Bernucci, S.P. Chong and V.J. Srinivasan, “Can OCT Angiography Be Made a Quantitative Blood Measurement Tool?,” *Appl Sci (Basel)*. 2017 Jul;7(7):687. doi: 10.3390/app7070687. Epub 2017 Jul 4. PMID: 30009045; PMCID: PMC6042878.
- [5] V.J. Srinivasan, H. Radhakrishnan, E.H. Lo, E.T. Mandeville, J.Y. Jiang, S. Barry and A.E. Cable, “Oct methods for capillary velocimetry,” *Biomed Opt Express*. 2012;3:612–629
- [6] Y. Wang and R. Wang, “Autocorrelation optical coherence tomography for mapping transverse particle-flow velocity,” *Opt Lett*. 2010;35:3538–3540.
- [7] J. Tokayer, Y. Jia, A.H. Dhalla and D. Huang, “Blood flow velocity quantification using split-spectrum amplitude-decorrelation angiography with optical coherence tomography,” *Biomed Opt Express*. 2013;4:1909–1924.
- [8] W.J. Choi, Y. Li, W. Qin and R.K. Wang, “Cerebral capillary velocimetry based on temporal oct speckle contrast,” *Biomed Opt Express*. 2016;7:4859–4873.
- [9] A.E. Hartinger, A.S. Nam, I. Chico-Calero and B.J. Vakoc, “Monte carlo modeling of angiographic optical coherence tomography,” *Biomed Opt Express*. 2014;5:4338–4349.

- [10] P. Cimalla, J. Walther, M. Mittasch and E. Koch, “Shear flow-induced optical inhomogeneity of blood assessed in vivo and in vitro by spectral domain optical coherence tomography in the 1.3 μm wavelength range,” *J. Biomed Opt.* 2011;16:116020.
- [11] A. Lichtenegger, D.J. Harper, M. Augustin, P. Eugui, S. Fialová, A. Woehrer, C.K. Hitzenberger, and B. Baumann, “Visible light spectral domain optical coherence microscopy system for ex vivo brain imaging,” *Optics in the Life Sciences Congress*, Optical Society of America, p. JT4A.16 (2017).
- [12] P. Marchand, D. Szlag, A. Bouwens, and T. Lasser, “In vivo high-resolution cortical imaging with extended-focus optical coherence microscopy in the visible-NIR wavelength range,” *Journal of Biomedical Optics*. 23(03):1, 10.1117/1.JBO.23.3.036012 (2018).
- [13] P. Marchand, A. Bouwens, D. Szlag, D. Nguyen, A. Descloux, M. Sison, S. Coquoz, J. Extermann, and T. Lasser, “Visible spectrum extended-focus optical coherence microscopy for label-free sub-cellular tomography,” *Biomedical Optics Express*. 8:3343-3359. 10.1364/BOE.8.003343 (2017).
- [14] M. Maria, I.B. Gonzalo, T. Feuchter, M. Denninger, P.M. Moselund, L. Leick, O. Bang and A. Podoleanu, “Q-switch-pumped supercontinuum for ultra-high resolution optical coherence tomography,” *Opt. Lett.* 42, 4744–4747, 10.1364/OL.42.004744 (2017).
- [15] N. Møller Israelsen, M. Maria, M. Mogensen, S. Bojesen, M. Jensen, M. Haedersdal, A. Podoleanu, and O. Bang, “The value of ultrahigh resolution OCT in dermatology – delineating the dermo-epidermal junction, capillaries in the dermal papillae and vellus hairs,” *Biomed. Opt. Express*, 9(5): 2240-2265 (2018).
- [16] M. Bondu, M., C.D. Brooks, C. Jakobsen, K. Oakes, P.M. Moselund, L. Leick, O. Bang, and A. Podoleanu, “High energy supercontinuum sources using tapered photonic crystal fibers for multispectral photoacoustic microscopy,” *Biomedical Optics*, 21(6), 061005 (2016).
- [17] X. Shu, M. Bondu, B. Dong, A. Podoleanu, L. Leick, and H.F. Zhang, “High energy supercontinuum sources using tapered photonic crystal fibers for multispectral photoacoustic microscopy,” *Biomedical Optics*, 21(6), 061005 (2016).

- [18] M. Bondu, M.J. Marques, P.M. Moselund, G. Lall, A. Bradu, and A. Podoleanu, "Multispectral photoacoustic microscopy and optical coherence tomography using a single supercontinuum source," *Elsevier Photoacoustic*, 9:21-30 (2017).
- [19] J. Yi, Q. Wei, W. Liu, V. Backman, and H.F. Zhang, "Visible-light optical coherence tomography for retinal oxymetry," *Opt. Lett.* (11), 1796–1798, doi:[http:// dx.doi.org/10.1364/OL.38.001796](http://dx.doi.org/10.1364/OL.38.001796) (2013).
- [20] D.J. Harper, M. Augustin, A. Lichtenegger, P. Eugui, C. Reyes, M. Glösmann, C.K. Hitzenberger, and B. Baumann, "White light polarization sensitive optical coherence tomography for sub-micron axial resolution and spectroscopic contrast in the murine retina," *Biomed. Opt. Express* 9:2115-2129 (2018).
- [21] X. Shu, L. Beckmann, and H.F. Zhang, "Visible-light optical coherence tomography: a review," *Journal of Biomedical Optics*, 22(12), 121707 (2017).
- [22] F.K. Chen, M. Menghini, A. Hansen, D. A. Mackey, I. J. Constable, and D. M. Sampson, "Intrasession Repeatability and Interocular Symmetry of Foveal Avascular Zone and Retinal Vessel Density in OCT Angiography," *Transl Vis Sci Technol*, 7: 6. (2018).
- [23] C. Czako, G. Sandor, M. Ecsedy, Z. Recsan, H. Horvath, Z. Szepessy, Z. Z. Nagy, and I. Kovacs, "Intrasession and Between-Visit Variability of Retinal Vessel Density Values Measured with OCT Angiography in Diabetic Patients," *Sci Rep*, 8: 10598. (2018).
- [24] T. Hirano, K. Chanwimol, J. Weichsel, T. Tepelus, and S. Sadda, "Distinct Retinal Capillary Plexuses in Normal Eyes as Observed in Optical Coherence Tomography Angiography Axial Profile Analysis," *Sci Rep*, 8: 9380 (2018).
- [25] M.W. Lee, K. M. Kim, H. B. Lim, Y. J. Jo, and J. Y. Kim, "Repeatability of vessel density measurements using optical coherence tomography angiography in retinal diseases," *Br J Ophthalmol.* (2018).
- [26] H.B. Lim, Y. W. Kim, J. M. Kim, Y. J. Jo, and J. Y. Kim, "The Importance of Signal Strength in Quantitative Assessment of Retinal Vessel Density Using Optical Coherence Tomography Angiography," *Sci Rep*, 8: 12897 (2018).
- [27] K. Tarassoly, A. Miraftabi, M. Soltan Sanjari, and M. M. Parvaresh, "The Relationship between Foveal Avascular Zone Area, Vessel Density, and

- Cystoid Changes in Diabetic Retinopathy: An Optical Coherence Tomography Angiography Study," *Retina*, 38: 1613-19 (2018).
- [28] O. Yanik Odabas, S. Demirel, E. Ozmert, and F. Batioglu, "Repeatability of automated vessel density and superficial and deep foveal avascular zone area measurements using optical coherence tomography angiography: Diurnal Findings," *Retina*, 38: 1238-45 (2018).
- [29] F. Fleischhauer, S. Caujolle, T. Feuchter, R. Rajendram, L. Leick, and A. Podoleanu, "Spectroscopic low coherence interferometry using a supercontinuum source and an ultra broadband spectrometer," *Proc.SPIE*, 9697 (2016).
- [30] U. Morgner, W. Drexler, F.X. Krärtner, X.D. Li, C. Pitris, E.P. Ippen, and J.G. Fujimoto, "Spectroscopic optical coherence tomography," *Opt.Lett.*, 25(2):111-113 (2000).
- [31] C.C. Xu, D.L. Marks, M.N. Do, and S.A. Boppart, "Separation of absorption and scattering profiles in spectroscopic optical coherence tomography using a least-squares algorithm," *Opt. Express*, 12(20): 4790-4802 (2004).
- [32] B.E. Bouma, S.H. Yun, B.J. Vakoc, M.J. Suter, and G.J. Tearney, "Fourier-domain optical coherence tomography: recent advances toward clinical utility," *Curr Opin. Biotechnol*, 20(1):111-118 (2009).
- [33] R. Leitgeb, M. Wojtkowski, A. Kowalczyk, C.K. Hitzenberger, M. Sticker, and A.F. Fercher, "Spectral measurement of absorption by spectroscopic frequency-domain optical coherence tomography," *Opt. Lett.*, 25(11):820-822 (2000).
-